EXPERIMENTAL INVESTIGATION OF THE INTERACTION OF AN INTENSE RELATIVISTIC ELECTRON BEAM WITH A PLASMA

by

Anthony Keith Laurence Dymoke-Bradshaw

A Thesis submitted in partial fulfilment of the requirements for the degree of Doctor of Philosophy of the University of London and for the Diploma of Membership of the Imperial College.

Plasma Physics Group,
Physics Department,
Imperial College,
London SW7.

February 1980

ABSTRACT

An experimental investigation into the interaction of an intense relativistic electron beam with a magnetised plasma is reported. The beam has parameters, ~ 50kA, 350kV, 100ns duration and a current density of ~ 15kA/cm^2 which is greater than reported elsewhere for a magnetised system. The plasma is primarily that produced by injection of the beam into neutral hydrogen (0.1 to 10 torr). Some work on injection into a preformed plasma, with parameters n_e ~ 3.10^{15}/cc, T_e ~ 3eV is also presented.

The energy deposited in the plasma by dissipation of the return current is measured directly. The total energy content is measured by diamagnetic signals. The bulk electron energy is obtained by low α ruby laser scattering. Spectral linewidths of H_α and H_β are used to find the ion energies; the former is corrected by an experimentally determined optical depth. The presence of a high energy electron tail is investigated with soft X-ray measurements. An energy balance is sought on the basis of these measurements and a comparison between the total energy content and that deposited by the return current is made. The total energy transferred is found to be ~ 2.10^{18} eV/cc. The width of the H_α spectral line indicates a heavy particle energy density of ~ $1.5 \cdot 10^{18}$ eV/cc whilst the laser scattering indicates an electron energy density of ~ 4.10^{16} eV/cc. The effect of beam scatter and beam current rise time, on the deposited energy, is also investigated.

It is found that deposition into neutral hydrogen is greater than classical and maximum at low pressures. The interaction is also stronger for a fast rising beam current and low angular scatter. This last dependence is the main result of the investigation as it implies that the turbulence enhancing the return current dissipation is beam driven in accordance with present theories rather than return current driven. Reasonable agreement found between the total energy deposited and that

due to return current dissipation indicates that this is the primary deposition method.

CONTENTS

		Page
CHAPTER 1:	INTRODUCTION	
1.1	The application of Intense Relativistic Electron Beams to Plasma Heating	13
1.2	Intense Beams	14
1.3	Beam Strength ν/γ.	16
1.4	Space-Charge Neutralization	17
1.5	Ionization of Target Gas	18
1.6	Magnetic Neutralization	20
1.7	Beam Plasma Interaction Mechanisms	20
1.8	The Proposed Experiment and its Main Characteristics	28
1.9	Radial Confinement	28
1.10	Beam-Plasma Diagnostic Techniques	29
1.11	Brief Summary of the Findings of this Work	31
1.12	Units	32
1.13	Co-ordinate System	32
1.14	Trade Names	32
CHAPTER 2:	THE APPARATUS	
2.1	Introduction	34
2.2	The Beam Generator	34
2.3	Interaction Chamber and Guide Field	40
2.4	Z-Discharge	47
CHAPTER 3:	DIAGNOSTIC EQUIPMENT	
3.1	Introduction	51
3.2	Beam Generator Monitors	51
3.3	Beam Monitors	52
3.4	Plasma Magnetic Monitors	55
3.5	Optical Plasma Diagnostics	61
3.6	X-ray Diagnostics	74

		Page
3.7	Operational Notes	75
CHAPTER 4:	RESULTS OF INJECTION OF THE BEAM INTO NEUTRAL GAS	
4.1	Introduction	78
4.2	Gross Beam Behaviour	78
4.3	Beam and Net Currents	83
4.4	Spatial Variation of B_θ.	96
4.5	Plasma Resistivity and the Return Current Dissipation (nj_p^2).	100
4.6	Plasma Diamagnetism Results	107
4.7	Laser Scattering Results	117
4.8	Spectral Line Measurements	124
4.9	X-ray Measurements	134
CHAPTER 5:	DISCUSSION	
5.1	Introduction	137
5.2	Diamagnetism and Return Current Dissipation	137
5.3	Ion Temperature Time History	139
5.4	Electron Energy Balance	144
5.5	Integration Results	151
5.6	Estimates of the Limiting Parameters of a High Energy Electron Tail.	154
5.7	Detectability of a High Energy Electron Tail by Laser Scattering	157
5.8	Oscillation of Diamagnetic Signals.	158
5.9	Post-Beam Increase in I_{NET}.	160
5.10	Comparison of Energy Densities	162
5.11	Resistivity Comparisons	164
5.12	Beam-Plasma Stopping Length	168
5.13	Conclusions	168

Page

CHAPTER 6: CONCLUSIONS

6.1 Diagnosis of Beam-Plasma Systems 170

6.2 Plasma Resistivity 172

6.3 Conclusions 172

6.4 Future Work 173

APPENDIX I: NEUTRAL PARTICLE CONFINEMENT 174

APPENDIX II: THE EFFECT OF NEUTRALS ON THE MAGNETOSONIC WAVE VELOCITY 179

APPENDIX III: FOIL CLAMPING 182

APPENDIX IV: BEAM SCATTERING 183

APPENDIX V: SELF FOCUSSING IN THE DIODE 187

APPENDIX VI: OSCILLATOR STRENGTHS FOR HYDROGEN LINES 188

APPENDIX VII: NUMERICAL INTEGRATION OF ENERGY BALANCE EQUATIONS 190

APPENDIX VIII: INJECTION INTO A PREFORMED PLASMA 198

ACKNOWLEDGEMENTS 201

REFERENCES 203

LIST OF FIGURES

		Page
CHAPTER 1		
1.1	Typical beam, plasma and net current waveforms.	21
1.2	Plots of $(\Delta n/n_b)$ versus $(\theta^2)^{\frac{1}{2}}$ for various γ.	27
CHAPTER 2		
2.1	Schematic showing the main elements of the beam generator and their parameter regimes.	35
2.2	Schematic of the beam generator showing the components.	37
2.3	Equivalent charging circuit for the pulse forming line.	40
2.4	Examples of prepulse waveforms.	41
2.5	A field coil module.	43
2.6	Geometry for force calculation.	45
2.7	Plot of the axial applied magnetic field.	46
2.8	Schematic of neutral gas interaction chamber.	48
2.9	Schematic of z-discharge interaction chamber.	49
2.10	Example of the z-discharge current waveform.	50
CHAPTER 3		
3.1	Schematic of Faraday Cup.	53
3.2	Current paths within the Faraday Cup.	53
3.3	Schematic of a Rogowski coil.	54
3.4	Use of the Faraday Cup with the z-discharge.	56
3.5	Section through a Rogowski coil mounting flange.	57
3.6	The construction of a magnetic probe.	57
3.7	Diamagnetic loop in mounting flange.	59
3.8	In situ Rogowski coil calibration.	61
3.9	The laser scattering layout.	63
3.10	Schematic of fibre bundle and p.m. tube arrangement.	64
3.11	The circuit of the p.m. tube dynode chains.	65
3.12	Typical Raleigh scattered light signals.	69

		Page
3.13	A typical Thomson scattered light signal.	69
3.14	Photograph of dye laser system.	72
3.15	Layout of the absorption experiment.	72
3.16	Layout of the streak photography experiment.	73
3.17	A typical arrangement of the triggering circuit.	76
CHAPTER 4		
4.1	A plot of transmitted beam energy versus fill pressure.	79
4.2	Various anode foil damage patterns.	81
4.3	Damage to the calorimeter collector.	82
4.4	Examples of streak photographs.	84
4.5	Beam and net current waveforms.	86
4.6	Plots of the maximum net current versus fill pressure and the beam rate of rise.	88
4.7	A typical net current waveform.	90
4.8	An example of unneutralized beam current.	90
4.9	Difference in the net current decay with and without an applied B_z.	91
4.10	Plot of $^1/k$ versus fill pressure.	92
4.11	Examples of post beam rises in the net current.	93
4.12	Examples of beam and net current waveforms showing effect of anode foil type and beam rate of rise.	95
4.13	Plot of fractional current neutralization versus fill pressure.	96
4.14	B_θ waveforms.	98
4.15	Plot of net current at two radii.	99
4.16	Plot of ΔI_{NET} versus fill pressure.	101
4.17	Plots of plasma resistivity versus time.	104
4.18	Plots of $\eta_{\parallel} j_{pz}^2$ versus time.	105
4.19	Plots of W_{OHM} versus fill pressure.	106

		Page
4.20	Diagram showing field and diamagnetic loop configuration.	111
4.21	Plots of $^{3}/_{2}$ $NkT_{\perp}$ versus diamagnetic loop voltage.	114
4.22	Examples of diamagnetic loop waveforms.	115
4.23	Plots of W_{DL} versus fill pressure.	116
4.24	Example of laser scattering signals.	118
4.25	Scattered light spectra.	120
4.26	Plots of n_e and T_e versus time.	122
4.27	Example waveforms of H_α and H_β emission.	125
4.28	Copies of H_α absorption traces.	126
4.29	Plot of measured optical depth versus time.	127
4.30	Geometry for calculating the plasma optical depth.	128
4.31	H_α line profiles.	130
4.32	n_e and T_e versus $\Delta\lambda_{\frac{1}{2}\frac{1}{2}}$ for H_α and H_β.	131
4.33	Two examples of the deconvolution of Stark and Doppler components of the H_α and H_β lines.	133
4.34	Plot of T_i versus time.	134
4.35	Plot of peak X-ray signal versus fill pressure.	135
4.36	X-ray pinhole photograph and associated geometrical optics.	135

CHAPTER 5

5.1	Plot of T_i versus time.	140
5.2	Plot of χ_{ion} versus T_e for hydrogen.	151
5.3	Integration results.	152
5.4	Geometry for soft X-ray detection.	155
5.5	Plot of n_{tail} versus T_{tail}.	156
5.6	Plots of classical resistivity.	165

APPENDIX I

AI.1	Ion/neutral particle trajectories.	178

Page

APPENDIX II

AII.1 Plot of τ_A versus T_i. 181

APPENDIX III

AIII.1 Diagram of foil clamp. 182

APPENDIX IV

AIV.1 Plot of R.M.S. beam scatter angle. 186

AIV.2 Plot of $^{\Delta v}"/v_{"}$ versus r. 186

APPENDIX VIII

AVIII.1 Example waveforms of I_{NET} and I_{BEAM} for injection into a plasma. 199

LIST OF TABLES

CHAPTER 3

3.1 Diagnostic Combinations. 77

CHAPTER 6

6.1 Comparison of I.C. and P.I. parameters. 171

LIST OF ABBREVIATIONS

This is an incomplete list as the majority of abbreviations used are well known.

Al	Aluminium
Al/My	Aluminized Mylar
A-K	Anode-Cathode
A.W.R.E.	Atomic Weapons Research Establishment
B.I.C.C.	British Insulated Callender's Cables
br	Bremsstrahlung (subscript)
cond	conduction (subscript)

div	division
DL	Diamagnetic Loop (subscript)
E.M.I.	E M I Industrial Electronics Limited.
eq	equipartition (subscript)
f.w.h.m.	full width half maximum
I.A.E.A.	International Atomic Energy Agency
I.C.	Imperial College
L.E.D.	light emitting diode
N.D.	neutral density
P.F.L.	pulse forming line
P.I.	Physics International
recomb	recombination (subscript)
TOT	total (subscript)
U.K.A.E.A.	United Kingdom Atomic Energy Authority.

CHAPTER ONE

INTRODUCTION

1.1 The Application of Intense Relativistic Electron Beams to Plasma Heating

The advent of Intense Relativistic Electron beams in the late 1960's, following work at A.W.R.E. Aldermaston, has resulted in the applications of electron beams being extended to many new fields where either a very high power is required or where the large self fields of an intense beam can produce effects otherwise unobtainable. Within the plasma physics field, examples of such uses are:

1. Plasma heating
2. Pellet compression FREEMAN et al. (1977)
3. Laser excitation
4. Flash X-ray production
5. Microwave production NATION et al. (1971)
6. Reverse field generation FRIEDMAN (1970).

The great attraction of electron beams is the high efficiency with which they can be produced (up to ~ 70% overall) and low cost per unit of energy, particularly when compared with lasers.

The interaction of electron beams with plasmas has attracted much theoretical and experimental effort for many years. With the intense beams now available however, strong interactions at plasma densities of interest to the fusion programme have become a possibility. It is with this aspect in mind that the work presented here has been performed. That the energy of an electron beam can be transferred to a plasma at a rate exceeding that given by classical binary coulomb collisions has long been known. PIERCE (1948) observed ion fluctuations due to a relative drift between electrons and ions and inferred the presence of some turbulent interaction mechanism. Various streaming

instabilities have since been observed in beam plasma situations and it is the application of such effects to plasma heating that has lead to a renewal of interest in the field. The interaction by such instabilities is usually a function of the ratio of beam and plasma densities ($^{n_b}/_{n_p}$), with a peak near unity. Values of n_b now obtainable in unfocussed beams are typically $\lesssim 10^{13}$ cm^{-3} which means that significant interaction with fusion-like plasmas is a possibility. Schemes envisaged include injection into long solenoidally confined plasmas to the injection into a torus, HAMMER and PAPADOPOULOS (1975).

An additional effect of intense and relativistic beams is the induction of a return current in the plasma due to the rising self magnetic field of the beam. This allows the possibility of heating via the return current by both classical and anomalous resistive dissipation. In some cases return current dissipation may be dominant instead of the primary beam plasma interaction.

1.2 Intense Beams

An electron beam can be termed intense when the self magnetic field generated by the beam current becomes sufficiently large so as to grossly affect the individual beam particle orbits. Both electric and magnetic fields are present in the Laboratory frame of reference, the former arising from the beam space-charge. As long as no other particles or fields are present, the electrostatic repulsive forces will always dominate over the magnetic attractive forces. However, in the limit as the beam velocity approaches c they are equal.

Consider a uniform beam of radius a propagating in a vacuum. The force experienced by a peripheral electron at radius a is given by

$$\underline{F} = e(\underline{v} \wedge \underline{B} + \underline{E}) \qquad 1.1$$

where $\underline{E}$ and $\underline{B}$ are evaluated at radius a and $\underline{v}$ is the beam electron velocity.

Thus

$$\underline{B}\,(a) = \frac{\mu_0\, a\, j_0}{2}\ \hat{\theta} \qquad 1.2$$

$$\underline{E}\,(a) = \frac{a\rho_0}{2\varepsilon_0}\ \hat{r} \qquad 1.3$$

where j_0 and ρ_0 are the beam current and charge densities respectively. Using $v = \beta c$ $\rho_0 = j_0/\beta c$ gives

$$\underline{F} = \frac{ea\, j_0}{2\beta c\varepsilon_0\, \gamma^2}\ \hat{r} \qquad 1.4$$

This is always a radially outward force and tends to zero as $\gamma^2 \to \infty$. The ratio of the magnetic attractive force to the electrostatic repulsive force is

$$\frac{|F_M|}{|F_E|} = (\beta c\mu_0\, a\, j_0/2)/(a\, j_0/2\beta c\varepsilon_0) = \beta^2 \qquad 1.5$$

Consequently, all beams propagating in a vacuum will, in the absence of any applied field, diverge. However, if the beam is propagating through a background plasma, the space-charge fields can eject plasma electrons from the vicinity of the beam. This can result in a neutralization of the repulsive force so that the magnetic field can dominate the beam motion. If the self magnetic field is sufficiently strong it can result in a pinching or stopping of the beam. ALFVEN (1939) estimated the maximum current that could flow under these conditions. If one assumes that an electron at the beam's edge sees a constant magnetic field throughout its orbit, then equating its Larmor radius at the beam edge to half the beam radius gives a simplified condition for stopping. Thus the critical or Alfvén limiting current is

$$I_A = \frac{4\pi\, m_e \beta\gamma c}{e\, \mu_0} \simeq 17{,}000\ \beta\gamma \text{ amps.} \qquad 1.6$$

Currents in excess of this limiting current may be propagated by using different current density profiles, in particular annular beams. Also, the application of an axial guiding B_z field will enable larger currents to propagate. It has been found experimentally that the requirement on B_z is

$$B_z \gtrsim B_\theta$$

rather than

$$B_z >> B_\theta$$

where B_θ is the self field, HAMMER et al. (1972). An applied field is also desirable because it offers some degree of radial confinement of the plasma and stabilization of the beam to hose type and filamentary instabilities.

1.3 Beam Strength ν/γ

The ratio ν/γ is a generally accepted parameter useful in describing the strength of the beam. ν is the number of electrons in a length of beam equal to the electron classical radius in the Laboratory frame of reference. γ is the usual relativistic factor.

$$\nu/\gamma = \frac{N\, e^2 \mu_0}{4\pi m_e\, \gamma} \qquad 1.7$$

where N is the number of electrons per unit length of beam in the Laboratory frame, so that $N = I/e\beta c$. It is simply shown that

$$\frac{\nu}{\gamma} = \frac{I_B}{I_A} \qquad 1.8$$

ν/γ is the number of electrons in a length of beam equal to the classical radius of an electron in the frame of the beam.

Beams have been produced with ν/γ from << 1 to ~ 15 and beams with

ν/γ up to 10 have been used to investigate plasma heating. As ν/γ is related to the total beam current and most beams have comparable risetimes ~ 10 to 20 ns, ν/γ is related to the electric field induced by the rising beam current.

1.4 Space-Charge Neutralization

The injection of a magnetised intense relativistic electron beam into neutral gas is considerably more complicated than that of injection into a preformed plasma because of the ionization processes that occur. The lack of background electrons in the initial stages prevents the space-charge of the beam being neutralized by a divergent flow of plasma electrons. Consequently, the beam space-charge electric fields can reflect beam electrons back to the diode resulting in a stopping of the bulk of the beam. However, some electrons will always overcome the field and propagate. Hence a small space-charge limited current will flow. The magnitude of this current has been calculated by BOGDANKEVICH and RUKHADZE (1971) as

$$I_c = 1.7.10^4(\gamma^{2/3} - 1)^{3/2}/(1 + 2\,\mathrm{Ln}\,b/a)^{-1} \quad A \qquad 1.9$$

for $\gamma = 1.7$, $b/a = 3.8$ as used in this work

$$I_c = 1.28\ \mathrm{kA}.$$

This expression for I_c is in fact for an infinite system and may under estimate I_c for a finite length.

For unmagnetized systems space-charge neutralization may proceed via a radial flow of secondary electrons. Consequently, as ionization builds up so can the beam current. For magnetised systems however, this is not the case. Only an axial flow of electrons can charge neutralize the beam and the distances involved may be great. As there will be a large space-charge density near the anode, space-charge

neutralization will not occur efficiently until there is a conducting channel to the far end of the chamber.

1.5 Ionization of Target Gas

The propagation of a high current beam requires a high degree of space-charge neutralization so that beam electrons are not reflected. For injection into initially neutral gas, neutralization can only occur when the background electron density has risen to greater than the beam density. In addition in a highly magnetized system secondary electrons may not move freely in the radial direction unless $E \gg Bv$. A detailed study of the ionization processes has been made by OLSON (1975); consequently only the salient points will be presented here.

It is generally considered that the ionization in the very early stages is mainly by electron impact with the neutral atoms. The cross-section for this process S_{en} has a peak at ~ 20eV so that the rate coefficient $\beta c S_{en}$, where βc is the velocity of the incident electron, is fairly constant above 20eV. From this OLSON (1975) obtains an approximate time for the background density to rise to equal the beam density of

$$\tau_e \sim 5/p \text{ ns} \qquad \text{(zero beam rise-time)}$$

where p is the fill pressure of hydrogen in torr. For a fill pressure of 100mtorr this gives 50ns which is far greater than observed times which are typically $\lesssim$ 10ns.

OLSON (1975) has explained this descrepancy as due to ion-impact and ion-avalanche ionization. In general electron-avalanche processes are unlikely to contribute unless the electric field is in the range 10^4 - 10^5 V/m/torr. Fields of this small value are likely to be present only near to charge neutralization. For ions with energies > 50keV ion-impact ionization dominates over the charge-exchange processes :-

$$H^+ + H_2 \rightarrow H + H_2^+$$

$$H^+ + H \rightarrow H + H^+$$

Ions are more effective ionizers as they lose little energy in an ionizing collision and may consequently make many such collisions. OLSON (1975) estimates the time for the plasma density to rise to be of the order of the beam (of ions) to be

$$\tau_i \sim 0.55/p \qquad \text{ns} \qquad (E_i > 50\text{keV})$$

That energetic ions are produced when intense electron beams are injected into neutral gas is well known. DREIKE et al. (1977) have reported that electron beams can convert up to ~ 50% of their energy into ion beams in reflex triodes. OLSON (1975) presents an ion-avalanche model in which ions oscillate in the space-charge well at the head of the beam. Ions created at sufficient distance from the centre of a well with $E \geq 10^8 \text{V m}^{-1}$ will obtain enough kinetic energy (50keV) in the well to become ionizers. However, most of the ions will be created at the well centre where the ionizing ions' energy is highest. Although this reduces the efficiency of the process OLSON (1975) obtains an avalanche time t_i of approximately

$$\tau_i \sim 0.33/p \qquad \text{ns.} \quad \text{(zero rise time beam)}$$

which is much nearer the typical observed times.

Once the beam is space-charge neutralized, the current will rise and the electric field will be mainly due to the inductive effects. In this regime, the fields are typically 10^4 - 10^5 Vm^{-1} and electron-avalanche (Townsend-avalanche) is the dominant mechanism and is responsible for the subsequent bulk ionization.

1.6 Magnetic Neutralization

It has been well established experimentally by many workers that in addition to space-charge neutralization some degree of magnetic neutralization will occur. Magnetic neutralization is a result of the induction of a plasma return current by the electric field due to $\partial B_\theta/\partial t$ at the head of the beam. In the case of injection into a perfectly conducting plasma, complete magnetic neutralization can be expected so that the magnetic flux in the plasma remains constant. However, a finite net current, I_{NET}, is always observed ($\underline{I}_{NET} = \underline{I}_{BEAM} + \underline{I}_{PLASMA}$).

In the case of injection into neutral gas, the plasma resistivity is initially too high to permit significant magnetic neutralization. As the plasma density rises, the resistivity falls (turbulent resistivity may also fall) allowing the induced return current to follow changes in the beam current so conserving the B_θ flux at the value prior to the onset of falling resistivity. In this instance, the degree of magnetic neutralization is lower. When the beam switches off, the requirement that B_θ flux be conserved results in the plasma current reversing to a value equal to the previous net current. In Fig. 1.1 a typical example of beam and net currents is shown together with the calculated plasma current.

The main difference between intense and weak beams is that in the former the induced electric field can be strong enough to cause Townsend avalanche in a background target gas, resulting in a rapid rise in the plasma density.

1.7 Beam Plasma Interaction Mechanisms

The classical energy loss rate for relativistic electron beams in a plasma due to binary coulomb collisions is given by TAJIMA (1978) as

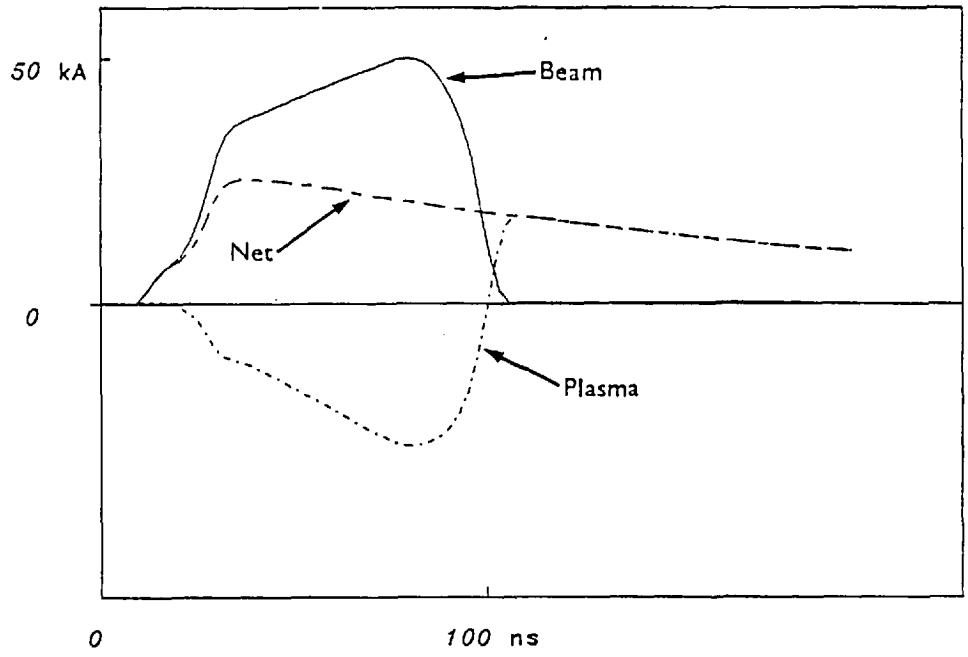

Fig. 1.1 Typical beam, plasma and net current waveforms. $I_{net} = I_{beam} + I_{plasma}$.

$$\frac{dE}{dx} = \frac{e^2 \, T \, \beta_0^2}{\lambda_D^2 \, E_0 (\gamma - 1)} \cdot \mathrm{Ln}\left(n\lambda_D^3 \frac{E_0}{T}\right) \qquad 1.10$$

where E_0 is the incident beam energy, λ_D the Debye length, β_0 and γ the usual relativistic factors, n the plasma number density. Under fusion conditions, this gives stopping lengths of many tens of kilometres.

The growth of turbulence in streaming plasmas has been well known since the observations of PIERCE (1948). It is thought that the presence of such turbulent mechanisms explains the observed stopping lengths of beams which are of the order of tens of metres, ALTYNTSEV (1972), MILLER (1973), KAPETANAKOS (1973), EKDHAL (1974), GOLDENBAUM (1974).

There are two main modes of coupling, a primary interaction between the beam electrons and the plasma and a secondary interaction between the induced return current and the relatively stationary plasma ions. It is generally considered, THODE and SUDAN (1973), that the

relative importance of each mode is dependent upon the beam strength parameter ν/γ, the turbulent dissipation of the return current being more important at higher ν/γ and dominant for $\nu/\gamma \gg 1$. Classical resistivity decay rates for the return current still give very large values for the stopping length.

The ion-acoustic instability is unstable for relative drifts of the electrons and ions in the range,

$$c_s < v_d < v_{th}$$

FRIED and GOULD (1961), where c_s is the sound speed, v_d the drift velocity and v_{th} the electron thermal speed. In addition it is required that $T_e > T_i$ otherwise severe Landau damping of the waves occurs CHEN (1974). The effective collision frequency and associated resistivity resulting from ion-acoustic turbulence has been estimated by SAGDEEV (1967) as

$$\nu_{eff} \sim 10^{-2} \frac{v_d}{c_s} \frac{T_e}{T_i} \omega_{pi} \qquad 1.11$$

and

$$\eta_{ia} \leq \frac{4\pi}{\omega_{pe}^2} \frac{v_d}{c_s} \frac{T_e}{T_i} \omega_{pi} \cdot 10^{10} \ \Omega \ m \qquad 1.12$$

for $v_d \sim c_s$, $T_e \sim T_i$ and $n_e \sim 3.10^{21} \ m^{-3}$

$$\eta_{ia} \sim 3{\cdot}7.10^{-4} \ \Omega \ m$$

This is to be compared with the classical resistivity given by SPITZER (1962) as

$$\eta_{class} \sim 5.2 \cdot 10^{-5} \ Ln\Lambda \ T_e^{-3/2} \ \Omega \ m \qquad 1.13$$

where $Ln\Lambda$ is the plasma parameter. At the initial low T_e ($\sim$ 10eV) this

yields

$$\eta_{class} \sim 1.2 \cdot 10^{-5} \quad \Omega\,m$$

For injection into neutral gas, electron-neutral collisions will also contribute

$$\eta_{en} \sim \frac{n_n \sigma_{en}}{n_e e^2} \sqrt{\frac{kT_e m_e}{2}}$$

$$\sim 6.10^{-} \quad \frac{n_n}{n_e} \quad T_e^{\frac{1}{2}} \quad \Omega\,m \qquad 1.14$$

The ion acoustic instability may therefore play a rôle in plasma heating but the limitations on the relative drift velocity for growth means that the instability can only heat to temperatures corresponding to thermal velocities $\sim (m_i/m_e)^{\frac{1}{2}} v_d$. This gives

$$T_e(max) \sim \frac{m_i}{k} \left(\frac{n_b}{n_e}\right)^2 \beta^2 c^2 f_m \qquad 1.15$$

where k is Boltzman's constant and f_m the degree of magnetic neutralization ($0 < f_m < 1$). For $\beta \sim 0.8$, $n_e/n_b \sim 10^3$, this gives $T_e \sim 280eV$

The primary interaction between the beam and plasma has been studied in detail by many workers, THODE (1975, 1976, 1977), THODE and SUDAN (1973), PAPADOPOULOS (1975, 1976), TAJIMA (1978), RUDAKOV (1971), FAINBERG et al. (1969), GALEEV et al. (1975), LAMPE and SPRANGLE (1975), NISHIKAWA (1968), SCHAMEL et al. (1976) and others. For a cold incident beam, i.e. one with little velocity spread in both the axial and transverse directions, a strong electrostatic (two-stream) instability develops. The overall strength of the interaction and subsequent energy transfer rate from the beam to plasma, depends upon the level at which non-linear processes cause the instability to saturate.

Saturation eventually results in the parametric generation of waves non-resonant with the beam (i.e. with phase velocities very

different from the beam velocity). For a cold incident beam the primary wave spectrum prior to saturation is dominated by a single large amplitude wave with a phase velocity equal to the beam velocity. It should be noted that although the linear growth rate of the initial beam plasma instability is highest for modes propagating at oblique angles to the beam, the problem is still considered to be one dimensional in the longitudinal direction due to the far lower level at which the transverse waves are saturated by a small spread in the beam perpendicular velocity. In addition, a strong axial magnetic field will reduce the perpendicular growth rate, THODE and SUDAN (1973), PAPADOPOULOS (1975), THODE (1976), TAJIMA (1978) and others.

As the wave grows, it will eventually trap beam electrons which have low kinetic energies in the wave frame of reference. Once this happens, a large momentum spread develops in the beam electrons and the monochromatic wave spectrum itself becomes unstable to parametric decay via the oscillating two-stream instability (alternatively named the aperiodic instability, the modified decay instability, spikon or soliton formation, the latter two being descriptive of the behaviour in real space as opposed to wavenumber space). This type of interaction is generally termed the hydrodynamic phase as all the particles interact non-resonantly with the wave spectrum. The low velocity waves produced by this spectral collapse can interact with the plasma electrons to form tails; 1D computer simulations, GALEEV et al. (1975) have shown the growth of tails up to 8 x $v_{thermal}$, whilst low density D.C. beam-plasma experiments have demonstrated the production of tails upto 7 x $v_{thermal}$, WONG and QUON (1975). In addition some energy is expected to go into the ions. GALEEV et al. (1975) calculate this as small, but SCHAMEL et al. (1976) believe it to be significant.

The strength of this single wave type of interaction is characterised by a single parameter S given by THODE and SUDAN (1973) as

$$S = \beta_0^2 \gamma (n_b/2n_p)^{1/3} \qquad 1.16$$

The beam energy loss at saturation is then given by, THODE (1976)

$$\Delta E = \gamma_0 \, m_e c^2 n_b \, S(S + 1)^{-5/2} \qquad S < 0.45 \qquad 1.17$$

and

$$\Delta E = 0.18 \, \gamma_0 \, m_e c^2 n_b \qquad S > 0.45 \qquad 1.18$$

This indicates that for a high enough energy beam, the beam energy loss can be independent of the beam to plasma number densities. This is in agreement with numerical work by THODE (1975), LAMPE and SPRANGLE (1975) and SCHAMEL et al. (1976) but not with experimental results.

In experiments the beams are not purely monochromatic due to scattering in the anode foil, motion in the beam self fields and by scattering at the anode foil due to the discontinuity in B_θ. (On the cathode side of the foil, B_θ is a result of I_B only whilst on the plasma side it is reduced by the plasma return current which then flows radially across the foil. As B_θ changes over a scale length less than a Larmor radius, the electrons will be scattered, see Appendix IV.) THODE (1976) distinguishes between two types of non-monoenergetic beams, scattered and warm. A scattered beam is one which has an angular spread of electrons but with little energy spread; this still results in a spread of parallel energies. A warm beam has a parallel velocity spread comparable to a scattered beam but much smaller angular scatter. The regimes defining the three types of beams are:-

1) Cold $\qquad \dfrac{\Delta v_{\parallel}}{c} << \dfrac{1}{\gamma}\left(\dfrac{n_b}{n_p}\right)^{1/3}$

2) Scattered $\qquad \overline{\theta^2} >> \dfrac{2}{\gamma^3}\,\Delta E$ and $\dfrac{\Delta v_{\parallel}}{c} \gtrsim \dfrac{1}{\gamma}\left(\dfrac{n_b}{n_p}\right)^{I/3}$

3) Warm $\qquad \overline{\theta^2} \lesssim \dfrac{2}{\gamma^3}\Delta E$ and $\dfrac{\Delta v_{\parallel}}{c} \gtrsim \dfrac{1}{\gamma}\left(\dfrac{n_b}{n_p}\right)^{1/3}$ $\qquad 1.19$

where $\overline{\theta^2}$ is the mean square angular scatter. It was generally considered that if $\frac{\Delta v_{\parallel}}{c} > \frac{1}{\gamma}\left(\frac{n_b}{n_p}\right)^{1/3}$ the beam-plasma instability entered the kinetic regime. In this case, Landau growth occurred in the linear phase until saturation occurred due to the parametric decay of the wave spectrum. The beats of two plasma waves react resonantly with a small group of plasma ions to produce ion wave fluctuations which are only lightly damped even for $T_e \sim T_i$, PAPADOPOULOS (1975). The waves resonant with the beam are stabilized by decay to a second plasma wave of lower phase velocity, and an ion wave. The secondary plasma wave is itself stabilized by the production of tails to the plasma electron velocity distribution, whilst the ion waves may be responsible for an enhanced plasma resistivity leading to an increased dissipation of the return current.

However, THODE'S (1976) criterion for the interaction to enter the kinetic regime is more stringent:-

$$\text{Kinetic for } \frac{\Delta n}{n_b} < 0.15 \pm 0.05 \text{ and } (\overline{\theta^2})^{\frac{1}{2}} > \frac{1}{\gamma_o}$$

where $(^{\Delta n}/n_b)$ is the fraction of beam electrons which can be considered as mono-energetic in the beam direction. In the intermediate regime between hydrodynamic and kinetic, quasi-hydrodynamic, the beam energy loss is simply $(^{\Delta n}/n_b)$ of that for the hydrodynamic case, $(^{\Delta n}/n_b)$ being the fraction of electrons that can interact.

THODE (1976) has calculated $(^{\Delta n}/n_b)$ for various values of $(\overline{\theta^2})^{\frac{1}{2}}$ and γ, as is shown in Fig. 1.2. It should be noted that the energy extracted from the beam is dependent upon both $(^{\Delta n}/n_b)$ and γ in such a manner that although the beam-plasma coupling is enhanced by going to less scattered beams, an increase in γ is more important.

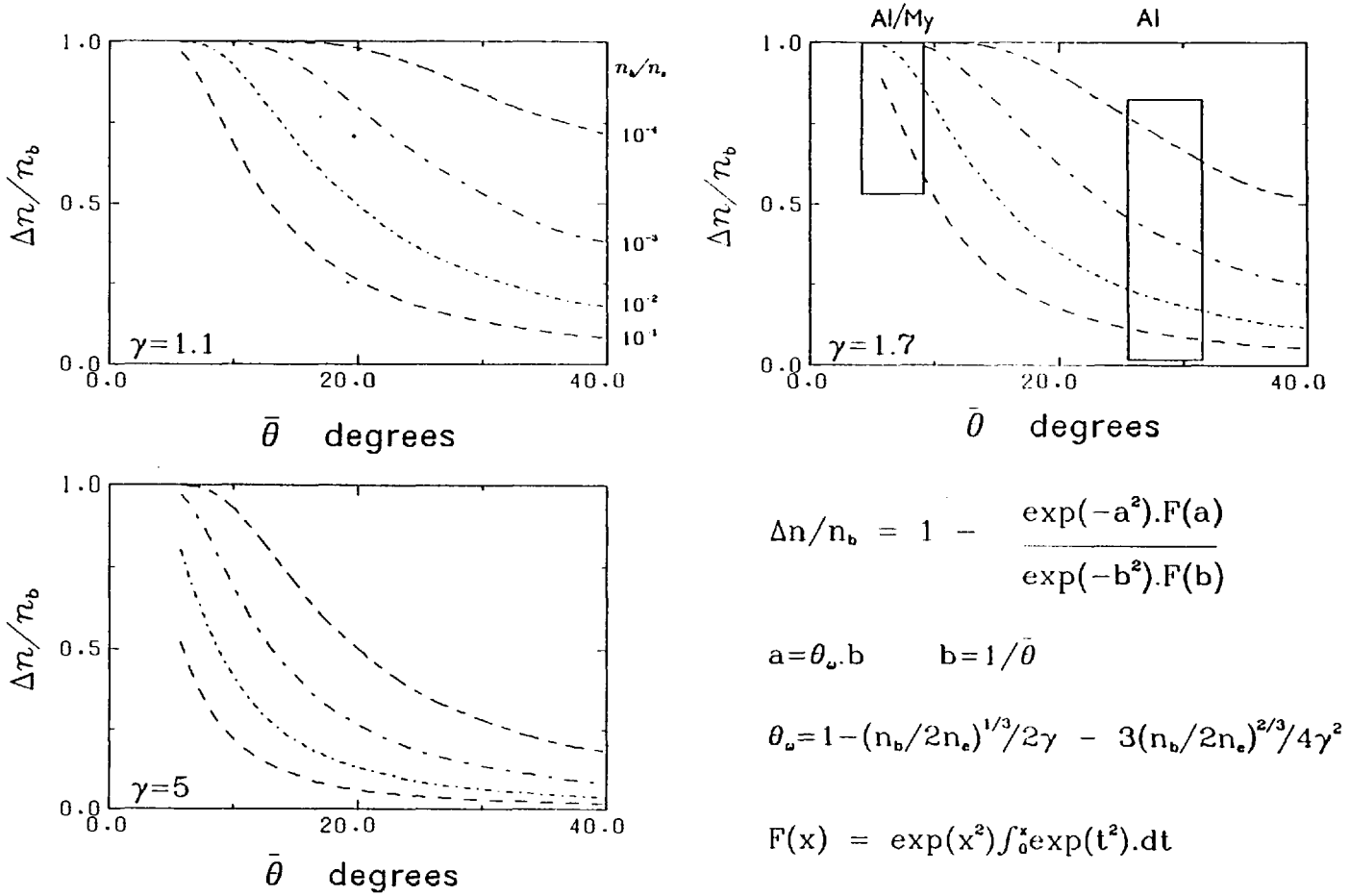

$$\Delta n/n_b = 1 - \frac{\exp(-a^2).F(a)}{\exp(-b^2).F(b)}$$

$a=\theta_\omega.b \qquad b=1/\bar{\theta}$

$$\theta_\omega = 1-(n_b/2n_e)^{1/3}/2\gamma - 3(n_b/2n_e)^{2/3}/4\gamma^2$$

$$F(x) = \exp(x^2)\int_0^x \exp(t^2).dt$$

Fig. 1.2 Plots of $(\Delta n/n_b)$ versus $(\theta^2)^{1/2}$ for various γ. The boxed areas indicate the regimes investigated in this work by using two types of anode foil.

1.8 The Proposed Experiment and its Main Characteristics

The experiments reported here concern the injection of an intense relativistic electron beam through an anode foil and into neutral gas. The object is primarily to find the efficiency with which such beams may interact with the plasma formed by the beam, and if possible to ascertain the nature of any contributory turbulent mechanisms. The types of diagnostics available, however, see Sec. 1.9 and Chapter 3, primarily investigate the more general plasma parameters and information about the turbulent mechanisms may only be inferred by parametric dependencies, e.g. the variation of the plasma energy density upon the initial beam angular scatter.

The basic parameters of the beam system are:-

Voltage	$\geq$ 350 kV
Current	$\leq$ 50 kA
Radius	= 1 cm
Duration	$\approx$ 100 ns
Estimated beam angular scatter	$\approx 6^{o}, 12^{o}, 25^{o}$
ν/γ	$\approx$ 2.4
Applied B_z	$\approx$ 1.5 tesla

The beam is injected into neutral hydrogen gas at atomic filling densities $\geq 6.10^{15}$ cm^{-3}. Some work on injection into a preformed plasma will also be discussed.

1.9 Radial Confinement

As has been indicated the present work uses a magnetized system. The reasons for this are threefold. Firstly, work with an unmagnetized system VANDEVENDER (1974) found that on injection into neutral hydrogen

gas, the plasma return current interacted with the net B_θ field to drive the plasma radially outwards during the beam pulse, i.e. an inverse pinch. When the beam terminated, the reversed plasma current formed a conventional pinch. The rapid expulsion of plasma from the vicinity of the beam resulted in little or no turbulent heating although the ions gained significant radial energies. In order to confine the plasma, therefore, the application of a guide field is necessary.

Secondly, VANDEVENDER (1974) found that injection into a preformed unmagnetized plasma lead to a highly divergent beam, there being little net B_θ confining field set up. Application of a guiding B_z field in this instance would radially confine both the beam and plasma.

The third reason concerns the beam production. The previous system as used by VANDEVENDER obtained a high beam current density by focussing down a beam of larger cross-section in a conical drift tube filled with air at ~1torr. This resulted in a beam with significant angular spread. In addition, the diode was being driven near the self focussing condition, see Appendix V, also giving a large angular scatter. By applying a sufficiently strong guide field, the beam could be produced in the diode at the working size, focussing eliminated and self focussing prevented thus resulting in a beam with low angular scatter. The angular scatter could then be increased controllably by the use of various thicknesses of anode foils. The relevance of the beam angular scatter to the strength of the beam plasma interaction is discussed in section 1.7.

1.10 Beam-Plasma Diagnostic Techniques

350 kV electrons have a penetrating range of ~ 250 milligrams cm^{-2}. The beam used also has an energy flux of $\lesssim$ 6 MJm^{-2}. Consequently, material objects placed in or near the beam suffer severe damage from

one shot. Diagnostic techniques are, therefore, limited to observations of the following:

1. Transmitted beam energy
2. External electric and magnetic fields
3. Spontaneously emitted radiation and particles
4. The use of electromagnetic probe radiation.

Whilst this still leaves many options, the inability to obtain magnetic probe measurements within the beam channel is unfortunate. Such information could give insight to the spatial variation of plasma resistivity and to the plasma diffusive properties. Recent developments by other workers at Physics International, have produced probes with disposable outer shells which may be inserted into the beam. Such probes are far too bulky to be considered here. They would cause gross perturbations to the fields under observation.

(i) The transmitted energy was measured with a simple thermocouple calorimeter.

(ii) The measurements made of the external magnetic fields include the following:

1. $\int \underline{B}_{NET} \cdot \underline{dl} = I_{NET}$ - Measured with Rogowski coils.
2. $\int \underline{B}_{BEAM} \cdot \underline{dl} = I_{BEAM}$ - Measured with Rogowski coils.
3. B_θ - Measured with small multiturn probes at two radial positions external to the beam.
4. ΔB_z (the change in the applied field) - Measured with a diamagnetic loop at two axial positions.

(iii) The measurements made of the emitted radiation include:

1. Time resolved spectral emission profiles of H_α and H_β
2. Time resolved emission near 6943 Å
3. Optical streak photography.

4. Hard and Soft X-ray emission, time resolved, time integrated and pin hole photography.

(iv) Measurements with electromagnetic probes include:

1. Ruby laser scattering.
2. Time resolved spectral absorption profiles of H_α.

1.11 Brief Summary of the Findings of this Work

Whilst a fair number of diagnostics have been applied to the system, a complete picture of the interaction is still far from clear. The overall isotropized energy density obtained from plasma diamagnetism can be typically $\geq 10^{18}$ eV cm^{-3} if the initial beam is cold (i.e. a beam with low angular scatter) and the beam current rises quickly. This energy density agrees well with the ion temperature obtained from spectral line profiles, which falls from $\sim$ 100 eV to $\sim$ 20 eV in 150 ns. However, the return current dissipation although measured directly as $\sim 10^{18}$ eV cm^{-3}, does not produce heating of the bulk electrons which remain at ~ 5 to 15 eV.

The diamagnetism is found to fall significantly as one moves away from the injection end of the chamber. This suggests a drop in the interaction strength possibly due to heating of the beam (the beam used was not highly relativistic, $\gamma \sim 1.7$). It has been well established, GREENSPAN (1976) that hot beams interact far less strongly than cold beams and further evidence has been found in this work. That this is the case, means that the energy transfer is by some collective process requiring correlation between the beam electron velocities.

The mechanism for ion heating is not clear. The probable existence of a tail to the electron velocity distribution at early times and the inability to temporally resolve the ion heating phase, which must occur in less than 20 ns, might indicate that heating occurs during the

transit of the beam front by ion acceleration in the large associated space-charge fields. However, the uncertainty in the theoretical work on the possibility of turbulent ion heating leaves considerable room for doubt.

1.12 Units

Units are in M.K.S. unless otherwise stated. However, in view of common usage in the field, many parameters will be defined in other units, for example:

1. Temperatures are in electron volts at all times so that Boltzman's constant becomes $1.6 \cdot 10^{-19}$ joules per eV.
2. Energy densities are quoted in eV cm^{-3}, some formulae use J m^{-3}.
3. Number densities are quoted in cm^{-3}, some formulae use m^{-3}.

1.13 Co-ordinate System

A right handed cylindrical co-ordinate system is generally used with positive z in the direction of beam propagation. In cases where a cartesian system is used, z is again in the beam direction, x in the horizontal plane, y in the vertical plane with the origin at the centre of the scattering volume.

1.14 Trade Names

A number of trade names have been used for the sake of brevity. These are:

1. Perspex - polymethylmethacrylate.
2. Mylar - polyethyleneterephthalate.
3. Poco graphite - Special highly isotropic graphite made by POCO, a subsidiary of Union Carbide.

4. Tufnol - Synthetic resin bonded paper or linen.

5. Pyrex - glass: heat resistant.

CHAPTER TWO

THE APPARATUS

2.1 Introduction

In this chapter the apparatus used is described. The apparatus is best divided into two sections for explanatory purposes: (i) the beam generator and (ii) the interaction chamber. The diagnostic equipment is described in Chapter 3. A schematic diagram of the system showing the main elements is shown in Fig. 2.1. The four main blocks are, the voltage multiplication stage, the pulse forming stage, the electron beam production and the interaction chamber.

Much of the generator was inherited from the previous user, J.P. VanDevender. A detailed description of the generator is given in VANDEVENDER (1974) and only an outline and modifications will be given here. The diode and interaction chamber have been replaced to allow the application of a magnetic guide field. The pulse forming line has been renewed.

2.2 The Beam Generator

The generator design is conventional in that it utilizes the technology initially developed by J.C. MARTIN and co-workers at A.W.R.E. Aldermaston.

Fig. 2.2 shows the layout and components of the generator; the numbers in the text refer to this figure. An eight stage Marx generator (2) is used for voltage multiplication. This pulse charges a water dielectric, pulse forming line (3). The line is switched into the load (4) (the diode) by a self closing sulphur hexafluoride gas switch (11). The diode is a vacuum field emission type and the electron beam it produces is extracted through a foil anode.

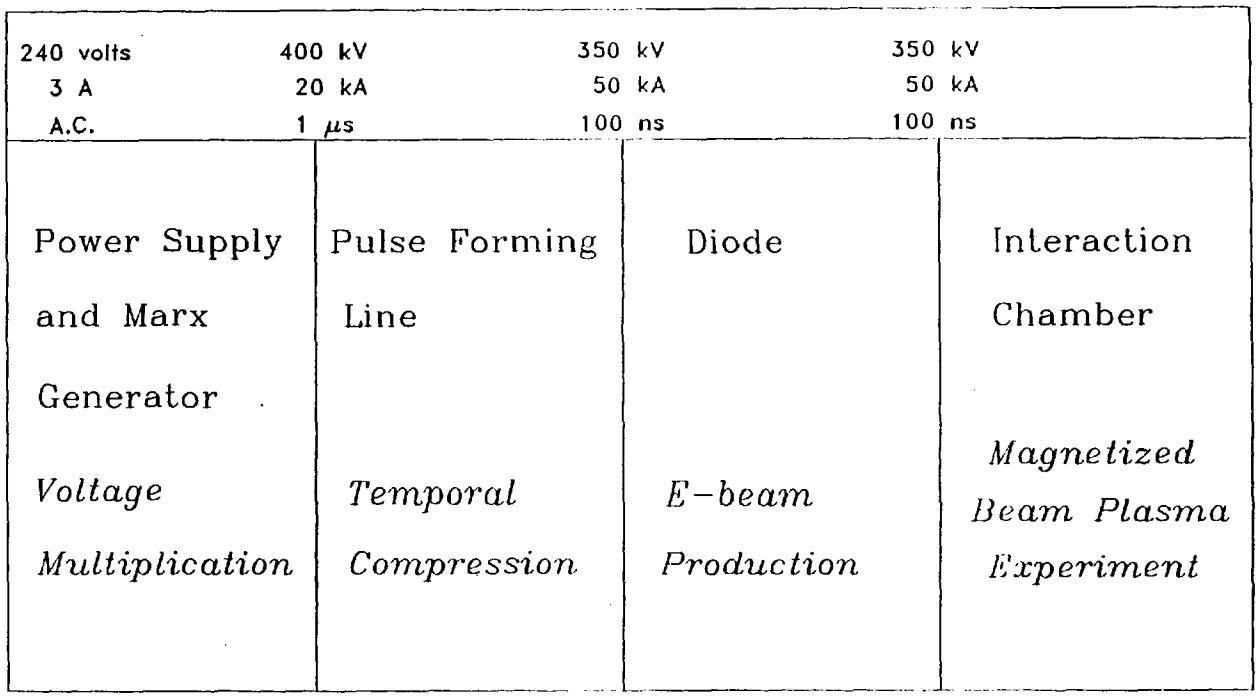

Fig. 2.1 Schematic showing the main elements of the beam generator and their parameter regimes.

2.2.1 The Marx Generator

The eight stage Marx generator runs in air. Each stage, rated at 100 kV, is charged plus and minus to reduce D.C. potentials with respect to ground and to reduce corona problems. The normal charging voltage is 64 kV per stage. The spark gaps run in compressed air (180 kPa absolute for a 64 kV charge). Triggering is achieved by applying a 100 kV trigger pulse to two of the nine gaps via field distortion electrodes.

2.2.2 The Pulse Forming Line

The pulse forming line (3) utilises switched transmission lines to produce a 100 ns pulse of ~ 400 kV into a matched load of 9.5 Ω. A folded Blumlein configuration is used, this being compact and able to deliver the full charging voltage into a matched load. The lines are constructed from three, 6 mm thick, parallel aluminium plates mounted on edge and immersed in the deionized water dielectric (15). They are charged via a tunable charging inductor (10) of about 1μH per arm, which permits a degree of control over the charging rates of the two arms of the line.

The line is switched by a self-closing pressurized sulphur hexafluoride gas switch (11). The switch has brass electrodes with a separation of about 2.5 cm. The self closing voltage may be varied by changing the gas pressure. Approximately 240 kPa absolute gives a 400 kV pulse into a matched load with the normal charge of 64 kV per stage on the Marx. The jitter in the switching time is determined by the rate of rise of the line voltage. In order to keep the jitter low, the self closing voltage of the switch is maintained well below the maximum voltage of about 550 kV to which the line would charge if unswitched. The resulting jitter is < 20 ns for the majority of shots.

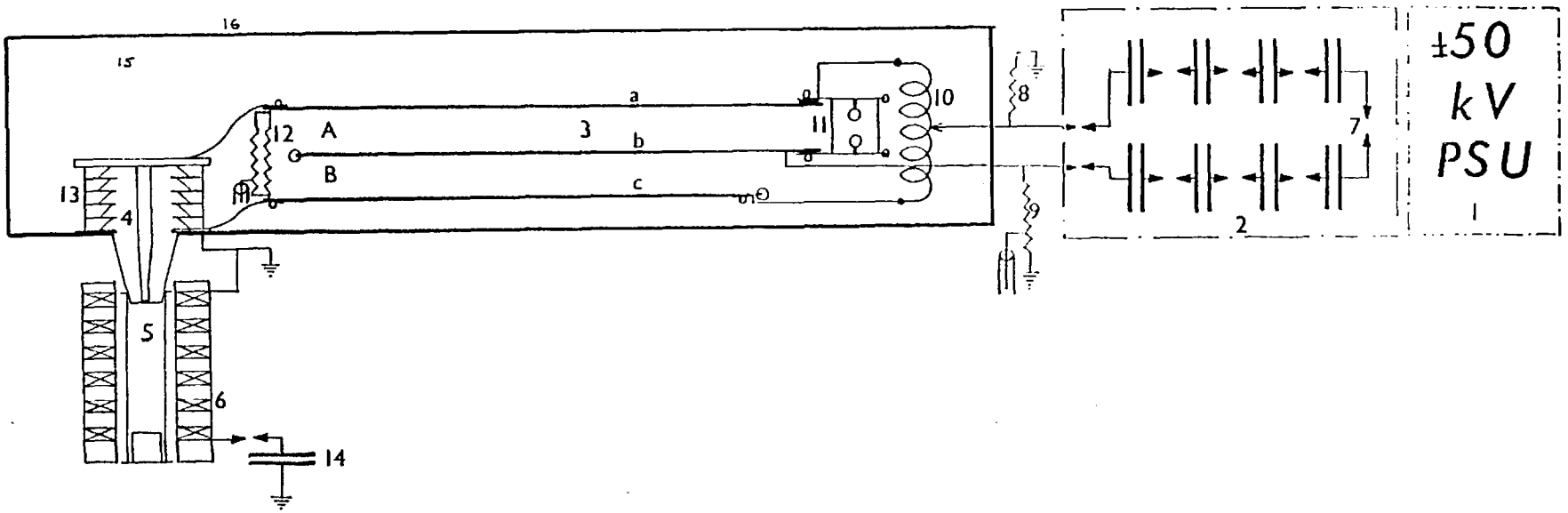

Fig. 2.2 Schematic of the beam generator showing the components. 1 Power supply ±50kV, 2 Marx generator: eight 100kV capacitors, 3 Pulse forming line, Blumlein configuration, 4 Vacuum field emission diode, 5 Interaction chamber, 6 Guide field coil modules, 7 Marx spark gaps, 8 Grounding resistor, approximately 20 ohms, 9 Marx voltage monitor, 10 Tunable charging inductor, 11 SF_6 self closing switch, 12 Prepulse limiting resistor and line voltage monitor, 13 Graded insulator, 14 Guide field capacitor bank 5nf, 15 Deionized water dielectric, 16 Tank for water.

2.2.3 The Diode

The diode is a vacuum field emission type with a plane anode and cathode. A five section graded Perspex insulator forms the water-vacuum dielectric interface. The vacuum surfaces are angled at about 45^{o} to the electric field as shown in Fig. 2.2. This has been found to maximize the surface tracking voltage, MARTIN (1971). The cathode is of Poco graphite, grade AXF5Q, 2 cm diameter, mounted on a stainless steel shank. The anode is either an aluminium or aluminized Mylar foil mounted on a stainless steel conical anode feed which protrudes from the side of the water tank (16) as shown in Fig. 2.2. The use of stainless steel enables penetration of the applied guide field. All the diode vacuum surfaces with the exception of the anode and cathode are coated with type 704 silicon vacuum oil to reduce parasitic electron emission and reduce damage in the event of a breakdown.

The anode-cathode gap is normally set to 3.5 mm. This gives an observed impedance of about 7 Ω. The mismatch to the line enables a slightly higher current density to be achieved. This impedance is lower than that predicted by the relativistic Child-Langmuir law for space-charge limited current flow in plane diodes.

$$Z = \frac{136}{V^{\frac{1}{2}}} \left(\frac{d}{r}\right)^{2} \quad \Omega \qquad 2.1$$

where the voltage V is in mega-volts and d and r are the A-K gap separation and diode radius respectively. For Z = 7Ω with V = 0.35 and r = 1 cm. this yields an A-K gap of 1.75 mm. This discrepancy arises because gap closure occurs; plasmas which form at the anode and cathode expand into the gap effectively reducing d at a rate of about 4 cm μs^{-1}. This rate is estimated by assuming an A-K gap spacing which varies linearly with time, and calculating the rate required to give the observed optimum A-K gap spacing of ~ 3.5 mm.

The inductance of the diode, estimated by considering it as two co-axial cylinders, is ~ 130 nH. This gives an $^{L}/_{R}$ rise time for the beam current of about 8 ns. (R is the sum of the diode and generator impedances ≈ 16.5Ω.) As the line switch feeds an impedance of only 4.75 Ω it is likely that the switch inductance is the main rise time limiting element of the system. The observed current rise time is ≳ 20 ns but the changing diode impedance will contribute to this also.

Evacuation of the diode is effected with a 25 cm oil diffusion pump. The pumping line contains a large Perspex insulator to electrically isolate the pump from the generator.

2.2.4 The Prepulse

The equivalent circuit for the line charging cycle is shown in Fig. 2.3. It is asymmetric with respect to the two line capacities C_{L1} and C_{L2}. In addition C_{L2} is about 10% lower than C_{L1} as it is shorter to reduce the possibility of flash-over to the line switch. This is illustrated in Fig. 2.2 (line c is shorter than line b). A result of these asymmetries is a prepulse voltage which appears across the load R_L during charging of the lines. It has been found that for reliable beam generation, especially with Al/My anode foils and small A-K gaps, the prepulse should be as small as possible and in the opposite polarity to the main pulse. For the A-K gap used (~ 3.5 mm) a prepulse must be less than 7 kV in order to use Al/My foils. To provide control over the prepulse the charging inductors L_1 and L_2 in Fig. 2.3 have an adjustable tapping point. In addition, a 70 Ω resistor (12) (of Cupric Sulphate) is placed in parallel with the load to increase the prepulse decay rate. Complete elimination of the prepulse is not possible by this means as one has to balance two charging rates and their phases. The optimum condition is found by trial and error. Example prepulse waveforms are shown in Fig. 2.4.

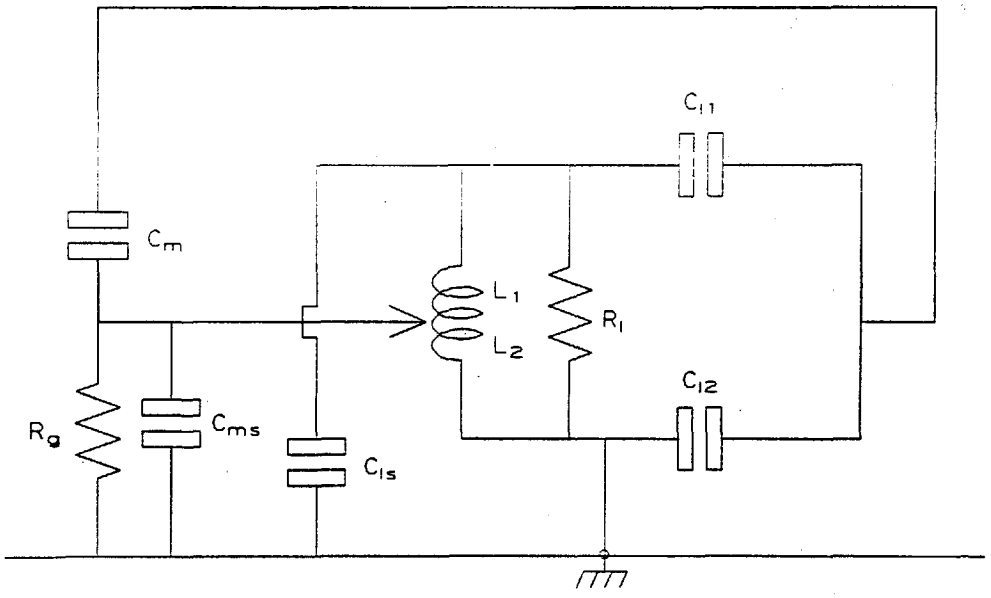

Fig. 2.3 Equivalent circuit for charging the pulse forming line The symbols are referred to in the text.

2.3 Interaction Chamber and Guide Field

2.3.1 Guide Field Requirements

The magnitude of the guide field required is dictated by the beam parameters. The field is required both to radially confine the plasma against the outward $\underline{j}_p \wedge \underline{B}_\theta$ force which persists during beam injection, VANDEVENDER et al. (1976), and to prevent beam pinching in the diode under the $\underline{j}_b \wedge \underline{B}_\theta$ force, HAMMER et al. (1972), where $\underline{j}_p$ and $\underline{j}_b$ are the plasma and beam current densities and B_θ the net azimuthal magnetic field. (In the diode B_θ is the result of j_b whilst in the plasma the result of $j_b - j_p$. As $|j_p| < |j_b|$ the latter criterion is more stringent.)

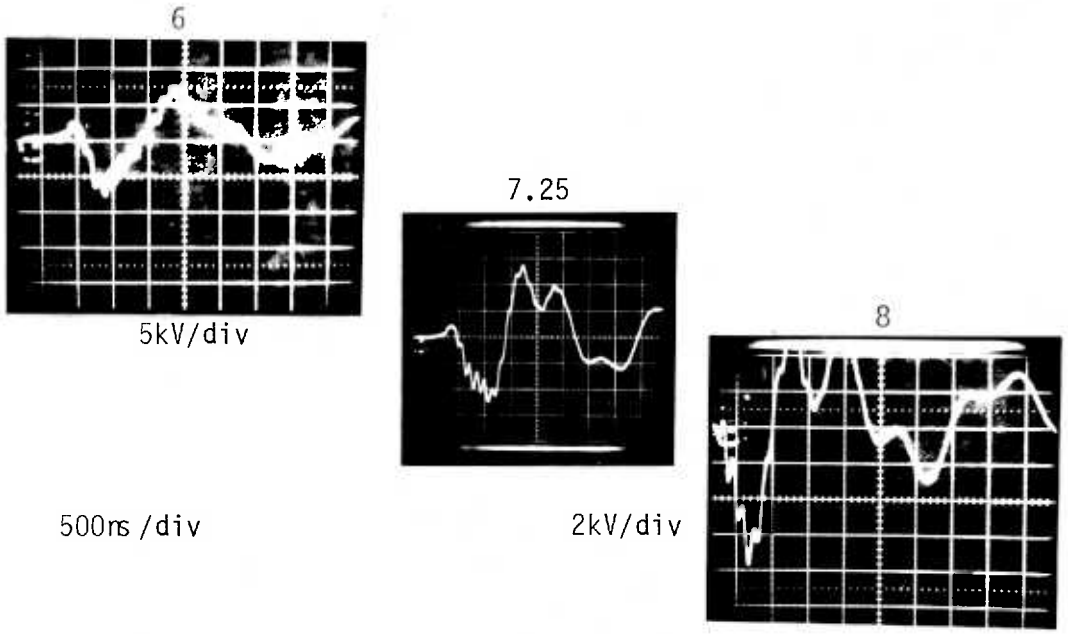

Fig. 2.4 Examples of prepulse waveforms. The numbers above each trace refer to the number of inductor turns to ground.

To prevent pinching in the diode it has been shown by HAMMER et al. (1972) that the applied B_z field must obey

$$B_z > \frac{r_b \gamma}{2s\nu} \; B_\theta \Big|_{r=r_b} \qquad 2.2$$

where

r_b is the beam radius

s is the A-K gap

$\gamma = (1 - \beta^2)^{-\frac{1}{2}}$, the usual relativistic factor

$\nu = Ne^2/4\pi \varepsilon_o m_e c^2$ is the number of beam electrons per classical electron radius of beam length.

N is the beam line density, $n_b \pi r_b^2$

B_θ is the azimuthal field in the diode.

i.e.

$$B_\theta\Big|_{r=r_b} = \frac{\mu_0}{2\pi}\frac{I_B}{r_b} \qquad 2.3$$

Maximum values of I_B are ~ 50 kA giving B_θ ~ 1T, $r_b = 10^{-2}$, $s = 3.5.10^{-3}$ and $\nu/\gamma \simeq 2.6$. Hence the required B_z is

$$B_z > \mu_0 I_B/(4\pi s\nu/\gamma) = 0.6\ T \qquad 2.4$$

The guide field was designed for up to 5T giving a large safety margin and room for possibly uprating the generator at a later date. The available capacitor bank energy of ~ 40 kJ and the required coil inner diameter of 11.5 cm (to give room for diagnostic access to the interaction chamber), then fixes the system length to $\lesssim$ 35 cm. A lower limit on the coil inductance is given by the requirement that the field rise time be longer than the time to diffuse into the diode and interaction chamber, coupled with bank capacitance of 5 mF. In order to speed up the field diffusion process nearly all components were made from stainless steel, this having a resistivity some 30 times that of copper. A condition on the coil parameters is that the resistance be low enough so that too much energy is not dissipated before the field reaches its peak.

2.3.2 Guide Field Design

The design was a compromise to the above requirements as high inductance coils are harder to make to withstand the forces generated with large fields. The final version consists of six identical series connected modules spaced 7 cm between centres. A module, shown in Fig. 2.5, consists of 18½ turns of half-hard copper strip. The strip (0.9 mm thick and 12.7 mm wide) is insulated with tape (Scotch, type No. 57, Mylar base). The coil is vacuum potted with epoxy resin (Ciba-Geigy, MY753 plus HY951) into Tufnol holders which are then mounted

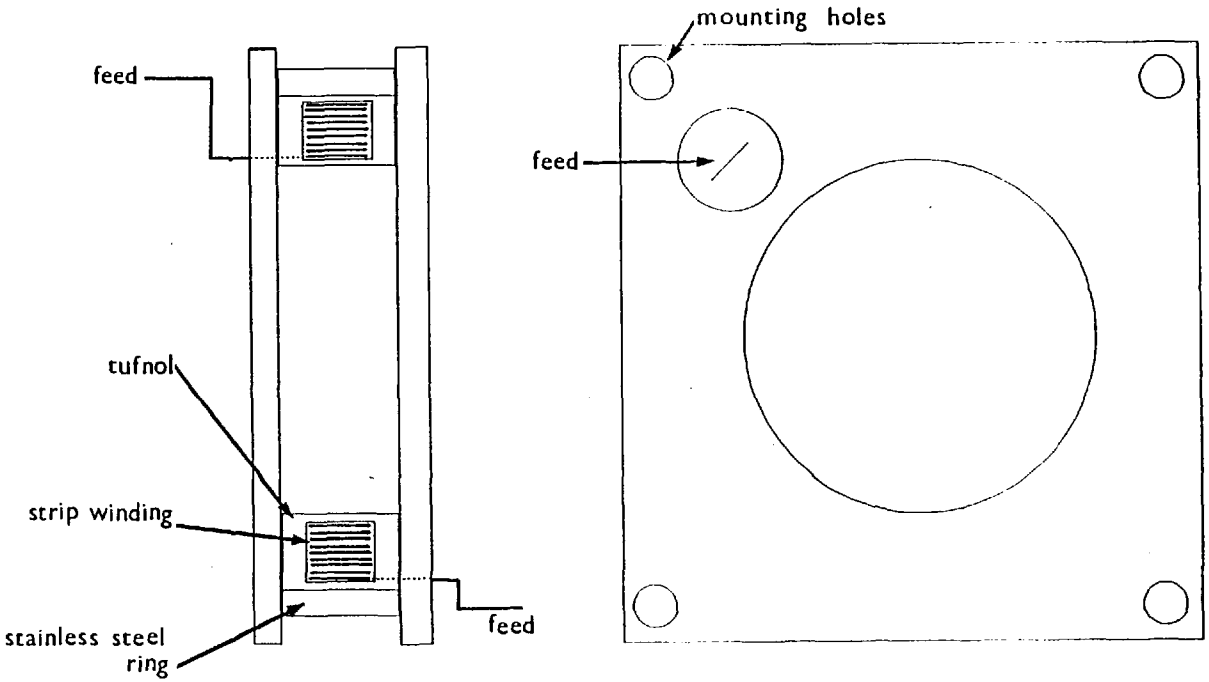

Fig. 2.5 A field coil module comprising 18½ turns of copper strip insulated with Mylar tape and vacuum impregnated with epoxy resin into Tufnol liners. These are then mounted in a stainless steel jacket.

in a stainless steel jacket.

The purpose of the jackets is to relieve the stress set up in the copper coil from the outward $\underline{j} \wedge \underline{B}$ forces. The force F_{TOT} so generated can be estimated from the Biot-Savart law. Consider the force acting per unit length of coil (around its circumference) at A due to the current in an element of coil dl, in Fig. 2.6:

$$\begin{aligned} \delta F_r &= I(\mu_o I \, dl \, . \sin\alpha/4\pi r^2) \\ &= \mu_o I^2 \tan^2\alpha \, dl/16\pi a^2 \end{aligned} \qquad 2.5$$

Using $dl = 2ad\alpha$, integrating over all α, multiplying by the circumference of the loop and the number of turns N, gives the total force

$$F_{TOT} = \frac{2\pi a \mu_o I^2 N}{8\pi a} \int_{-\frac{\pi}{2}}^{+\frac{\pi}{2}} \tan^2\alpha . d\alpha = \pi \mu_o \frac{I^2}{4} N \qquad 2.6$$

For 5 tesla, $\sim 3.10^5$ ampere-turns are required. Also N = 18.5. These give

$$F_{TOT} = 1.85 \, . \, 10^6 \quad \text{newtons}$$

This force has to be taken up by tension in the steel jacket. The typical tensile strength of stainless steel is 1 to 1.5 GNm^{-2}, giving a required cross-sectional area of ≥ 1 cm^2. The dimensions adopted gave about 2.4 cm^2. In addition, the strain in the steel is required to be less than the breaking strain of the copper conductor by more than the ratio of their diameters. This ensures that the steel takes the strain before the copper breaks. This is achieved by more than a factor of four.

2.3.3 Coil Operation and Performance

The capacitor bank is switched into the coil through a single triggered spark gap operating at 960 torr of argon and triggered with a

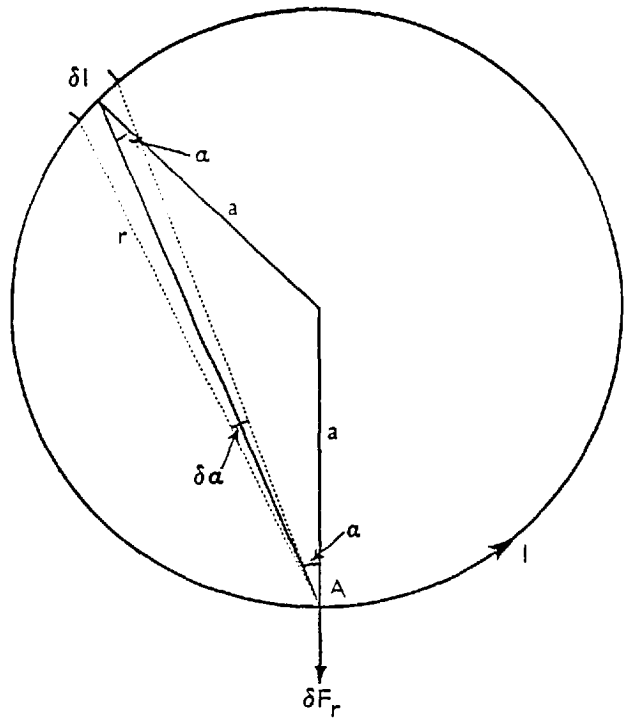

Fig. 2.6 Geometry for coil force calculation. a *is the radius, a force* δF_r *results from the interaction of current element* δl *with the applied magnetic field.*

fast 15 kV pulse. Whilst the quarter period (rise time) of the coil alone is ~ 1.6 ms, on insertion of the interaction chamber this rises to ~ 2.5 ms as a result of the inductance being higher while the field diffuses into the chamber. The coil resistance effects a convenient damping rate which depresses the peak field ~ 15%, but which stops the circuit ringing for more than a few cycles.

The spatial variation in the field was investigated with both Hall probes and small multiturn coils. Results are shown in Fig. 2.7. No correction to the end droop has been attempted but both the A-K gap and the Faraday cup (see later) are well within the end coils.

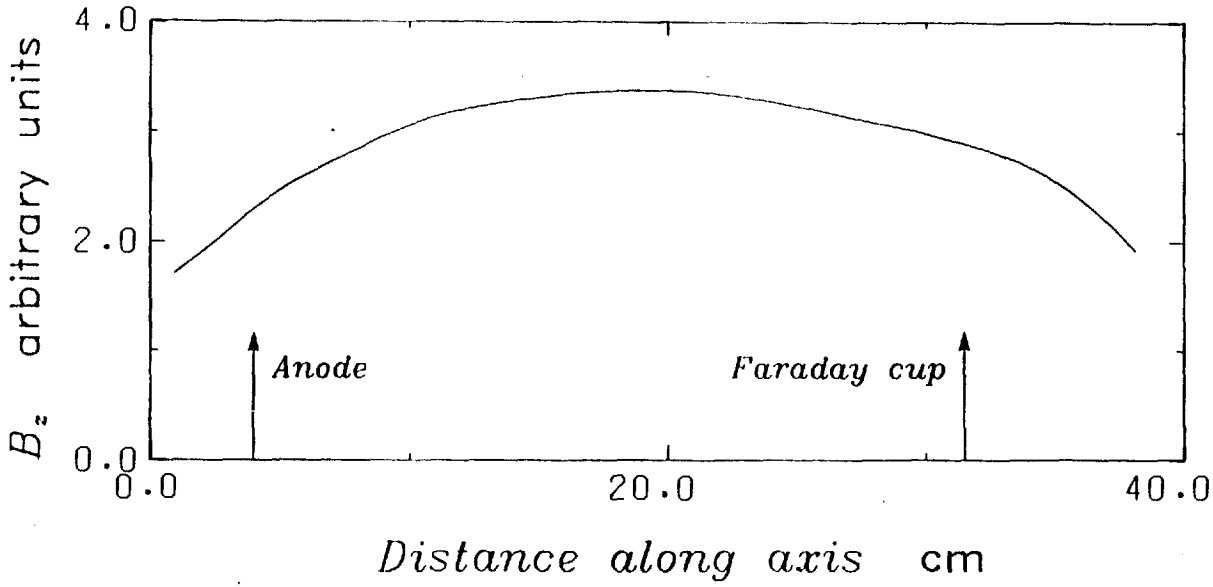

Fig. 2.7 Plot of the axial applied magnetic field versus distance from anode.

2.3.4 The Interaction Chamber

The chamber is shown schematically in Fig. 2.8. It is of modular construction permitting sections to be moved or replaced as required for a particular experiment. Four modules are clamped together with flanges mounted to the modules with "Wilson" seals. Extra flanges containing Rogowski coils, diamagnetic loops, etc.(see Section 3.4) can be inserted between the modules.

The usual chamber configuration contained three Rogowski coils, one diamagnetic loop and one set of ports for optical diagnostics.

As the anode foil has to be renewed for every shot, the guide field coils, interaction chamber and associated vacuum equipment was mounted on a trolley which could be rolled back giving access to the diode.

2.4 Z-Discharge

For injection into a preformed plasma preionization of the hydrogen was effected with a Z-discharge. The applied guide field prevented pinching of the current channel. The beam was injected into the afterglow of this discharge when the Z-discharge current was negligible. Fig. 2.9 shows the device schematically. The anode foil and the Faraday cup formed the electrodes, the former being the ground. When using Al/My anode foils, the aluminized side faced the cathode in order to avoid the aluminium being vaporised by the Z-discharge. Four ports built into the Pyrex tube permitted laser scattering from the plasma. The capacitor used for the discharge was a single 40 kV, 2μF, BICC capacitor charged to 20 kV. This was switched with a three electrode spark gap of UKAEA (Culham Laboratory) design. The discharge period was ~ 7 μs which indicates that about half the circuit inductance is in the Z-discharge. A typical current waveform is shown in Fig. 2.10.

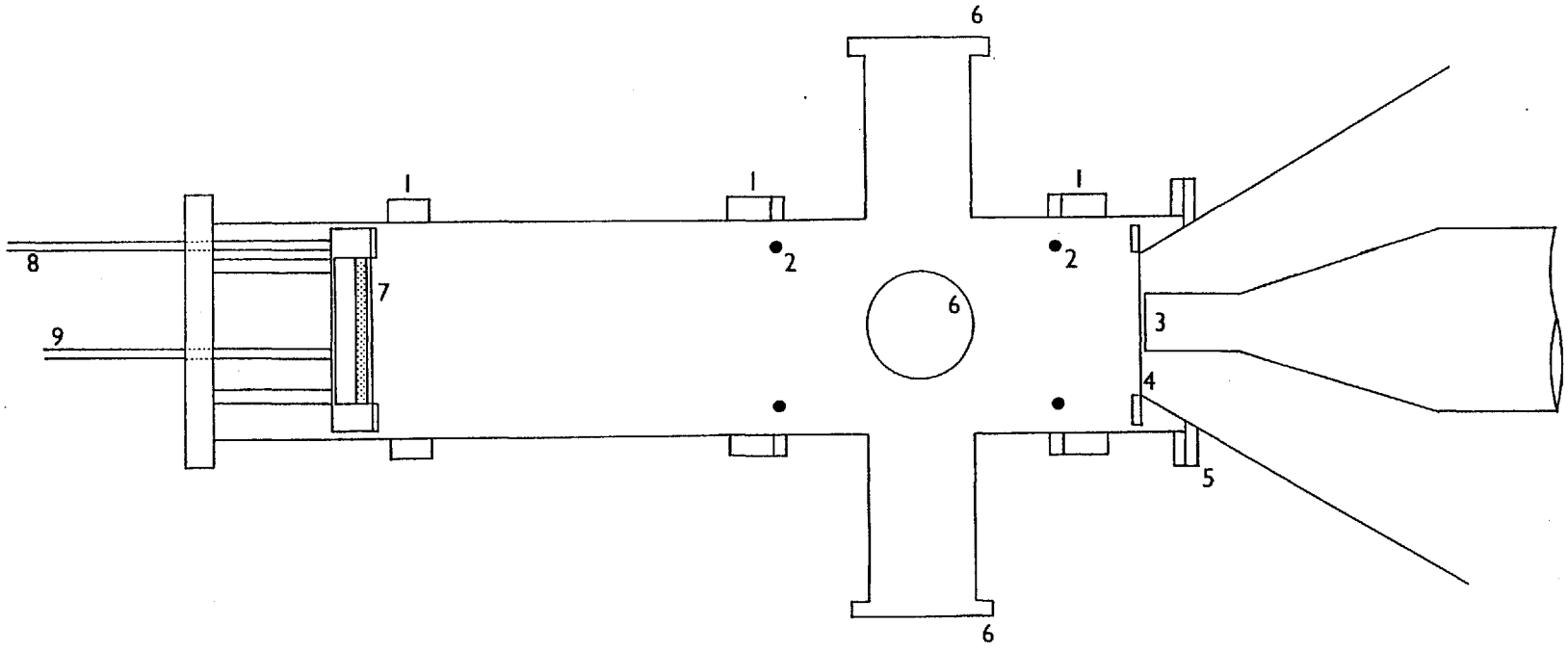

Fig. 2.8 Schematic of neutral gas interaction chamber. 1 Rogowski coils, 2 Diamagnetic loops, 3 Cathode, 4 Anode foil, 5 Demountable seal, 6 Scattering ports, 7 Faraday cup, 8 Faraday cup signal, 9 Calorimeter signal.

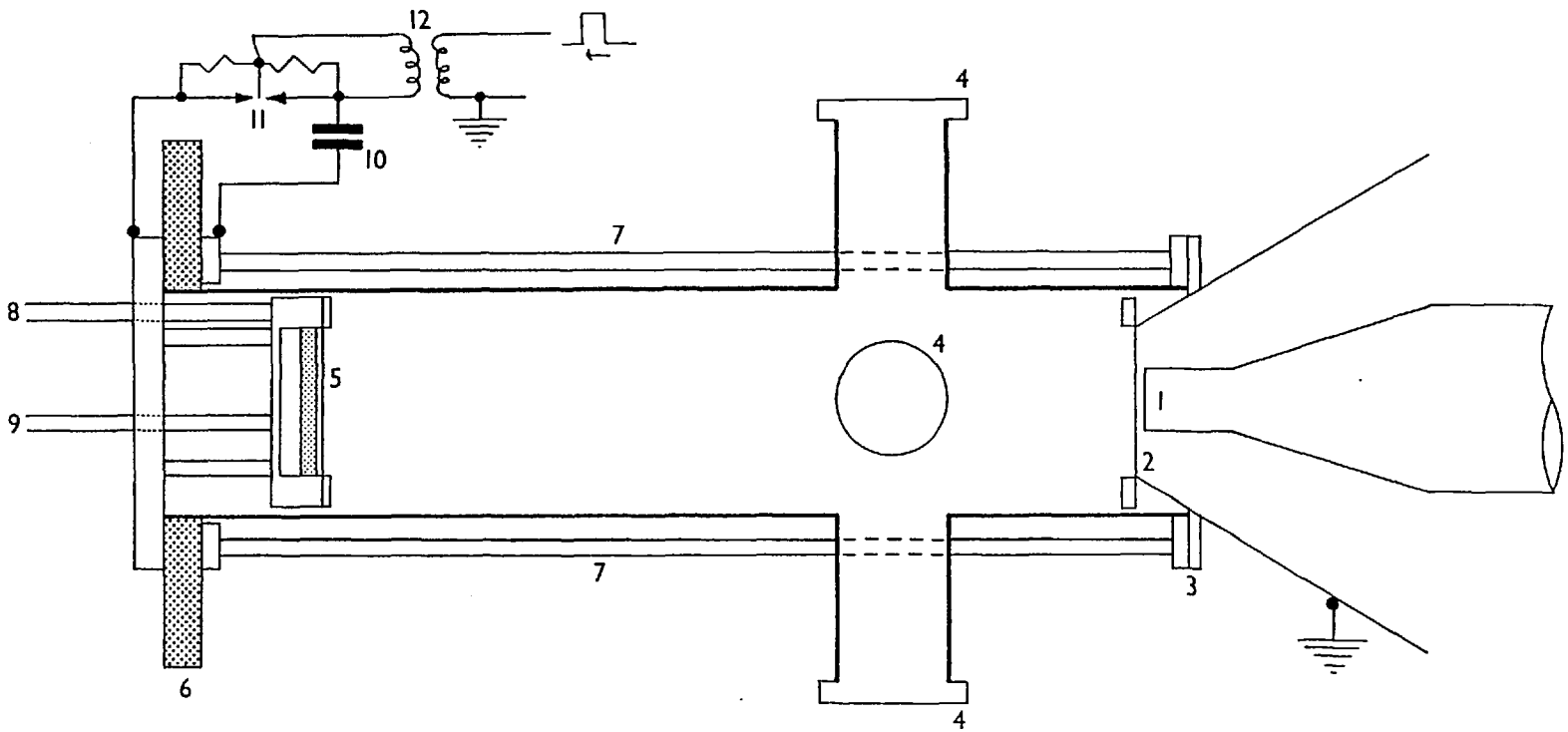

Fig. 2.9 Schematic of z-discharge interaction chamber. 1 Cathode, 2 Anode foil, 3 Demountable seal, 4 Scattering ports, 5 Faraday cup, 6 Insulator, 7 Return rods (4), 8 Faraday cup signal, 9 Calorimeter signal, 10 Capacitor, 11 Spark gap, 12 Trigger transformer.

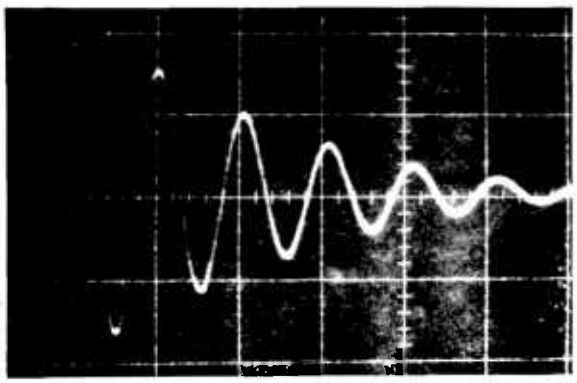

Fig. 2.10 Example of the z-discharge current waveform measured with a simple Rogowski coil.

CHAPTER THREE

DIAGNOSTIC EQUIPMENT

3.1 Introduction

A variety of techniques were used to investigate the beam and plasma parameters. These include:-

1. Measurements of magnetic fields.
2. Observations of emitted light and X-rays.
3. Laser scattering.
4. Spectral line absorption.
5. Measurement of transmitted beam energy.

In addition a number of monitors were used to check on the correct functioning of the beam generator, field coils and, if used, the Z-discharge. Most signals were recorded on Tektronix oscilloscopes situated in a screened room. This was made of aluminium and has a well filtered mains supply. Signal leads entered by means of tubular extensions rather than by bulkhead connections. All trigger signals entered by solid state infra-red links to reduce ground loop problems. Signals not recorded in the screened room include the line and Marx monitor and the calorimeter.

All the diagnostics measured parameters which can lead to only an overall view of the beam-plasma interaction. No attempt has been made to directly investigate any turbulence that may exist. That turbulent interactions are present and some aspects of their nature may however be inferred from the results obtained.

3.2 Beam Generator Monitors

The voltages on both the Marx generator and the pulse forming

line were monitored with simple Cupric Sulphate voltage dividers. Both monitors give ~ 1000:1 voltage division and have total resistances ~ 1kΩ. They are positioned approximately along the electric field lines to reduce the stray capacities and give good rise times.

3.3 Beam Monitors

The primary beam diagnostic is a combined Faraday cup and calorimeter, the former giving the beam current as a function of time, the latter the total energy transmitted through the plasma.

Faraday cup design is quite critical. The problem of measuring the beam current is that it is coincident with the plasma return current, hence their paths must be separated to make the measurement. This separation is achieved by means of a 12.5 μm Mylar foil through which the high energy beam electrons may pass but not the lower energy plasma electrons.

The construction of the device used is shown in Fig. 3.1. The beam is incident on the carbon collector after passing through the Mylar window and the 1 mm intervening vacuum gap. Fig. 3.2 shows schematically the paths of the beam and plasma currents around the device. The plasma current flows across the surface of the Mylar whilst the beam current passes around the self integrating Rogowski coil detector. The main advantage of Rogowski coils over resistive shunts is the improved decoupling from the current to be measured, which results in a higher signal to noise ratio. The advantage over simple magnetic probes is their insensitivity to the current distribution within the loop, ANDERSON (1971) and COOPER (1963). Fig. 3.3 shows a schematic of the type of coil used. It was constructed from miniature 50Ω co-axial cable by removing the outer screen and winding a closely packed uniform coil with 34 S.W.G. enamelled copper wire onto the insulator.

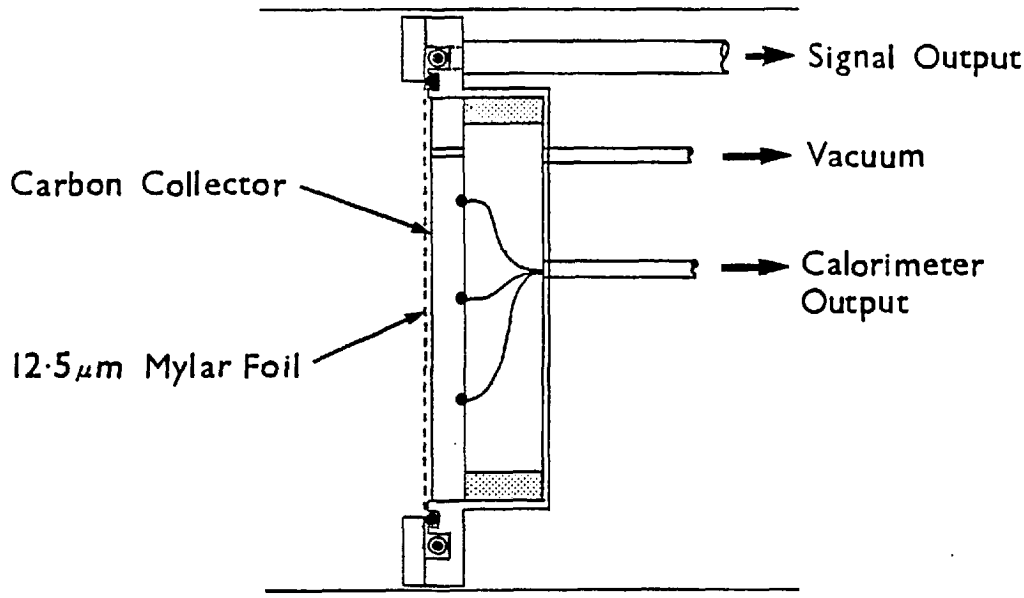

Fig. 3.1 Schematic of Faraday cup

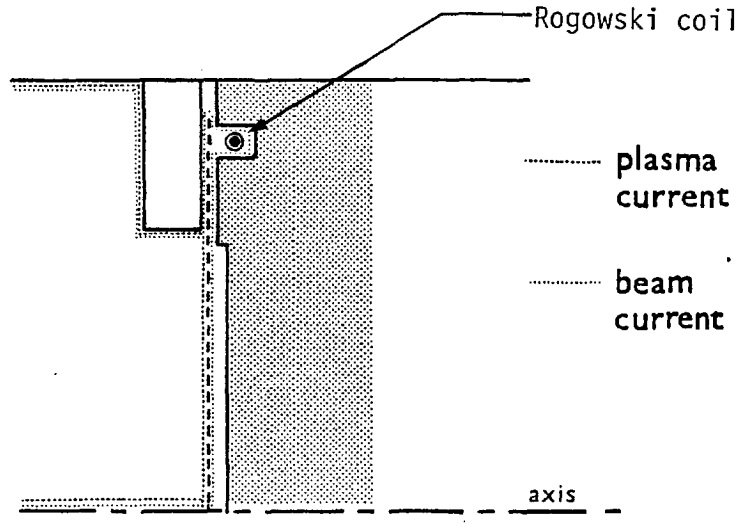

Fig. 3.2 Current paths within and around the Faraday cup

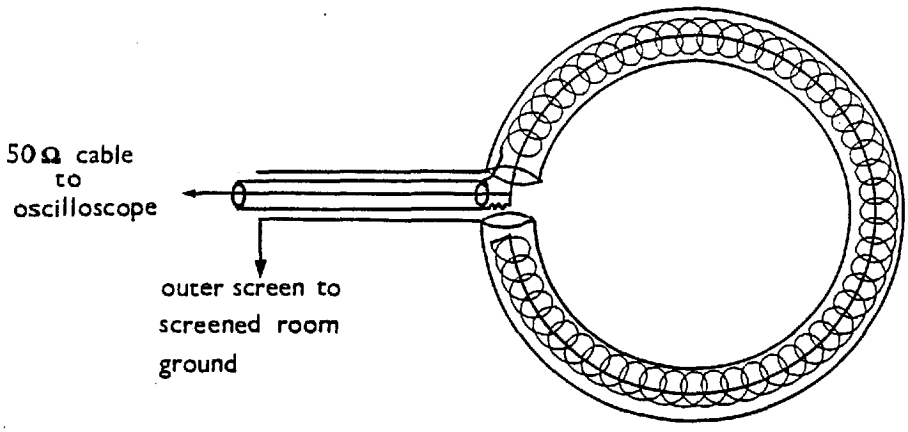

Fig. 3.3 Schematic of a Rogowski coil showing the screening and close proximity of the self integrating resistor of ∿1 ohm.

The centre conductor of the co-axial cable was used as the return so reducing the sensitivity of the coil to the B_z field. The coil is screened by the Faraday cup, there being a narrow gap in the screen in the poloidal direction to admit the magnetic field. This gap is insulated by the Mylar foil as shown in Fig. 3.1. The self integrating 1 Ω resistor was a 1 cm. length of Constantan resistance wire, connected as shown in Fig. 3.3 and folded back on itself to reduce its inductance. The coil has a sensitivity of 1 V/kA and a useful integration time of - 500 ns.

The calorimeter consisted of six series connected copper-Constantan thermocouples, three attached to the back of the collector of the Faraday cup and three as a reference outside the interaction chamber. The signal was monitored on a spot galvanometer; however, as this drew a significant current the observed voltage did not equal the

tabulated e.m.f. of a copper-Constantan thermocouple. The calorimeter was calibrated by depositing a known amount of energy in it with a heating coil and measuring the spot galvanometer deflection. The method is described more fully by VANDEVENDER (1974). Typical sensitivities obtained were ~ 13.4 cm/kJ. The calibration was checked by comparing the response of the calorimeter with that of a commercial laser calorimeter, to a short ruby laser pulse of ~ 10 joules. Agreement was ~ 10% in spite of the fact that the calorimeter surface was not designed for laser irradiation.

When the Faraday cup/calorimeter was used in conjunction with the Z-discharge it was not possible to connect it directly to the oscilloscope as it formed the live electrode of the 20 kV discharge. An inductor was placed in the signal lead; it consisted of about 17 m of insulated solid outer co-axial cable wound around 'C'-cores. This gave a very high inductance to the 20 kV common mode signal although the discharge frequency of ~ 140 kHz was a little high for the 'C'-core material, the high permeability of which begins to fall in this region. Ferrites, however, would have been saturated by such large fields. The full circuit diagram is shown in Fig. 3.4. Whilst the Z-discharge current was flowing a small signal was detectable, from the Faraday cup, at the discharge frequency. The inductor also served as a simple means of eliminating ground loops between various diagnostics and always improved the common mode rejection of the oscilloscopes.

3.4 Plasma Magnetic Monitors

3.4.1 Net Current Monitors

The total net current was measured at three axial positions with self integrating Rogowski coils mounted in the wall of the interaction chamber and on occasions by the Faraday cup with the Mylar foil omitted.

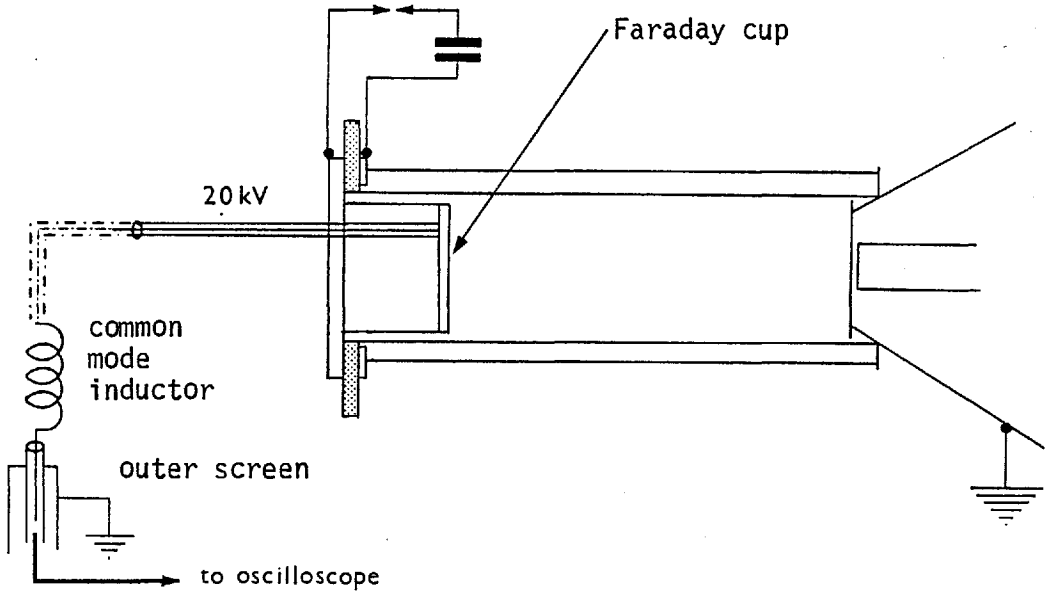

Fig. 3.4 When the Faraday cup is used as a live electrode the 20kV common mode signal is removed with a large inductor made from solid coaxial cable.

The radial distribution of the net current and the net B_θ field outside the beam channel were investigated with two B_θ probes which could be positioned between the chamber wall and the beam channel.

The three Rogowski coil monitors were positioned at 1, 12 and 23 cm from the anode plane (for future reference they are numbered 1, 2 and 3 respectively). The coils are similar to that used in the Faraday cup, but slightly longer. Each coil is mounted in a flange, which acts as the screen and is inserted between the modules of the interaction chamber as shown in Fig. 3.5.

The probes used to measure the B_θ field were inserted through the scattering ports of the interaction chamber. The construction is shown in Fig. 3.6. They could be orientated to pick up the slow B_z guide field or at 90^o to pick up the fast B_θ field. However, they could not be used for the fast diamagnetic B_z signal which occurs on beam injection, as it

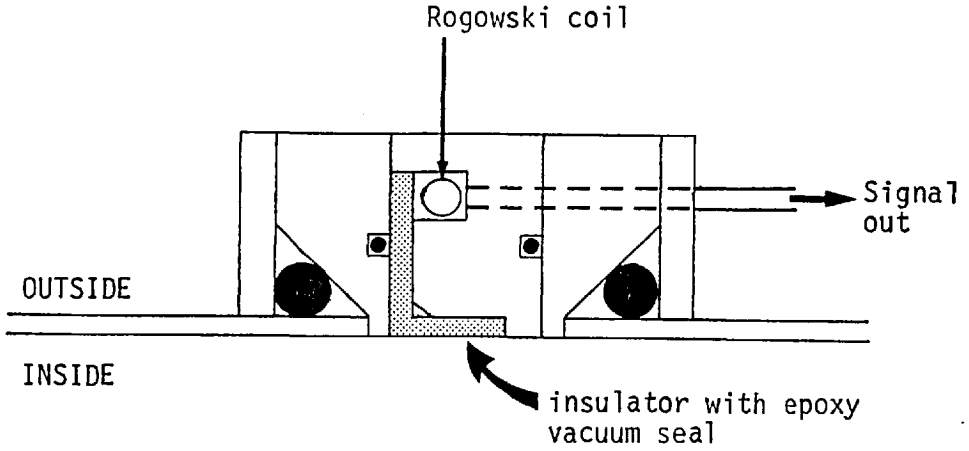

Fig. 3.5 Section through Rogowski coil mounting flange showing the vacuum seals and the gap insulator through which the B_θ field can pass.

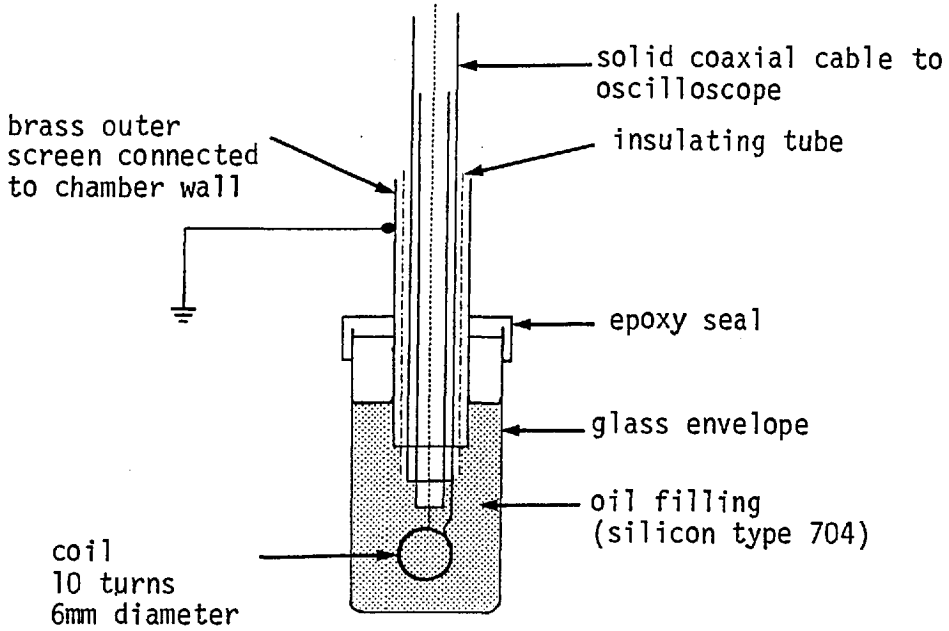

Fig. 3.6 The construction of a magnetic probe to measure the radial variation of B_θ.

was always swamped by B_θ field components generated by the beam plasma system. The B_θ signals were integrated with a 2 μs R.C. integrator at the oscilloscope to give typical sensitivities of ~ 1 V/kA of net current, dependent upon its exact radial position.

3.4.2 Plasma Diamagnetism Monitor

The plasma diamagnetism was measured with a diamagnetic loop, the construction of which is shown in Fig. 3.7. A balanced system was used with an insulated floating screen, the signals being integrated with a balanced 2 μs R.C. integrator. With this arrangement signal reversal with reversal of the applied B_z guide field was good, any non reversing component being less than the system reproducibility, as shown in Fig. 4.22. The diamagnetic loop and its mounting flange was used in two positions, position (1) being 2 cm from the anode foil and position (2) at 11 cm. As the applied B_z field was slightly higher at position (2) the calibrations (see below) had to make allowance for this: see Fig 2.8.

3.4.3 Calibration of Monitors

All methods used to calibrate the Rogowski coils were basically the same, i.e. to put a current through the coil loop and measure it with a resistive shunt. Such calibrations were performed with the coils in situ. The main problem is one of signal level. The sensitivities are ~ 1 V/kA so that some tens of amps are required to get signals above the pick-up noise of a few millivolts. Whilst this may be achieved by passing a small current many times through the coil, this leads to a current path with an inductance high enough to preclude fast rising pulses. The most successful method to date is to use switched transmission lines (co-axial cables) as fast pulse generators. The switching has been achieved with transistors in an avalanche mode,

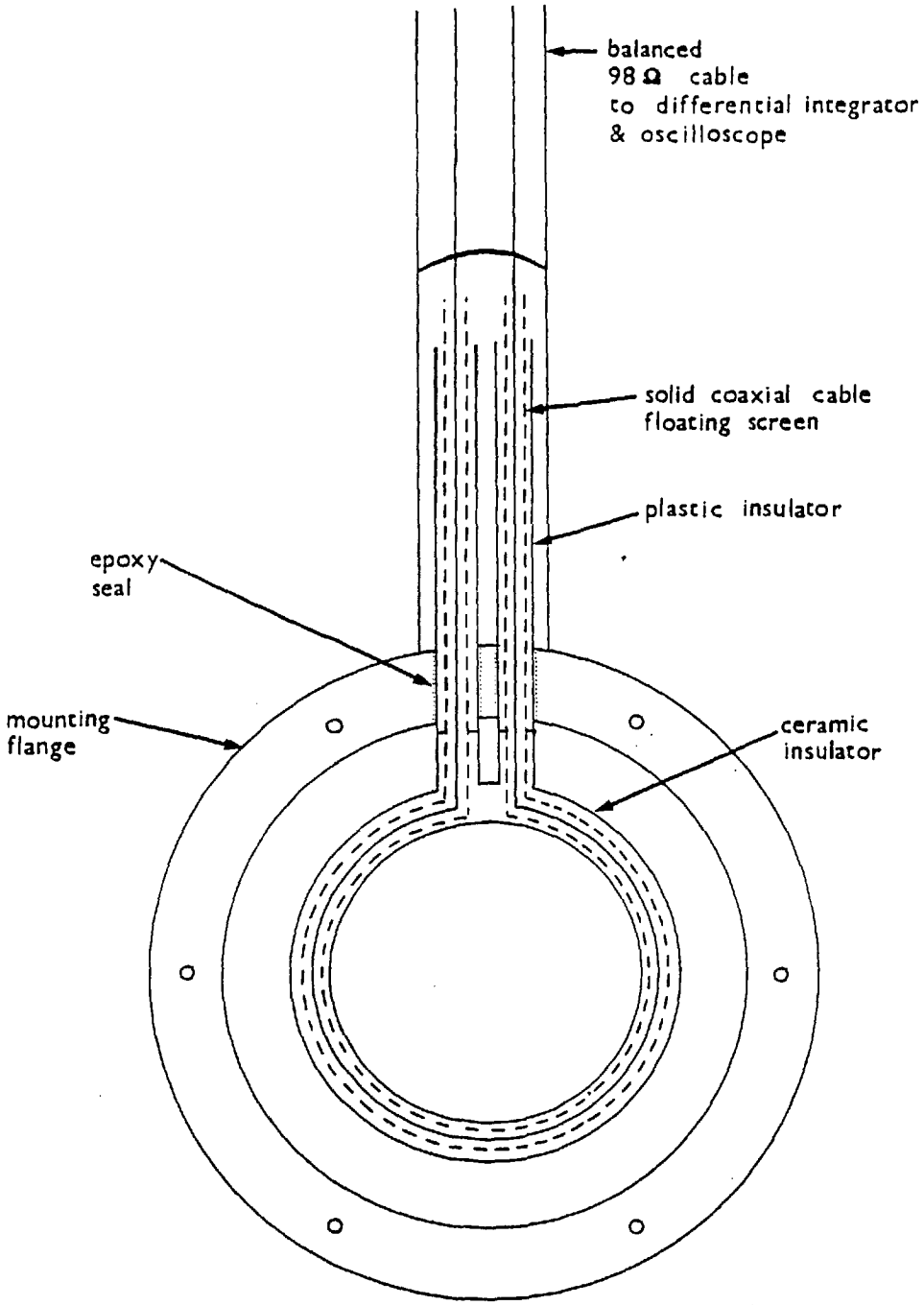

Fig. 3.7 Diamagnetic loop in mounting flange

krytrons and reed relays. In general, transistors will not handle high enough powers and krytrons are too noisy. The use of mercury wetted reed relays enables the generation of 1 kV pulses of 60 A for durations up to ~ 1 μs at 50 Hz. Rise times are typically ≤ 1 ns and the pulses have very flat tops for resistive loads. Such pulses permit a good estimate of the Rogowski coil response to be obtained, in addition to the calibration. Typical results are shown in Fig. 3.8 giving

Sensitivity	1.13 V/kA
Rise time	6 ns
Time for 10% droop	1.5 μs

The B_θ probes were calibrated by the same method assuming a spatial dependence of B_θ inside the interaction chamber, of the form

$$B_\theta(r) = \frac{\mu_0 I}{2\pi r} \qquad r \geq a \qquad 3.1$$

where a is the diameter of the current carrying conductor placed down the axis of the chamber. In addition the B_θ probes were calibrated directly against an accurately wound probe by placing them alternately at the same place in the guide field. The same R.C. integrator was used for both probes giving a direct comparison of the turns-area. The former method requires an accurate knowledge of the R.C. time of the integrator to obtain the turns-area, but can give a direct calibration for the current. The turns-areas obtained were typically:-

2.34 cm^2 from direct comparison

2.1 cm^2 from a current measurement.

To obtain the plasma diamagnetism from the integrated diamagnetic loop voltage the turns-area is required so that the change of field within the loop can be found. The turns-area was obtained both

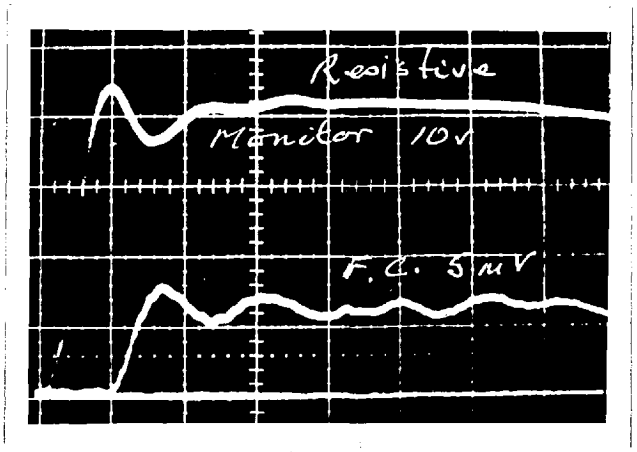

Fig. 3.8 In situ Rogowski coil calibration against a resistive monitor. The lower trace is the Rogowski coil signal.

by direct measurement and by comparing its response to the slow rising guide field with that of the accurately wound probe used for the B_θ probe calibration. However, the magnetic field was not quite radially uniform (it increases with radius especially near the ends of the coil assembly), hence the probe did not average over the radius as did the loop. The difference in signal was ~ 15% and the results of direct measurement were used, the response being ~ 10^3 V/T.

3.5 Optical Plasma Diagnostics

The four optical diagnostics employed were:-

1) Laser scattering
2) Spectral Line Emission
3) Spectral Line Absorption
4) Streak Photography.

3.5.1 Laser Scattering

Laser scattering was performed to measure the electron temperature and number density. Scattering at 90^{o} with a low α parameter was employed ($\alpha = {}^{1}/k\lambda_D$, where $\underline{k}$ is the differential scattering vector and λ_D the Debye length of the plasma).

The laser available, a Q-switched ruby oscillator - amplifier combination, produces a 2 cm diameter beam of up to 15 J in 28 ns (f.w.h.m.) The general layout is shown in Fig. 3.9. The laser output is focussed with a 20 cm lens to a focal spot of $\leq$ 1 mm in the centre of the scattering chamber. Unscattered light is absorbed in the laser dump which is made from OB10 glass positioned at the Brewster angle. Light scattered into an ${}^{f}/6$ cone centred on a direction mutually perpendicular to both the incident laser light and the electron beam is collected with a two lens system, giving a magnification close to unity, and focussed onto the entrance slit of an ${}^{f}/6$ grating polychromator. The polychromator provides a dispersion of 13 Å/mm, there being ten output channels of 1 mm width. These connect to seven photomultiplier tubes, one having 3, one 2 and the rest just one output channel from the polychromator as shown in Fig. 3.10. The p.m. tubes used were six 9658's and one 9558 (used on the central channel at 6943 $\pm$ 6.5 Å) manufactured by E.M.I. They were heavily screened both electromagnetically and with lead and brick against hard X-rays produced by the e-beam. The spectrometer and some of the collecting optics were also lightly screened. The dynode chains on the p.m. tubes were not purely resistive and capacitive, but contained six zener diode stages as shown in Fig. 3.11. The first diode across the photocathode and first dynode holds the voltage high, independent of the applied H.T. This ensures that all the photo-electrons are collected even when the tube is operated at low gain. The diodes on the last five stages hold the respective voltages high to reduce the effect of space-charge, permitting useful near linear operation upto 10 mA anode current

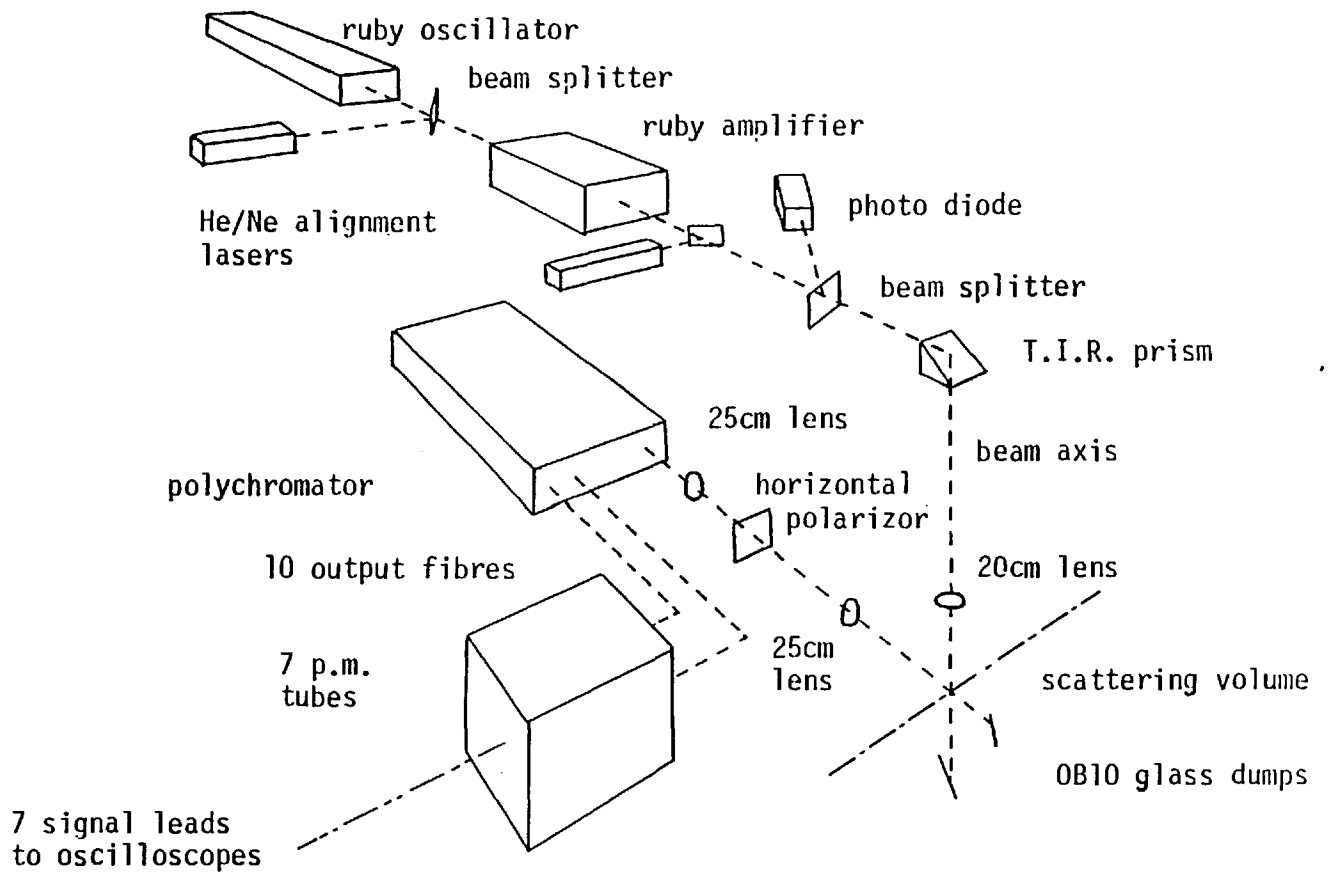

Fig. 3.9 The laser scattering layout.

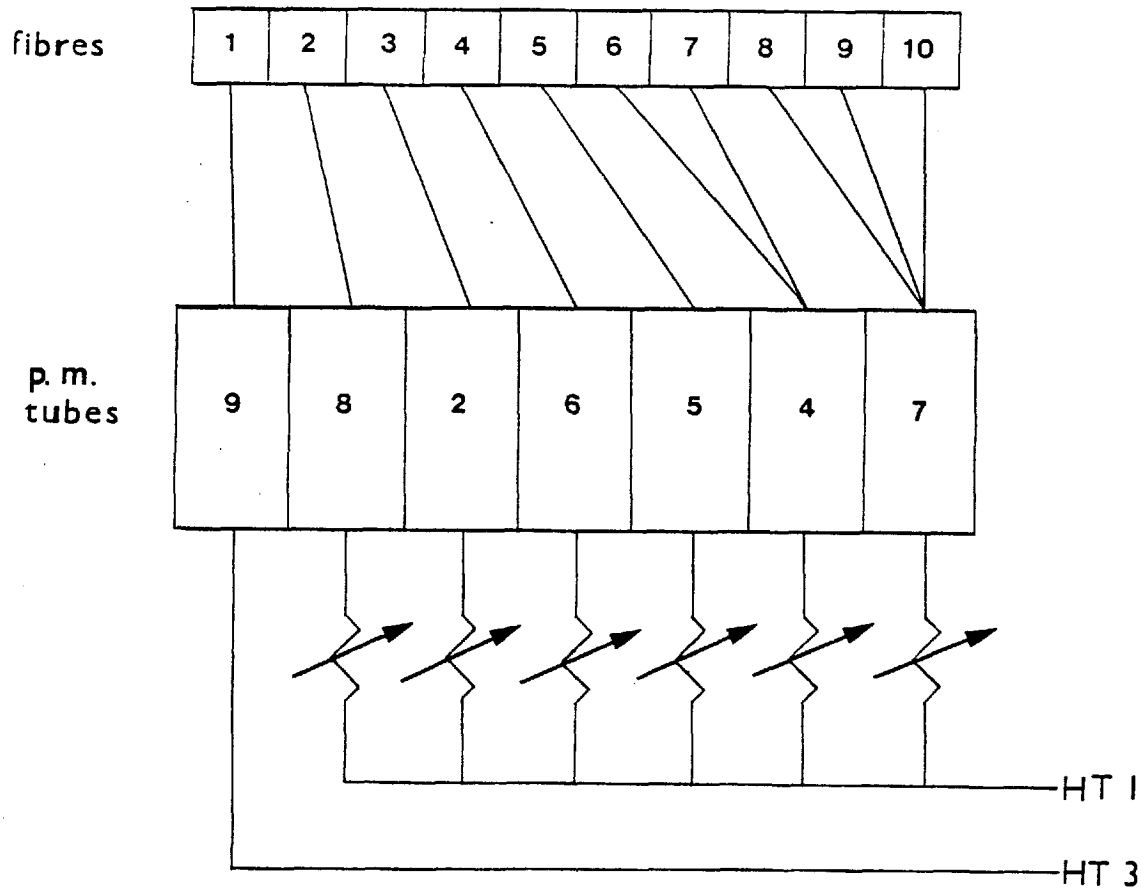

Fig. 3.10 Schematic of fibre bundle and p.m. tube arrangement. Resistors for varying each channel gain independently are shown.

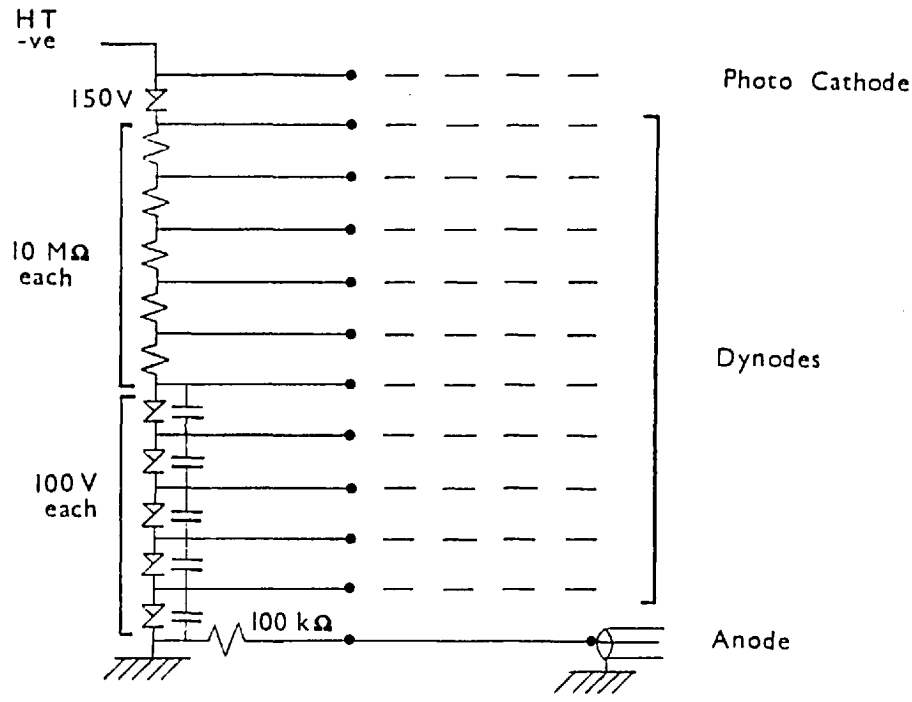

Fig. 3.11 The circuit of the p.m. tube dynode chains.

(for short pulses). Unfortunately the dynode chains on the p.m. tubes were not identical resulting in large differences in their respective gain versus applied H.T. voltage characteristics. As the useful dynamic range of the p.m. tubes was limited by pick up noise levels on the one hand and non-linearity on the other, the gain of each tube had to be set independently every time an overall gain change was required. This was achieved using preset potentiometers in series with each H.T. supply, the supplies originating from the same source. The 9558 p.m. tube had a completely separate supply. Ideally, the sensitivities of each channel should be set so that the signal produced is well inside the dynamic range of the system.

The p.m. tube signals were displayed on 500 series Tektronix double beam oscilloscopes. The relative timing between the incident laser pulse and the e-beam was monitored using the output of the photo

diode, used to normalize the laser output, and some beam generated signal. The actual signal used varied, depending on which was convenient. These include, (a) net current, (b) beam current, (c) hard X-ray emission, (d) light from the line spark gap. The timing of each of these with respect to the beam pulse was measured on a separate shot; zero time being taken as the time the beam reaches the Faraday cup.

Calibration and Alignment

Calibration of the scattering system was obtained by Rayleigh scattering from carbon dioxide, the cross-section being readily available EVANS and KATZENSTEIN (1969). Rayleigh scattering from gases at room temperature produces a very narrow band scattered spectrum which is observed only on the centre channel of the polychromator. To obtain the sensitivity of the other channels a tungsten ribbon lamp, placed at the scattering volume, was used. This produces a broad band D.C. emission which was corrected with the Plank black body radiation formula. For example, if the signals at wavelengths λ_1 and λ_2 are S_1 and S_2 then the sensitivity ratio is not S_1/S_2 but

$$\frac{S_1\ \lambda_1{}^5[\exp(hc/k\lambda_1 T)\ -1]}{S_2\ \lambda_2{}^5[\exp(hc/k\lambda_2 T)\ -1]}$$

where h is Planck's constant and kT the temperature of the ribbon lamp filament. The emissivity of tungsten varies little over the range of the polychromator. The bulb temperature was found using an optical pyrometer. In this way the response of the seven p.m. tubes were compared.

In order to check that the D.C. calibrations give results relevant under pulsed conditions, cross calibrations were also performed by placing a red Monsanto L.E.D. inside the polychromator facing the exit fibre bundle array. Output signals with the L.E.D. pulsed (~ 25 ns pulse)

could then be compared with running the L.E.D. D.C. and both of these could be compared to the tungsten lamp method. This indicated that D.C. measurements gave results within 10% of the pulsed measurements and that the tungsten lamp method was adequate. It should be noted that the p.m. tube quantum efficiencies are dropping very fast at the ruby wavelength so that the pulsed measurements with non-spectrally resolved light from the L.E.D. are not themselves suitable.

Alignment of the scattering system, although initially a lengthy process, required only minor adjustments from day to day. All the optics, on both the input and collecting arms, were mounted such that the interaction chamber on its trolley could be rolled away from the diode for anode foil replacement, without disturbing the alignment. Initial alignment was made using a continuous He - Ne laser beam co-axial with the pulsed ruby laser. This was used to align the beam steering prism and lenses so that the focal spot was central inside the interaction chamber. Burn marks on developed, unexposed Polaroid film were used at each stage to check the coincidence of the ruby and He - Ne laser beams. A roughly surfaced piece of aluminium was positioned inside the scattering chamber at the desired centre of the scattering volume. The incident laser beam was focussed onto this and the bright spot formed was imaged normally onto the polychromator entrance slit with the collecting optics. The alignment obtained in this way could be checked by Rayleigh scattering and scanning the final focusing lens across the polychromator entrance slit and noting the position of maximum scattered light.

The relatively high power of the ruby laser system led to problems of damage to optical components. This could be tolerated to some extent in the prisms and lenses but not in the amplifier rod. Consequently all components of the input optics were angled off normal to the laser beam so that reflected light could not enter the amplifier rod.

Damage to optical components was observed in particular in the T.I.R. prism, presumably as the intensity here is increased where the beam crosses itself. Damage to the input window of the scattering chamber was found to be due to its positioning at a caustic of the input lens. Damaged components scatter the laser light and if near the scattering chamber could lead to very high stray light levels. Damage to the T.I.R. prism was not a problem. However, damage to the input window which was a problem was eliminated by reducing the focussing lens focal length from 25 cm to 20 cm and bringing it closer to the input window, retaining the position of the focal spot.

System Performance

A number of factors are important in determining the performance of a laser scattering system and they operate at different parts of the scattered spectrum.

At and around the laser wavelength, stray light entering the detector by paths other than via a single scatter in the scattering volume is the most severe. Light scattered by both the input lens and window are generally the chief sources of stray light. The low optical cross-section of electrons, ~ $6.65 \cdot 10^{-29}$ m^2, means that light multiply scattered around the interaction chamber may easily swamp the true signal. In practice stray light levels were measured as equivalent electron densities and typical figures obtained were ~ 3.10^{14} cm^{-3} on the centre channel. Fig. 3.12 shows scattered light from 50 torr of carbon dioxide and from vacuum. (100 torr of carbon dioxide is equivalent to ~ 2.10^{16} cm^{-3}.) Rejection by the polychromator of the centre channel to the first neighbour channels was ~ 300, giving stray light levels equivalent to ~ 10^{12} cm^{-3} on these channels. Rejection to other channels was significantly higher.

Away from the centre wavelength the limiting factor was the large

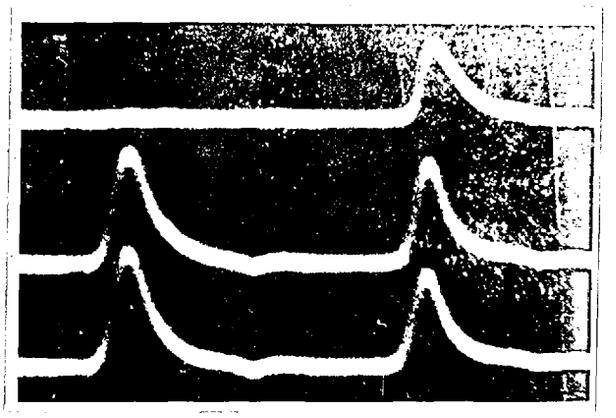

Fig. 3. ——2 *Typical Rayleigh scattered light signals from 50torr of carbon dioxide gas. The top trace is with no gas. The delayed pulse is the laser photo diode monitor.*

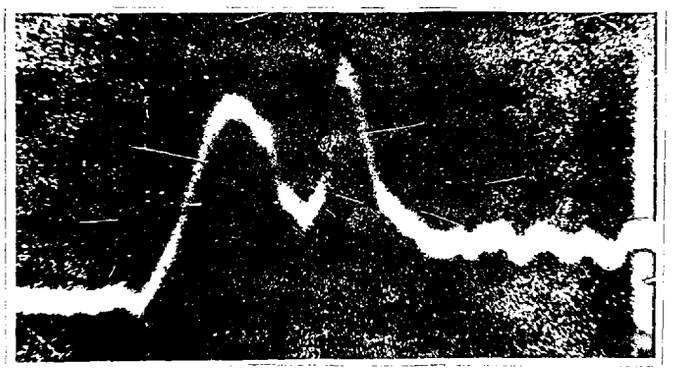

Fig. 3. ——13 *A typical Thomson scattered light signal. The initial peak is plasma light, the second peak being the scattered light.*

ratio of plasma light to scattered light. A typical trace is shown in Fig. 3.13 indicating the problem of distinguishing the signal from the background. The observed level of plasma light was much larger than that predicted by Bremsstrahlung and free-bound transitions; this is discussed in Section 4.7. The high plasma light level prevented scattering measurements to be made earlier than about 80 ns.

3.5.2 Spectral Line Emission

The H_α and H_β emission lines of atomic hydrogen were observed in order to find T_i and n_e. Their amplitude and spectral profiles were monitored as a function of time. The apparatus used was the same as the detection apparatus of the laser scattering experiment. However, the resolution of the polychromator was increased to six 2.2 Å channels by fitting a fibre bundle with $\frac{1}{6}$ mm channels. The higher light levels enabled operation of the p.m. tubes at significantly lower gains and giving less shot noise. The polychromator entrance slit was narrowed to obtain a rejection to the adjacent channels greater than 20:1 for a spectrally narrow input light source. To obtain good temporal resolution Tektronix 7000 series oscilloscopes were used. The polychromator was tuned with the aid of a conventional hydrogen lamp. The absolute sensitivity at both the H_α and H_β wavelengths was measured with a standard tungsten ribbon lamp placed at the intersection of the e-beam and the axis of the collecting optics. The emission of the lamp was assumed to be black body with a correction for the emissivity of tungsten as a function of wavelength WEAST (1972). The filament temperature was obtained from the calibration of the manufacturer (Philips National Laboratory) and the brightness temperature was checked with a n optical pyrometer. This yielded temperatures within 1%.

3.5.3 Spectral Line Absorption

This experiment, the measurement of the optical depth of the plasma to H_α radiation, was performed in conjunction with the Spectroscopy group at Imperial College who provided a tunable dye laser system. The optical depth was required to correct the H_α emission profiles for self absorption. Only measurements in the linear regime of the absorption profile of H_α as a function of time, will be reported here. The requirements for a background light source in this type of measurement are that it be much brighter than the absorber but not so bright as to affect significantly the population densities of any of the atomic levels of the absorber. In addition it must be broad band compared to the spectral width of the absorption line. To this end, the dye laser was used purely as a fluorescent cell, the front mirror and tuning elements being removed. The laser prior to these modifications is shown in Fig. 3.14. Fig. 3.15 shows the layout of the experiment. A broad beam of light was incident on the plasma and a fraction of the transmitted light was selected with a small aperture and neutral density filters and admitted to the collecting optics. The beam was then focussed onto the polychromator entrance slit, the $f/6$ aperture being nearly filled. Although there was sufficient light to do away with the focussing this would result in a very small area of the diffraction grating being illuminated and would give poor spectral resolution. The polychromator was set up in a manner similar to that used in the spectral line emission measurement. However, only the central channel and the two adjacent channels had sufficient optical depth to warrant their use. The output of the fluorescing dye cell was monitored with the same photo diode as used in the laser scattering measurements. More details of the dye laser system are described in SKINNER (1974).

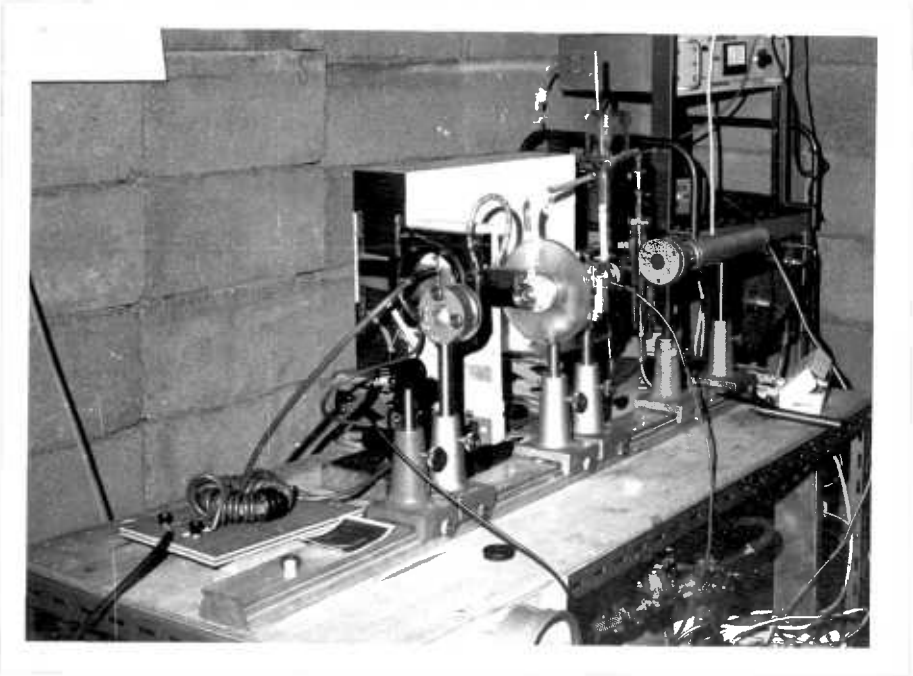

Fig. 3.14 Photograph of dye laser system used for the absorption experiment.

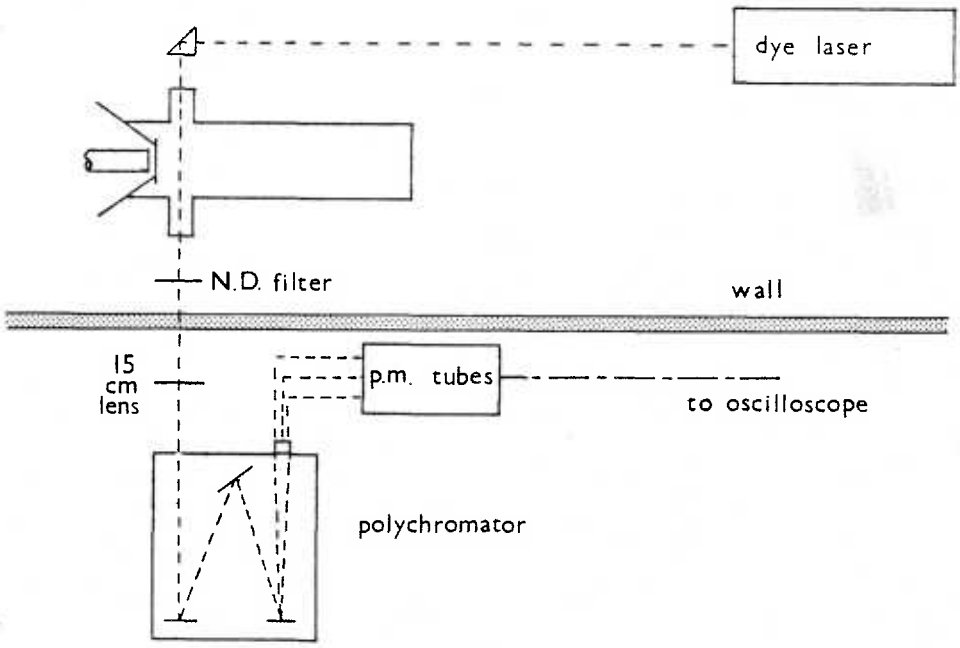

Fig. 3.15. Layout of the absorption experiment.

3.5.4 Streak Photography

The plasma was observed with a streak camera to obtain information on the temporal history of the light emitted and on its spatial dependance. The 90^{o} scatter chamber was used so that the camera could view the plasma perpendicularly to the beam propogation direction. The camera used was an IMA~CON made by Hadland. The slit was placed in the plane of the port rather than in a confocal plane of the plasma. This was possible because the depth of field was large enough to include the slit and the plasma. The experimental arrangement is shown in Fig. 3.16. In order to reduce the noise level on the sweep generator and intensifier gain, the camera was electromagnetically screened and the power and trigger leads originated from the screened room.

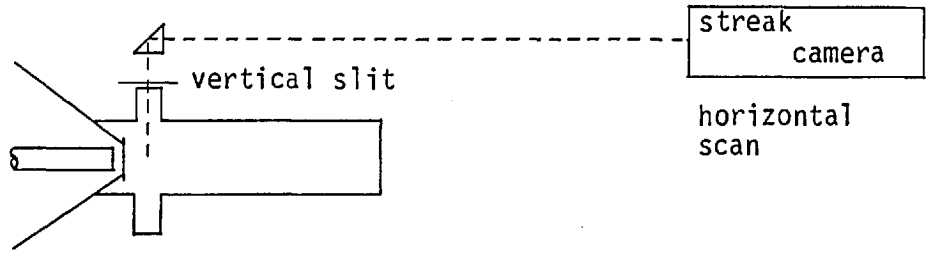

Fig. 3.16 Layout of the streak photography experiment.

3.6 X-ray Diagnostics

3.6.1 Hard X-rays

Hard X-rays are only produced by electrons at high energies. Thus they can give information on the beam behaviour rather than the plasma. In addition hard X-rays give definite information on the failure of both the generator and the guide field system during a shot. If time resolved they can indicate when the beam fired with respect to other events. All real time hard X-ray measurements were made with p.m. tubes both with and without scintillators. If used the scintillator material was 'Pilot B' or its equivalent as this has a fast fluorescent decay time of ~ 1.5 ns.

Time integrated measurements were obtained with quartz fibre dosimeters. These were used primarily to determine if the equipment was working properly, low doses indicating diode or generator failure, high doses indicating guide field failure.

The presence of the guide field coil modules around the system precluded the use of hard X-ray measurements to obtain information on the angular scatter of the beam electrons as this requires a polar plot of the intensity, FORSTER et al. (1971).

3.6.2 Soft X-rays

The interest in the emission of soft X-rays (~ few keV) stemmed from the possible existence of a high energy tail to the plasma electron velocity distribution which would lead to soft X-ray production by Bremsstrahlung.

Time integrated measurements were made using Kodirex film as a detector. Access to the plasma was via the ports on the 90^{0} scattering chamber but as glass and quartz strongly absorb at the wavelengths of interest the film was placed inside the vacuum system. Foil filters were placed over the film to obtain information on the spectral distribution

of the emission. Filters used were, polyethylene, aluminium, cobalt, nickel, copper, titanium and lead. In addition a layer of 5 μm light-tight aluminium foil was used to cover the film to prevent exposure at optical wavelengths.

Pin hole photography was performed in a similar manner, a 2 mm diameter "pin hole" being placed in the arm of the scattering chamber.

Measurements of the temporal history of the soft X-ray emission were obtained using a solid state pin detector (type 100-PIN-250, made by the Quantrad Corporation). As the detector was also sensitive to hard X-rays it was screened with ~ 2 cm thickness of lead which also formed a collimator. The required close proximity of the detector to the interaction chamber leads to severe noise problems. The detector 'saw' the plasma through one of the scattering ports, the glass window being replaced with 100 μm polyethylene. As with the time integrated measurements 5 μm aluminium foil was used to exclude optical wavelengths. Signals were monitored on 7000 series Tektronix oscilloscopes.

3.7 Operational Notes

The experiment operates on a number of distinct time scales, ranging from milliseconds for the guide field and ruby laser flash tubes to nanoseconds for the beam and laser pulses.. A typical arrangement for triggering the various components is shown in Fig. 3.17.

When possible, numerous diagnostics were used simultaneously on a given shot. Many combinations were, however, precluded as either too much equipment would have to be duplicated or the noise levels became too high. Table 3.1 shows the combinations used.

The repetition rate of the system was typically one shot per hour depending upon the exact experiment. The main limiting factor was the diode pump down time, the diode being released to atmospheric pressure every shot for anode foil replacement.

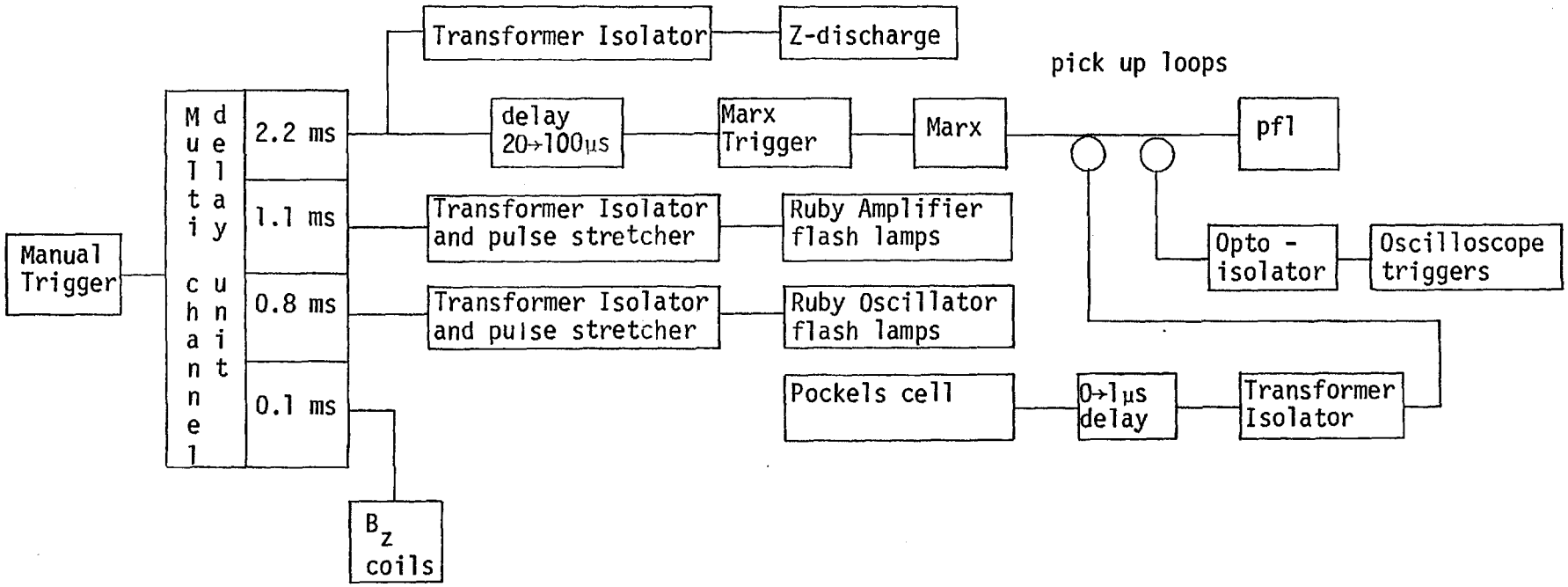

Fig. 3.17 A typical arrangement of the triggering circuit for laser scattering when injecting into a preformed plasma.

TABLE 3.1 DIAGNOSTIC COMBINATIONS

Diagnostic	Combinations used							
H_α Emission	•							
H_β Emission		•						
H_α Absorption			•					
Laser Scattering				•				
Diamagnetic Loops					•	•		
B_θ Probes						•		
I_{NET}				•	•	•		
Faraday Cup				•	•	•	•	
Streak Photography					•			
Real Time Soft X-rays							•	
Real Time Hard X-rays	•	•	•	•			•	

CHAPTER FOUR

RESULTS OF INJECTION OF THE BEAM INTO NEUTRAL GAS

4.1 Introduction

In this chapter the results of injection into neutral gas are presented. A detailed interpretation of the major diagnostics is left to chapter 5. However, some of the more basic interpretation is presented here. The chapter begins with a description of the gross beam behaviour and then proceeds to give the results of each of the diagnostics described in chapter 3.

The main results are as follows: the plasma diamagnetism and return current dissipation indicate a strong interaction between the beam and the plasma but this may be localized to a region close to the anode foil. These two diagnostics give plasma energy densities of up to 3.10^{18} $eVcm^{-3}$, which for fill pressures of $\sim$ 100 mtorr indicate temperatures $\sim$ 500 eV. In sharp contrast to this are the line broadening and laser scattering results which indicate $T_i \sim 100$ eV, $T_e \leq 15$ eV and $n_e \leq 4.10^{15}$ cm^{-3}.

4.2 Gross Beam Behaviour

4.2.1 Space-charge neutralization

The space-charge current limitation, discussed in chapter 1, has some macroscopic effects on the system. Firstly, if the beam pulse duration is not significantly longer than the space-charge neutralization time a substantial portion of the beam will not be injected. Secondly, a virtual cathode is set up in front of the anode foil by the electron space-charge. This reflects the bulk of the beam electrons back into the diode. These electrons then oscillate about the anode, between the real

and virtual cathodes. On each traversal of the anode foil they give up some energy. This heats the foil, forming a plasma or increasing an already existing plasma that can expand across the A-K gap, so shorting it out and stopping any further beam generation. In addition the large space-charge fields generated in the region of the virtual cathode may accelerate ions as has been observed by many other workers, for example SUNKA (1977), RANDER (1970).

Experimentally one observes a reduction in the transmitted energy as the pressure of hydrogen is reduced from a few torr to a few hundred millitorr, as is shown in Fig. 4.1. This reduction is not due to absorption of the beam by the plasma (this being relatively insignificant) but is due to the beam reflection prior to space-charge neutralization.

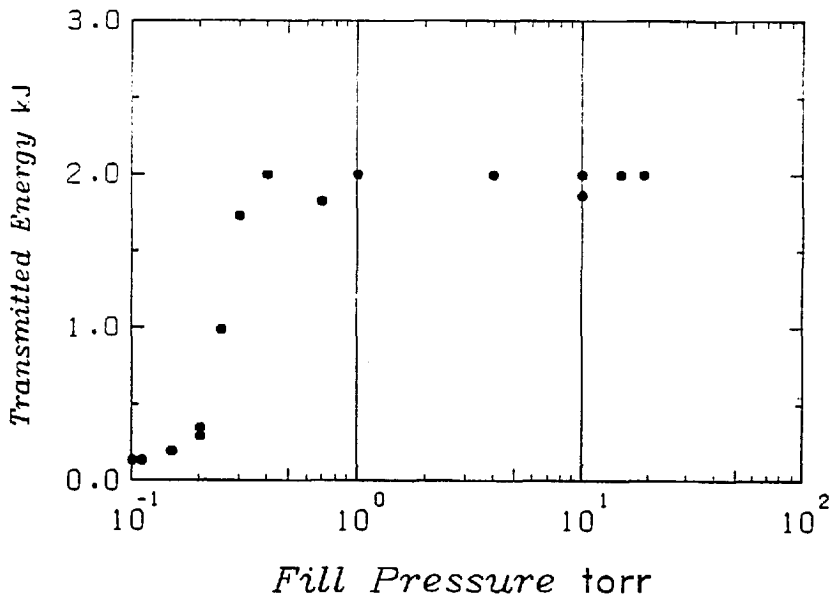

Fig. 4.1 A plot of transmitted beam energy versus fill pressure of hydrogen as measured with the calorimeter at the far end of the interaction chamber.

At filling pressures below 100 mtorr the A-K gap closure is so severe and the space-charge neutralization time so long as to preclude interaction measurements. Even in the range 100 to 200 mtorr one has to ensure that the prepulse, discussed in section 2.2.4, is very low (< 2.5%) otherwise the diode behaviour becomes erratic. The use of aluminium foils instead of Al/My generally results in more reproducible behaviour even with prepulses up to 10% of the main pulse. This may be due either to there being more material present which will hold the temperature of the foil down, or because there are far less light ions in Al foils. Both these explanations could lead to a reduction in the expansion rate of the anode plasma.

4.2.2 Anode foil damage

The damage to the anode foil is consistently indicative of the system behaviour. Some examples under various conditions are shown in Fig. 4.2. At the higher pressures, with Al/My anodes, damage consists of a central hole about 2 cm in diameter with a surrounding annulus of about 5 mm radial width, where aluminium has been evaporated off the Mylar. As the pressure is reduced both features enlarge. At 100 mtorr the hole is some 2½ cm in diameter and no aluminium is left on the foil. In the event of a system failure the foil damage is a helpful diagnostic. If the guide field fails, beam generation still occurs. However, the absence of a strong B_z field permits the secondary plasma electrons to escape radially, rapidly increasing the space-charge neutralization rate. The resulting anode foil damage is a clean hole ~ 2 cm in diameter but with no intermediate region where the aluminium is evaporated and with the Mylar still intact. A possible explanation of the damage resulting from a normal shot is that the anode foil provides a path across the field lines for currents to neutralize the large space-charge which

exists in a magnetized system. This is not required in the absence of the guide field.

If alternatively the beam generator fails, due to either a very large prepulse or too high a base pressure in the diode, the Mylar may be left intact but the aluminium evaporated to a varying degree.

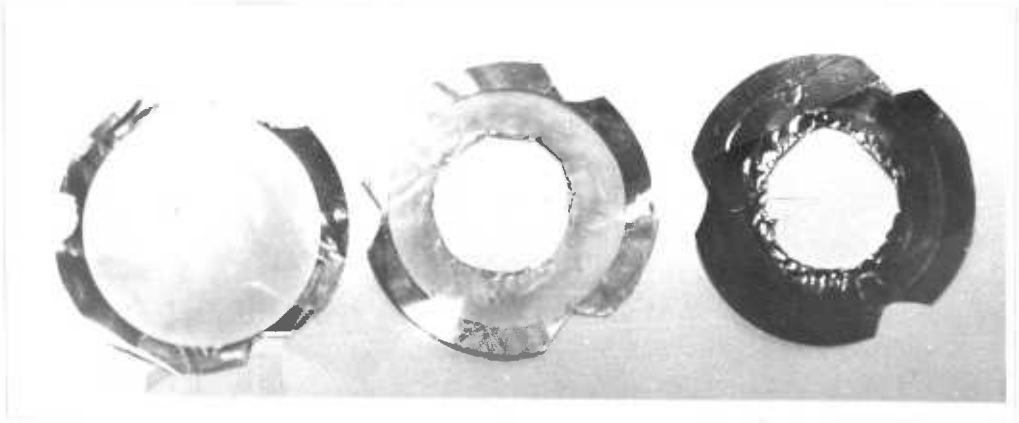

(a) (b) (c)

Fig. 4.2 Various anode foil damage patterns, (a) high diode base pressure or very large prepulse, (b) normal and (c) no guiding B_z field.

4.2.3 Beam uniformity

The inability to place probes inside the beam channel because of either damage to the probe or disruption of the beam or both, means that the current distribution within the beam is not measurable directly.

However, damage patterns on targets placed in the path of the beam indicate that the beam distribution is uniform. In particular the crater formed in the calorimeter after ~ 100 shots has a very flat bottom with a well defined circular edge corresponding to the cathode diameter, as shown in Fig. 4.3. Similarly, damage patterns on other targets, e.g. stainless steel and polyethylene, have indicated good uniformity. However, no control experiment with other profile beams has been attempted and consequently the uniformity, which has been assumed throughout this experiment has not been definitely established.

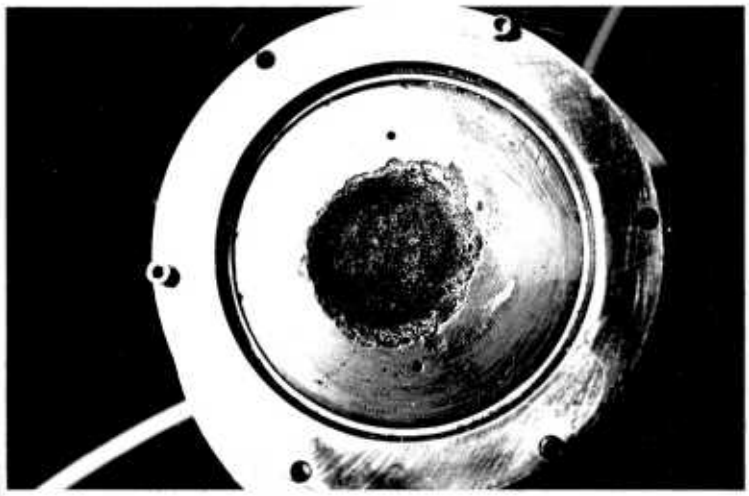

Fig. 4.3 Damage to the calorimeter collector after many shots shows a flat bottomed crater with a well defined boundary.

4.2.4 Streak Photography Measurements

Streak photography is one of a number of diagnostics used to check that the size of the main plasma channel corresponded to the beam diameter of 2 cm. This dimension has been assumed in many calculations regarding energy density, resistivity, inductance, etc.

Some examples of streak photographs, taken side-on, are shown in Fig. 4.4. As a very high contrast film, Polaroid 410, was used, little if any of the cylindrical nature of the plasma is discernible. However, the measurements indicate a 2 cm diameter plasma channel with no expansion and also a continual emission of light post-beam at high pressures. At low pressures only an intense flash on beam injection which lasts about 100 ns, is observed, agreeing well with the observation of the continuum at $\lambda \sim 6943\text{Å}$, discussed in section 4.7.

The lack of any radial expansion is in agreement with laser scattering and H_α absorption measurements made outside the plasma channel, see sections (4.7 and 4.8). Neither of these indicate any plasma present. In addition the diamagnetic results discussed in section 4.6.2 indicate plasma expansions of ~ 1 mm which is beyond the resolution of these techniques.

4.3 Beam and Net Currents

4.3.1 Gross Trends

Fig. 4.5 shows net current waveforms obtained under various conditions. A number of overall trends are immediately apparent. As the filling pressure of the target gas is increased from 100 mtorr to 1 torr of hydrogen, the peak value of the net current decreases.

In addition at a given pressure, especially at the low end of the range, there is a correlation between the peak net current and the rise

0.1 torr
33 ns/mm

0.2 torr
33 ns/mm

1.0 torr
83 ns/mm

Fig. 4.4 Examples of streak photographs at three pressures. The vertical axis is the diameter, the horizontal axis, time.

time of the beam, and also between the peak net current and the type of foil used. Maximum values for the net current are obtained with Al/My anode foils, with a fast rising beam current and into low pressure hydrogen. These correlations are shown in Fig. 4.6.

The beam current shows little dependence on the filling pressure above 200 mtorr. Below this pressure the diode performance is affected, reducing the beam current. This is reported by PRONO et al. (1975) and discussed in section 4.2.1.

4.3.2 Time history of a typical net current

Fig. 4.7 shows a typical net current waveform which can be split into three regimes for the purpose of discussion. Section AB is not always observable but when present it can also be seen on the beam current waveform with a similar amplitude and time history. An example is shown in Fig. 4.8. The similarity of the two indicates that little or no return current is flowing at this time. This corresponds approximately to the critical or space-charge limited current discussed in section 1.4. Equation 1.9 gives a value ~ 1.3 kA for the critical current in an infinite system with no space-charge neutralization. Values measured at point B are typically 2-4 kA.

At point B the plasma number density is sufficient to permit space-charge neutralization of the beam by a divergent axial flow of electrons. Consequently, beam electrons are no longer reflected and the beam current rises. As the net current rises also, resulting in fractional current neutralization, the plasma resistivity must be sufficiently high so that the return current decays on the timescale of the beam rise time. For pressures below 350 mtorr the net current risetime is comparable with that of the beam but clamps at point C. For higher pressures no clamping is observed, the current rises more slowly and throughout the beam pulse. This is shown in Fig. 4.5.

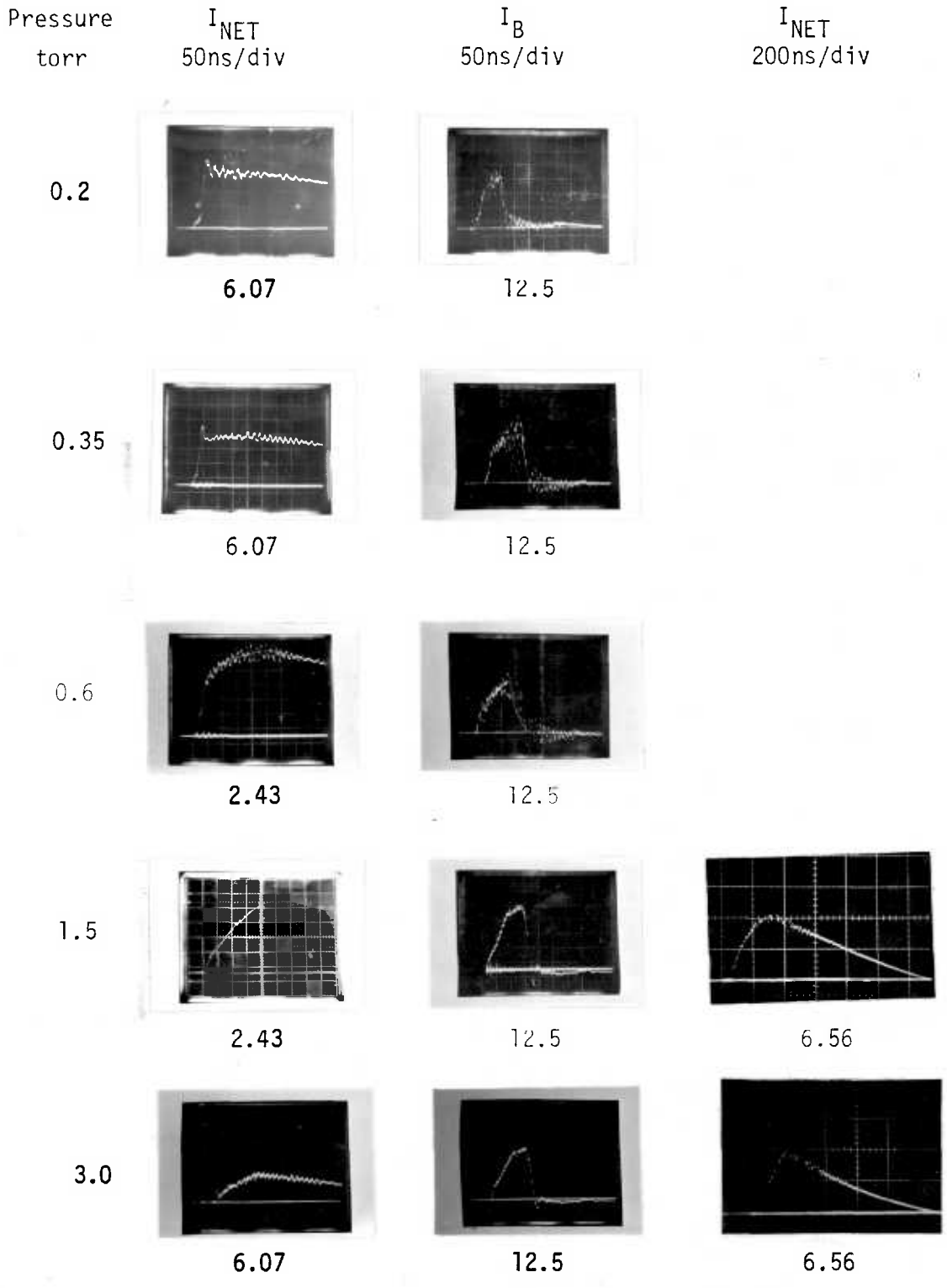

Fig. 4.5a Beam and net current waveforms at various pressures. Al/My anode foils. The figures under each trace are the scales in kA/div.

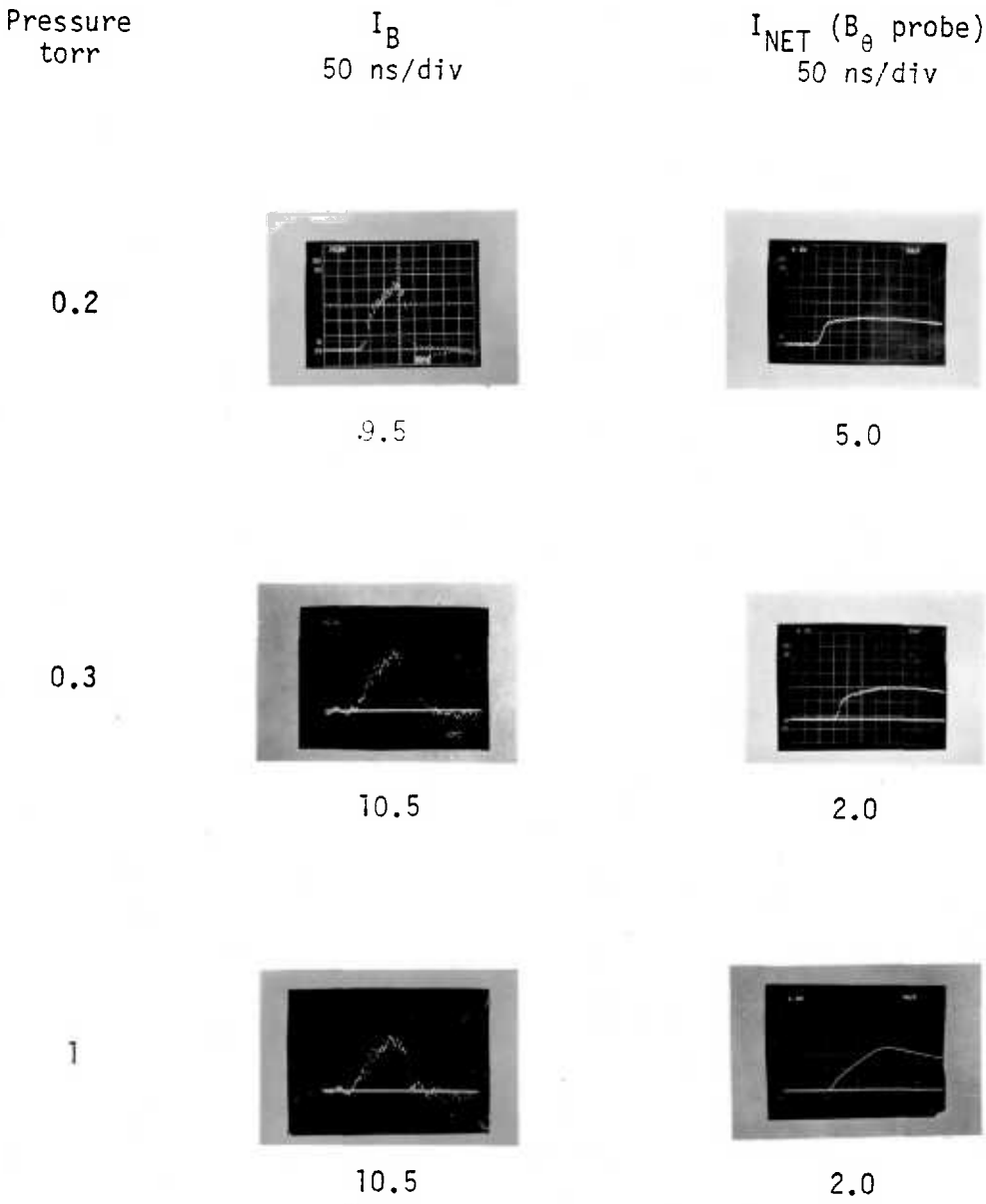

Fig. 4.5b Beam and net current waveforms at various pressures. Al anode foils. The figures under each trace are the scales in kA/div.

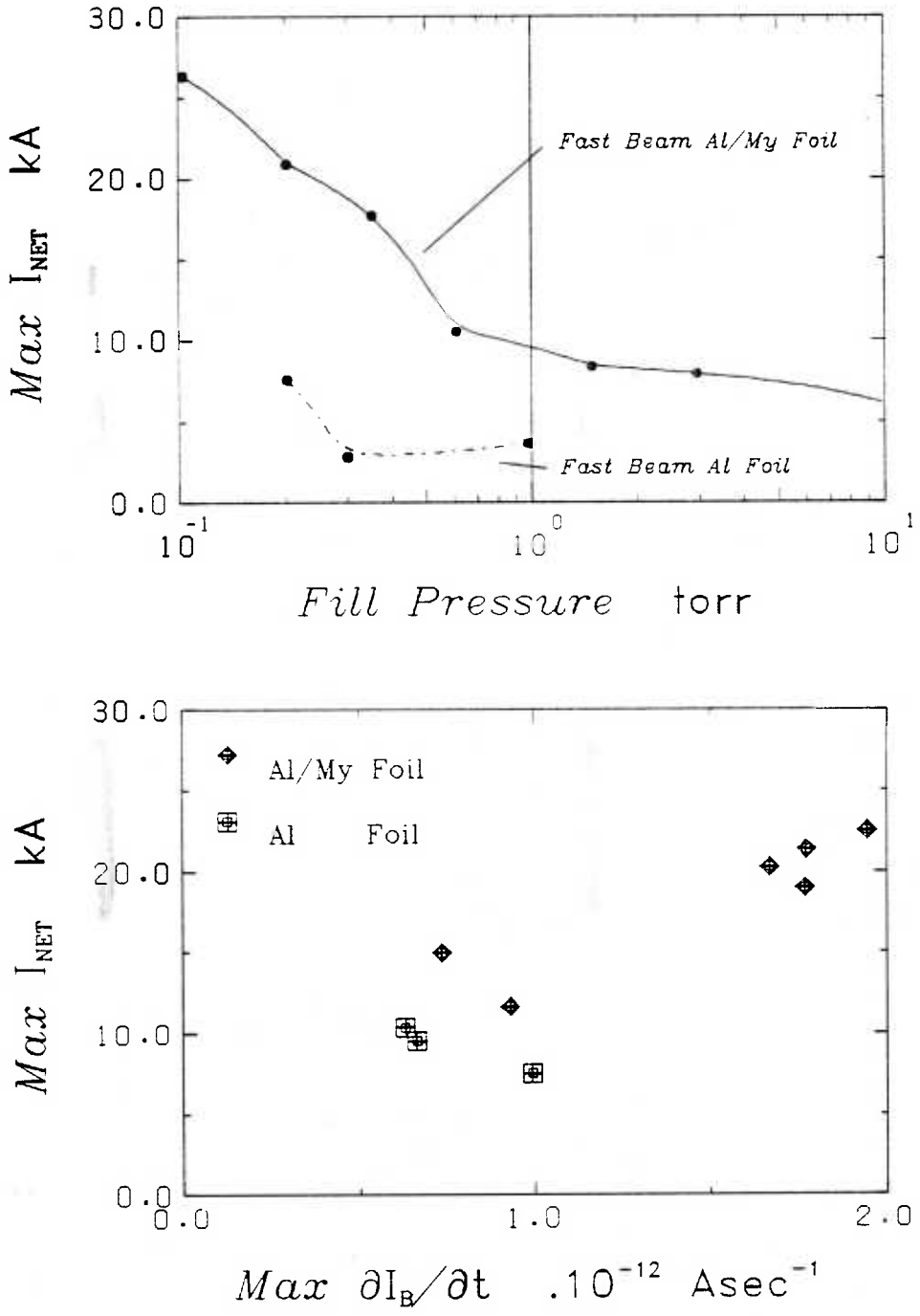

Fig. 4.6 Plots of the maximum net current versus both fill pressure and the beam rate of rise. A general trend to higher net currents at low fill pressures with fast rising beams is indicated.

At point C the plasma resistivity drops abruptly freezing the B_θ field into the plasma and preventing any further gross changes. The values of the resistivity η prior to point C are ~ 10^{-3} Ωm. The full temporal history of the resistivity is shown in Fig. 4.17.

The region CD is an L/R decay of the plasma current. Whilst the beam is still on, the plasma current opposes the beam and its decay results in an increase of the net current. On beam termination the plasma current reverses and becomes the net current, its decay being seen directly.

4.3.3 The L/R decay of the plasma current

The inductance of the current path is given by GROVER (1962).

$$L_1 = \frac{100\ \mu_0}{2\pi}\left[\text{Ln}\ \frac{b}{a} + \frac{1}{4}\right]\ \text{Hm}^{-1} \qquad 4.1$$

where $\frac{b}{a}$ is the ratio of the chamber to beam radii and a uniform current distribution has been assumed. For b = 0.038, a = 0.01 m, L_1 = 317 Hm^{-1}. The inductance is insensitive to small changes in a which may occur from diffusion and expansion of the plasma. That changes in a are small has been checked by streak photography, laser scattering, spectral line absorption and measurements of $B_\theta(r)$ for r > a. Only the plasma diamagnetic results discussed in section 4.6 yielded an estimate of the expansion, of $\lesssim 10^{-3}$ m. If L/R is constant, the current decay is exponential. All observed decays were nearly linear, with the exception of shots without the applied B_z field. In this case the decay is closely exponential as can be seen in Fig. 4.9. This observation is in agreement with work on an unmagnetised system. As it is known in a magnetised system that the inductance is constant it follows that the resistivity is changing. Without the guide field, changes in both L and R are possible and large changes in the plasma radius have been reported by VANDEVENDER (1974). The decay with a guide field cannot be truly linear

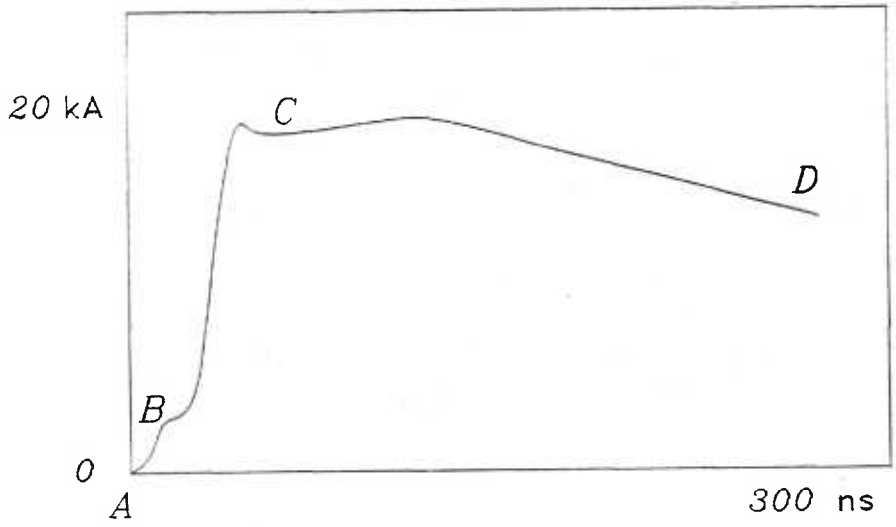

Fig. 4.7 A typical net current waveform showing, unneutralized beam current (AB), bulk gas breakdown (BC) and plasma current decay (CD).

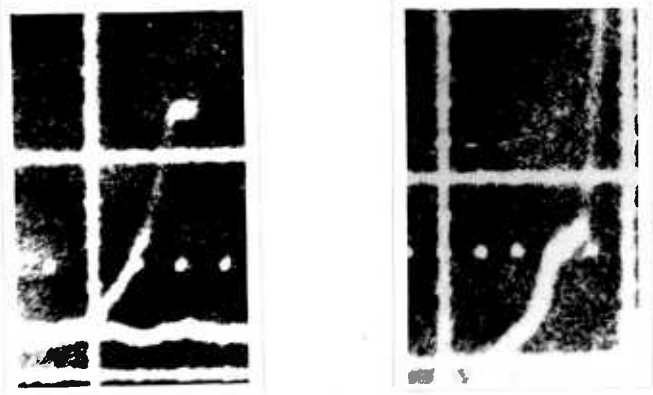

Fig. 4.8 An example of unneutralized beam current. (a) is the Faraday cup signal and (b) the net current monitor in the wall. Both traces indicate about 1.5kA before the rapid current rise occurs on gas breakdown.

as this implies that $I_{NET} = 0$ in a finite time whereas the decay must always be asymptotic to zero current in the absence of capacitive effects.

The decay is given by

$$IR = - L \frac{dI}{dt} \qquad 4.2$$

for $I = I_o + kt$

$$R = \frac{- Lk}{I_o + kt} \qquad 4.3$$

and η is given by

$$\eta = \frac{-\pi a^2 k L}{I_o + kt} \qquad 4.4$$

(note: $k < 0$)

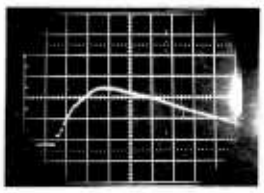

$B_z = 1.4$ tesla

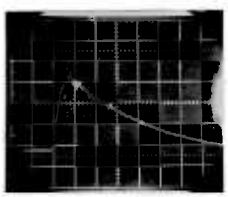

$B_z = 0$

Fig. 4.9 The two traces show the difference in the net current decay with and without an applied B_z. (Rogowski coil (3) 2.6kA/div, 100ns/div, 1torr H_2)

This implies that the resistivity increases in time during this decay period. In Fig. 4.10 observed values of ($^1/k$) are plotted against the fill pressure.

4.3.4 Post beam increase in I_{NET}

On some shots for fill pressures of < 500 mtorr and with Al/My anode foils, the net current was observed to increase slightly after the beam had terminated. Some examples are shown in Fig. 4.11. This has not been observed at high pressures or with Al anode foils. The third example in Fig. 4.11 shows an increase very late after the beam and the time correlates well with the turning point of the associated diamagnetic signal.

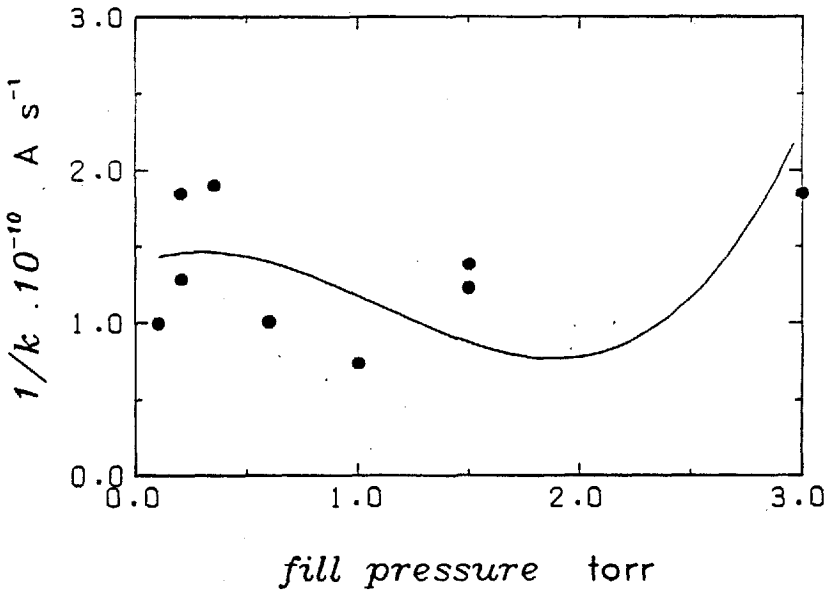

Fig. 4.10 A plot of 1/k versus fill pressure. k is the net current decay rate.

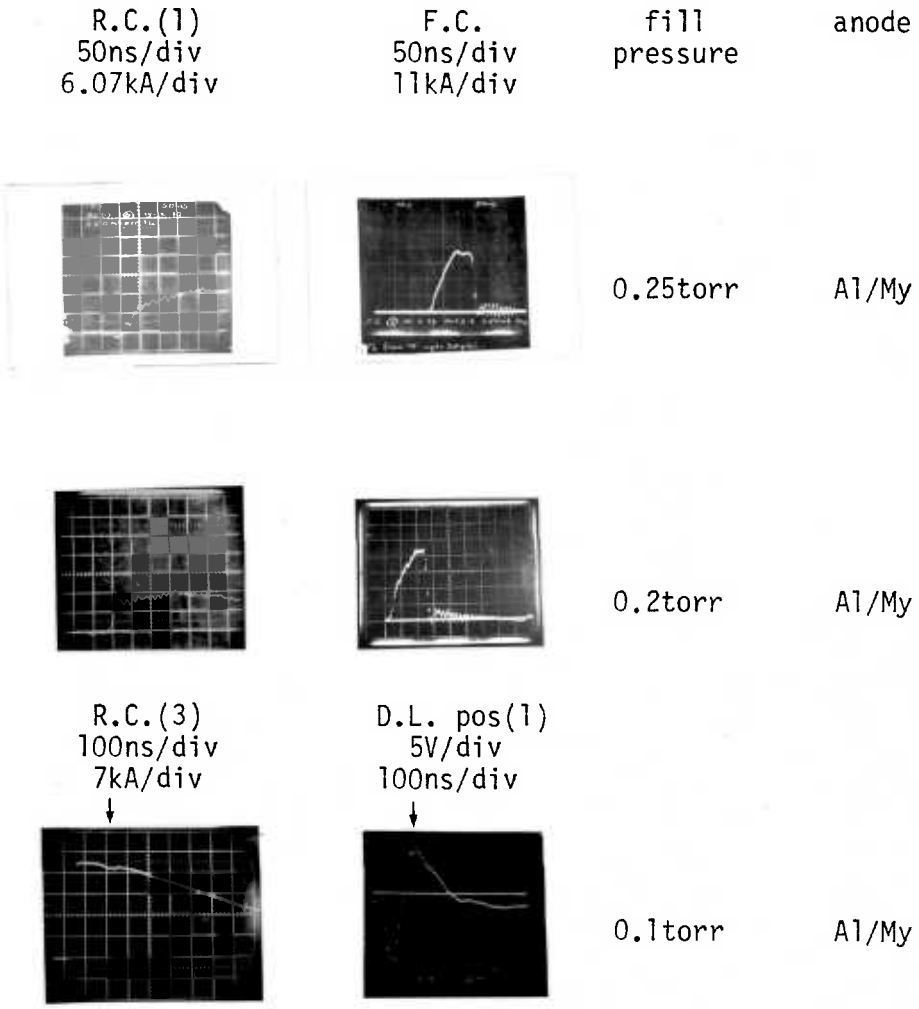

Fig. 4.11 Examples of post beam rises in the net current. The last example shows temporal correlation with the turning point of the diamagnetic signal.

4.3.5 Net current overshoot

On many net current waveforms at lower pressures, overshoot at point C has been observed. Its absence on occasions is indicative that the effect is genuine and not produced by the diagnostics which are likely to be more reproducible than the plasma. This is supported by two observations. Firstly, it was not possible to produce such an overshoot by injecting a fast rising square current pulse down the centre of the chamber, and secondly, net current waveforms shown by PRONO (1975) also indicate an overshoot. However, their measurements were made with resistive current shunts in the wall of the interaction chamber.

4.3.6 Beam current waveforms

Beam current waveforms varied considerably and in addition were significantly less reproducible at lower target gas pressures. In general however, two classes of pulse could be distinguished by their rise time, although intermediate shapes did occur. Examples of the classes, which will be referred to as fast and slow rising, are shown in Fig. 4.12.

The conditions under which a particular pulse is generated is not fully understood but the presence of a diode prepulse is thought to be an important factor. The occurrence of a fast pulse at low filling pressures invariably leads to a lower degree of magnetic neutralization.

The use of Al anode foils does not greatly affect the beam waveforms obtained and it has been assumed that the only effect is to increase the r.m.s. scatter angle of the beam electrons. Fig. 4.13 shows a plot of percentage current neutralization versus fill pressure for various combinations of foil and class of pulse.

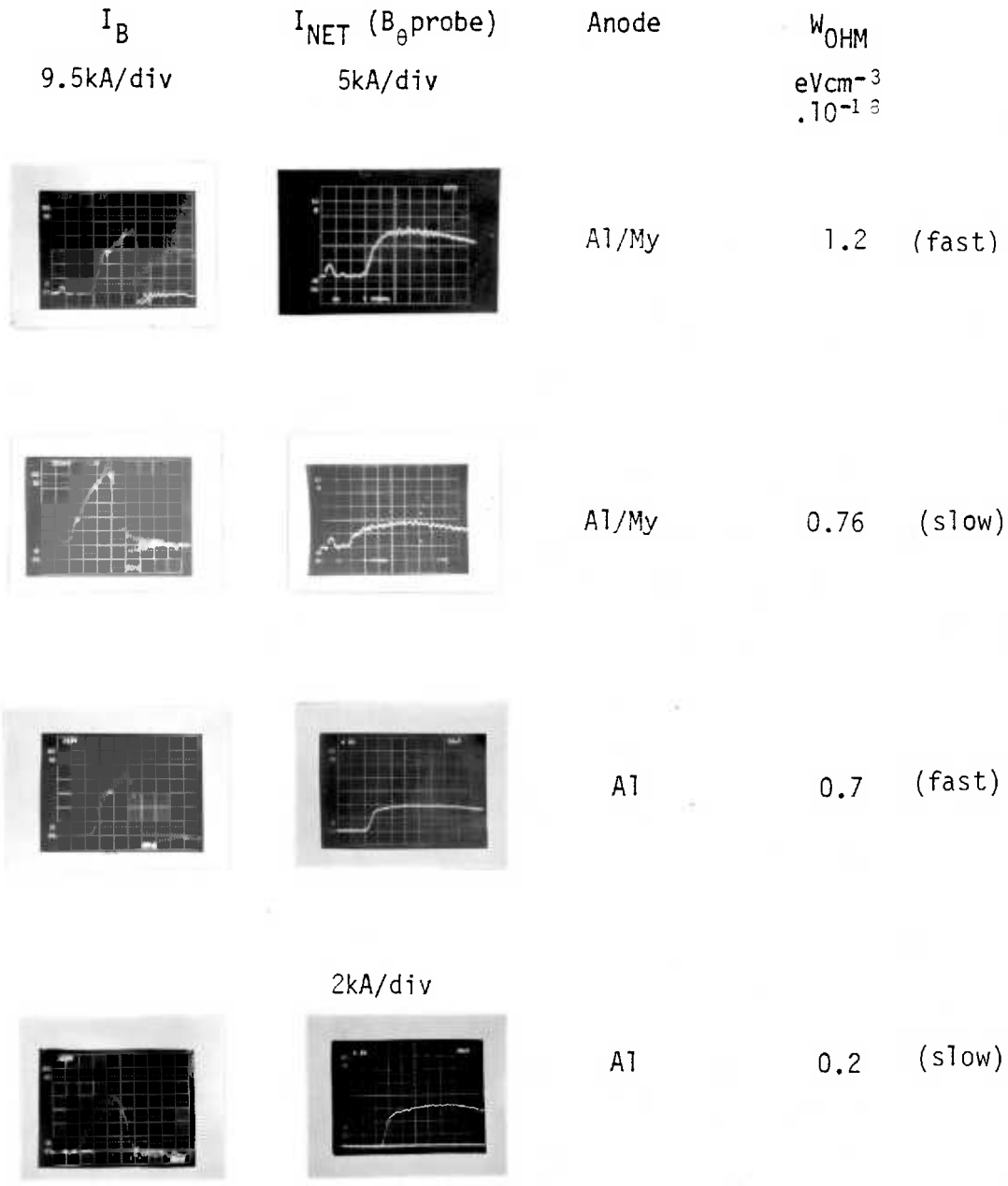

Fig. 4.12 Examples of beam and net current waveforms, at 0.2 torr, showing the effect of beam rise time and anode foil type.

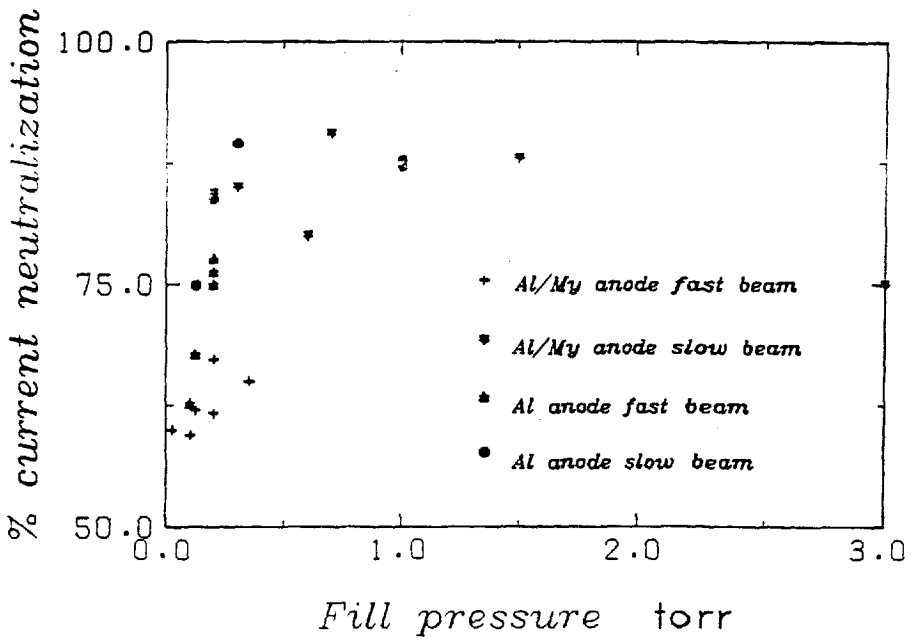

Fig. 4.13 Plot of fractional current neutralization versus fill pressure for fast and slow beams with Al/My and Al anode foils.

4.4 Spatial Variation of B_θ

The B_θ self field of the plasma was investigated in both the radial and axial directions. The three Rogowski coils mounted in the chamber wall served to give axial information whilst the two B_θ probes gave information on the radial distribution. No measurements of B_θ very close to or inside the beam channel could be made. This was because the very high energy density of the beam would destroy a small probe, whilst a more rugged probe would have seriously disrupted the beam.

4.4.1 Radial variation

For the simultaneous measurement of B_θ at two radial positions,

probes were placed at different azimuths and consequently the interpretation requires that there is no θ variation in B_θ. Some typical traces are shown in Fig. 4.14. For comparison purposes the B_θ field has been assumed to have the form

$$B_\theta = \frac{\mu_o}{2\pi r} I_{NET} \qquad 4.5$$

where I_{NET} flows in the beam channel. The probe signals obtained after integration with a 2 μs RC integrator may then be related to I_{NET}.

$$V_{OUT} = -\frac{\Delta\phi}{RC} = -\frac{NA}{RC}\Delta B_\theta = -\frac{NA}{RC}\frac{\mu_o}{2\pi r} I_{NET} \qquad 4.6$$

Hence

$$I_{NET} = -2\pi r\, RC\, V_{OUT}/NA\, \mu_o \qquad 4.7$$

where NA is the probe turns area discussed in section 3.4.3. Deviations from equality of the two signals normalized by equation 4.7 indicate the presence of an axial current of $\lesssim$ 2 kA flowing in the region between the probes, i.e. between radii 24.5 mm and 34 mm as shown in Fig. 4.15. This gives a mean current density of $\sim 10^6$ Am^{-2} compared with $4.8 \cdot 10^7$ Am^{-2} in the beam channel. Another estimate of this current density can be obtained from measurements of I_{NET} made with the first (small aperture) Faraday cup, used without a foil, and comparing them with simultaneous measurements of I_{NET} from Rogowski coil 3. At a fill pressure of 200 mtorr (as used for the above measurement) a current density of $8.2 \cdot 10^5$ Am^{-2} is indicated and is in reasonable agreement with that obtained from the B_θ probes.

The electron number density in this region may be estimated from the current density and the electric field given by the rate of change of the total net current. If the resistivity is entirely due to electron

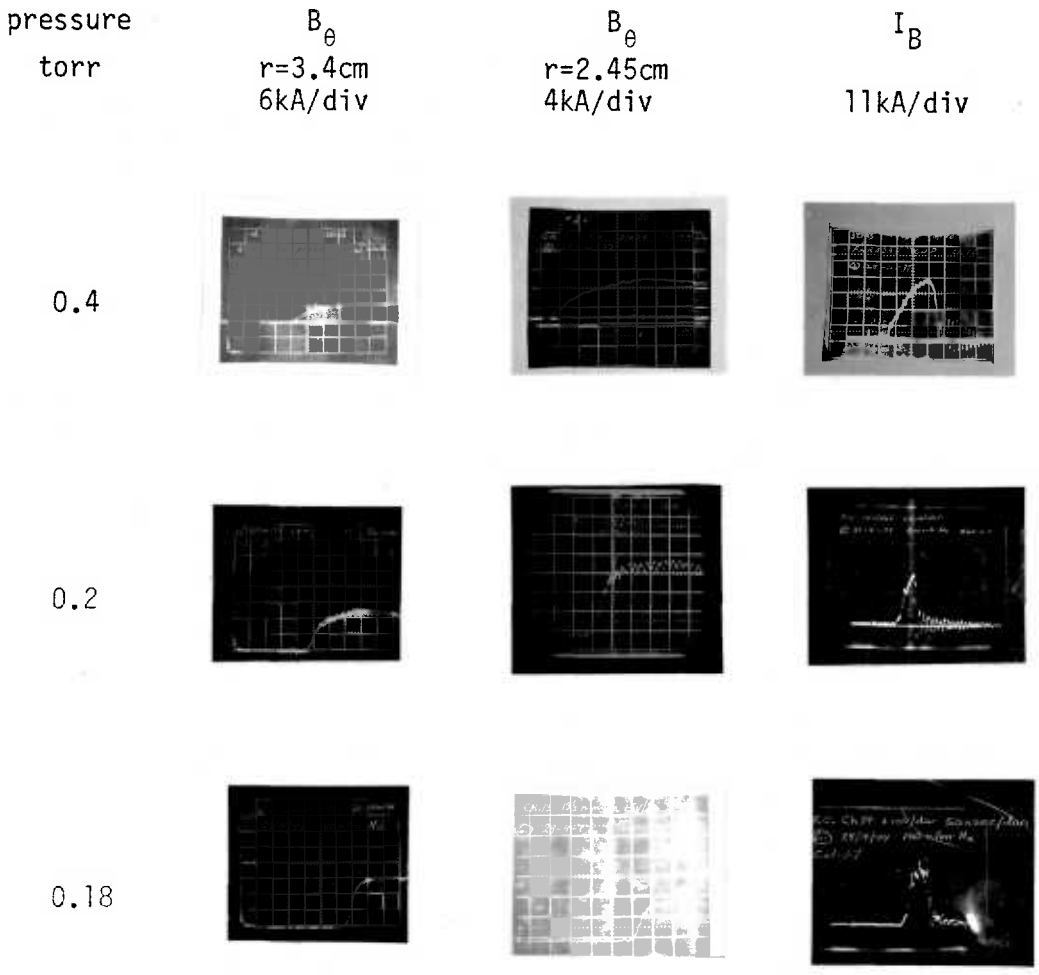

Fig. 4.14 *B_θ waveforms at two radial positions and associated beam currents, for three fill pressures.*

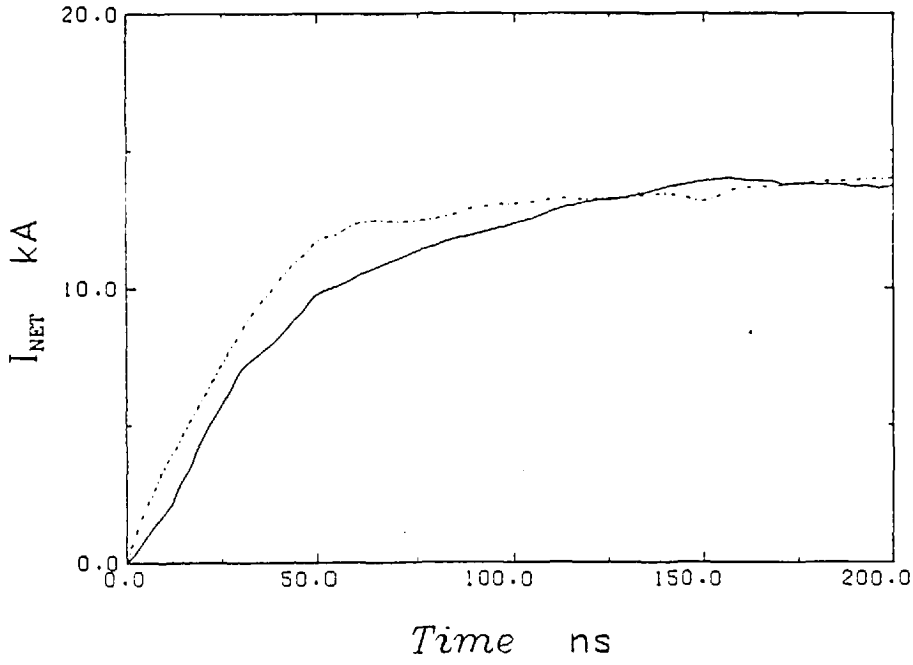

Fig. 4.15 Plot of net current at two radii (solid line, 2.45cm; broken line, 3.4cm) indicating some current outside the beam channel and showing its decay.

neutral collisions then from Ohm's law

$$\eta = \frac{E}{j} = \frac{m_e \nu_{en}}{n_e e^2} \qquad 4.8$$

where ν_{en} is the electron neutral collision frequency given by

$$\nu_{en} = n_n \sigma_{en} v_e \qquad 4.9$$

with

$$v_e = j/en_e \qquad 4.10$$

Combining equations 4.8, 9 and 10 yields

$$n_e^2 = j^2 \frac{m_e n_n \sigma_{en}}{e^3 E} \qquad 4.11$$

using the following values

$$j = 10^6 \text{ Am}^{-2}$$
$$n_n = 1.2 \cdot 10^{22} \text{ m}^{-3}$$
$$\sigma_{en} = 10^{-19} \text{ m}^{-2}$$
$$E = -L \frac{dI_{NET}}{dt} \simeq 10^5 \text{ Vm}^{-1}$$

gives

$$n_e \sim 1.6 \cdot 10^{18} \text{ m}^{-3}$$

corresponding to a fractional ionization of about 0.01%.

4.4.2 Axial variation

The Rogowski coil measurements typically show an increase in the net current of ~ 20% between 1 and 12 cm downstream from the anode foil. Fig. 4.16 shows a plot of the increase in this region against the fill pressure. No further increase is observed between 12 cm and 23 cm. This increase indicates a radially outward plasma current in the first region corresponding to ~ $1.3 \cdot 10^4$ Am^{-2} at the edge of the beam. This figure should be compared with a peak net current density of ~ 5.10^7 Am^{-2} in the centre of the plasma channel and ~ 10^6 Am^{-2} in the surrounding neutral gas.

4.5 Plasma Resistivity and the Return Current Dissipation (ηj_p^2)

4.5.1 Method of measurement

The plasma resistivity and return current dissipation can both be calculated from the beam and net current waveforms. Considering the z-component of Ohm's law with the Hall and pressure gradient terms neglected gives

$$E_z + v_\theta B_r - v_r B_\theta = \eta j_{pz} \qquad 4.12$$

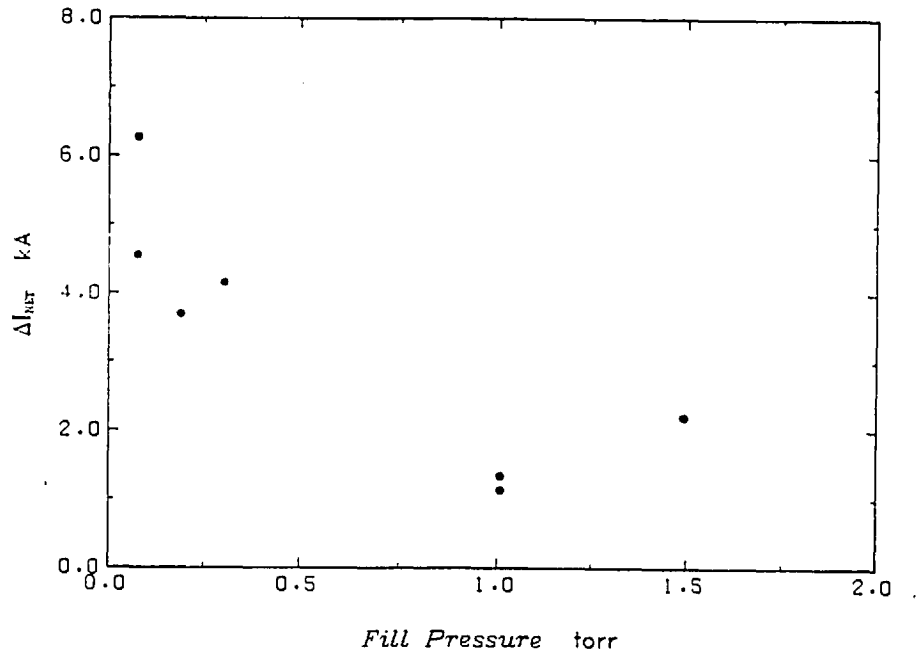

Fig. 4.16 Plot of ΔI_{NET} (the axial change in net current) versus fill pressure.

Axial symmetry will remove the $v_\theta B_r$ term, however, the $v_r B_\theta$ is only negligible for large E_z. E_z is given by Faraday's law:-

$$E_z = - L_1 \frac{dI_{NET}}{dt} \qquad 4.13$$

where L_1 is given by equation 4.1. At low pressures I_{NET} is typically $\geq$ 10 kA and rises in $\leq$ 30 ns giving values for $E_z \sim 10^5$ Vm^{-1}. However, when the net current waveform flattens out E_z falls to $\sim 1 \rightarrow 2.10^4$ Vm^{-1}. Estimates of the $v_r B_\theta$ term may be found from the diamagnetic signals, see section 4.6, which indicate values of $v_r \sim 2.5 \cdot 10^4$ ms^{-1}. At early times B_θ is small but for low pressures after 30 ns rises to $\leq$ 0.5 Tesla giving values for $v_r B_\theta \sim 1.3 \cdot 10^4$ Vm^{-1}. Hence at low pressures after the net current clamps, see section 4.3.2, this term should be considered. At high pressures v_r and B_θ are lower and although E_z does not exceed

10^5 Vm^{-1} it always dominates over the $v_r B_\theta$ term. (The Hall term $j_r B_\theta$ is typically some three orders of magnitude smaller than $v_r B_\theta$).

Hence with these terms neglected equation 4.12 becomes

$$\eta = -\frac{L_i}{j_{pz}} \cdot \frac{dI_{NET}}{dt} \qquad 4.14$$

For a uniform current distribution j_{pz} is given by

$$j_{pz} = (I_{NET} - I_B)/\pi a^2 \qquad 4.15$$

so that the resistivity is

$$\eta = L\pi a^2 \frac{dI_{NET}}{dt} (I_B - I_{NET})^{-1} \qquad 4.16$$

The dissipation rate of the return current is given by

$$\eta j_{pz}^2 = \frac{L}{\pi a^2} (I_B - I_{NET}) \frac{dI_{NET}}{dt} \qquad 4.17$$

and the total energy dissipated, W_{OHM}, is

$$W_{OHM} = \int_0^t \eta j_{pz}^2 \cdot dt' \qquad 4.18$$

All the parameters of equations 4.16 to 4.18 are known, I_{NET}, I_B are measured, dI_{NET}/dt may be reduced numerically from the I_{NET} waveform and consequently η, ηj_{pz}^2 and W_{OHM} may be calculated as functions of time.

In order to obtain $(I_B - I_{NET})$ accurately as a function of time the relative timing of the two signals has to be accurately determined. Initially fiducial markers were used on the traces and the time bases were calibrated with a crystal controlled oscillator. It was found generally however, that providing the noise level was low the beginning of the traces could be accurately determined and no difference in the time at which the signals began could be resolved.

To digitize the waveforms the traces, on Polaroid film, were first copied onto 35 mm film and then enlarged onto graph paper. The waveform was then read at 5 or 10 ns intervals for the first 100 ns or so. After 100 ns the value for dI_{NET}/dt would be lost in the noise level as the current decays slowly at late times. Consequently contributions after 100 ns were either neglected or averaged over longer periods if the contribution was significant.

4.5.2 Results

For the various conditions of anode foil material and beam current rise time Figs. 4.17 and 4.18 show the time history of $n_{\parallel}$ and $n_{\parallel} j_{pz}^2$ whilst Fig. 4.19 plots values of W_{OHM} against fill pressure. It can be seen that the highest values of W_{OHM} are obtained when the following conditions are met:

1. Low fill pressure (0.1 to 0.2 torr)
2. 12.5 μm Al/My anode foil
3. Fast rising beam current pulse, see Fig. 4.12

Under these conditions values for W_{OHM} up to 3.10^{18} eV cm^{-3} have been obtained and the corresponding peak in $n_{\parallel} j_{pz}^2$ is typically 10^{26} eV cm^{-3} s^{-1}, an order of magnitude higher than under other conditions. In addition the peak occurs late at ~ 50 ns rather than ~ 13 ns under other conditions. Even as the pressure of the target gas is raised to ~ 1 torr, the use of an Al/My anode foil with a fast rising beam current tends to increase the return current deposition. At high pressures $n_{\parallel} j_{pz}^2$ becomes far less peaked temporally, energy is deposited fairly uniformly throughout the pulse and the resistivity does not fall below 10^{-4} Ωm, as shown in Figs. 4.16 and 4.17.

Results obtained with Al anode foils show some evidence of higher deposition with fast rising beam but not nearly as dramatic as with Al/My

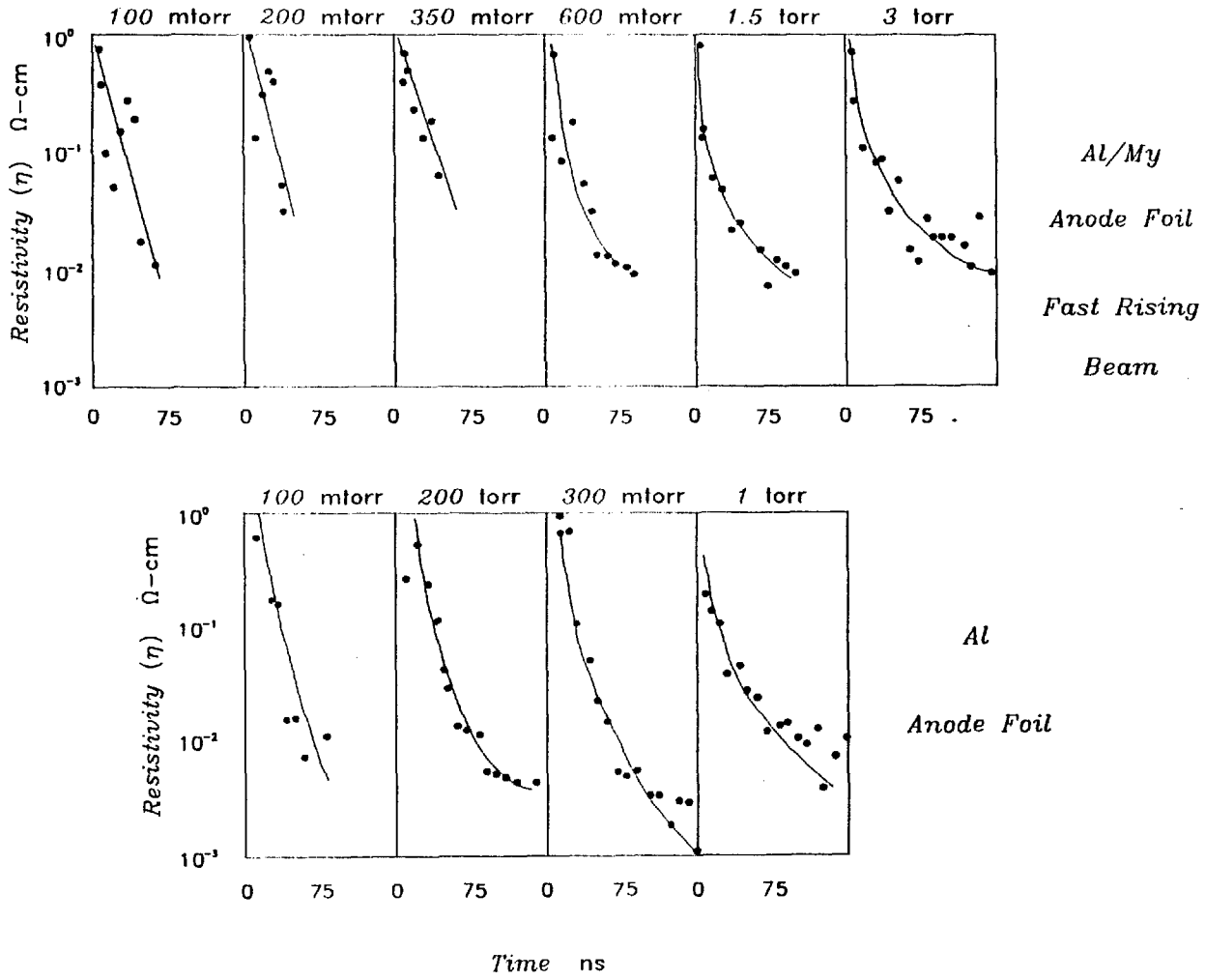

Fig. 4.17 Plots of plasma resistivity versus time for a range of pressures and both Al/My and Al type anode foils. All shots had fast rising beams.

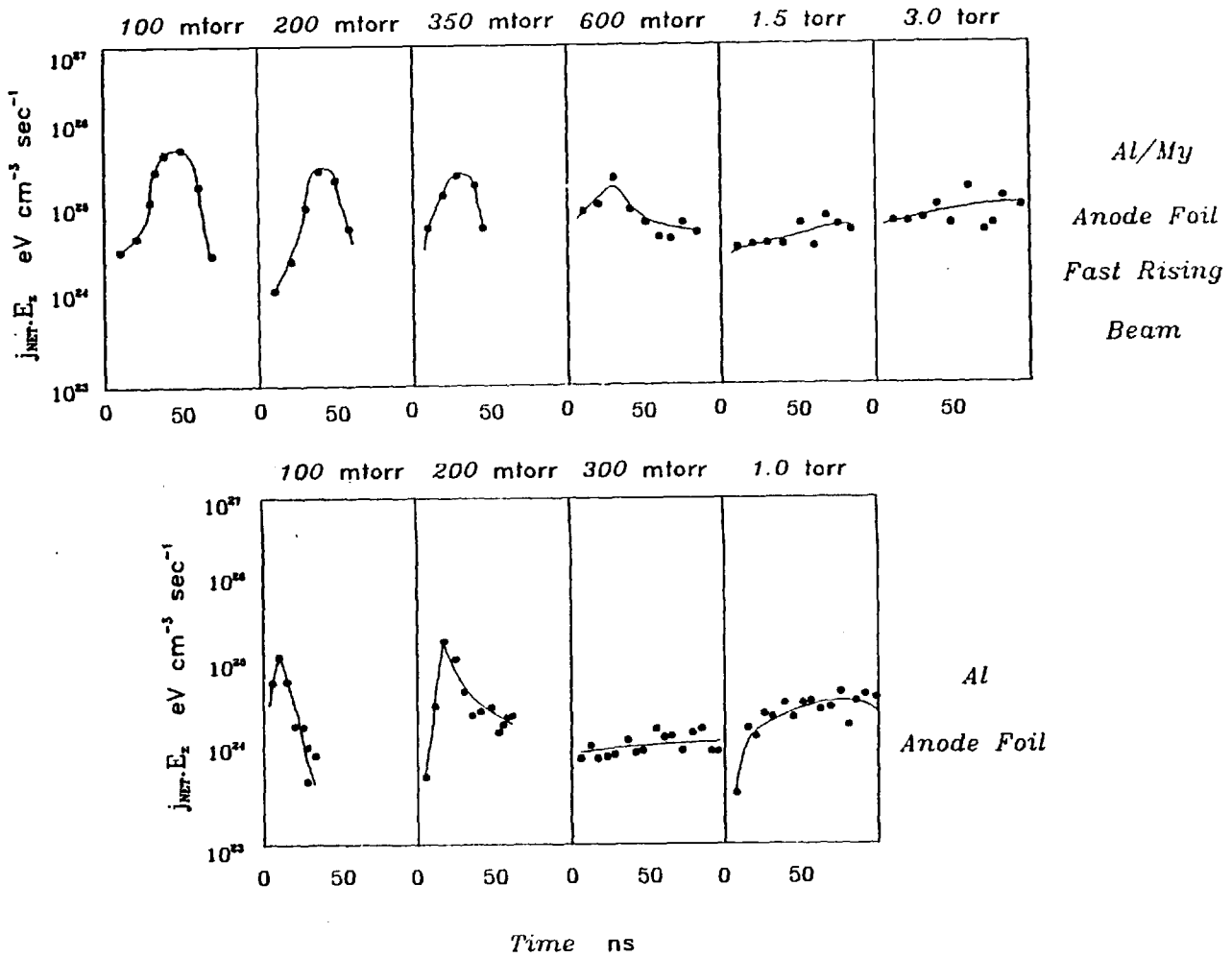

Fig. 4.18 Plots of $\eta_{\parallel} j_{pz}^2$ versus time for a range of fill pressures and for both Al/My and Al type anode foils. All shots had fast rising beams.

$$\eta_{\parallel} j_{pz}^2 = j_{NET} \cdot E_z$$

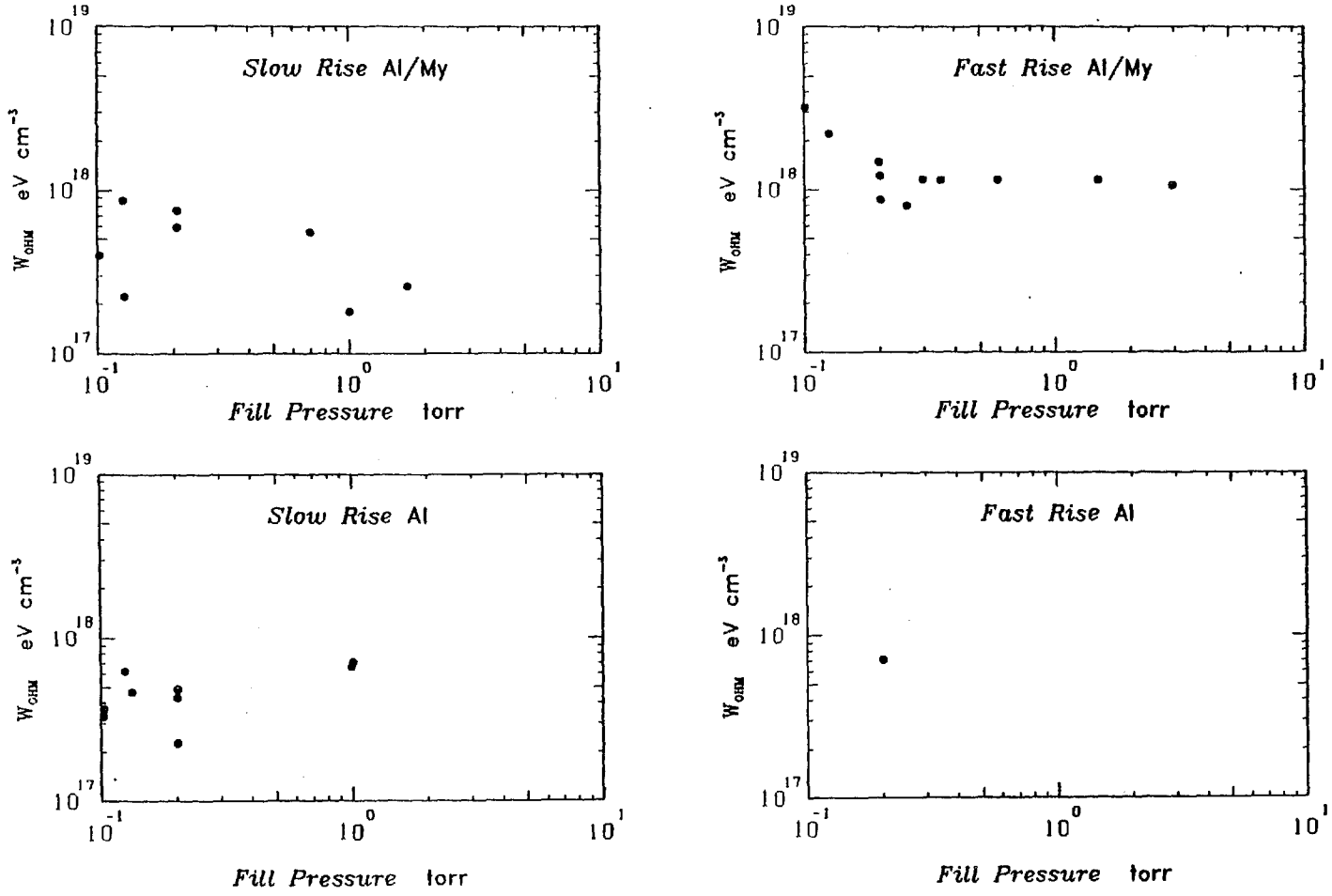

Fig. 4.19 Plots of W_{OHM} versus fill pressure for both Al/My and Al type anode foils and for both fast and slow rising beam currents.

foils. In addition W_{OHM} does not increase as the fill pressure is reduced.

4.6 Plasma Diamagnetism Results

4.6.1 Introduction

Hot magnetised plasmas in equilibrium with an applied magnetic field are diamagnetic. By measuring the difference between the magnetic field within and without of the plasma, i.e. the degree of diamagnetism, the perpendicular kinetic pressure of the plasma may be estimated. The diamagnetic current is the result of incomplete cancellation of the diamagnetism of individual electrons in the region of a pressure gradient. The interaction of this current with the magnetic field produces a force balancing the pressure gradient. This is represented by the magnetostatic equation

$$\nabla p = \underline{j} \wedge \underline{B} \qquad 4.19$$

Applying Ampere's law this reduces to

$$\mu_o \nabla p = (\nabla \wedge \underline{B}) \wedge \underline{B}$$

$$= - \tfrac{1}{2}\nabla(\underline{B}.\underline{B}) - (\underline{B}.\nabla)\underline{B} \qquad 4.20$$

The second term describes variation in $\underline{B}$ in the direction of $\underline{B}$, i.e. field curvature and is small compared to the former term. Taking the radial component gives

$$\frac{\partial p}{\partial r} = - \frac{1}{2\mu_o} \frac{\partial}{\partial r} B^2 \qquad 4.21$$

which on integration becomes

$$p + \frac{B^2}{2\mu_o} = \text{constant (in space)} \qquad 4.22$$

Consider now the injection of an electron beam into neutral gas contained in a conducting vessel and permeated with a B_z field. As has been described a plasma forms, is heated and expands radially under ∇p forces. Two simplifying assumptions will now be considered; firstly, that the resistivity is sufficiently low that the magnetic field is effectively "frozen" into the plasma and moves with it, and secondly, that the Alfvén wave transit time across the plasma is short compared with the heating time. These mean that the plasma and magnetic field are in dynamic equilibrium and that the magnetostatic equation can be applied.

Some idea of the applicability of these assumptions may be obtained using the results of sections 4.3 and 4.7. Plasma resistivity will cause the diamagnetic j_θ current to decay, enabling the B_z field to diffuse back into the plasma. In the limit of high resistivity the plasma may move across the magnetic field, uncontained, and producing no diamagnetism. The magnitude of this effect can be estimated from the diffusive timescale of B_z through the plasma. From Faraday's law

$$\nabla \wedge \underline{E} = - \frac{\partial \underline{B}}{\partial t} \qquad 4.23$$

Applying Ohm's law and neglecting the $\underline{v} \wedge \underline{B}$ and $\underline{j} \wedge \underline{B}$ terms, i.e. $\underline{E} = \eta \underline{j}$

$$\nabla \wedge (\eta \underline{j}) = - \partial \underline{B} / \partial t \qquad 4.24$$

from Ampere's law with the displacement current neglected

$$\underline{j} = \frac{1}{\mu_o} (\nabla \wedge \underline{B}) \qquad 4.25$$

hence

$$\frac{1}{\mu_o} \nabla \wedge (\eta [\nabla \wedge \underline{B}]) = - \partial \underline{B} / \partial t \qquad 4.26$$

Taking the z-component and assuming azimuthal symmetry with $\partial / \partial \theta \equiv 0$

$$-\frac{\partial B_z}{\partial t} = \frac{1}{\mu_o r}\frac{\partial}{\partial r} r\,(\eta\,\nabla \wedge \underline{B})_\theta \qquad 4.27$$

using $\eta_\perp$ equal to the value of η perpendicular to $\underline{B}$,

$$\frac{\partial r B_z}{\partial t} = \frac{\partial}{\partial r}\left(\frac{r\,\eta_\perp}{\mu_o}\frac{\partial B_z}{\partial r}\right) \qquad 4.28$$

This is a diffusion equation for B_z with a timescale $\tau_d \sim \mu_o a^2/\eta_\perp$ where a is the plasma radius equal to 10^{-2} m. With $\eta_\perp = 2\,\eta_{||}$ and $\eta_{||}$ being given by the decay of the axial plasma current as shown in Fig. 4.17, then at 20 ns $\eta_\perp$ is typically 4.10^{-3} Ωm giving $\tau_d \sim 30$ ns. As the resistivity drops continually throughout the beam pulse, τ_d increases and consequently diffusion is only significant early in the interaction leading to less plasma diamagnetism and an under estimate of the plasma pressure.

The validity of the second assumption that the Alfvén transit time across the plasma be short compared to the heating time, may also be estimated. The Alfvén velocity is

$$v_A = B/(\mu_o\, n_i\, m_i)^{\frac{1}{2}} \qquad 4.29$$

For a plasma radius of 10^{-2} m this gives a transit time $\tau_A = 2.8\ 10^{-19}\ n_i^{\frac{1}{2}}$ (MKS). As charge exchange collisions between the ions and neutrals mean that the ions are momentum coupled to the neutrals, the Alfvén velocity will be decreased from the value given by equation 4.29. This is discussed in Appendix II, and indicates that τ_A is generally significantly longer than the heating time except in the early stages whilst n_i is low and $n_i << n_n$, when the times are comparable. However, even if this second assumption is not met fully, the effect can at most increase the apparent signal by a factor of 2 if the plasma motion remains small. This is because with fast heating, compared to τ_A, the equilibrium position of the plasma is shifted but not the plasma itself

which will then start to oscillate about the new equilibrium. The zero to peak amplitude will then be equal to the shift in the equilibrium. This means that the maximum excursion of the plasma from the initial position will equal twice the shift in the equilibrium.

4.6.2 Reduction of signals to give energy densities

The plasma diamagnetism was measured with the diamagnetic loop described in Chapter three. A relationship is required linking the observed output voltage from the loop after integration, with the amount of plasma expansion and hence with the total perpendicular plasma pressure. The 'freezing in' of the magnetic field in the plasma means that flux is conserved within the plasma. The stainless steel interaction chamber has a resistivity sufficiently low to prevent the field diffusing through it on the timescale of the plasma lifetime and consequently the flux within the chamber is also conserved. The expanding plasma will push the magnetic field with it causing the total field within the diamagnetic loop to fall, as shown in Fig. 4.20. The voltage induced around the loop is calculated from Faraday's law,

$$\nabla \wedge \underline{E} = - \frac{d\underline{B}}{dt} \qquad 4.30$$

$$\therefore \quad \oint \underline{E}.d\underline{l} = - \frac{d}{dt} \int \underline{B}.d\underline{s}$$

$$V_{loop} = - \frac{d}{dt} \phi_c \qquad 4.31$$

where ϕ_c is the total B_z flux within a radius c. This voltage is integrated with an RC integrator to give

$$V_{out} = - \frac{1}{RC} \int_0^t \frac{d\,\phi_c(t')}{dt'} \cdot dt' = \frac{\Delta\phi_c(t)}{RC} \qquad 4.32$$

where $\Delta\phi_c(t)$ is the total change of flux within the loop. $\Delta\phi_c$ is calculated from the magnetostatic equation

$$p + \frac{B^2}{2\mu_o} = \text{constant (in space)} \qquad 4.33$$

Initially the plasma has a radius a. It is then heated and expands to a new radius a_1. Flux conservation within the plasma yields

$$\pi a^2 B_o = \pi a_1^2 B_{IN} \qquad 4.34$$

where B_{IN} is the new field inside the plasma and B_o the initial uniform field. Conservation of flux within the vacuum vessel gives

$$\pi b^2 B_o = \pi a_1^2 B_{IN} + \pi(b^2 - a_1^2) B_{OUT} \qquad 4.35$$

where B_{OUT} is the new field outside the plasma.

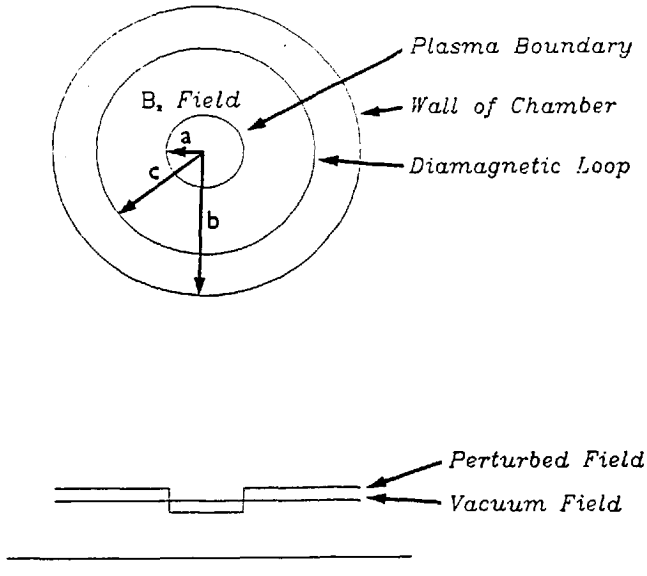

Fig. 4.20 Diagram showing field and coil configuration for calculating the plasma diamagnetism.

Hence

$$\pi\, b^2\, B_o = \pi\, a^2\, B_o + \pi(b^2 - a_1^2)\, B_{OUT} \qquad 4.36$$

$$\therefore \quad B_{OUT} = \left(\frac{b^2 - a^2}{b^2 - a_1^2}\right) B_o \quad \text{and} \quad B_{IN} = \frac{a^2}{a_1^2}\, B_o \qquad 4.37$$

From the magnetostatic equation 4.33

$$NkT_\perp + \frac{1}{2\mu_o}\, B_{IN}^2 = \frac{1}{2\mu_o}\, B_{OUT}^2 \qquad 4.38$$

Hence

$$2\mu_o \frac{NkT_\perp}{B_o^2} = \left(\frac{b^2 - a^2}{b^2 - a_1^2}\right)^2 - \frac{a^4}{a_1^4} \qquad 4.39$$

The change of flux inside the loop $\Delta\phi_c$ is given by

$$\Delta\phi_c = \pi\, a_1^2\, B_{IN} + \pi(c^2 - a_1^2)\, B_{OUT} - \pi\, c^2\, B_o \qquad 4.40$$

letting

$$\alpha = \Delta\phi_c / \pi\, B_o \qquad 4.41$$

gives

$$a_1^2 = \frac{a^2(b^2 - c^2) - b^2\,\alpha}{b^2 - c^2 - \alpha} \qquad 4.42$$

Substitution into equation 4.39 gives

$$2\mu_o \frac{NkT_\perp}{B_o^2} = \left[\frac{(b^2 - a^2)(b^2 - c^2 - \alpha)}{b^2(b^2 - c^2 - a^2) + c^2 a^2}\right] - a^4 \cdot \left[\frac{b^2 - c^2 - \alpha}{a^2 b^2 - c^2 a^2 - b^2\alpha}\right]^2 \qquad 4.43$$

As

$$V_{OUT} = \Delta\phi / RC$$

from equation 4.38

$$\alpha = - \frac{V_{OUT} \cdot RC}{\pi B_o} \qquad 4.44$$

Equations 4.43 and 4.44 give the required relationship. If $T_\perp$ is interpreted as the perpendicular component of an isotropic temperature distribution, we have,

$$^3/_2 \, Nk(T_e + T_i) = {}^3/_2 \, NkT_\perp = W_{DL} \qquad 4.45$$

In Fig. 4.21 $^3/_2 \, NkT_\perp$ (in $eVcm^{-3}$) is plotted against V_{OUT} for the following values:

$a = 10^{-2}$ m

$b = 3.8 \cdot 10^{-2}$ m

$c = 2.8 \cdot 10^{-2}$ m

$RC = 2.10^{-6}$ s

$\mu_o = 4\pi \cdot 10^{-7}$ H m^{-1}

B_o = 1.42, 1.14, 1.86 tesla.

The values of B_o are chosen to correspond to those used experimentally. These data show that for energy densities $\sim 2.5 \cdot 10^{18}$ eV cm^{-3} an expansion of ~ 5% by radius occurs.

4.6.3 Results

Four parameters were varied for the diamagnetic measurements, B_z (1.1 to 1.9 tesla), fill pressure (0.1 to 3 torr), anode foil type (25 and 12.5 μm Al. and 12.5 μm Al/My) and axial position (2 and 11 cm from the anode). Some typical traces obtained are shown in Fig. 4.22, and in Fig. 4.23 the peak value of $^3/_2 \, NkT_\perp$ is plotted against fill pressure for the four combinations of foil type and loop positions. No dependence of $^3/_2 \, NkT_\perp$ upon B_z was observed in the limited range over

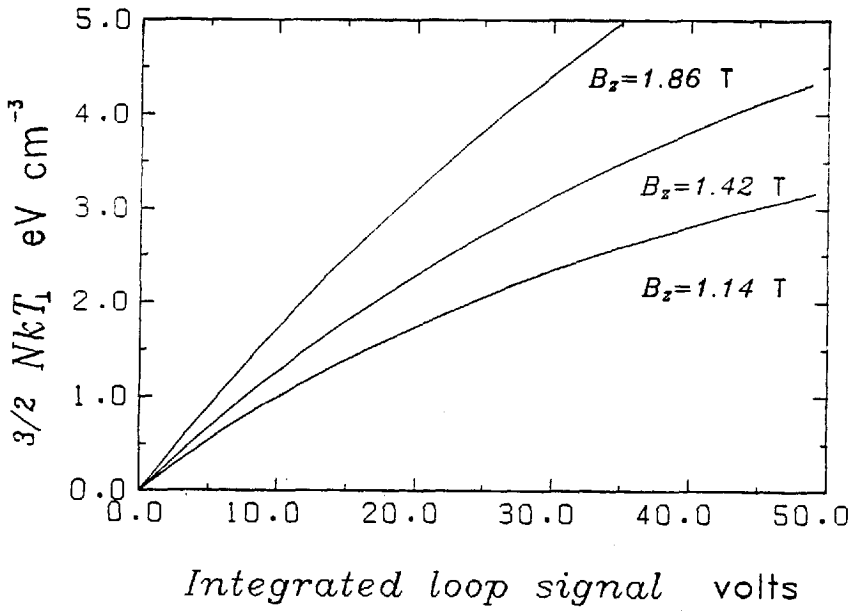

Fig. 4.21 Plots of 3/2 $NkT_\perp$ versus diamagnetic loop voltage for various magnetic fields.

which B_z has been varied. In all cases no difference in the observed signal was discernable for 25 and 12.5 μm Al. anode foils. Also at position (2) (11 cm from the anode) no difference with Al/My anode foils was found. However, at position (1) (2 cm from the foil) the Al/My anode gave significantly larger results as shown in Fig. 4.22. This applied over the whole range of pressures. If one assumes that $T_i \sim T_e$ and that both these temperatures are isotropic then the diamagnetic loop results indicate temperatures of the order of 500 eV for densities of about $5.6 \cdot 10^{15}$ cm^{-3} (about the maximum density observed in the laser scattering experiments, see section 4.7).

The other difference observed at position (1) with an Al/My anode was that the oscillation period was about twice as long as under any other condition and also the periods were independent of the filling pressure.

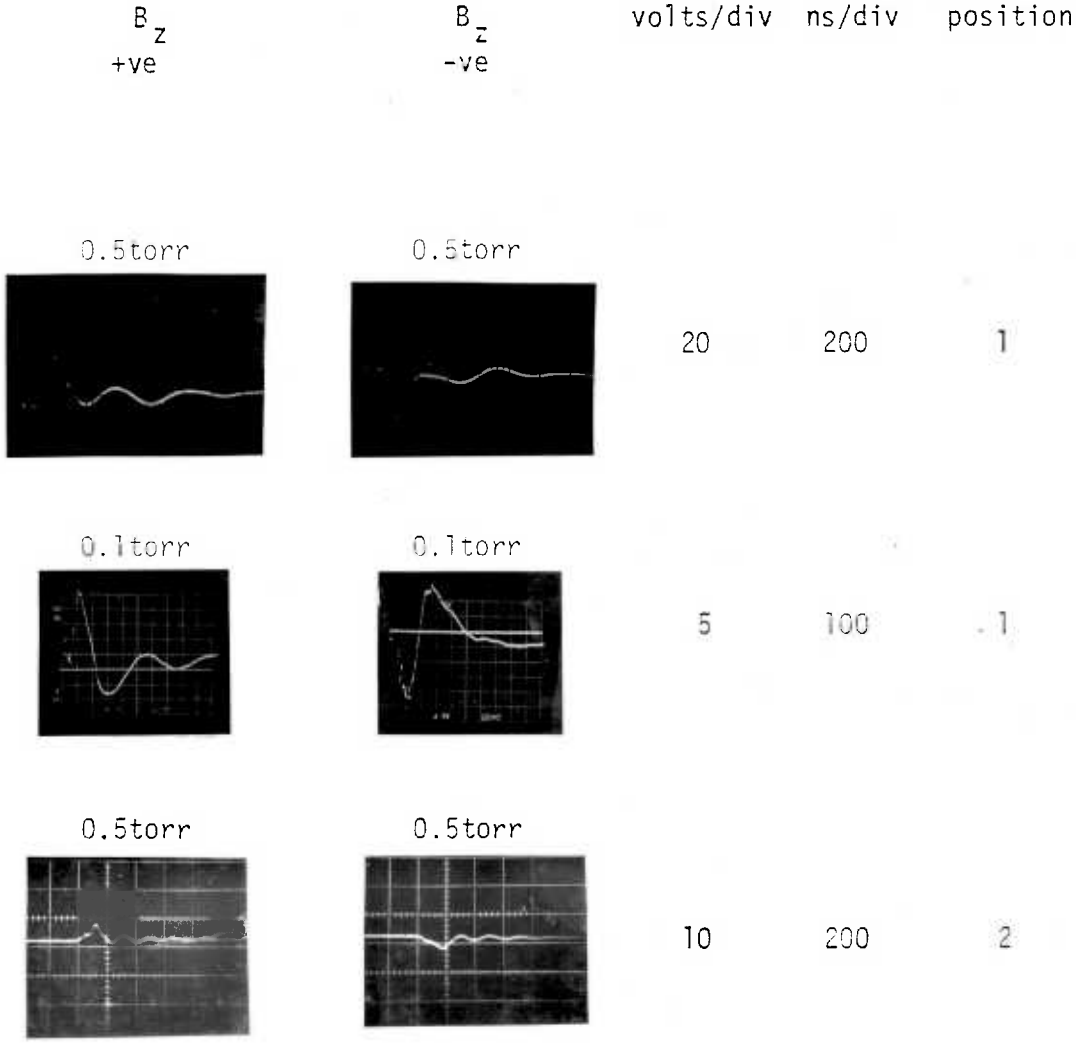

Fig. 4.22 Examples of diamagnetic loop waveforms. Good signal inversion under all conditions is observed for reversal of the applied field.

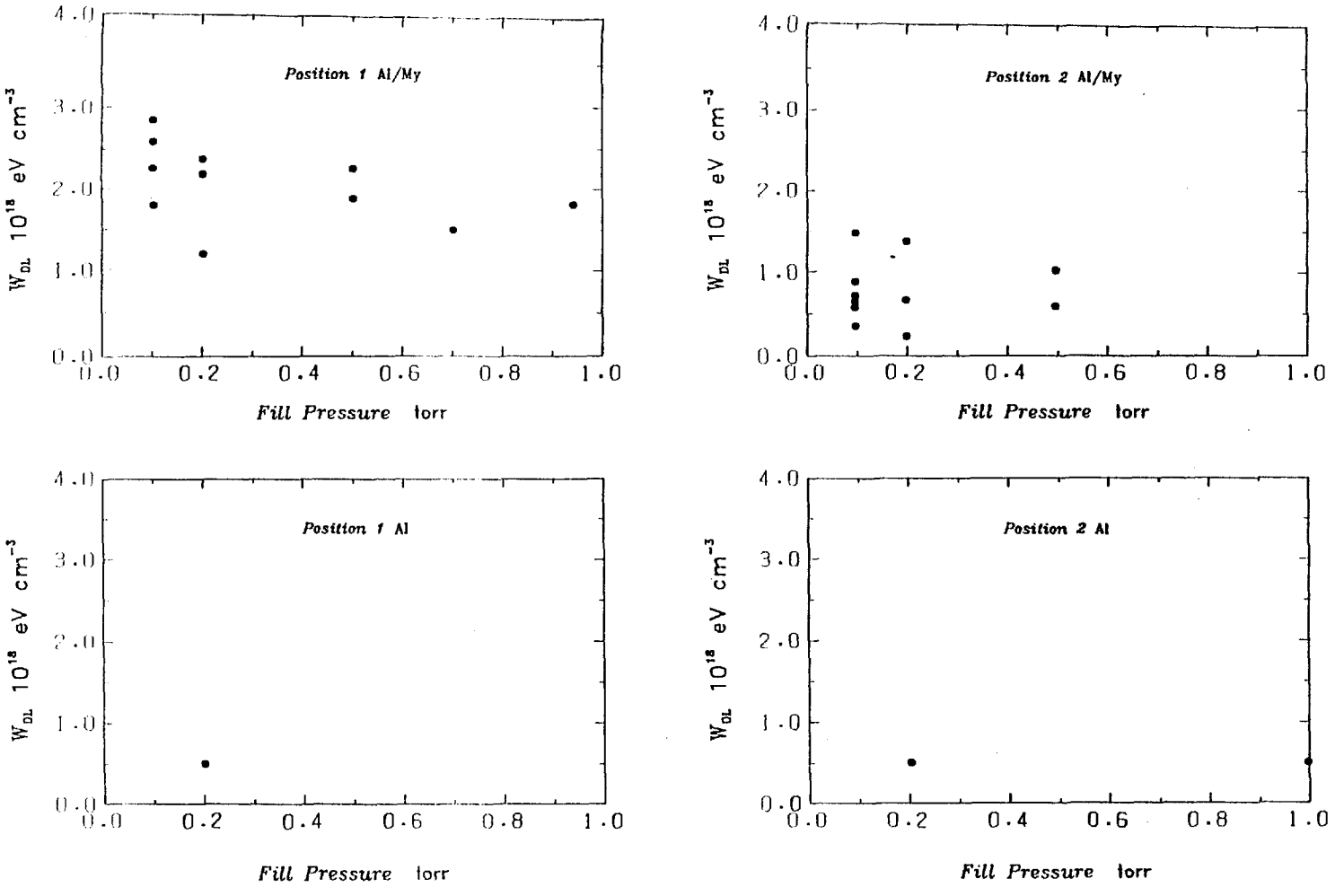

Fig. 4.23 Plots of W_{DL} versus fill pressure for both Al/My and Al type anode foils at positions (1) and (2).

The periods were ~ 500 and 250 ns respectively. This result contrasts sharply with the expected $n_i^{\frac{1}{2}} B^{-1}$ dependence of the oscillation period as observed by others, PRONO (1975).

4.7 Laser Scattering Results

Whilst the laser scattering measurements were intended to give information on n_e and T_e throughout the duration of the plasma, the combination of high plasma light and low scattered light levels meant that only values at times later than ~ 80 ns could be obtained. Low scattered light levels may have been due to either a large T_e or low n_e. The large plasma light level is as yet unexplained but has been observed by HAMMER (1977) and is thought to result from molecular hydrogen bands of emission. Some typical traces are shown in Fig. 4.24. Scattered spectra obtained at times after 80 ns indicate T_e ~ 10 eV and n_e ~ 3.10^{15} cm^{-3} with no definite temporal dependence. Some examples are shown in Fig. 4.25. As the scattering parameter α is low the plots are in the form of Log_{10} (n_e/13 Å) against $(\Delta\lambda Å)^2$ so that a Maxwellian velocity distribution will appear as a straight line. In Fig. 4.26 the electron number densities and temperatures obtained are plotted against time for various conditions. The number densities have been obtained from the total scattered light using calibrations as discussed in section 3.5.1. A symmetrical spectrum has been assumed although only the blue side of the ruby wavelength has been investigated. Many of the spectra obtained at early times are non-Maxwellian and may be interpreted as two temperature distributions. The results indicate that the degree of ionization is always high varying from ~ 0.2 to nearly 1, with little variation in time. Reasonable correlation with the Stark broadening measurements presented in section 4.8 is indicated. The Stark broadening results for n_e are also plotted in Fig. 4.26.

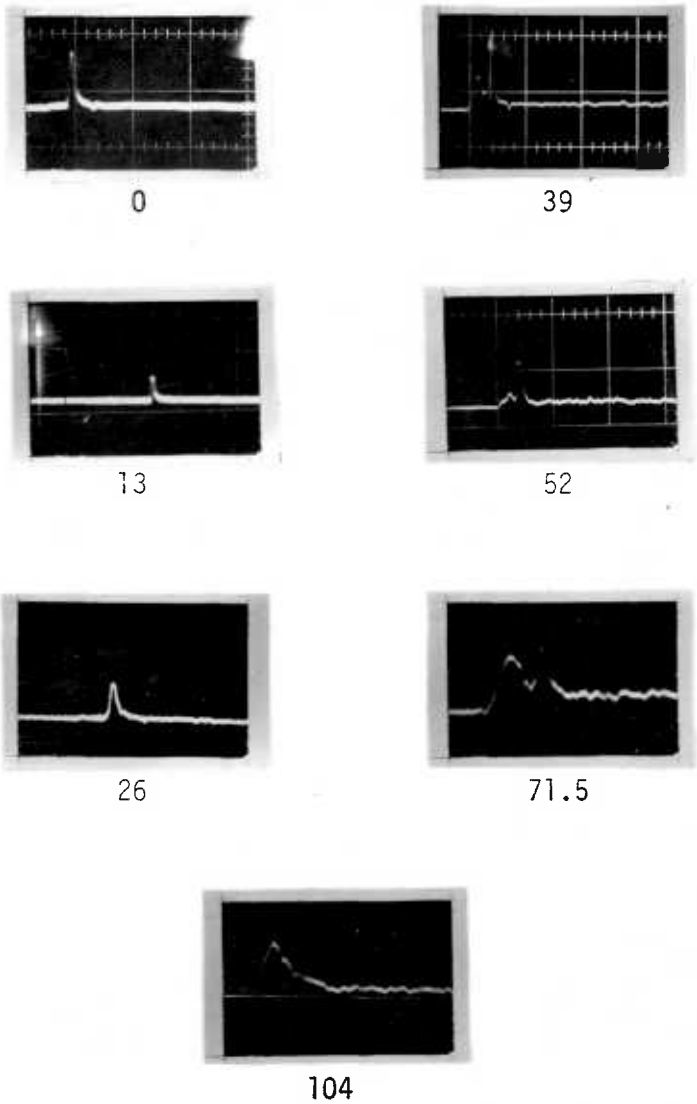

Fig. 4.24a Example of laser scattering signals at 180ns after start of the beam at 100mtorr fill pressure. Numbers below each trace indicate the blue shift in Angstroms from the central channel.

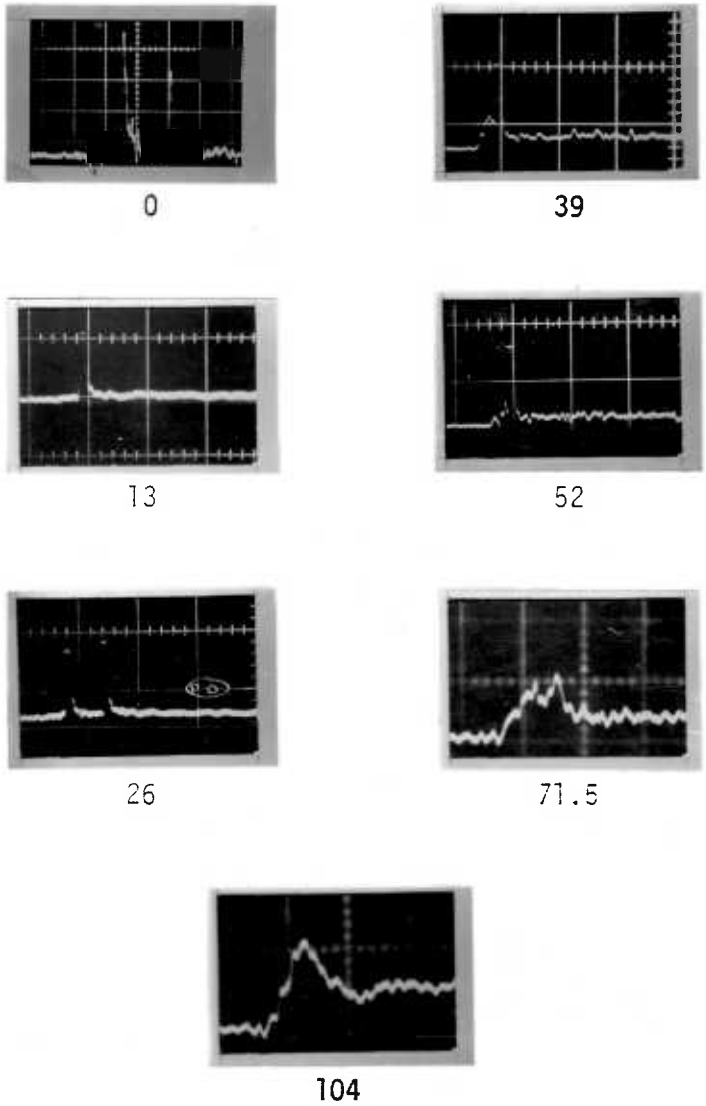

Fig.4.24b Examples of laser scattering signals at 200ns after start of the beam at 120mtorr fill pressure. Numbers below each trace indicate the blue shift in Angstroms from the central channel.

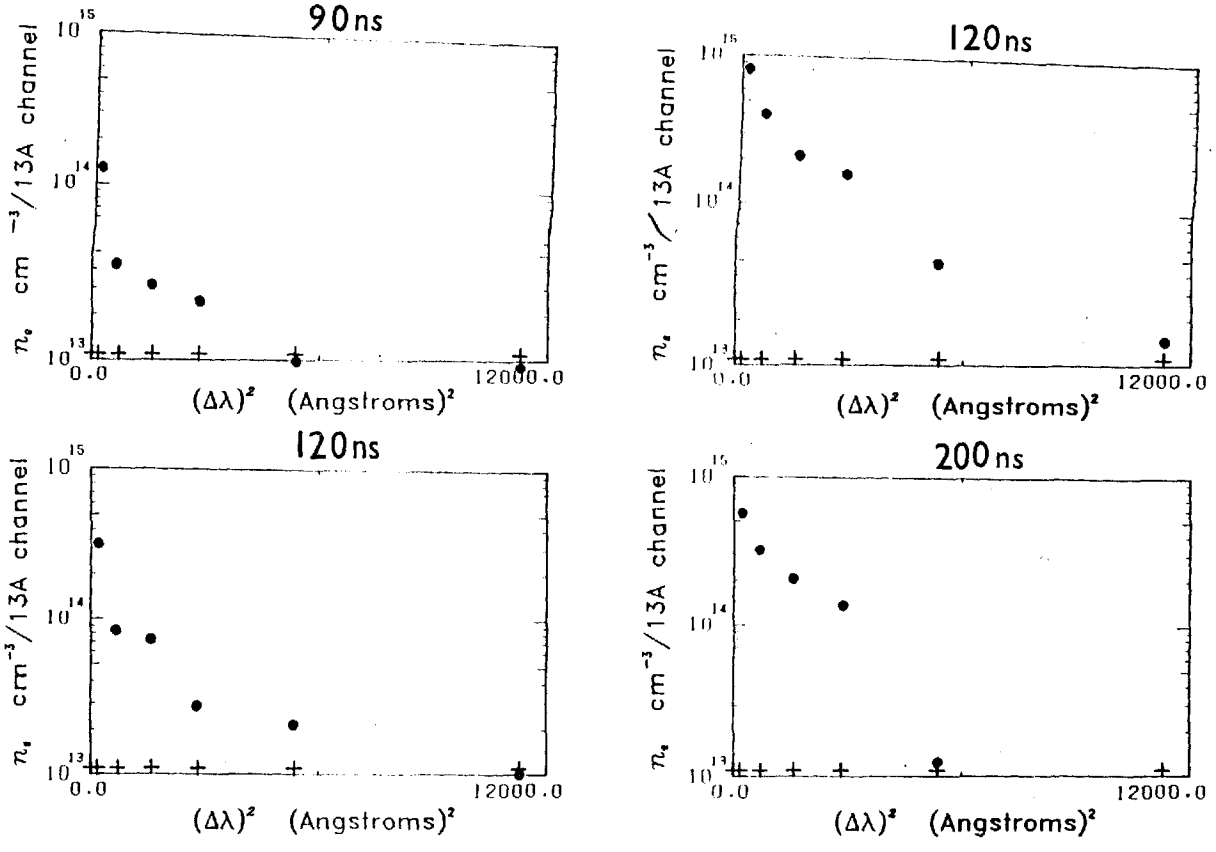

Fig. 4.25a Scattered light spectra obtained at 100 mtorr fill pressure at the times indicated. Error bars approx. 15% near central channel and approx. 50% in the wings.

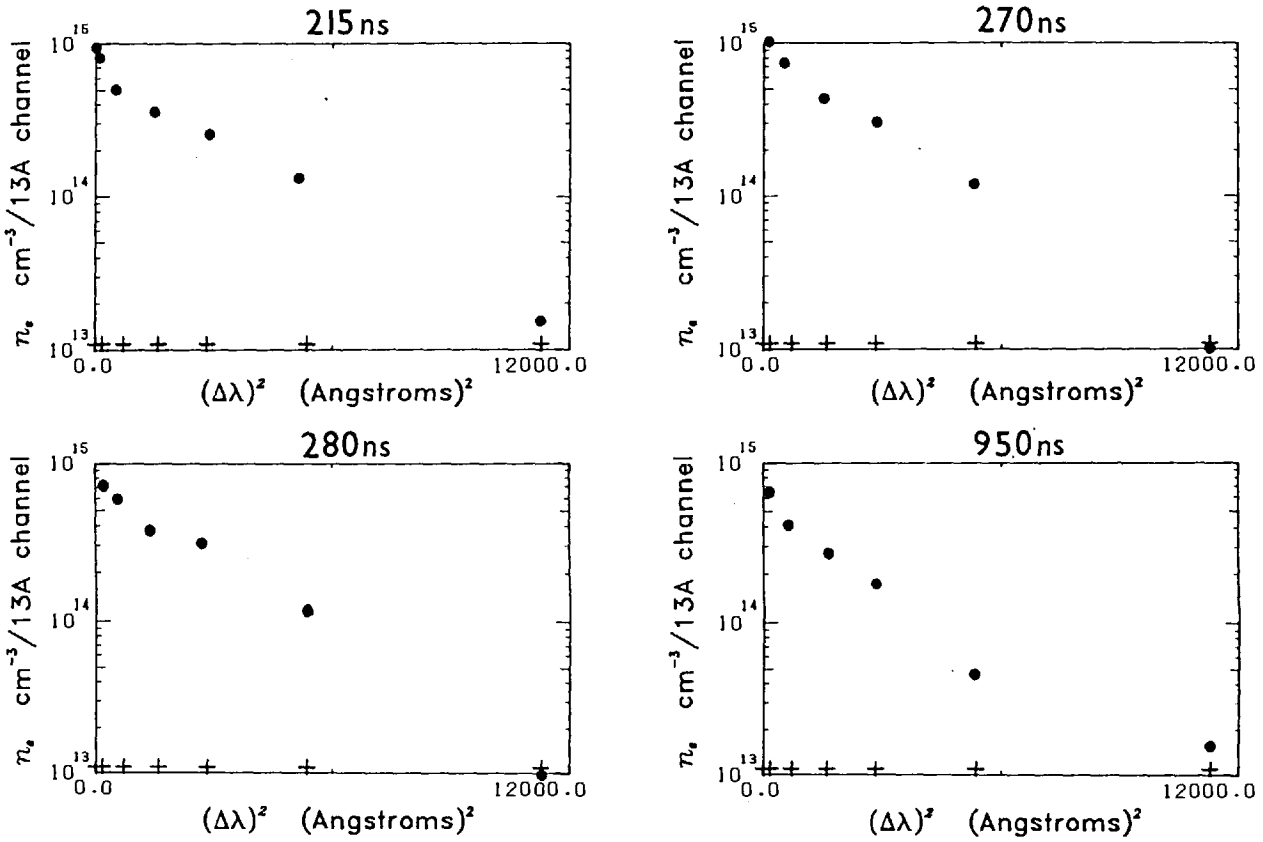

Fig. 4.25b Scattered light spectra obtained at 100 mtorr fill pressure at the times indicated. Error bars approx. 15% near central channel and approx. 50% in the wings.

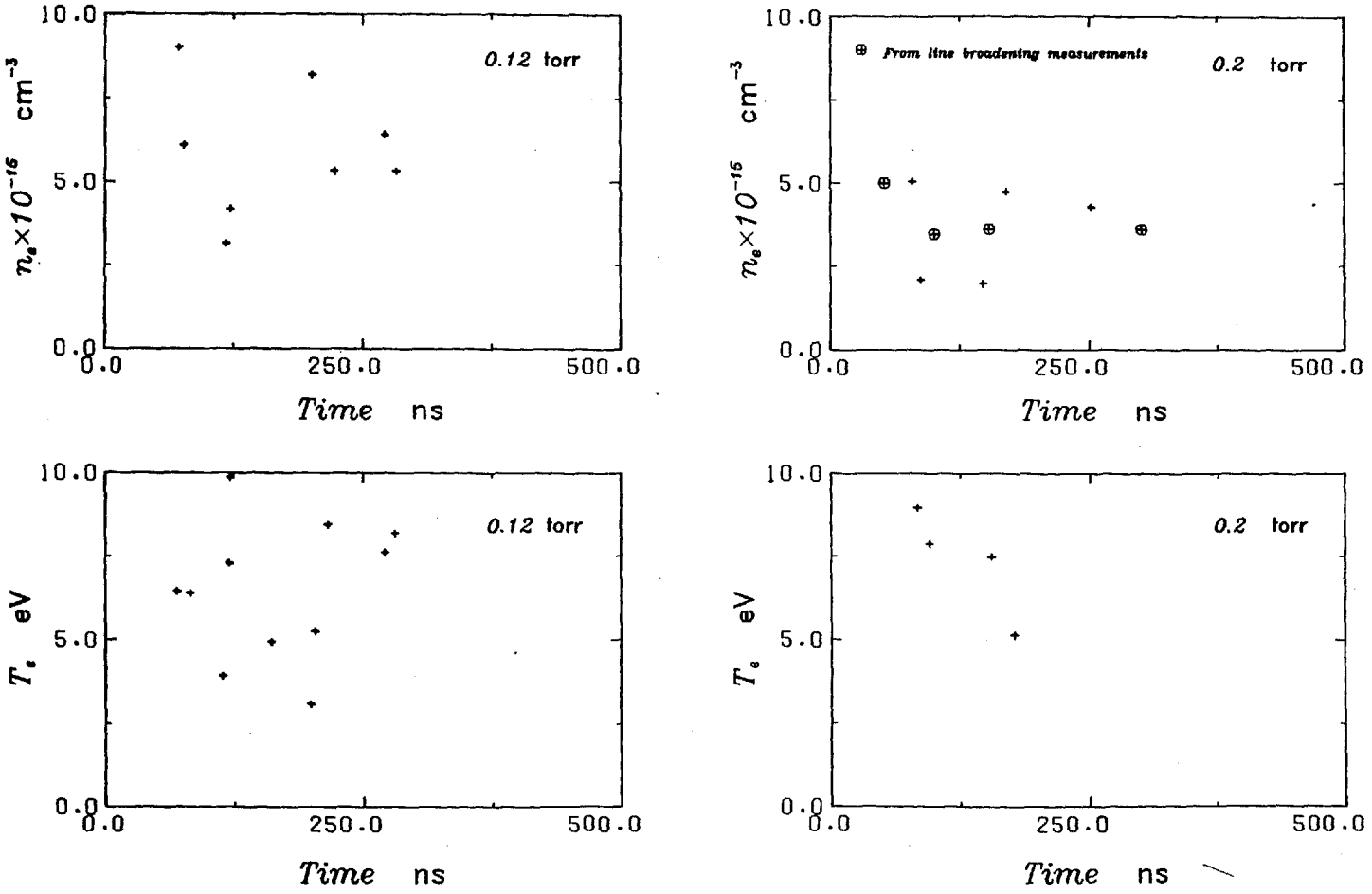

Fig. 4.26 Plots of n_e and T_e versus time obtained by laser scattering and Stark broadening (n_e only). The Stark broadening points are ringed.

The electronic energy density observed in these measurements is $\sim 3.10^{16}$ eV cm^{-3} assuming an isotropic distribution. Inclusion of the molecular dissociation and atomic ionization energies boosts this figure to $\sim 10^{17}$ eV cm^{-3}. However, this energy will not contribute to diamagnetism although it will contribute to nj_p^2 if collisions by plasma electrons is the dominant ionization process.

It is of interest to compare the observed plasma light emission near the ruby wavelength with the expected plasma bremsstrahlung emission. The intensities of the observed plasma and scattered light are about equal at 6865 Å. If it is assumed that the plasma light has no wavelength dependence then the ratio of scattered to plasma light at 6943 Å is given by the ratio of the scattered light at these two wavelengths which is ~ 5.

To calculate the expected plasma light level due to bremsstrahlung from a thermal plasma the result of EVANS and KATZENSTEIN (1969) may be used, i.e.

$$\frac{I_s}{I_p} = \frac{4.1 \cdot 10^{13} I_o \lambda_o v_s}{n_e \sin(\theta/2) v_p} \qquad 4.46$$

where I_s and I_p are the scattered and plasma light intensities from the respective source volumes v_s and v_p. I_o and λ_o are the incident laser intensity and wavelength. θ is the scattering angle. v_s and v_p differ as plasma light is observed from throughout the line of sight. A rough estimate of v_s/v_p can be obtained by comparing the radial width of the plasma column with the diameter of the focussed laser beam, giving $v_s/v_p \sim 0.1$.

For
$$\lambda_o = 6943 \text{ Å}$$
$$n_e = 4.10^{15} \text{ cm}^{-3}$$
$$I_o = 10^{10} \text{ W cm}^{-2}$$
$$v_s/v_p = 0.1$$

equation 4.46 gives I_s/I_p - 10^3 hence the observed figure of - 5 indicates plasma light emission ~ 200 times the Bremsstrahlung level.

4.8 Spectral Line Measurements

In contrast to laser scattering techniques spectral line measurements can provide information with full temporal history from a single shot, but with an associated loss of spatial resolution. Interpretation of plasma parameters from spectral lines is not straightforward especially under the highly transient conditions prevailing in beam produced plasmas.

Fig. 4.27 shows example waveforms of the line emission from H_α and H_β at 200mtorr. Shots were done with Al and Al/My anode foils. No range of pressures is available for shots with Al/My foils, all these shots being at 200 mtorr. Self absorption near the line centre of H_α is apparent from the differing time histories as a function of wavelength. In Fig. 4.28 examples of traces obtained from the absorption experiment are shown. A fast fall in the level of the transmitted light occurs on beam injection.

Fig. 4.29 shows a plot of the line centre optical depth $\tau(\lambda)$ against time, obtained from the absorption experiment. Here $\tau(\lambda)$ is defined by

$$\tau(\lambda) = \mathrm{Ln}\left[I_o(\lambda)/I_t(\lambda)\right] \qquad 4.47$$

where I_o and I_t are the incident and transmitted intensities respectively at the various wavelengths, λ. From the now known optical depths the emission profiles may be corrected to those expected from an optically thin plasma.

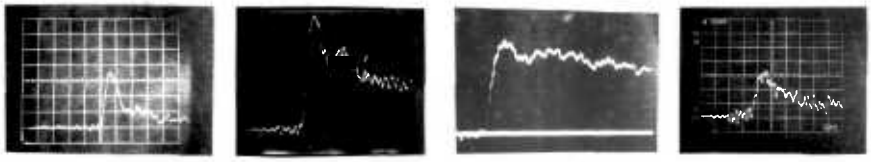

Fig. 4.27a Example waveforms of H_α emission. The numbers below each trace refer to the shift from line centre.

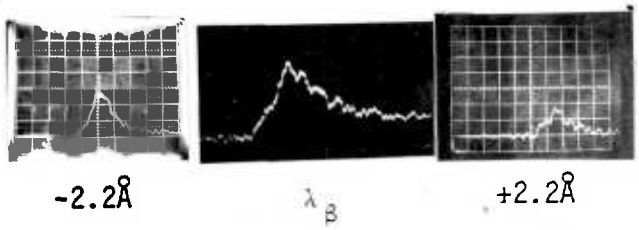

Fig. 4.27b Example waveforms of H_β emission. The numbers below each trace refer to the shift from line centre.

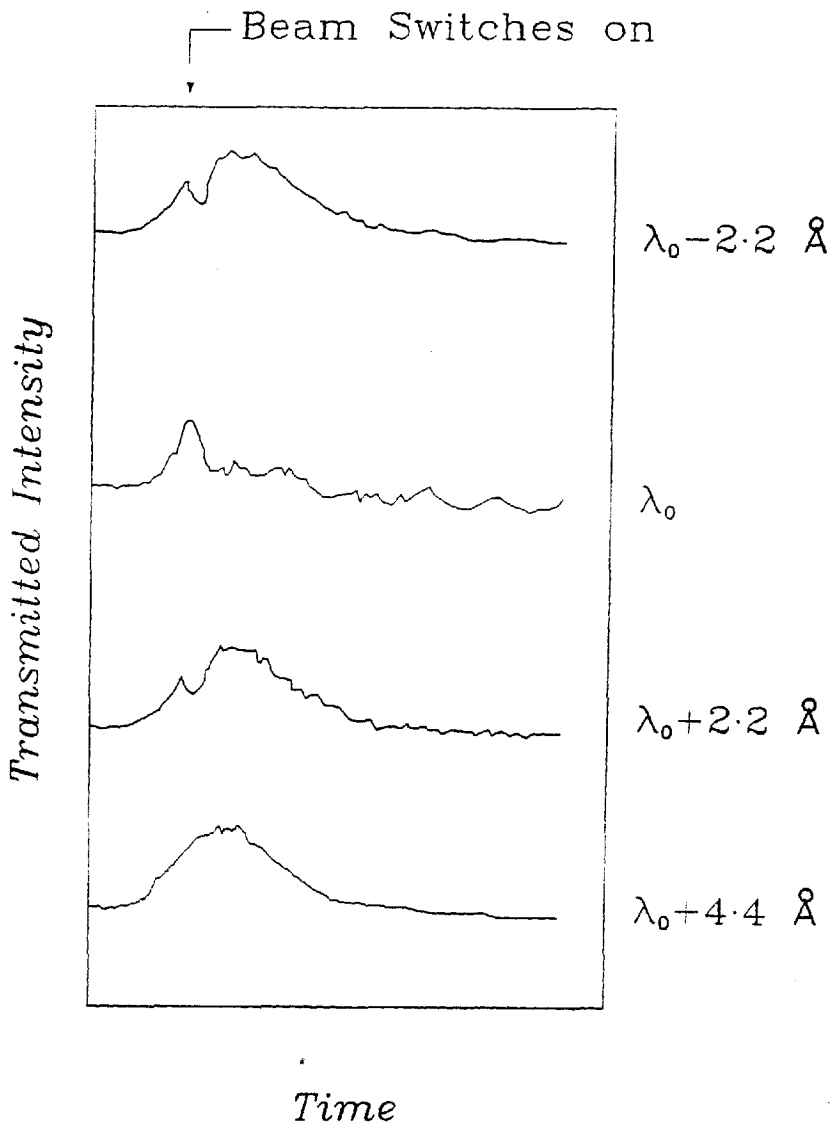

Fig. 4.28 Copies of H_α absorbtion traces on four channels.

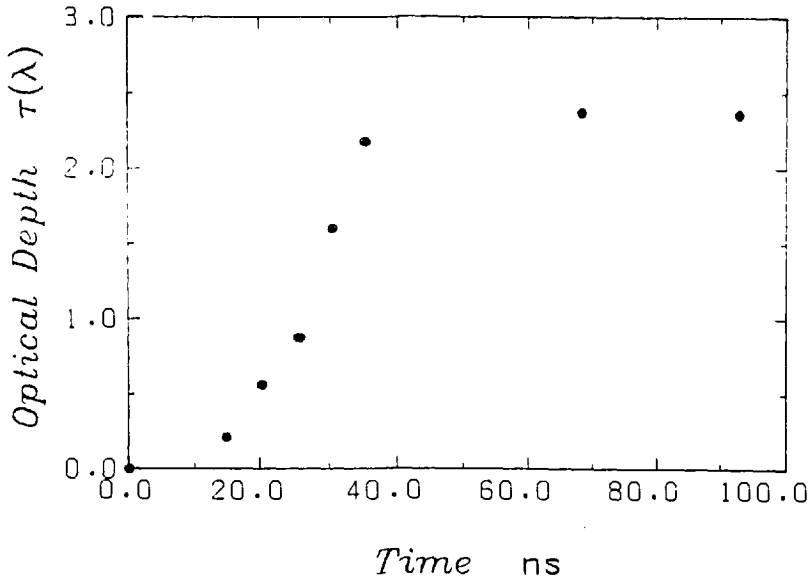

Fig. 4.29 Plot of measured optical depth at H_α line centre versus time for a 200mtorr fill pressure.

Assuming that the level populations are not disturbed by the self absorption and letting the emission and absorption per unit volume in the direction of observation be $E(\lambda)$ and $A(\lambda)$ respectively, consider a plasma of length L illuminated from behind with a plane wave source. The amount of light $dI(\lambda)$ reaching the detector due to emission in the volume element dx is, see Fig. 4.30

$$dI(\lambda) = E(\lambda) \exp\left[-xA(\lambda)\right].dx \qquad 4.48$$

Hence the total observed emission intensity is

$$I(\lambda) = \int_0^L dI(\lambda).dx = \int_0^L E(\lambda) \exp\left[-xA(\lambda)\right].dx$$

$$= \frac{E(\lambda)}{A(\lambda)} \left[1 - \exp\{-LA(\lambda)\}\right] \qquad 4.49$$

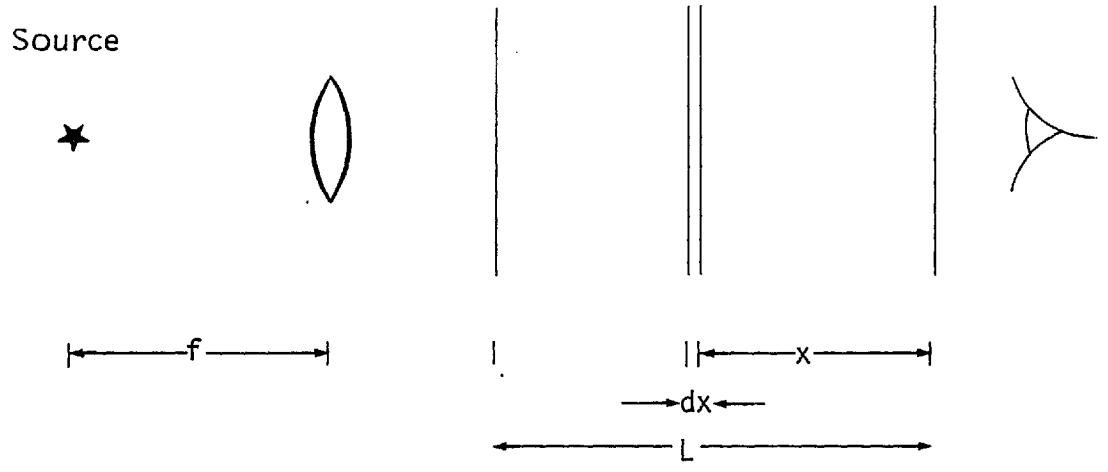

Fig. 4.30 Geometry for calculating the plasma optical depth, $\tau(\lambda)$.

Now consider the absorption of the light from the backlight source. The transmitted intensity I_T and the incident intensity I_0 are related by

$$I_T = I_0 \exp\left[-LA(\lambda)\right]$$

Hence from Eq. 4.47

$$LA(\lambda) = \tau(\lambda) \qquad 4.50$$

Substitution into 4.49 yields

$$E(\lambda) = \frac{I(\lambda)}{L}\left[\frac{\tau(\lambda)}{1 - \exp\{-\tau(\lambda)\}}\right] \qquad 4.51$$

$E(\lambda)$ can be identified with the line profile for an optically thin line whilst $I(\lambda)$ is the observed optically thick line. The quantity L,

related to the size of the plasma, does not affect the line shape when corrected in this manner. Fig. 4.31 shows H_α profiles before and after correction.

The line profiles obtained may be reduced to provide n_e and T_i as functions of time. T_i is obtained from the Doppler broadening of the H_α line which has a very low Stark broadened component. The H_β line is approximately equally broadened by Stark and Doppler effects. However the Doppler component can be found from the now known value of T_i. To deconvolve the Stark width from the observed width the following relationship is used,

$$\Delta\lambda^2_{TOT} = \Delta\lambda^2_{STARK} + \Delta\lambda^2_{DOPPLER} \qquad 4.52$$

This is only accurate if applied to convolved Maxwellians but gives reasonable results for other similar profiles. It should be noted that Stark profiles are not true Maxwellians.

The Doppler half-half widths are given by

$$\Delta\lambda_{D\frac{1}{2}\frac{1}{2}} = \left[\frac{2Ln(2)\ kT}{mc^2}\right]^{\frac{1}{2}} \lambda_o \qquad 4.53$$

where λ_o is the central wavelength, T and m are the temperature and mass of the emitter. For the H_α and H_β lines this reduces to

$$H_\alpha \qquad \Delta\lambda_{D\frac{1}{2}\frac{1}{2}} = 0.252\ T^{\frac{1}{2}}\ \text{Å} \qquad 4.54$$

$$H_\beta \qquad \Delta\lambda_{D\frac{1}{2}\frac{1}{2}} = 0.187\ T^{\frac{1}{2}}\ \text{Å} \qquad 4.55$$

The Stark profiles have half-half widths given by

$$n_e = c(n_e, T_e)\ (2\ \Delta\lambda_{S\frac{1}{2}\frac{1}{2}})^{3/2} \qquad 4.56$$

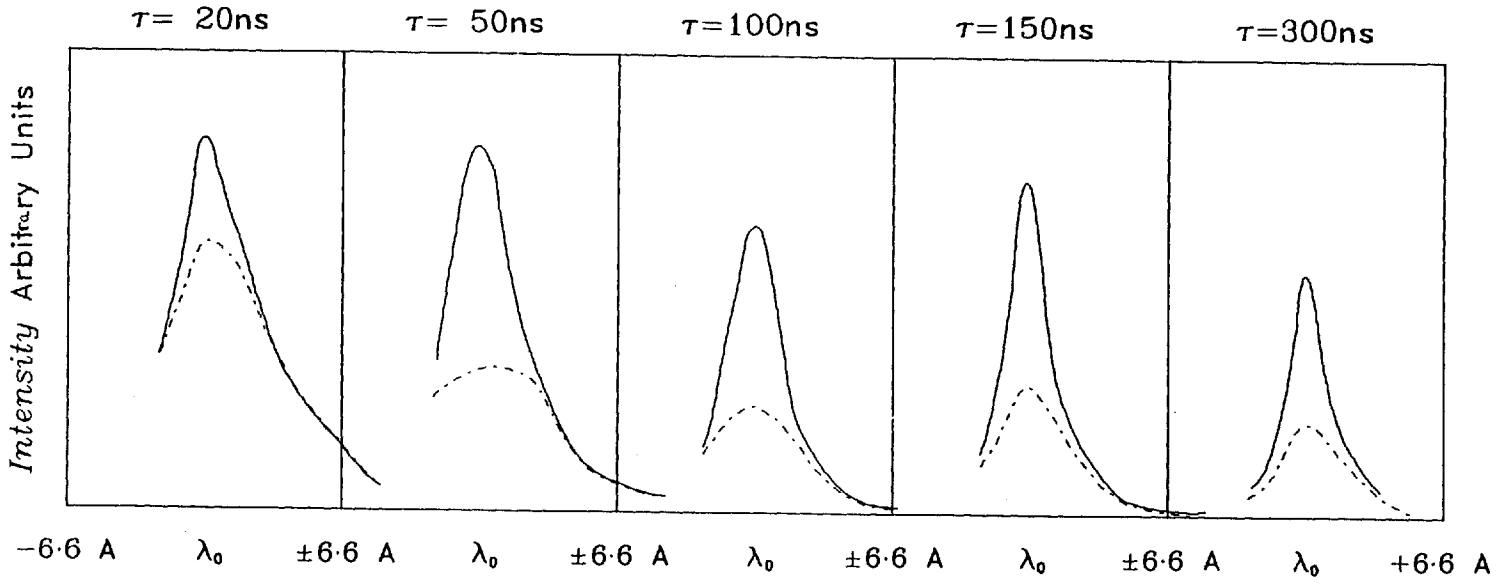

Fig. 4.31 H_α *line profiles over a range of times, with respect to the start of the beam. The broken lines are the uncorrected emission profiles, the solid lines the profiles after correction for self absorbtion.*

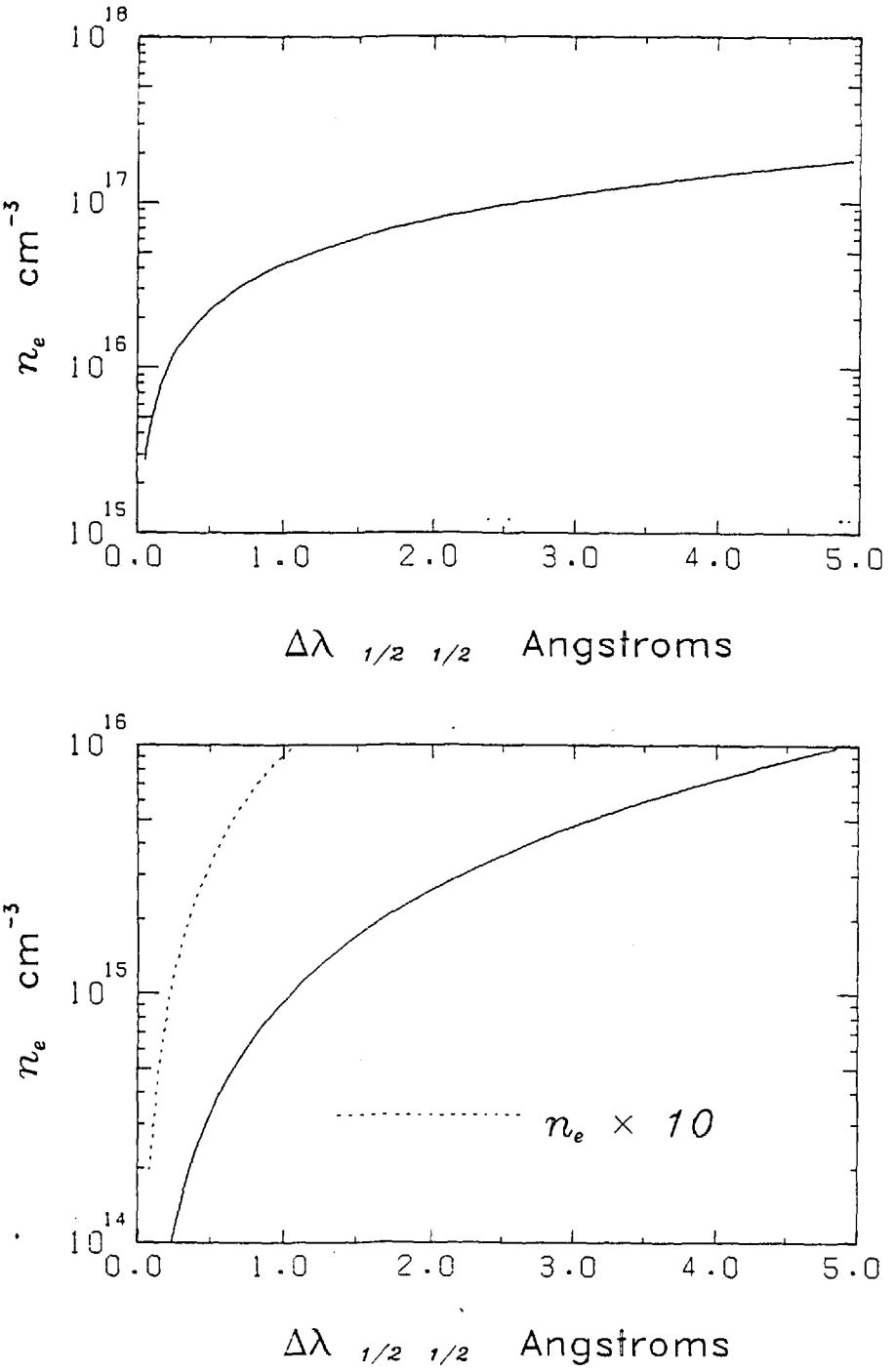

Fig. 4.32a n_e *versus* $\Delta\lambda_{\frac{1}{2}\frac{1}{2}}$ *for* H_α *(upper figure) and* H_β *(lower). Calculation taken from GRIEM(1964).*

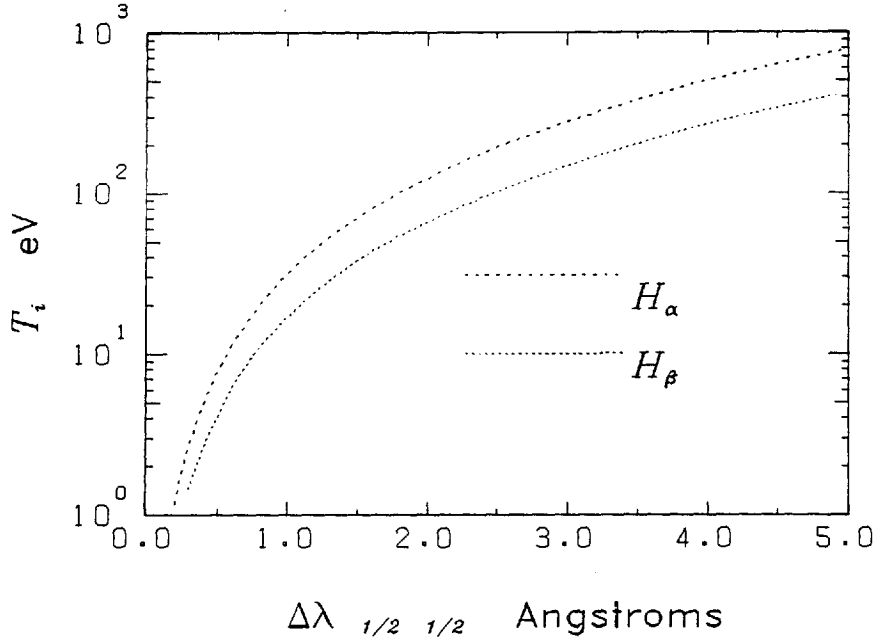

Fig. 4.32b T_i versus $\Delta\lambda_{\frac{1}{2}\frac{1}{2}}$ for the H_α and H_β lines.

The coefficients $c(n_e, T_e)$ are tabulated by GRIEM (1964). Equations 4.54 to 4.56 are plotted in Fig. 4.32. It can be seen here that the Stark width of H_α at $n_e \lesssim 10^{16}$ cm^{-3} is negligible. Using these expressions for the widths, the values of $n_e(t)$ and $T_i(t)$ have been found following the example shown in Fig. 4.33 and are plotted in Figs. 4.26 and 4.34. The values obtained for $n_e(t)$ of $\sim 3.10^{15}$ cm^{-3} are in reasonable agreement with those obtained from laser scattering and again show no definite trend. As with the laser scattering measurements it has not been possible to evaluate n_e at very early times. In this case it is due to the transient nature of emission coupled with the limited temporal resolution of the optical detection equipment, $\sim$ 10 ns, and the difficulties in accurately cross timing the channels.

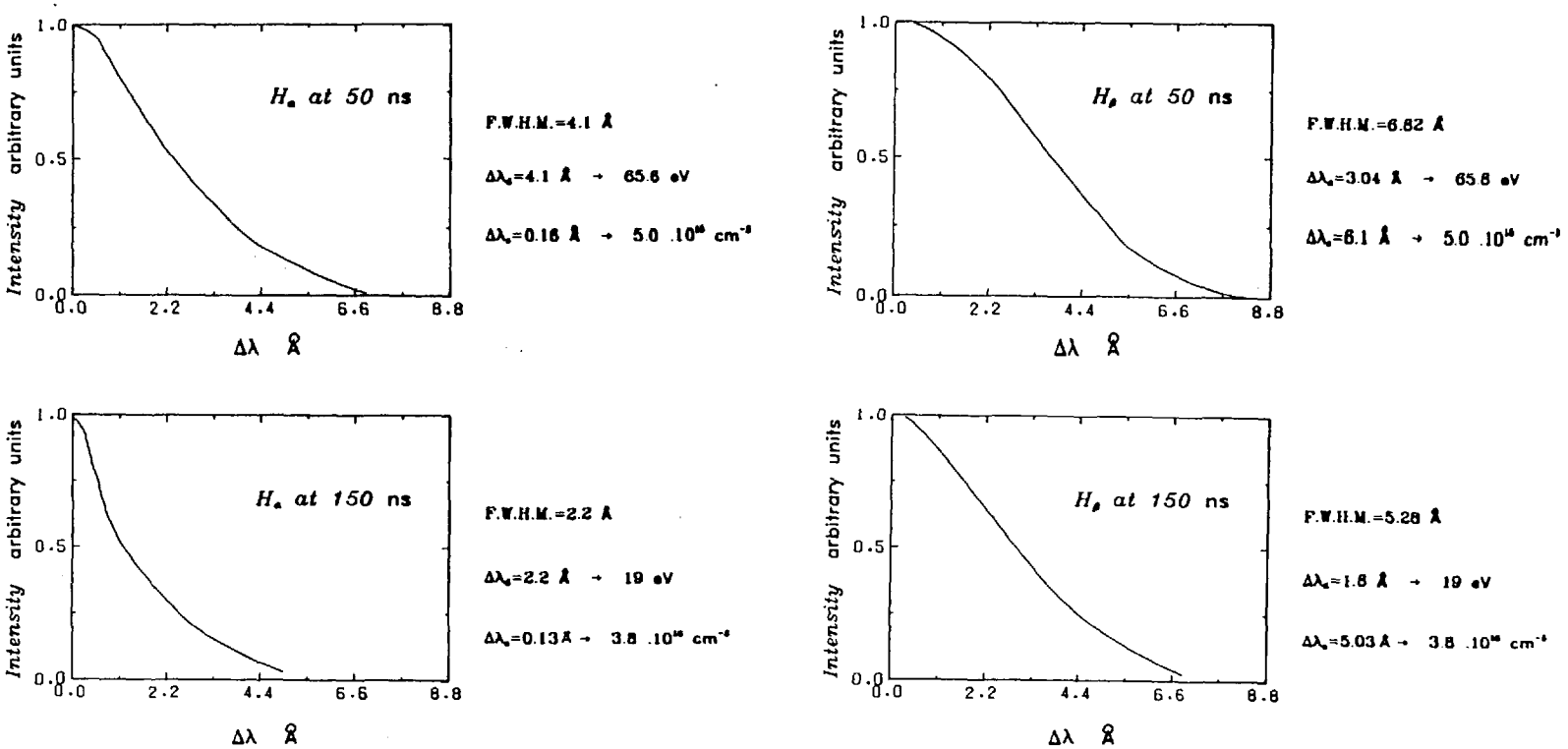

Fig. 4.33 Two examples of the deconvolution of the Stark and Doppler components of the H_α and H_β lines.

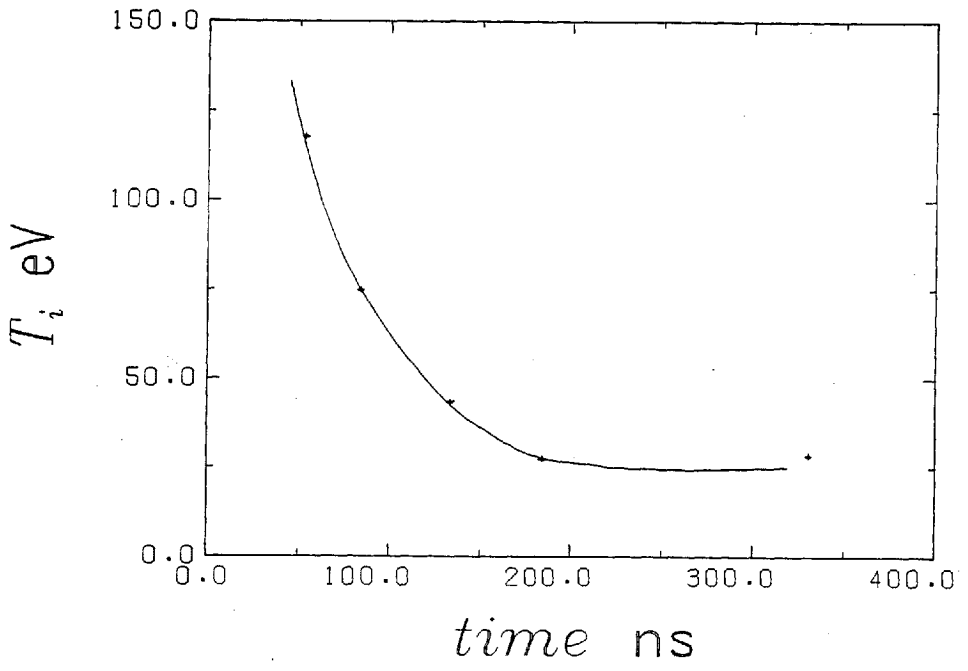

Fig. 4.34 Plot of T_i versus time obtained from the H_α and H_β line profiles.

4.9 X-ray Measurements

4.9.1 Time resolved hard and soft X-rays

The duration of the emission of both hard and soft X-rays correlated well with the beam duration measured on the Faraday cup. In Fig. 4.35 the peak intensities obtained are plotted against filling pressure. The observed rise in the soft X-ray signal at low pressures is however, due to fluorescence of the chamber wall (a small portion of which could be "seen" by the detector) under irradiation from soft X-rays originating at the anode foil. That the wall was the source and not the plasma was indicated by geometrical optical effects and later confirmed by pin-hole X-ray photography as shown in Fig. 4.36. Changing the anode foil material from Al/My to Al caused a much larger signal to be obtained and leads to

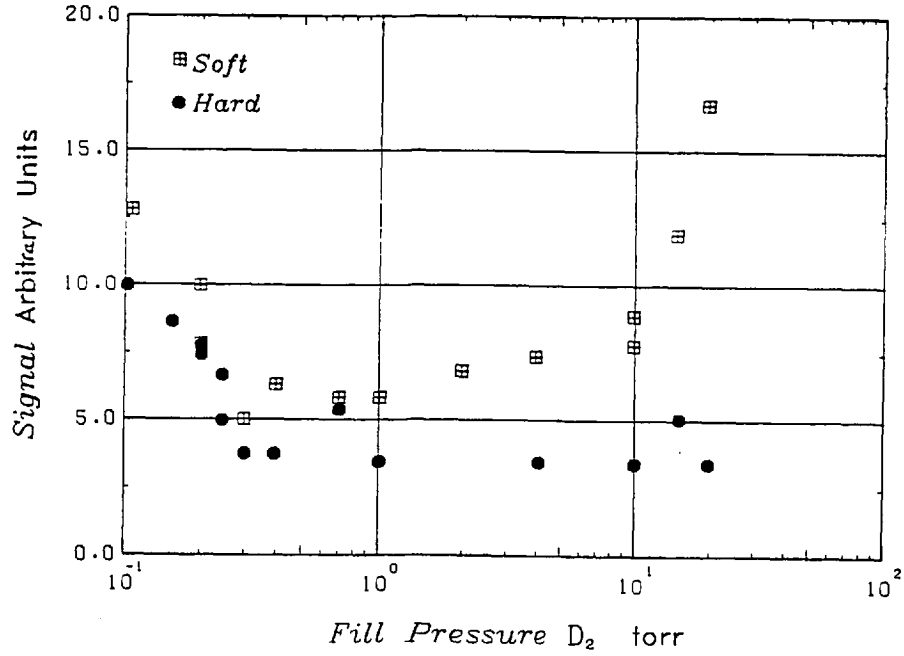

Fig. 4.35 Plot of peak X-ray signals versus fill pressure of deuterium for both hard and soft X-rays.

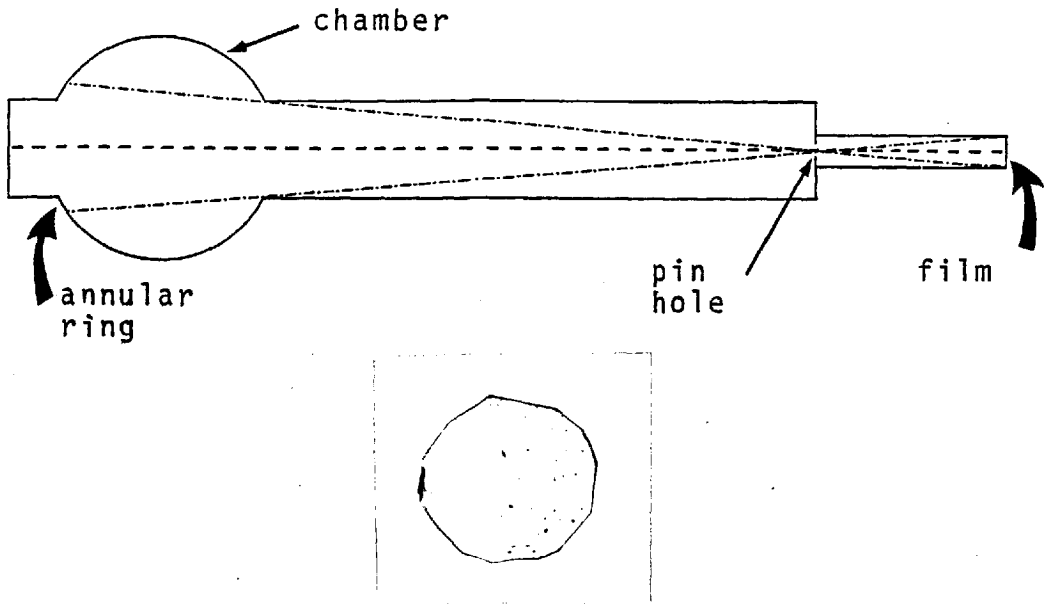

Fig. 4.36 X-ray pin hole photograph and associated geometrical optics.

the conclusion that the beam-foil interaction is the primary source. Fig. 4.35 also indicates a minimum in the soft X-ray emission at ~ ½ torr. It is in this pressure range that beam propagation is most efficient. The drop in soft X-ray signal at these moderate pressures must be the result of a faster space-charge neutralization time, causing a reduction in the amount of multipassing of the anode foil by beam electrons. The rise in signal level again at high pressures (greater than 1 torr) is probably due to increased beam-gas bremsstrahlung. This is supported by no increase in the hard X-rays as occurs at the low pressures as is shown in Fig. 4.35. No check with pin-hole photography has been made at these high pressures.

With the soft X-ray detector sufficiently well collimated to eliminate the wall source, the overall sensitivity to any plasma source was considerably reduced and no signal was detected above the noise level (mainly pick-up from the generator).

4.9.2 Time integrated measurements

Measurements with the foil filters and film were intended to reveal information regarding the X-ray spectrum. However, these measurements were made prior to the realization that the wall was the X-ray source. This is shown clearly by the X-ray pin-hole photograph in Fig. 4.36. The annular exposure is formed by the limiting aperture of the camera and the opposite port. As no exposure of the centre of the annulus has been obtained for low pressure shots, the foil measurements were not repeated with the wall obscured.

Integrating the exposure over four shots still produced no image. This can also be used to estimate the maximum possible plasma emission.

As the emission of X-rays at high pressures was thought to be beam-gas bremsstrahlung and not an electron tail, no foil-film measurements were made at high pressures.

CHAPTER 5

DISCUSSION

5.1 Introduction

In this chapter the results presented in the previous chapter are discussed and interpretations considered.

Aspects of the results requiring explanation are:-

(i) The dependencies of W_{OHM} and W_{DL} upon the anode foil type, the beam current rise time and axial position (in the case of W_{DL})

(ii) Ion energy balance. Modes of both heating and cooling.

(iii) The electron energy balance. The discrepancy between W_{OHM} and $\frac{3}{2} n_e k T_e$.

(iv) The independence of the diamagnetic oscillation period upon the initial fill pressure and its dependence on the axial position.

(v) The occasionally observed post-beam increase in the net current.

Comparisons that need to be made are between the various energy density measurements, W_{OHM}, W_{DL} and $\frac{3}{2} Nk(T_e + T_i)$ and also between the measured and classically calculated resistivity.

5.2 Diamagnetism and Return Current Dissipation

The observation of a strong axial dependence of the plasma diamagnetism when Al/My anode foils are used, coupled with the lack of any such dependence for Al foils, is indicative that some kind of turbulent beam-plasma mode of interaction is occurring. The strength of such an interaction depends upon the level at which non-linear mechanisms cause the turbulence level to saturate, see Section 1.7. The non-linear

theories due to THODE (1976) indicate a strong dependence of the saturation turbulence level, and consequently the energy transfer rate, upon the beam velocity spread, with a lower level for warmer beams. The theory further predicts that the turbulence acts back upon the beam increasing its velocity spread and mean scattered angle. Observations of such an effect have been made directly by GREENSPAN (1976) and of axial energy modulation by JURGENS (1976). The introduction of beam scatter to an initially cold (unscattered) beam would explain the fall in diamagnetic signals with distance and the consistently lower signals observed when Al foils are used. Unfortunately the measurements presented here are not comprehensive enough to establish the amount of beam scattering that the turbulence introduces.

It is likely that the diamagnetic signals observed with Al foils and downstream with Al/My foils, consist primarily of the hot ion component. It has been established, (section 4.8) that the ions have transverse energies ~ 100 eV at early times. For ion densities ~ 3.10^{15} cm^{-3} this would result in a contribution of 3.10^{17} eV cm^{-3} to the diamagnetic signals, in reasonable agreement with the downstream observations.

In order to find the dependence of the saturation turbulence level on the beam angular scatter, measurements with a wide range of foils and with good spatial resolution in the axial direction are required. This would enable a comparison between foil and plasma scattering to be made and fix an upper limit on the temperature of a useful beam.

It should be noted that the use of a significantly more relativistic beam than used in this work would result in less scattering of the beam by both the foil and the induced turbulence. However, very relativistic beams are not desirable as the interaction strength falls off with increasing γ, THODE (1976). Some optimum value needs to be obtained.

That the return current dissipation W_{OHM} also depends on the foil type, implies that the low frequency turbulence, which is responsible

for the plasma resistivity, is a result of the primary turbulence, i.e. that the primary Langmuir spectrum, the level of which depends upon the foil type, decays to produce the low frequency turbulence. It is only by such a method that the return current can be dependent upon the degree of beam scattering. Parametric decay of this type has been proposed by PAPADOPOLOUS (1975, 1976), (Section 1.7).

5.3 Ion Temperature Time History

The heating phase of the ions has not been fully time resolved. It is known however, that at ~ 20 ns after the onset of beam injection the temperature is ~ 120 eV and from then on falls approximately exponentially. In addition it is known that from about 80 ns onwards n_e and T_e are fairly constant with values ~ 5.10^{15} cm^{-3} and $\gtrsim$ 5 eV respectively. The rate at which energy may be given to the electrons by collisions with the ions is given by

$$\frac{d\,T_i}{dt} = -\nu^{i/e}\,(T_e - T_i) \qquad 5.1$$

where $\nu^{i/e}$ is the effective ion-electron collision frequency given by BOOK (1976) as

$$\nu^{i/e} = \frac{1.8\,.\,10^{-19}\,(m_e\,m_i)^{\frac{1}{2}}\,n_e\,Ln\Lambda}{(m_i\,T_e + m_e\,T_i)^{3/2}} \qquad 5.2$$

Solution of equation 5.1 with $T_i(t = 20\ ns) = 120$ eV, $T_e = 5$ eV and $n_e = 5.10^{15}$ cm^{-3} yields

$$T_i = 148\,\exp(-1.36\,.\,10^{7}t) + 5 \quad eV \qquad 5.3$$

In Fig. 5.1 this curve is superimposed upon the observed time history, as given in Fig. 4.33, showing reasonable agreement.

Such a model presupposes that the electron temperature is cold

from early times and that some anomalous mechanism is responsible for electron energy loss, so maintaining the low temperatures. If the electron density and temperature are the same at early times as are measured at later times, i.e. $\gtrsim$ 80 ns, then this mode of ion cooling must occur. That the agreement is reasonable implies that this is also the dominant ion cooling mechanism.

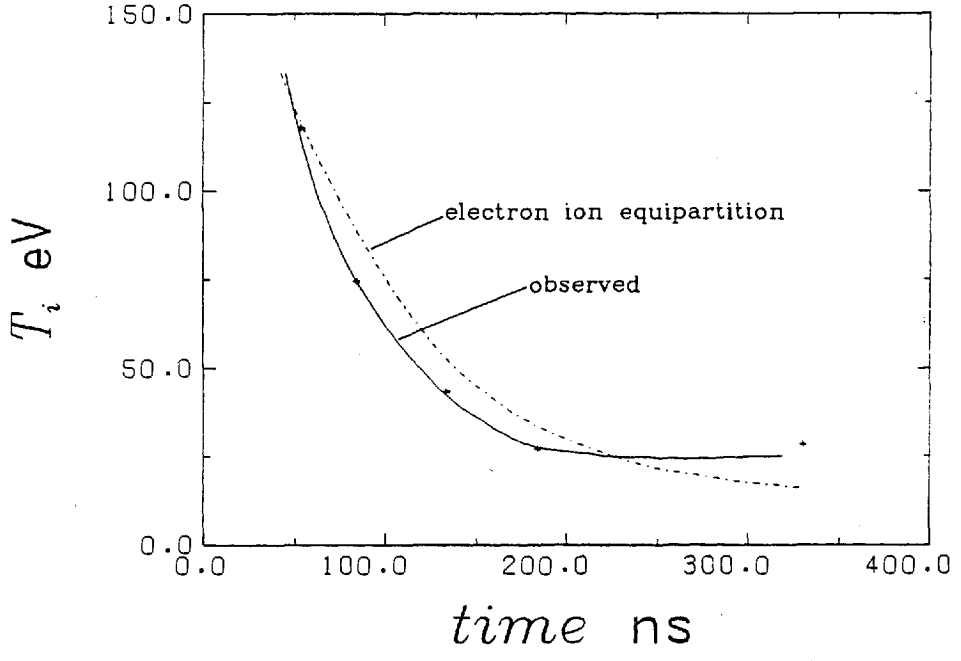

Fig. 5.1 Superimposed plot of the measured T_i versus time with that calculated on the basis of electron ion equipartition as the only ion energy loss mechanism.

Modes of heating are not so clear. Electron-ion equipartition, from an initially hot electron distribution, is not a possible explanation as at a specified density there is a maximum equipartition rate. This is due to the competing effects of temperature difference and the drop in the effective collision rate with increasing temperature. From equations 5.1 and 5.2, neglecting terms $\sim {}^{m_e}/_{m_i}$ gives

$$\frac{d\,T_i}{dt} \;\alpha\; \frac{n_e}{T_e^{3/2}}(T_e - T_i) \;\alpha\; n_e\,(T_e^{-\frac{1}{2}} - T_e^{-3/2}\,T_i)$$

$$\frac{d^2T_i}{dT_e dt} \;\alpha\; n_e\left(\frac{T_e^{3/2}}{2} + \frac{3}{2}\,T_e^{-5/2}\,T_i\right) \qquad 5.4$$

For a maximum equipartition rate $d^2T_i/dT_e dt = 0$ hence

$$3\,\frac{T_i}{T_e} = 1 \qquad \text{or} \qquad T_e = 3\,T_i \qquad 5.5$$

At an electron density of 3.10^{21} m^{-3} and $T_i \sim 50$ eV, the maximum classical heating rate is $\sim 1.6 \cdot 10^8$ eVs^{-1}, compared with the observed rate of $\sim 6.10^9$ eVs^{-1}. Consequently classical electron-ion collisions cannot be responsible for the heating.

Ion heating by turbulent mechanisms is possible. The return current is unlikely to drive ion-acoustic turbulence as the drift velocity is low and T_i high (the normal conditions may be relaxed somewhat for a non-Maxwellian velocity distribution), but it could be driven by the parametric decay of beam induced Langmuir turbulence, as has been discussed in the previous section. However, in the case of Al/My anode foils, the return current deposition rate peaks at $\gtrsim$ 30 ns, i.e. later than T_i. This is consistent with equipartition not being responsible for ion heating and also indicative that the turbulence level (if related to the plasma resistivity which is still large at 30 ns, see section 4.5.2), is not responsible either.

The high ion temperature may be due to the existence of a large

space-charge field at the head of the beam. Such fields can exist prior to space-charge neutralization by the background plasma while the plasma density is still low compared with the beam density. The space-charge forms a virtual cathode which reflects beam electrons back to the diode causing them to oscillate between the real and virtual cathodes. Neutralization requires the expulsion of plasma electrons or the radially inward flow of ions. The velocity of the virtual cathode through the chamber is dependent upon the ionization rate and consequently upon the fill pressure. It is well known that virtual cathode systems accelerate ions. Ion beams are produced routinely in reflex triode systems which use this method, S. HUMPHRIES et al. (1975), whilst both axial and radial acceleration of ions has been observed in a propagating virtual cathode system, SUNKA et al. (1977). In this experiment radial acceleration is inhibited by both the strong axial magnetic field and the large neutral particle density. In the early stages the neutral density n_n will be larger than the ion density n_i so that particles may be accelerated for one mean free path before they are neutralized by charge exchange. Provided the fields involved do not exceed ~ 500 MVm^{-1}, at which point the charge-exchange cross-section rapidly drops permitting continual acceleration, then the typical energies expected are given by

$$T_i \sim E_r/n_n\sigma_{ex} \qquad 5.6$$

For T_i ~ 100 eV, $n_n \sim 10^{22}$ m^{-3} and $\sigma_{ex} \sim 10^{-18}$ m^2 this gives E_r ~ $1MVm^{-1}$.

The degree of non-neutralization required may be estimated from $\nabla.\underline{E} = \rho/\varepsilon$ assuming a spherical uniform charge distribution.

$$\frac{1}{r^2}\frac{\partial}{\partial r}(r^2E_r) = -\frac{e}{\varepsilon_o}\{n_b + n_e - n_i\} \qquad 5.7$$

Using $E_r = 0$ at $r = 0$ gives

$$E_r = -\frac{re}{3\varepsilon_o}\left[n_b + n_e - n_i\right] \qquad 5.8$$

For $E_r = -10^6\ Vm^{-1}$ at $r = 10^{-2}m$ gives

$$n_b + n_e - n_i = 1.7 \cdot 10^{10}\ cm^{-3} \qquad 5.9$$

where $n_b \sim 6.10^{12}\ cm^{-3}$ and $n_e \sim n_i$ range from $0 \rightarrow 5.10^{15}\ cm^{-3}$. Hence a net charge density of ~ 0.3% of the beam density is sufficient to produce the observed 100 eV ions (neutrals).

The electrons are not free in the radial direction to compensate such a space-charge field as

$$\omega_{ce}\,\tau_{en} = \frac{eB}{m_e} \cdot \frac{1}{n_n\,\sigma_{en}}\sqrt{\frac{m_e}{2e\,T_e}} \qquad 5.10$$

for typical values of n_n

$$\omega_{ce}\,\tau_{en} = 417.4\ T_e^{-\frac{1}{2}} \qquad 5.11$$

at low energies. At higher energies the cross-section is smaller and consequently all the electrons are always well magnetised.

In the axial direction there are few electrons in front of the virtual cathode, whilst behind it the density is probably still low (~ n_b) until the virtual cathode has reached the end of the chamber, the full beam current starts to propagate and the return current rises.

The possibility arises that the observed neutral particle transverse temperature is just the perpendicular component of a bunch of ions accelerated in an essentially axial direction. Ions accelerated to energies in excess of the beam energy have been observed by many other workers since 1968, GRAYBILL (1970), and arise from the large space-charge fields present at a travelling virtual cathode formed in front of the anode prior to bulk ionization of the gas. However, at

energies greater than ~ 50 keV the charge-exchange cross-section drops rapidly. This implies that only lower energy ions can contribute to an observed neutral temperature. The energy spectrum of axially accelerated ions is not yet available.

5.4 Electron energy balance

The values of W_{OHM} obtained, see section (4.5), would indicate electron temperatures in the range of hundreds of electron volts. However, the temperatures measured directly with laser scattering from the bulk of the electrons are of the order of 10 eV. By examining the energy balance of these electrons it is possible to see if there is a true discrepancy or if the deposited energy has been lost by some process.

The main processes that contribute to the energy content of the electrons are:

1.	Return current heating	ηj_p^2
2.	Ion-electron equipartition	P_{eq}
3.	Thermal conduction	P_{cond}
4.	Bremsstrahlung radiation	P_{br}
5.	Line radiation	P_{line}
6.	Ionization	P_{ion}

Hence the net rate of change of energy of the bulk electrons per unit volume is given by

$$\frac{d}{dt}\left[\frac{3}{2} n_e k T_e\right] = \eta j_p^2 + P_{eq} - P_{cond} - P_{br} - P_{line} - P_{ion} \qquad 5.12$$

The two source terms ηj_p^2 and P_{eq} have been discussed in sections 4.5 and 5.3 respectively. Examples of their temporal history are shown in Figs. 4.15 and 5.1. Typical values of ηj_p^2 are $\gtrsim 10^{25}$ eV $cm^{-3}s^{-1}$.

P_{eq} is obtained from the expression given by BOOK (1976)

$$P_{eq} = n_e \nu_{eq} (T_i - T_e) \quad eV\ cm^{-3}\ s^{-1} \qquad 5.13$$

where ν_{eq} is the equipartition rate.

$$\nu_{eq} = \frac{1.8 \cdot 10^{-19} (m_i m_e)^{\frac{1}{2}} n_i \ln\Lambda_{ei}}{(m_e T_i + m_i T_e)^{3/2}} \quad s^{-1} \qquad 5.14$$

For $m_i T_e >> m_e T_i$ and using $m_i = m_p$ this reduces to

$$\nu_{eq} = 3.23 \cdot 10^{-9} n_i \ln\Lambda_{ei} T_e^{-3/2} \quad s^{-1} \qquad 5.15$$

For $n_i \sim n_e \sim 4.10^{15}$ cm^{-3}, $T_e \sim 5$ eV, $T_i \sim 100$ eV

$$P_{eq} \sim 4.10^{24}\ eV\ cm^{-3}\ s^{-1} \qquad 5.16$$

To estimate the loss due to thermal conduction we require a scale length for the temperature gradient. The maximum dimension is that from the anode foil, where there exists a cold dense plasma, to the scattering region, some 7 cm, for conduction parallel to B_z.

$$P_{cond} = \frac{\partial}{\partial z}\left[\kappa \frac{\partial Te}{\partial z}\right] \simeq \frac{1}{\Delta z^2} T_e \kappa \qquad 5.17$$

where κ is the thermal conductivity. From SPITZER (1962)

$$\kappa_{\parallel} = 2.16 \cdot 10^{20} T_e^{5/2} \quad s^{-1}cm^{-1} \qquad 5.18$$

for $\Delta z \sim 7$ cm, $T_e \sim 10$ eV

$$P_{cond} \sim 1.4 \cdot 10^{22}\ eV\ cm^{-3}\ s^{-1} \qquad 5.19$$

but $P_{cond} \propto T_e^{7/2}$ and may be a dominant loss mechanism at higher temperatures. Perpendicular to B_z the thermal conductivity is given

by SPITZER (1962) as

$$\kappa_{\perp} = 9.97 \cdot 10^{-4} \frac{n_i^2 \, Ln\Lambda_{ei}}{B^2 \, T_e^{\frac{1}{2}}} \left[\frac{m_i}{m_p}\right]^{\frac{1}{2}} z^2 \quad s^{-1}cm^{-1} \qquad 5.20$$

for $n_i = 4.10^{15}$ cm^{-3}

$z = 1$

$Ln\Lambda_{ei} = 9$

$T_e = 5$ eV

$B = 1.5 \cdot 10^4$ gauss

$m_i = m_p$

$$\kappa_{\perp} = 2.9 \cdot 10^{20} \; s^{-1}cm^{-1}$$

and 5.21

$$P_{\perp cond} \simeq 1.4 \cdot 10^{21} \text{ eV cm}^{-3}s^{-1}$$

The power radiated from a hydrogen plasma by bremsstrahlung radiation is given by BOOK (1976) as

$$P_{br} = 1.06 \cdot 10^{-13} \, n_e^2 \, T_e^{\frac{1}{2}} \quad \text{eV cm}^{-3}s^{-1} \qquad 5.22$$

for $n_e = 4.10^{15}$ cm^{-3}, $T_e = 5$ eV

$$P_{br} = 3.8 \cdot 10^{18} \text{ eV cm}^{-3}s^{-1} \qquad 5.23$$

However, observed continuum emission at 6943 Å was ~ 200 times the bremsstrahlung radiation, see Section 4.7, so it may be more relevant to use $P_{br} \sim 7.5 \cdot 10^{20}$ eV cm^{-3}s^{-1}.

Power radiated as a result of recombination radiation is given by BOOK (1976) as

$$P_{recomb} \simeq 1.06 \cdot 10^{-13} \, n_e^2 \, T_e^{-\frac{1}{2}} \, E_{\infty} \quad \text{eV cm}^{-3}s^{-1} \qquad 5.24$$

where E_{∞} is the ionization potential of hydrogen ≃ 13.56 eV.

Hence, with $n_e \sim 3.10^{15}$, $T_e \sim 10$ eV

$$P_{recomb} \simeq 4.10^{18} \text{ eV cm}^{-3}\text{s}^{-1} \qquad 5.25$$

In order to estimate the power radiated by line emission some simplifying assumptions will be made.

1. Lyman series is optically thick.
2. All downward transitions are radiative.
3. All upward transitions are collisional.
4. $n(1) >> n(p)$ for $p > 1$ i.e. the ground state population dominates the excitation rate to any higher level.

That the plasma is optically thick to the Lyman series is a reasonable assumption as the ionization rate from excited levels is high and hence the majority of neutrals will be in the ground state. If the degree of ionization becomes high, the Lyman series may become thin but little Lyman radiation will be present. It should be noted that the excitation temperature will be similar to the electron temperature, not the ion and neutral translational temperature. The second and third assumptions whilst not necessarily true will result in an over estimate of the line radiation loss and need to be corrected only if this is a dominant process. These assumptions lead directly to the equation

$$P_{line} = \sum_{n=3}^{\infty} \chi_{1n} \Delta E_{2n} n_e n(1) \qquad 5.26$$

where χ_{1n} is the collisional excitation rate from

level 1 to n,

ΔE_{2n} is the difference in energy from

levels n to 2,

n(1) is the ground state population density.

The use of ΔE_{2n} is the direct result of the Lyman series being optically thick. χ_{1n} is given by BOOK (1976)

$$\chi_{1n} = \frac{1.6 \cdot 10^{-5} f_{1n} g(n, m)}{\Delta E_{1n} T_e^{\frac{1}{2}}} \exp - (\Delta E_{1n}/T_e) \qquad 5.27$$

hence

$$P_{line} = n_e n(1) \; 1.6 \cdot 10^{-5} T_e^{-\frac{1}{2}} \sum_{n=3}^{\infty} f_{1n} g(n,m) \frac{\Delta E_{2n}}{\Delta E_{1n}} \exp-(\Delta E_{1n}/T_e) \qquad 5.28$$

Using Rydberg's formula for ΔE gives, with an ionization potential of 13.53 eV,

$$P_{line} = n_e n(1) \; 1.6 \cdot 10^{-5} T_e^{-\frac{1}{2}} \sum_{n=3}^{\infty} f_{1n} \frac{n^2-4}{4(n^2-1)} \exp-\left[\frac{13.53}{T_e}(1-\frac{1}{n^2})\right] \qquad 5.29$$

f_{1n} may be calculated from JOHNSON (1972) with g(n,m) included. Some values are tabulated in Appendix VI. The summation term converges fairly rapidly to ~ $2.2 \cdot 10^{-3}$ for T_e = 5 eV.

$$\therefore \quad P_{line} = n_e n(1) \; 1.57 \cdot 10^{-9} \quad \text{eV cm}^{-3}\text{s}^{-1} \qquad 5.30$$

for $n_e \sim 4.10^{15}$ cm^{-3} and $n(1) \sim n_o - n_e \sim 10^{16}$ cm^{-3} (n_o from 200 mtorr fill pressure)

$$P_{line} = 6.3 \cdot 10^{22} \quad \text{eV cm}^{-3}\text{s}^{-1} \qquad 5.31$$

To estimate the power going into ionization of the background gas the ionization rate is required for a plasma optically thick to the Lyman series. Attempts have been made to produce analytic forms for such a rate coefficient. These generally take the form of a rate coefficient for ionization from the ground state of an optically thin plasma corrected for optical depth, e.g.

$$\chi_{ion} \simeq \left(\frac{13.6}{10}\right)^2 . \exp\left(\frac{3.6}{T_e}\right) \quad \frac{5.4 \; . \; 10^{-8} \; T_e^{\frac{1}{2}} \exp-(13.6/T_e)}{6 + (T_e/13.6)} \qquad 5.32$$

where $\left(\frac{13.6}{10}\right)^2 . \exp \frac{3.6}{T_e}$ is the optical depth correction. Such formulae normally produce accurate values over a limited temperature range (the rate coefficient is insensitive to the number density for T_e higher than a few eV). The problem has been solved numerically by BATES et al. (1962) and extended to higher temperatures by JOHNSON and HINNOV (1973). In Fig. 5.2 equation 5.32 and the JOHNSON and HINNOV tabulated rates are plotted for comparison. For T_e ~ 25 eV agreement is good but at the extremes of the plotted range ($\lesssim$ 3 eV and $\gtrsim$ 1 keV) the discrepancy is ~ 50%.

The power going into ionization is given by

$$P_{ion} = \chi_{ion} \; n_e \; n(1) \; E_{ion} \qquad 5.33$$

where n(1) is the ground state population density. From assumption 4 $\sum_{p=2}^{\infty} n(p)$ is negligible compared to n(1) so that n(1) can be replaced by $(n_{fill} - n_e)$, where n_{fill} is the atomic filling density. For an estimate of P_{ion} we take $n_{fill} \sim 10^{16}$ cm^{-3}, $n_e \sim n_{fill}/2$ (to maximize P_{ion}), $\chi_{ion} \sim 6.10^{-8}$ cm^3 sec^{-1} and E_{ion} = 13.53 eV giving $P_{ion} \sim 4.10^{25}$ eV cm^{-3} sec^{-1}. Such a high estimate (~ ηj_p^2) means that the temporal behaviour of the electron temperature could be dominated by a balance between ηj_p^2 and ionization. To gain more insight into the time history of the various processes numerical integration of the energy balance equation was performed.

Numerical Integration of the Energy Balance Equation

Equation 5.12 is

$$\frac{d}{dt}\left[\frac{3}{2} n_e k T_e\right] = \eta j_p^2 + P_{eq} - \left[P_{cond} + P_{br} + P_{im} + P_{ion}\right] \qquad 5.12$$

and

$$P_{ion} = n_e\, n(1)\, \chi_{ion}\, E_{ion}$$

so that

$$\frac{\partial n_e}{\partial t} = n_e\, n(1)\, \chi_{ion} \qquad 5.34$$

Substituting equation 5.34 into equation 5.12 will give a pair of simultaneous 1st order differential equations

$$\frac{3}{2} k\, n_e \frac{\partial T_e}{\partial t} + \frac{3}{2} k\, T_e \frac{\partial n_e}{\partial t} = \eta j_p^2 + P_{eq} - \left[\text{loss terms}\right] \qquad 5.35a$$

$$\frac{\partial T_e}{\partial t} = - T_e\, n(1)\, \chi_{ion} + \frac{2}{3kn_e}\left[\eta j_p^2 + P_{eq} - \{\text{loss terms}\}\right] \qquad 5.35b$$

using units of eV $cm^{-3}sec^{-1}$ makes k = 1

$$\frac{\partial T_e}{\partial t} = \frac{2}{3n_e}\, \eta j_p^2 + P_{eq}(n_e,T_e,t) - P_{line}(n_e,T_e) - P_{cond}(n_e,T_e,B_z)$$

$$-P_{br}\,(n_e,T_e) - \chi_{ion}(n_{fill} - n_e)(T_e - \frac{2}{3} E_{ion}) \qquad 5.36$$

$$\frac{\partial n_e}{\partial t} = n_e(n_{fill} - n_e)\, \chi_{ion} \qquad 5.37$$

These equations were integrated by a simple predictor corrector method. The long time history is insensitive to the initial temperature so that more complex integration schemes were not considered. The only non-analytic functions are ηj_p^2 and χ_{ion}. For the former, interpolation of smoothed experimental data was used, whilst for the second interpolation from the JOHNSON and HINNOV values was used. The interpolation routine used fitted cubic spline functions to points near the desired point, but was inclined to oscillate near discontinuities. The initial conditions from which the equations were integrated were chosen as $n_e = 10^{13}$ cm^{-3} and T_e = 20 eV. In fact the integration is highly

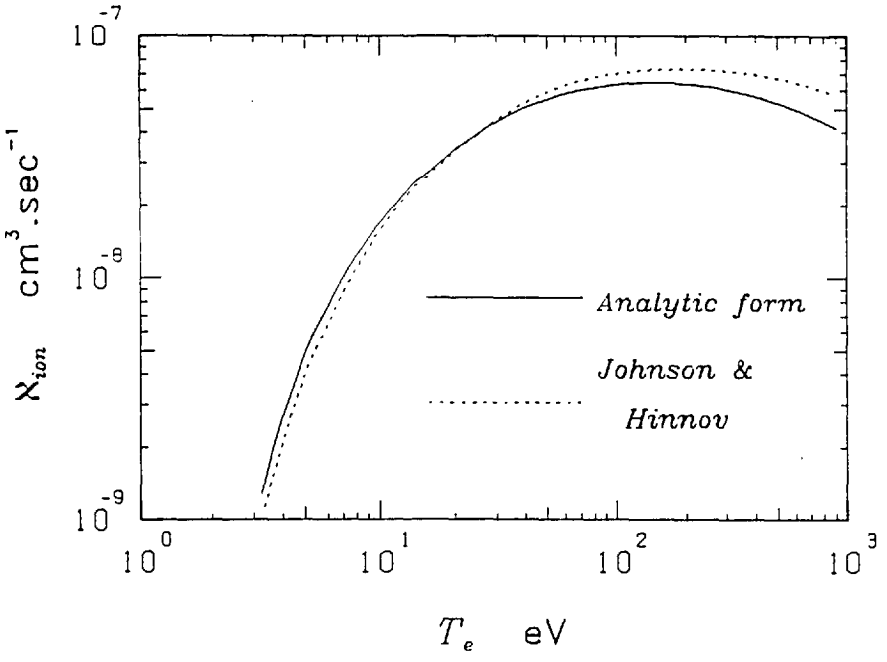

Fig. 5.2 Plot of χ_{ion} (the ionization rate coefficient) versus T_e for hydrogen. The figure compares the Johnson and Hinnov values with an analytic form.

insensitive to the initial value of T_e which rises rapidly to ~40 eV when a balance between ηj_p^2 and P_{cond} is reached. The model used for P_{cond} is not very realistic in view of its $T_e^{7/2}$ dependence and its importance in determining the temperature evolution of the plasma. Figures for P_{cond} obtained in the integration are often in excess of the particle flux limit. In addition no spatial dependence of ηj_p^2 has been included either so the model is at best only capable of indications.

5.5 Integration Results

Some results of the integrations are shown in Fig. 5.3. In all cases the temperature is held down by one of the loss terms. However, the particular dominant loss term varies with fill pressure. For a 100 mtorr shot with Al/My anode foil and fast rising beam current the

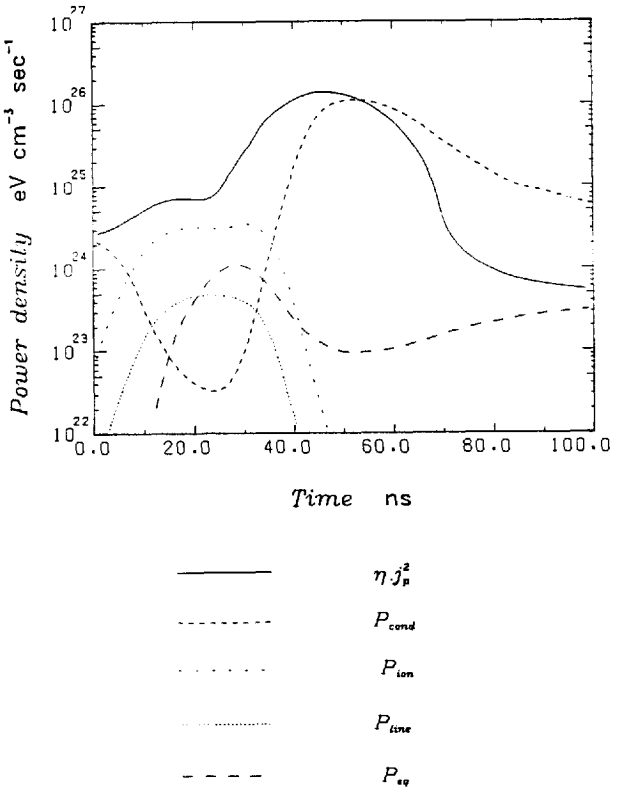

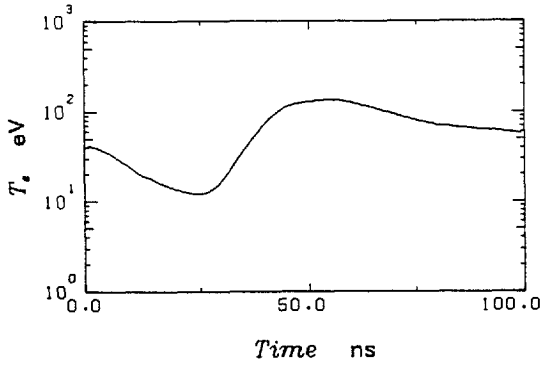

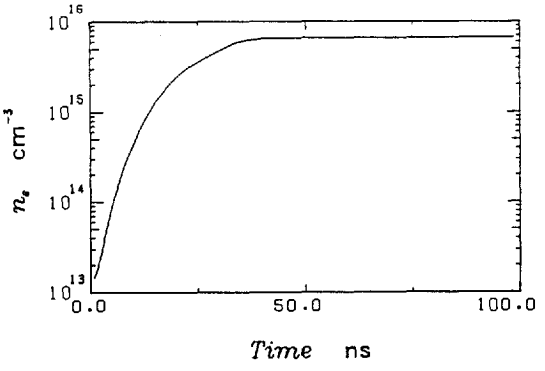

Fig. 5.3a Integration results for 100 mtorr fill pressure with a fast rising beam and Al/My anode foil.

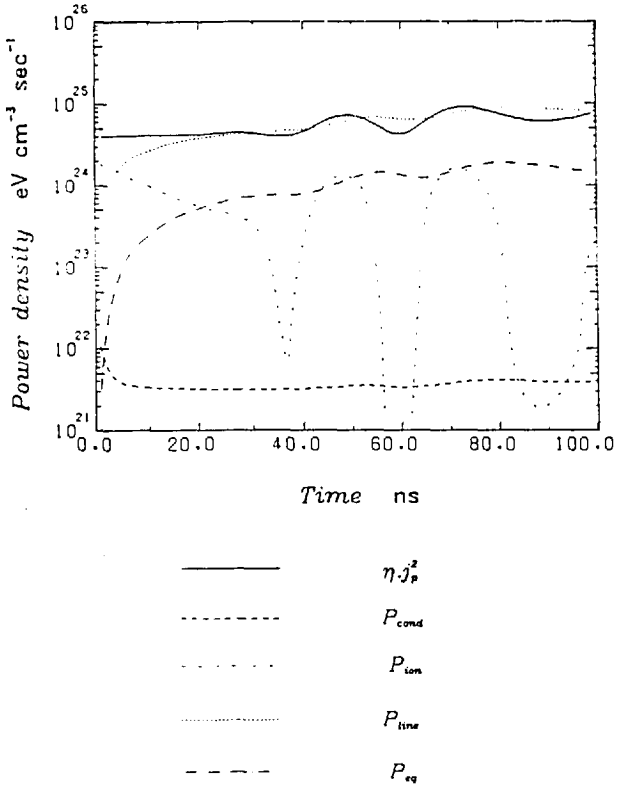

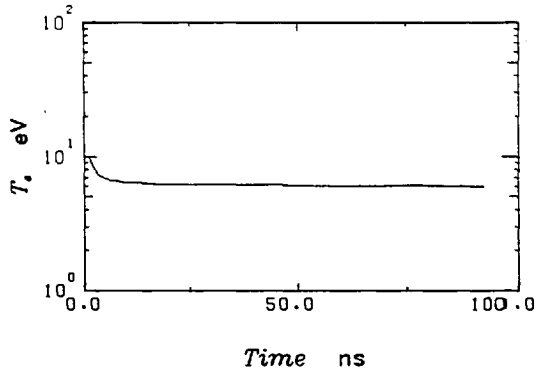

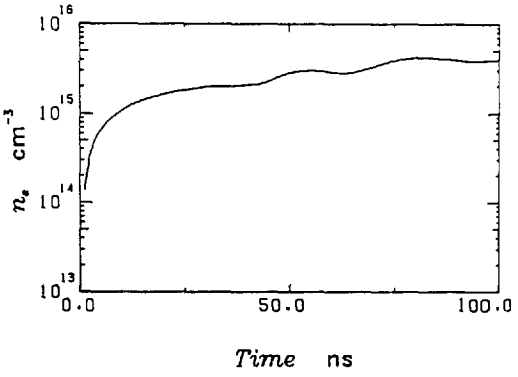

Fig. 5.3b Integration results for 1.5torr fill pressure with a fast rising beam and Al/My anode foil.

ionization holds T_e down until ~ 25 ns, T_e then rises until at ~ 50 ns the thermal conduction rises to stabilize T_e at ~ 120 eV. At 1.5 torr fill pressure but again with an Al/My anode foil and fast rising beam current it is the line radiation which dominates the temperature stabilization to ~ 6.5 eV. It should be remembered that n_n has been taken as $(n_{fill} - n_e)$ rather than $n_n = n_e$ as may be justified by the arguments on neutral expulsion given in Appendix I.

The main conclusion from these integrations however, is that whilst we may not expect a T_e of many hundreds of eV it should at least be ~ 50 eV for injection into low pressures. The discrepancy strongly indicates that electrons are being heated in a region of either real or velocity space which is unobservable, i.e. near the anode or in a high energy tail.

5.6 Estimates of the Limiting Parameters of a High Energy Electron Tail

The lowest detectable exposure of the Kodirex X-ray film used is a little less than 10^6 photons cm^{-2}. As the photons were integrated over up to four shots without any visible exposure of the film, the total number of photons per shot is probably less than 2.10^5 cm^{-2}. For a 100 ns duration beam this is a flux of 2.10^{12} photons cm^{-2} s^{-1}, which, after geometrical considerations is also near the noise limit of the solid state detector system. (The signal is also dependent upon photon energy.) The geometry shown in Fig. 5.4 then indicates the maximum X-ray emission as $2.77 \cdot 10^{14}$ photons cm^{-3} s^{-1}. From BOOK (1976) the bremsstrahlung emission from an electron tail may be estimated as

$$P_{br\ tail} = 10^{-13}\, n_i\, n_{tail}\, T_{tail}^{\frac{1}{2}} \quad eV\ cm^{-3}\ s^{-1} \qquad 5.38$$

At early times one may assume $n_i \sim n_{tail}$ and at late times this assumption can only result in an under estimate of the radiated power.

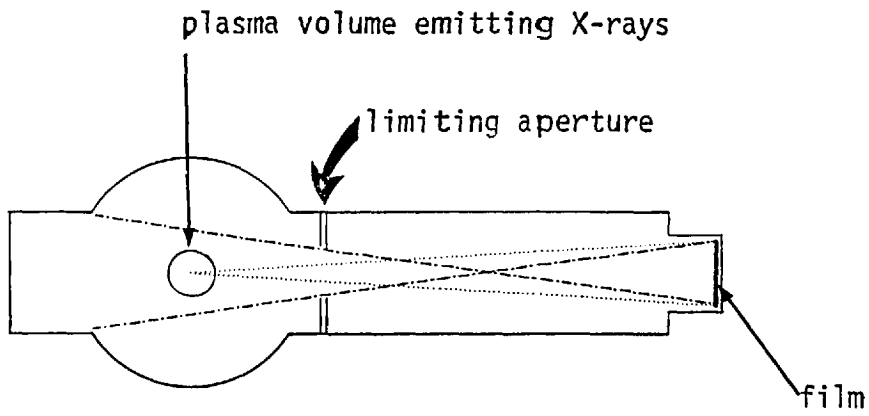

Fig. 5.4 Geometry for soft X-ray detection.

In order that the emission be unobservable we require

$$P_{br\ tail} < 2.77 \cdot 10^{14} T_{tail}$$

or 5.39

$$n_{tail}^2 T_{tail}^{\frac{1}{2}} < 2.77 \cdot 10^{27}$$

This condition is also subject to a total energy density $nT \leq 10^{18}$ eV cm^{-3} from the W_{DL} and W_{OHM} measurements. (Strictly, the tail could be of parallel velocities only and produced by a direct beam plasma interaction. In this case it may not contribute to W_{DL} or W_{OHM} and could exceed 10^{18} eV cm^{-3}.) Fig. 5.5 shows a plot of n_{tail} against T_{tail} with the shaded region indicating the range of possible parameters for an unobservable tail to exist. In addition the detection limit of the Thomson scattering system is shown; see section 5.7.

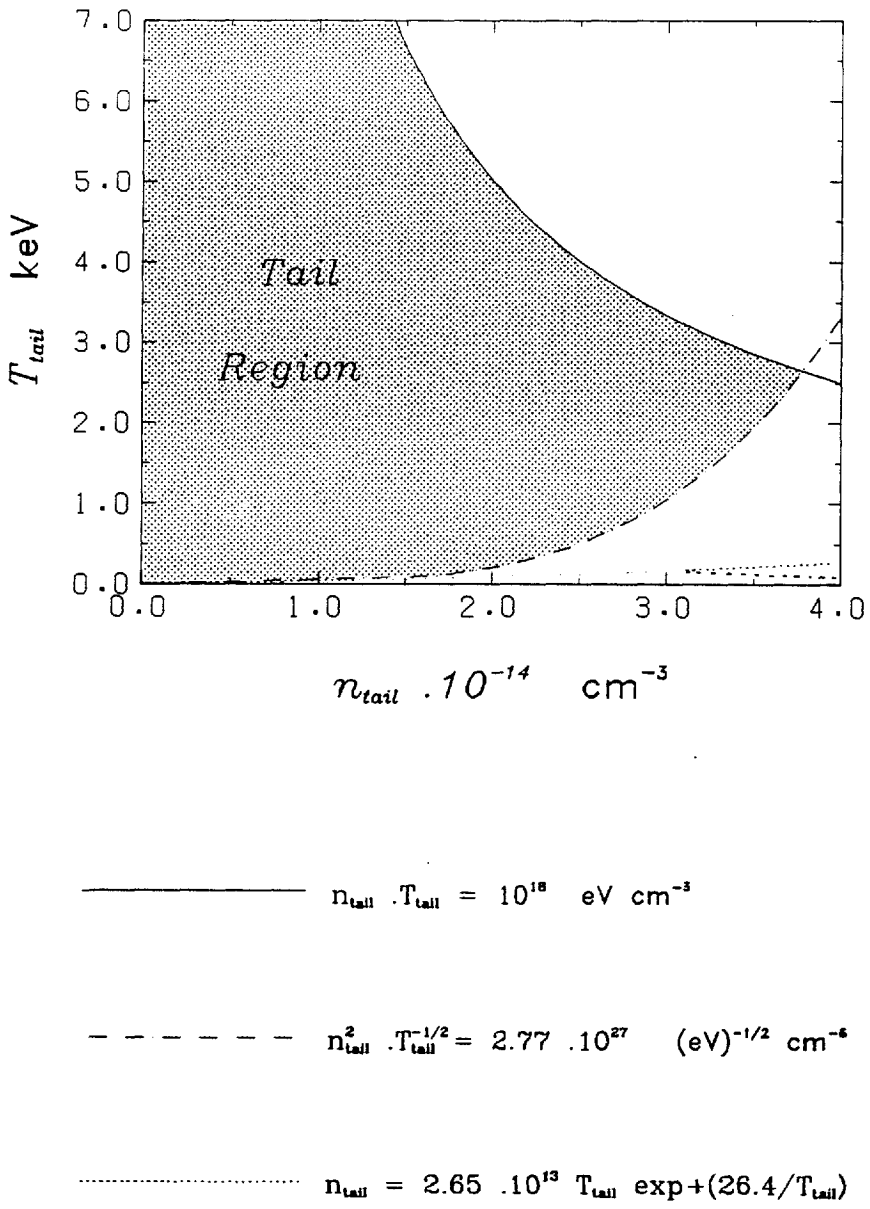

Fig. 5.5 Plot of n_{tail} versus T_{tail} showing region in which a tail could exist and remain undetected by both the soft X-ray experiment and the laser scattering, subject to a total energy constraint.

5.7 Detectability of a High Energy Electron Tail by Laser Scattering

The relationship between electron temperature and the observed spectral width for a low α scattering system is

$$T_e = \frac{\Delta\lambda_{\frac{1}{2}\frac{1}{e}}}{757.8 \sin^2\theta/2} \qquad 5.40$$

where θ is the scattering angle and $\Delta\lambda_{\frac{1}{2}\frac{1}{e}}$ the half width, in Å, at the $1/e$ point. Assuming a spectral profile of the form

$$I(\Delta\lambda) = a \exp - (\Delta\lambda/\Delta\lambda_{\frac{1}{2}\frac{1}{e}})^2 \qquad 5.41$$

and normalizing with respect to number density gives (for $\theta = 90^o$)

$$n(\Delta\lambda) = n_e(378.8\ \pi\ T_e)^{-\frac{1}{2}} \exp - (\Delta\lambda^2/378.8\ T_e)\ \text{Å}^{-1} \qquad 5.42$$

With the system set up as described in Chapter 4, the detection limit is $\sim 10^{13}$ cm^{-3}/channel, where a channel is 13Å, i.e. $7.7 \cdot 10^{11}$ cm^{-3} Å^{-1}. The spectral range covered is $\sim$ 100Å. Substituting this into equation 5.33 with $n(\Delta\lambda) = 7.7 \cdot 10^{11}$ and $\Delta\lambda = 100$ gives

$$7.7 \cdot 10^{11} = n_e(378.8\ \pi\ T_e)^{-\frac{1}{2}} \exp - (10^4/378.8\ T_e)$$

$$n_e = 2.65 \cdot 10^{13}\ T_e^{\frac{1}{2}} \exp + (26.4/T_e) \qquad 5.43$$

This relationship gives the minimum density n_e which is detectable at 100Å from the ruby wavelength at a given temperature. The expression has a minimum of $n_e = 3.18 \cdot 10^{14}$ cm^{-3} at $T_e = 52.8$ eV. For higher temperatures n_e(min) rises slowly to $1.2 \cdot 10^{15}$ cm^{-3} at 2 keV. Consequently for a tail to be detectable it must have $n_e > 3.18 \cdot 10^{14}$. As the detection limit is set by both the total number of photons collected by a channel and by the ratio of scattered to plasma light, it does not follow that increasing the spectral range of a channel will

help. The plasma light has an intensity equivalent to ~ 10^{13} cm^{-3}/ 13Å channel. As the plasma light is transient at the times when one might expect to observe a tail, it is the ratio of scattered to plasma light which is relevant rather than scattered to plasma fluctuation light levels.

The limiting parameters of a detectable tail are shown in Fig. 5.5.

5.8 Oscillation of Diamagnetic Signals

In Chapter four the observed diamagnetic signals were shown to oscillate with either a 200 or 400 ns period, the larger occurring close to the anode foil. This could be due to two effects. Firstly, if the plasma is heated locally the resulting disturbance in the magnetic field may travel along the field lines as an Alfvén wave. It may then be repeatedly reflected at the ends of the chamber returning to the diamagnetic loop so producing an oscillation of the signal. For typical values of v_A ~ 1.7 . 10^5 ms^{-1}, see Appendix II, the disturbance would take ~ 3 μs to travel back to position 1. Although a disturbance may also be reflected from the anode in 200 ns this could not reappear for another 3 μs. Such a reflection could well affect the shape of the observed signal but could not give rise to the observed persistent oscillations at periods of 200 and 400 ns.

The second possibility is that the plasma undergoes radial oscillations as a result of departure from the equilibrium of the magnetostatic equation. The frequency for small amplitude oscillations may be obtained from the radial potential function V(r), given by

$$V(r) = Nk\,T_{\perp} - \frac{1}{2\mu_o}\left[B_{OUT}^2 - B_{IN}^2\right] \qquad 5.44$$

where B_{OUT} and B_{IN} are the axial magnetic fields inside and outside the plasma boundary, see section 4.6.2. Using the expressions from that section, equation 5.44 reduces to

$$V(r) = NkT_{\perp} - \frac{B_o^2}{2\mu_o}\left[\left(\frac{a^2 - b^2}{b^2 - r^2}\right)^2 - \left(\frac{a}{r}\right)^4\right] \qquad 5.45$$

where B_0 is the initial unperturbed axial field. The radial equation of motion is

$$\rho\ddot{r} = -\left.\frac{\partial^2 V(r)}{\partial r^2}\right|_{r=a_1} r \qquad 5.46$$

where a_1 is the equilibrium radius and ρ the mass density of the plasma. The period for S.H.M. is given by

$$\tau = 2\pi\left(\left.\frac{\partial^2 V(r)}{\partial r^2}\right|_{r=a_1}\right)^{-\frac{1}{2}} \rho^{\frac{1}{2}} \qquad 5.47$$

with

$$\frac{\partial^2 V(r)}{\partial r^2} = -\frac{2B_o}{\mu_o}\left[\frac{(a^2 - b^2)^2}{(b^2 - r^2)^3} + \frac{6r^2(a^2 - b^2)^2}{(b^2 - r^2)^4} - \frac{5a^4}{r^6}\right] \qquad 5.48$$

If one considers oscillations about a instead of a_1 then r is replaced by a and

$$\left.\frac{\partial^2 V(r)}{\partial r^2}\right|_{r=a} = \frac{2B_o^2}{\mu_o}\left[(a^2 - b^2)^{-1} + 6a^2(a^2 - b^2)^{-2} + 5/a^2\right] \qquad 5.49$$

with $a = 10^{-2}$ m, $b = 3.8 \cdot 10^{-2}$ m τ is given by

$$\tau = 3.15 \cdot 10^{-16}\, n_i^{\frac{1}{2}}\, B_o^{-1} \quad \text{secs} \qquad 5.50$$

with n_i in cm^{-3} and B_0 in tesla. This agrees with the period at $r = a_1$ to better than 10% for the values of $(a_1 - a)$ observed and is also approximately equal to $2a/v_A$.

Although typical values of n_i and B_0 yield periods of $\lesssim$ 50 ns, allowance should be made of the mass loading by the neutrals. The neutral density should also be corrected for radial expulsion, see Appendix I. If the treatment of Appendix II is used to correct the

Alfvén velocity we have

$$\tau = 2\,\tau_A^* \qquad 5.51$$

where τ_A^* is the corrected Alfvén wave transit time across the plasma. For B_o = 1.6 tesla, T_i = 20 eV (late time value), the values of n_i and n_n required to fit the 200 and 400 ns observed periods, with $n_n \leq n_i$ from the results of Appendix I, are

(a) 400 ns period $n_i = 6.3 \cdot 10^{15}$ cm^{-3}, $n_n = 3.10^{14}$ cm^{-3}

(b) 200 ns period $n_i \simeq n_n = 3.3 \cdot 10^{15}$ cm^{-3}

Condition (b) is in agreement with the values of n_e obtained from both laser scattering and the Stark broadening measurements. However, for condition (a) we must propose that the plasma conditions are significantly different near the anode foil This is reasonable in any case in view of the amplitude of the diamagnetic signal near the foil. The constancy of the 200 ns period over a large pressure range can be explained by the expulsion of neutrals which can reduce n_n to n_i in $\leq$ 40 ns. The constancy of the 400 ns period is harder to explain and a full time history of n_i and n_n is needed to justify the argument that the bulk of the neutrals are expelled before ionization is complete so resulting in a low final value of n_n.

5.9 Post-Beam Increase in I_{NET}

The observations of a post-beam increase in I_{NET} described in section 4.3 are probably attributable to radial motion of the plasma. Equation 4.12 with the B_r term neglected is

$$\frac{dI_{NET}}{dt} = \frac{Vr\,B_\theta}{L} - \frac{n}{L}\,j_{pz} \qquad 5.52$$

During the beam I_{NET} and B_θ are negative whilst j_{pz} is positive, so a

decay of j_{pz} leads to an increase in I_{NET}. When the beam switches off j_{pz} reverses to conserve B_θ flux so that I_{NET}, B_θ and j_{pz} are all negative, then only the $v_r B_\theta$ term can lead to an increase in I_{NET} with v_r positive, i.e. the plasma is still expanding. From the plasma diamagnetism results, the velocity of expansion at times after the beam may be estimated. Equation 4.42 is

$$a_1^2 = \frac{a^2(b^2 - c^2) - b^2\,\alpha}{b^2 - c^2 - \alpha} \qquad 4.42$$

Letting $a_1 = a + \Delta a$ and neglecting terms of $O(\Delta a^2)$

$$a_1^2 = a^2 + 2a\Delta a = \frac{a^2(b^2 - c^2) - b^2\,\alpha}{b^2 - c^2 - \alpha} \qquad 5.53$$

$$\Delta a = \frac{a(b^2 - c^2) - b^2\alpha/a^2}{2(b^2 - c^2 - \alpha)} - \frac{a}{2}$$

$$= \frac{\alpha}{2a}\left(\frac{a^2 - b^2}{b^2 - c^2 - \alpha}\right) \qquad 5.54$$

using $a = 10^{-2}$, $b = 3.8 \cdot 10^{-2}$ and $c = 2.8 \cdot 10^{-2}$ gives

$$b^2 - c^2 = 6.604 \cdot 10^{-4} \qquad 5.55$$

From equation 4.44

$$\alpha = -\frac{VRC}{\pi B} \qquad 4.44$$

with $RC = 2.10^{-6}$, $V \sim 10$, $B \sim 1.4$ gives

$$\alpha \sim 4.5 \cdot 10^{-6}$$

Hence

$$|\alpha| << |b^2 - c^2| \qquad 5.56$$

neglecting α in equation 5.54 gives

$$\Delta a = \frac{VRC}{2\pi Ba}\left(\frac{b^2 - a^2}{b^2 - c^2}\right) \qquad 5.57$$

with B = 1.4

$$\Delta a = 4.63 \cdot 10^{-5} V \qquad 5.58$$

The expansion velocity $\frac{\partial a}{\partial t}$ is therefore ~ $4.63 \cdot 10^{-5} \frac{\partial V}{\partial t}$. Typical rates of change of diamagnetic signal voltage are < 20 volts in 10^{-7} secs. This gives radial velocities ~

$$\frac{\partial a}{\partial t} \sim 4.63 \cdot 10^{-5} \cdot \frac{20}{10}\text{-}7 \sim 10^4 \text{ ms}^{-1} \qquad 5.59$$

Typical net currents are ~ 20 kA at lower pressures (and with Al/My anodes) indicating a B_θ field at the edge of the beam of ~ 0.4 Tesla. With L = 317 nHm^{-1} as obtained in section 4.3, this gives a value of $1.26 \cdot 10^{10}$ A s^{-1} for the $v_r B_\theta / L$ term. If η is sufficiently small that the first term in equation 5.52 dominates, then I_{NET} can be expected to rise ~ 600 A in 50 ns, which is in reasonable agreement with the observed figure of ≤1 kA.

The absence of any such increase for Al anode foils is expected as the radial velocities found are some 3 or 4 times lower. At higher pressures the large late time resistivity due to the neutrals means that the ηj_{pz} term will always dominate. In addition the radial velocities found are not quite as high as for low pressures.

5.10 Comparison of Energy Densities

Figures for the plasma energy density have been obtained from four independent diagnostic measurements. These are:

(i) plasma diamagnetism, W_{DL}, which gives the overall perpendicular energy density.

(ii) return current dissipation, nj_p^2, which is expected to result in heating of the bulk electrons

(iii) laser scattering which directly measures the bulk electron energy density and

(iv) spectral measurements giving the ion energy density.

It should be noted however that the plasma diamagnetism has been measured at different positions along the axis from spectral and laser scattering measurements. In addition nj_p^2 is an axial average over the entire chamber length. This is important in view of the strong axial dependence of observed diamagnetic signals for the case of cold beam injection. Consequently, discrepancies among the various energy density measurements may be expected.

The laser scattering results indicate that the electronic energy density is ~ 3.10^{16} eV cm^{-3}, far less than the ~ 10^{18} eV cm^{-3} expected from the nj_p^2 measurements. However, agreement between W_{DL} ~ 2.10^{18} eV cm^{-3} and the early time ion-neutral temperature measurements, which yield ~ 120 eV x 10^{16} cm^{-3}, is more reasonable, especially in view of the observed spatial decay of W_{DL} with distance from the anode foil (W_{DL} falls to ~ 3.10^{17} at 11 cm and the spectral measurements giving T_i were made midway between the two diamagnetic loop positions). Correlations between W_{DL} (near the anode) and W_{OHM} are reasonable and generally within a factor of two. Both exhibit the same strong dependence on the type of anode foil, the Al/My foils giving significantly increased energy densities.

In addition the very large values of W_{DL}, up to ~ $2.8 \cdot 10^{18}$ eV cm^{-3} were only obtained at 100 mtorr fill pressure as is the case of the large W_{OHM} results, up to 3.10^{18} eV cm^{-3} at 100 mtorr.

If it is the case that the return current dissipation does not go into the bulk electrons, and it is hard to envisage it going into the ions, then it is likely that it goes into a fast uncontained electron tail.

If this is true then any correlation between W_{OHM} and W_{DL} arises from their common basis for being large rather than measurements of a common energy density component of the plasma. Alternatively if turbulence is localized to the region of plasma near the anode foil, then the local value of W_{OHM} will be much larger and the correlation with W_{DL} then breaks down. Consequently it appears that the energy resulting from the return current dissipation is not contained.

That the return current dissipation is a function of the anode foil material immediately implies some form of direct beam-plasma turbulent interaction, as otherwise the beam is purely a source of E_z (from $\partial B_\theta/\partial t$) and just produces a return plasma current. Only some turbulent interaction between the beam and plasma electrons can give rise to a dependence of nj_p^2 on the beam angular scatter. This has been discussed in section 5.2.

5.11 Resistivity Comparisons

The resistivity experienced by the plasma return current has been measured directly, hence it may be compared to classical values based upon binary electron-ion and electron-neutral collisions. The values of n_e, n_i and T_e have been obtained from laser scattering and n_n may be inferred from the fill pressure. This last step is somewhat dubious as the ion/neutral temperature at early times is ~ 100 eV giving a neutral expansion velocity ~ 15 cm μs^{-1}. This implies that at ~ 100 ns many neutrals will have left the beam channel. Coupling of the neutrals to the magnetically confined ions by charge-exchange collisions is very efficient for $\lambda_{mfp} << a$ and times $> \lambda_{mfp}/v_{th}$. However at early times $n_n > n_i$ and $\lambda_{mfp} > a$ so that the neutral confinement is not good, see Appendix I. Unfortunately the early evolution of n_i has not been observable, whilst estimates of n_n from the ratio of the H_α and H_β Balmer line intensities are not likely to yield results meaningful in the beam channel as they are line of sight averaged.

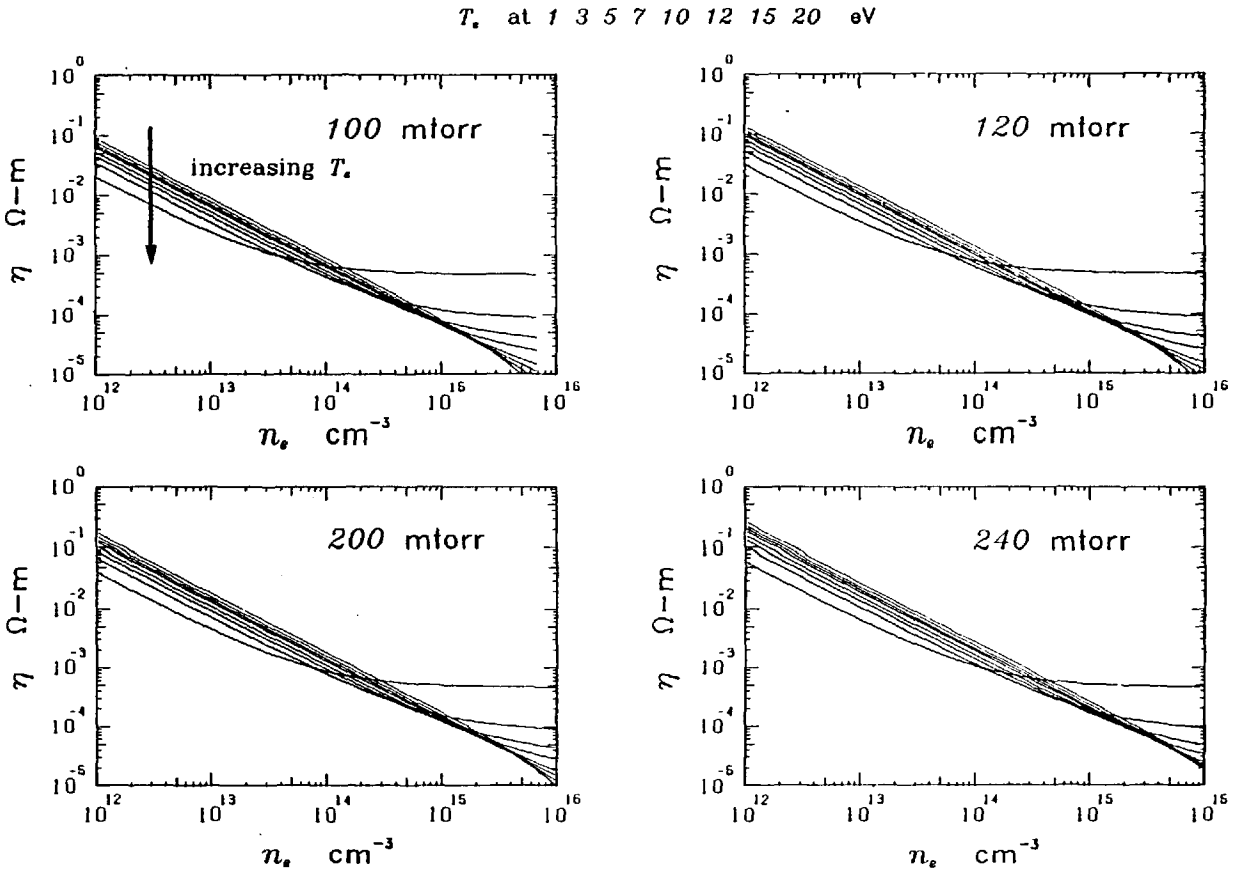

Fig. 5.6 Plots of classical resistivity for a range of T_e, n_e and fill pressures. Both electron ion and electron neutral terms are included.

The classical resistivity is then

$$\eta_{\parallel\ class} = \frac{m_e\ \nu_{en}}{n_e\ e^2} + 5.2\ .\ 10^{-5}\ Ln\Lambda\ T_e^{-3/2} \quad \Omega m \qquad 5.60$$

where ν_{en} is the electron neutral collision frequency and $Ln\Lambda$ the plasma parameter equal to ~ 9, SPITZER (1962). ν_{en} is given by

$$\nu_{en} = n_n\ \sigma_{en}\ (kT_e/2m_e)^{\frac{1}{2}} \quad s^{-1} \qquad 5.61$$

where σ_{en}, the electron-neutral collision cross-section, is given by BOOK (1976) as $\sim 5.10^{-15}\ cm^{-2}$. This gives

$$\eta_{\parallel class} = 3.02\ .\ 10^{-6}\ \frac{n_f}{n_e} - 1\ \ T_e^{\frac{1}{2}} + 4.68\ .\ 10^{-4}\ T_e^{-3/2} \quad \Omega m \qquad 5.62$$

where n_f is the atomic fill density, equal to $\sim 6.67\ .\ 10^{22}\ m^{-3}\ torr^{-1}$. This function is plotted in Fig. 5.6 for various values of n_f and T_e.

Only at times > 70 ns are any electron density and temperature measurements available. These indicate $n_e \sim 2 \rightarrow 6\ .\ 10^{15}\ cm^{-3}$ and $T_e \sim 4 \rightarrow 15$ eV. For a 100 mtorr fill pressure these give $\eta_{class} \sim 1 \rightarrow 6\ .\ 10^{-5}$ Ωm, whereas observed values of Al/My anodes are $\sim 10^{-4}$ Ωm at 100 ns and $\sim 10^{-5}$ Ωm for Al anodes. Hence there is only indication of anomalous resistivity at this time with Al/My anodes. In view of the known axial dependence of the interaction it is likely that near the anode foil the resistivity is considerably higher, i.e. more anomalous.

If plasma turbulence is the explanation of the higher value for the resistivity with Al/My foils it is unlikely to be driven by the relative electron-ion drift velocity and in any case this would not result in a foil dependence. The ion sound speed c_s is $\sim 3.10^4\ ms^{-1}$, the electron thermal speed v_{th} is $\sim 8.10^5\ ms^{-1}$, whilst the drift velocity v_d is $\sim 6.5\ .\ 10^4\ ms^{-1}$. Although $v_d \geq c_s$ it is known also that $T_i > T_e$.

SAGDEEV (1967) gives the effective ion-acoustic collision frequency as

$$\nu_{eff} \sim 10^{-2} \, (v_d/c_s)(T_e/T_i) \, \omega_{pi} \quad s^{-1} \qquad 5.63$$

hence the resistivity will be

$$\eta_{ia} \sim \frac{m_e \, \nu_{eff}}{n_e \, e^2} \sim 5.6 \, . \, 10^{-6} \, \frac{v_d}{c_s} \, \frac{T_e}{T_i} \quad \Omega m \qquad 5.64$$

which is negligible compared to the classical value unless $T_e >> T_i$ or $v_d >> c_s$. As $v_d << v_{th}$ the two stream instability is also unlikely to be be driven. If turbulence is driven by a parametric decay of beam induced turbulence it will be heavily damped because of the high ion temperature. The decay process probably requires the maintenance of a large amplitude daughter wave. However the dependence of resistivity upon the anode foil material is strong evidence that turbulence is present at early times when the resistivity drops far more slowly for the Al/My anode foil shots. It is possible that at early times, with low densities, energetic electrons experience turbulence and as the density rises the electric field becomes short circuited by the cold bulk electrons which also damp any waves present.

At late times the resistivity is known to increase, see section 4.33. The plasma resistance having the form

$$R = \frac{-kl}{I_o + kt}$$

where k is the slope of the linearly decaying current and I_o its initial value (at the beginning of the linear decay). It is likely that this rise in R is due to a fall in T_e. At these late times the resistivity is primarily electron-ion with a $T_e^{-3/2}$ dependence. The changes in the observed resistivity are typically factors of $2 \rightarrow 3$ over this decay requiring changes by factors of $\sim 1.6 \rightarrow 2$ in T_e. Such changes are within the shot to shot variation of T_e measured by laser scattering

precluding verification of this argument.

5.12 Beam-Plasma Stopping Length

The stopping length of the beam may be simply calculated if one assumes a deposition proportional to the local beam energy; i.e. one assumes the beam energy to obey

$$E = E_o \exp(- x/\lambda) \qquad 5.65$$

where E is the local beam energy, E_o the incident beam energy and λ the stopping length.

If the plasma energy density near the anode, i.e. at x = 0, is W_p then

$$\lambda = E_o/W_p\, A \qquad 5.66$$

where A is the beam cross-sectional area = π cm^2. At the lower pressures E_o ~ 500 joules, W_p ~ 10^{18} eV cm^{-3} giving a stopping length

$$\lambda \simeq 10 \text{ m} \qquad 5.67$$

As the interaction is a collective one this deposition rate will only hold above some threshold intensity. However, stopping lengths of this order are quite reasonable for injection into mirror or toroidal type machines. By careful choice of the operating regime and utilizing 'cold' beams significant improvements on this figure may be expected.

5.13 Conclusions

The main conclusions to be drawn are:-

(i) The ion heating is due either to turbulence or acceleration in the space-charge fields at the beam head. Cooling is due to electron-

ion equipartition.

(ii) The electron energy balance indicates some sink of energy or the presence of hot electrons which are unobservable due to their location in either real or velocity space.

(iii) The beam plasma interaction is a strong function of the beam mean scattered angle indicating that a beam plasma mode is exciting turbulence.

(iv) The interaction strength drops rapidly downstream indicating that the turbulence acts back upon the beam, increasing its mean scattered angle.

(v) The dependence of heating upon the beam rise time is probably a result of the ionization time being longer than the beam rise time.

(vi) On the basis of the W_{DL} and W_{OHM} results, the $^{1}/_{e}$ stopping length is ~ 10 m.

CHAPTER SIX

CONCLUSIONS

6.1 Diagnosis of Beam-Plasma Systems

The interaction of a high current relativistic electron beam with a plasma is complex and far from fully understood. An applied magnetic field and neutral gas target, as is used here, complicate matters to such a degree so as to preclude the direct application of most beam-plasma theories. It is neutral gas targets however, rather than preionized gas, that have produced the most promising results.

It is hard to make measurements of the microscopic interactions. Most results reported here and elsewhere are of macroscopic fields, density and temperature measurements. The interdependencies, spatial and temporal variation of the parameters may be compared to theories. However, with a neutral gas target, plasma parameters change grossly during the beam rise time. Unless high temporal resolution is obtained, comparison with simulations is difficult.

In spite of these problems, several important facts have been established. Plasma heating does appear as a real possibility. For short interaction lengths high density, high ν/γ, cold beams are required. High ν/γ leads to strong return current interaction. The work of PRONO et al. (1975) indicates that with a beam having $\nu/\gamma \sim 10$ the return current dissipation was the only significant heating mechanism and that energy densities $\sim 10^{19}$ eV cm^{-3} are obtainable at plasma densities $\sim 4.10^{15}$ cm^{-3}. This is to be compared with the work presented here showing $W_{OHM} \sim 1 \rightarrow 3.10^{18}$ eV cm^{-3} at similar densities but with $\nu/\gamma \sim 2.5$.

Experiments with low ν/γ and those with a pre-ionized target indicate very low W_{OHM} and total plasma energy densities $\lesssim 10^{17}$ eV cm^{-3}.

Generally j_b and ν/γ are varied simultaneously, hence it is necessary to establish the effect of each. In Table 6.1 the work reported here is compared with that performed at Physics International (P.I.) by PRONO et al. (1975). It can be seen that, with similar induced fields and plasma density, the P.I. experiment produced comparable plasma current densities yet achieved W_{OHM} some 3 → 10 times higher. This must be due to the different time histories of E_z and j_p. The P.I. group also attribute their anomalously high resistivity to an unspecified effect of non-linear e-e mode saturation and subsequent parametric decay. Such effects are likely to be stronger in their case due to a higher γ ($\gamma \sim 2$) which will tend to reduce modulation of the beam velocity distribution enabling beam electrons to remain in phase with the excited Langmuir waves for longer times. Consequently higher turbulence levels will be achieved.

TABLE 6.1 COMPARISON OF I.C. AND P.I. PARAMETERS

		I.C. (Al/my)	P.I.
I_B	kA	40 → 50	200
I_{NET}	kA	20 → 30	20 → 60
I_{PLASMA}	kA	10 → 20	140 → 180
j_b	$kAcm^{-2}$	10 → 15	5 → 13
j_p	$kAcm^{-2}$	3 → 6	3.5 → 4.5
ν/γ		2.4	4 → 10
$L\frac{\partial I_{NET}}{\partial t}$	Vm^{-1}	$\sim 2.5 \cdot 10^5$	$\sim 2.5 \cdot 10^5$
W_{OHM}	$eVcm^{-3}$	$1 \rightarrow 3 \cdot 10^{18}$	$\lesssim 1.5 \cdot 10^{19}$
a	cm	1	3.6

It is not clear which parameter has resulted in the stronger interaction at P.I. Clearly ν/γ only, cannot be assumed to be responsible; experiments which independently vary ν, γ, j_b and L are required.

6.2 Plasma Resistivity

Enhancement of plasma resistivity has been observed here and elsewhere and is generally attributed to the non-linear stages of the e-e mode primary interaction. In this work it has been demonstrated to be dependent upon the anode foil type and consequently the beam angular scatter. As it is well known that the scatter reduces the primary interaction strength, THODE (1976), GREENSPAN (1977), this result has been taken to imply that the return current resistivity is enhanced by the decay of primary Langmuir waves.

Recent work by DANGOR et al. (1979), on the same apparatus as used here, has shown that for injection at pressures $< 5.10^{-2}$ torr the different foil types not only change the beam scatter angle but also the number of fast ions accelerated axially from the anode. If such effects also occur at higher pressures (0.1 → 0.3 torr) then this could cause changes in the whole plasma evolution. This is because of the important role ions play in the early ionization stages of the target gas, see Section 1.5.

6.3 Conclusions

Interaction lengths orders of magnitude less than those predicted by binary collisions are obtainable with intense relativistic beams. This is due to collective effects, in particular, for strong beams, resistive dissipation of the induced plasma return current. Whilst enhancement of this dissipation rate by plasma turbulence, as is observed, is desirable it is not essential for the injection of intense beams into

toroidal geometries. Such experiments have been proposed by HAMMER and PAPADOPOULOUS (1975) and others and performed on small Tokamaks in Japan and U.S.A. with some success.

It has been shown here that a large energy transfer only occurs over a limited range of fill pressures of neutral gas. Below 0.1 torr, beam propagation is poor whilst above 0.3 torr the plasma resistivity drops too fast. The use of a preformed plasma target permits beam propagation at lower number densities but results in low energy transfer rates when $n_b << n_e$.

The use of cold beams certainly enhances the overall deposition rate, whilst a beam voltage higher than used here is necessary to increase the lengths over which a strong primary interaction will grow.

6.4 Future Work

In order to optimize the energy transfer rate a good theoretical model of beam-neutral gas interaction is required in which the ionization and turbulence are self consistently calculated.

Further work is required to establish the detailed effects of beam rise-time and beam velocity spread. Improved plasma confinement, especially axially, is needed to trap high-energy electrons which may be produced by the turbulence. Measurements of n_e, T_e, T_i at various axial positions are required to determine the length over which the interaction takes place. This could be done by moving the A-K gap into the interaction chamber rather than moving the diagnostics.

To expedite these experiments an "in vacuum" foil changer is desirable and also improved control of the gas fill pressure. With such a system, reproducibility would be improved and the firing rate limited by safe X-ray emission levels.

APPENDIX I

NEUTRAL PARTICLE CONFINEMENT

Radial diffusion of ions, neutrals and electrons across the axial magnetic field affects plasma energy confinement and plasma diamagnetism. In the plasma considered here the dominant collision for ions and neutrals is charge-exchange. The cross-section is ~ 10^{-18} m^2, an order of magnitude larger than any other. When the densities of ions and neutrals are comparable then any one particle spends a similar time as a neutral and an ion. Whilst an ion it is subject to the local macroscopic fields of the plasma. Diffusion theories of ions and neutrals in this regime must include this collision.

For the neutrals to be magnetically confined it is necessary for the effective Larmor radius of the ion/neutral orbit to be much less than the plasma dimensions. The effective Larmor radius is given by:

$$r_L^* = r_L \, (1 + {}^{n_n}/_{n_i}) \qquad \text{AI.1}$$

where r_L is the ion Larmor radius. Hence we require

$$\frac{(2k\ T\ m)^{\frac{1}{2}}}{e\ B} \; (1 + {}^{n_n}/_{n_i}) \ll 10^{-2} \qquad \text{AI.2}$$

for B ~ 1.3 T this reduces to

$$T^{\frac{1}{2}} \, (1 + {}^{n_n}/_{n_i}) \ll 92 \qquad \text{AI.3}$$

for T ~ 100 eV, as observed, confinement requires $n_n \lesssim n_i$. Further to this it is necessary that the neutral mean free path also be less than the plasma radius, i.e.

$$\lambda_{n\ mfp} \ll 10^{-2} \qquad \text{AI.4}$$

or for $\sigma_{ex} = 10^{-18}$

$$n_i \gg 10^{20} \quad m^{-3} \qquad \text{AI.5}$$

Consequently good confinement of ions and neutrals will only occur for $n_n \lesssim n_i \gg 10^{20}$. In the early stages of the plasma $n_i \lesssim 10^{20}$ and $n_n \gg n_i$ so that neutrals acquiring large energies via charge-exchange will be lost from the plasma, although heating of the background neutrals via neutral-neutral collisions will also occur. The majority of hot ions produced in the early stages will be lost in this manner and replaced by cold ones. As the neutral density falls and the ion density rises, the conditions for confinement will be approached stabilizing the plasma losses. Note however that the above condition is independent of the filling pressure, indicating that the moderate to late time plasma and neutral densities will always be similar.

The diffusion rate of the ion/neutral particles across the plasma may be estimated. However, as the ions and neutrals are to be treated as one particle, the ion-ion, neutral-neutral and elastic ion-neutral collisions all contribute little to diffusion, being self collisions. It is the charge-exchange collision which dominates.

In the case when the charge-exchange rate is slower than the ion cyclotron frequency, the direction of a neutral emerging from a collision is random. To find the neutral diffusion rate we have to sum random vectors - a normal diffusion problem. In the other extreme, when there are many charge-exchange collisions to a Larmor orbit, there is a degree of correlation between sequential vectors of the neutral motion. However, there is no long term correlation and the problem is identical to normal diffusion.

This last point was confirmed by numerical simulation. The simulation produced particle orbits in a uniform magnetic field and density. The r.m.s. distances moved by a particle were compared for

various ratios of collision frequency to cyclotron frequency. After many collisions the r.m.s. displacement appeared independent of this ratio confirming the necessity for correlations to be long term in order to have any effect.

The simulation used a random number generator to produce a number p in the range $0 \rightarrow 1$. When substituted into the equation:

$$\Delta t = - \text{Ln} (1 - p)/(n_j \sigma_{ex} v) \qquad \text{AI.6}$$

where σ_{ex} is the charge-exchange cross-section

v is the particle velocity

n_j is the particle density of the other species.

a time Δt with a distribution corresponding to that of the free path lengths was produced, i.e.:

$$p(\lambda) = \lambda_{mfp} \exp - (\lambda/\lambda_{mfp}) \qquad \text{AI.7}$$

The particle was then moved as an ion (neutral) for the time Δt in the applied magnetic field, then changed to a neutral (ion) and a new value of Δt obtained using the relevant choice of n_j. In this manner the particle orbit was calculated, see Fig. AI.1. Numerous runs with identical parameters, each of which produced different orbits, were averaged and compared to runs with differing ratios of mean free path and Larmor radius. This showed that for long enough times, i.e. more than about 3 orbits, increasing the magnetic field does not improve neutral particle confinement.

In the case of low collision frequency to mean free path length ratio, the diffusion constant may be calculated directly. In view of the above result it may then be applied more generally. In the case of a low collision frequency the particle will spend its time as an ion doing many circular orbits about a field line. As a neutral it will move off

at a tangent to the orbit for a distance generally much greater than the orbit size. Small changes in the free path length as an ion will result in large changes in the direction of the ensuing neutral. The overall effect is a random walk process with a "dead" time spent as an ion orbiting a field line. The apparent neutral motion will be a diffusion across the magnetic field with "dead" points at collision pairs. The diffusion constant is

$$D \sim \frac{L^2}{T} \qquad \text{AI.8}$$

where L is the step length and T the time for one step.

$$T = {}^{1}/(n_n\ \sigma_{ex}\ v) + {}^{1}/(n_i\ \sigma_{ex}\ v) = \frac{1}{\sigma_{ex} v}\left\{\frac{1}{n_n} + \frac{1}{n_i}\right\} \qquad \text{AI.9}$$

$$L = \lambda_{n\ mfp}$$

giving

$$D_m \sim \frac{(\lambda_{n\ mfp})^2\ \sigma_{ex}\ v}{({}^{1}/n_n + {}^{1}/n_i)} = \frac{n_n}{n_i(n_i + n_n)\ \sigma_{ex}} \frac{kT}{m} \qquad \text{AI.10}$$

This is truely the momentum diffusion rate as we are following one ion/neutral orbit. The neutral diffusion rate is simply

$$D_n \sim (\lambda_{n\ mfp})^2\ \sigma_{ex}\ v\ \ n_i \qquad \text{AI.11}$$

whilst the ion diffusion rate is

$$D_i \sim r_L^2\ \sigma_{ex}\ v\ n_n \qquad \text{AI.12}$$

(i.e. L is r_L not $\lambda_{i\ mfp}$)

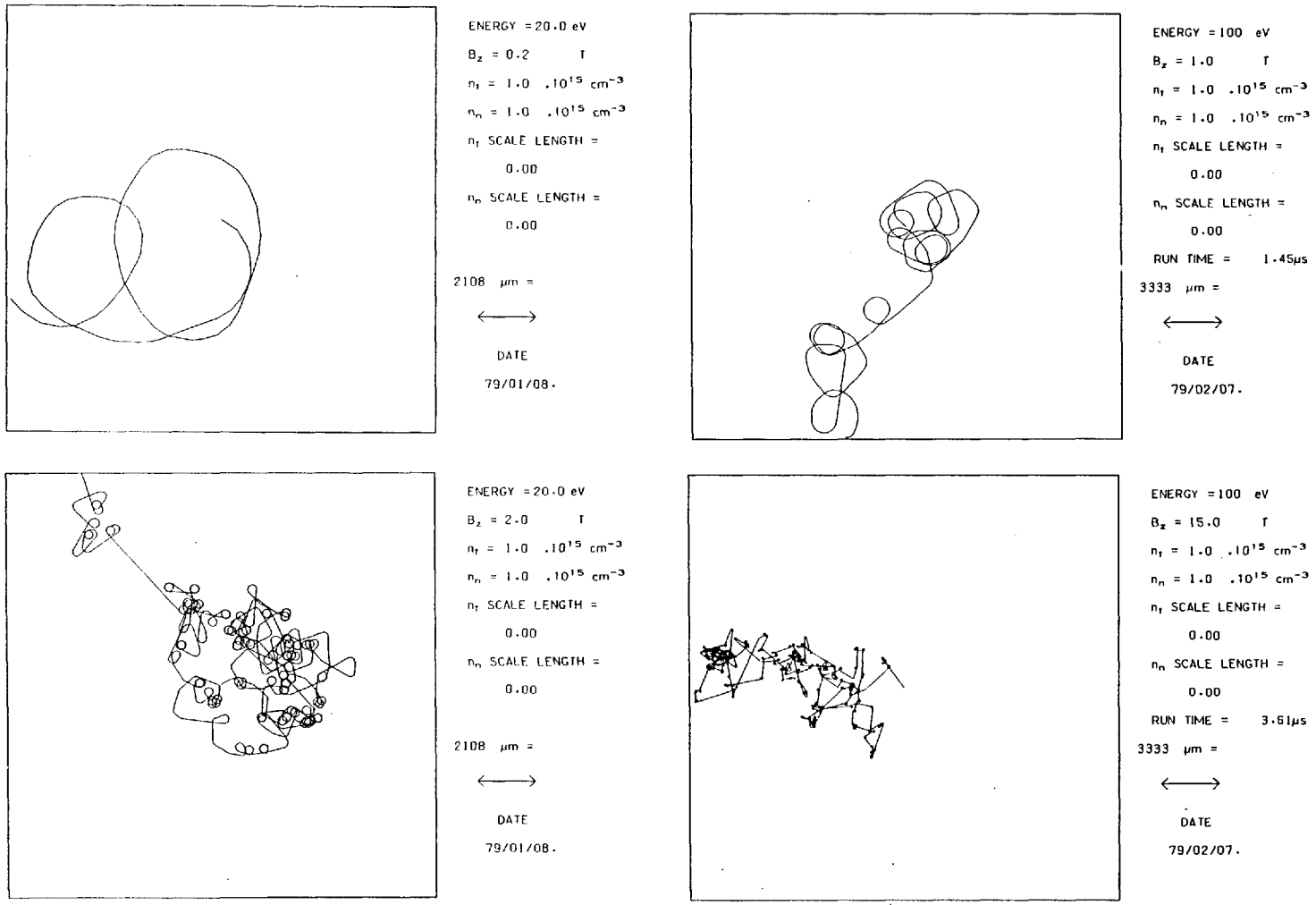

Fig. AI.1 Ion/neutral particle trajectories for various magnetic fields. n_n and n_i held constant.

APPENDIX II

THE EFFECT OF NEUTRALS ON THE MAGNETOSONIC WAVE VELOCITY

The normal expression for the velocity of Alfvén and magnetosonic waves is

$$v_A = B \left(\mu_o n_i m_i\right)^{-\frac{1}{2}} \qquad \text{AII.1}$$

giving a transit time across the plasma of

$$\tau_A = {}^{a}/_{v_A} \qquad \text{AII.2}$$

where a is the plasma size. In Chapter 5 the plasma oscillation is shown to be at $2a/v_A$.

In the presence of neutrals the mass loading $m_i n_i$ must be corrected. The dominant collision is the charge-exchange collision which will effectively reduce an ions momentum to zero. Two regimes must be distinguished.

$$\begin{aligned} &\underline{1} \qquad \tau_A >> \tau_{ex} \rightarrow m_i n_i + m_n n_n \\ &\underline{2} \qquad \tau_A \sim \tau_{ex} \rightarrow m_i n_i (1 + {}^{\tau A}/_{\tau_{ex}}) \end{aligned} \qquad \text{AII.3}$$

where τ_{ex} is the charge-exchange collision time for an ion. In case 1 the coupling between ions and neutrals is very strong and the neutrals move in phase with the ions. In case 2 the neutrals act as a momentum sink and ${}^{\tau A}/_{\tau_{ex}}$ is the number of collisions per wave transit. τ_{ex} is given by

$$\tau_{ex} = \frac{1}{n_n \sigma_{ex}} \sqrt{\frac{m_i}{2kT_i}} \qquad \text{AII.4}$$

This gives τ_A the form (case 2).

$$\tau_A = (\mu_o\, n_i\, m_i)^{\frac{1}{2}}\ \frac{a}{B}\left[n_n\, \sigma_{ex} \left(\frac{2kT_i}{m_i}\right)^{\frac{1}{2}} \tau_A + 1\right]^{\frac{1}{2}} \qquad \text{AII.5}$$

using the following values

$a = 10^{-2}$ m

$B = 1.6$ T

$\sigma_{ex} = 10^{-18}$ m^{-2}

yields

$$\tau_A^2 = 1{\cdot}11.10^{-51}\, n_i\, n_n\, T_i^{\frac{1}{2}}\, \tau_A + 7{\cdot}85.10^{-38}\, n_i$$

$$\tau_A = 5{\cdot}55.10^{-52}\, n_i\, n_n\, T_i^{\frac{1}{2}} + \left[3{\cdot}08.10^{-103}\, n_i^2\, n_n^2\, T_i + 7{\cdot}85.10^{-38}\, n_i\right]^{\frac{1}{2}} \qquad \text{AII.6}$$

Equation AII.6 is plotted (τ_A against T_i) for various values of n_i and n_n in Fig. AII.1. It can be seen that τ_A now goes as n_i instead of $n_i^{\frac{1}{2}}$ for $T_i \gtrsim 10$ eV and $n_i \gtrsim 10^{15}$ cm^{-3}. Values of $n_n \sim n_i$ should be used owing to the loss of neutrals, see Appendix I.

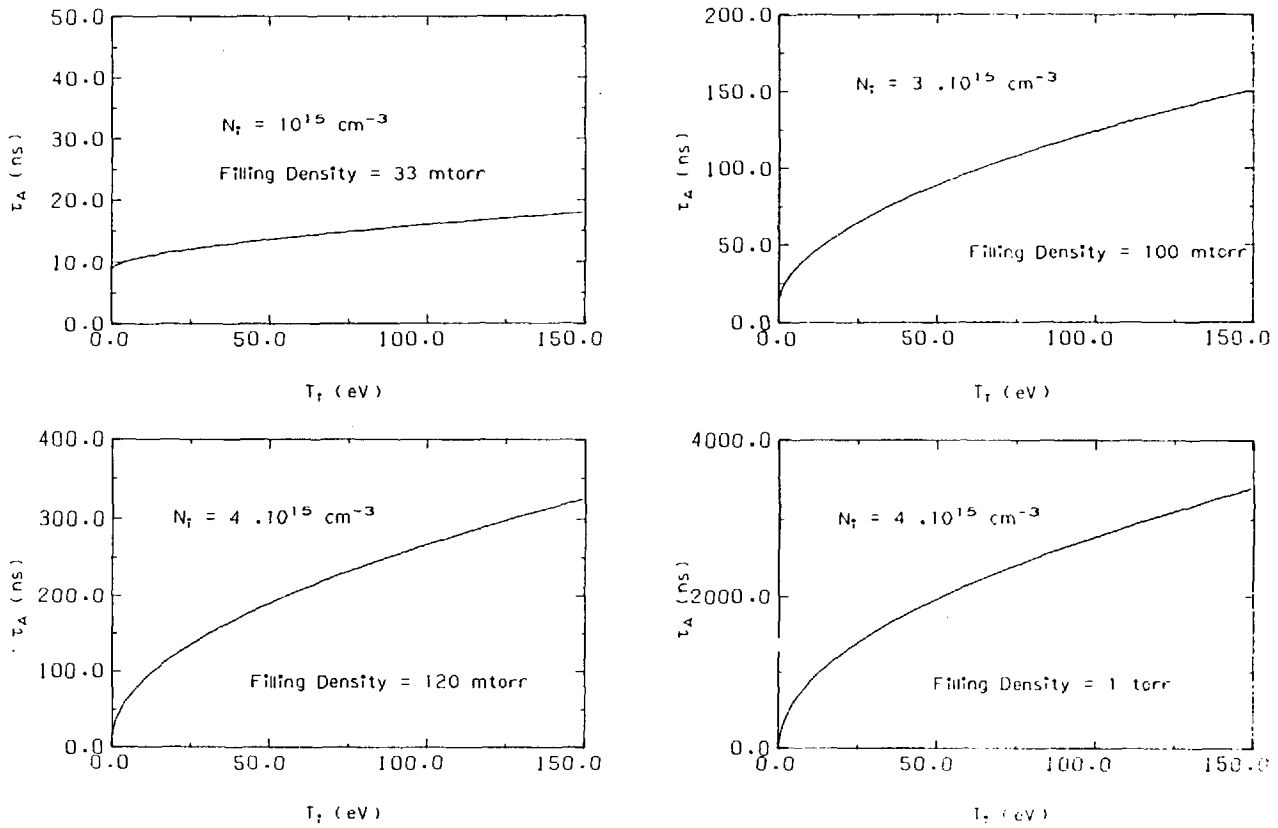

Fig. AII.1 Plot of τ_A versus T_i from Eqn. AII.6 for various n_i and n_n.

APPENDIX III

FOIL CLAMPING

Both the anode and Faraday cup foils have to be maintained taut and free from crinkles. This is achieved by making the internal diameter of the clamping ring equal to the mean diameter of the 'O' ring groove, see Fig. AIII.1.

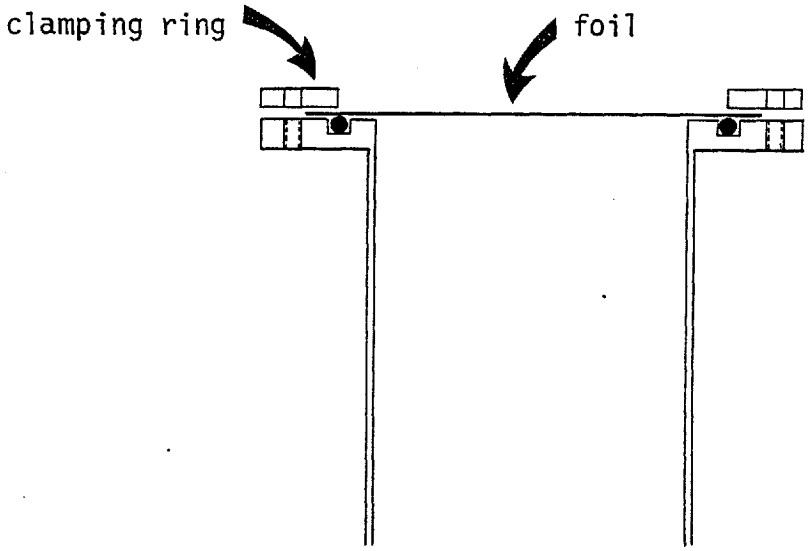

Fig. AIII.1 Diagram of foil clamp. The inner diameter of the clamping ring equals the mean diameter of the 'O' ring groove.

APPENDIX IV

BEAM SCATTERING

Most beam plasma interaction theories are in some way dependent upon scatter in the beam. Both variations in the direction of beam electrons and in their velocities parallel to the beam propagation direction are of interest. Beam electrons can gain momentum in the radial direction from acceleration in the $\underline{j}_b \wedge \underline{B}_\theta$ force. (Radial space-charge fields are shorted out in the diode by the proximity of the anode and cathode planes.) In a magnetized system this is significantly reduced. Two other processes degrade the beam, beam-foil scattering and scattering by the non-adiabatic discontinuity in the B_θ field at the anode.

Beam foil scattering is a well known process and produces a root mean square scattering angle, $\sqrt{\bar{\theta}^2}$, given by KAY and LABY (1959)

$$\sqrt{\bar{\theta}^2} = \theta_1 \, 2 \, \mathrm{Ln}(\theta_1/\theta_2)^{\frac{1}{2}} \quad \text{radians} \qquad \text{AIV.1}$$

where

$$\theta_1^2 = 4.019 \, . \, 10^{-13} \, (z/pv)^2 \, \rho \, \frac{z_t \, (z_t + 1)}{A_t} \, t \qquad \text{AIV.7}$$

and

$$\theta_2 = \frac{z_t^{1/3} \, \hbar}{p \, a_o} \qquad \text{AIV.8}$$

with

a_o = $5.3 \, . \, 10^{-9}$ cm

p = $m\beta\gamma c$

m_β = mass of incident particle at $v=\beta c$

z = charge of incident particle in units of e.

v = βc

ρ = specific gravity of target

Z_t = charge of target nucleii in units of e

A_t = mass Nr. of target nucleii

$\hbar$ = Plank's constant $/2\pi = 1.0546 \cdot 10^{-27}$ erg-secs.

c = velocity of light

t = target thickness

Units are c.g.s.

For an aluminium anode foil with a 350 keV beam

$\gamma = 1.7$ $\quad Z_t = 13$

$m = 9.10^{-28}$ $\quad A_t = 27$

$c = 3.10^{10}$ $\quad \rho = 2.7$

$\beta = 0.81$

gives $p = 3.712 \cdot 10^{-17}$

$\theta_2 = 1.2605 \cdot 10^{-2}$

$\theta_1^2 = 5.899\ t$

$\sqrt{\overline{\theta^2}}$ is plotted against t in Fig. AIV.1.

For an Al/My anode assuming the carbon atoms do most of the scattering

$Z_t = 12$ $\quad \theta_2 = 1.2273 \cdot 10^{-2}$

$A_t = 12$ $\quad \theta_1^2 = 4.21\ t$

$\rho \simeq 1$

Because of the returning plasma current, the value of B_θ post-anode is lower than in the diode. Consequently a discontinuity in the magnetic field occurs at the anode foil. The presence of the B_z guide field means that the field lines bend by an angle 'θ' as they pass through the foil. In addition B_θ is proportional to the radius so that the bending is radially dependent. The Larmor radius of the beam electrons is ~ 1.2 mm, much greater than the foil thickness, so that the discontinuity produces a non-adiabatic change in the electron trajectories.

It will be assumed that prior to the discontinuity $v_\perp \simeq 0$ and $v_\parallel \simeq v_0 = \beta c$. Beyond the foil $v_\parallel \simeq v_0 \cos\theta$ and $v_\perp \simeq v_0 \sin\theta$.

$$\theta = \mathrm{Tan}^{-1}(B_\theta/B_z) - \mathrm{Tan}^{-1}(B_\theta(1 - f_m)/B_2) \qquad \text{AIV.9}$$

where B_θ is the azimuthal field in the diode and f_m the degree of magnetic neutralization due to the plasma return current.

For a beam of radius 1 cm and current 50 kA, $B_\theta \simeq r(\mathrm{cm})$ tesla. The lowest value of f_m observed was ~ 0.5 for a 100 mtorr shot. After the discontinuity:

$$v_\perp = v_0 \,\mathrm{Sin}\left(\mathrm{Tan}^{-1}\frac{r}{aB_2} - \mathrm{Tan}^{-1}\frac{r(1 - f_m)}{aB_2}\right) \qquad \text{AIV.10}$$

$$v_\parallel = v_0 \,\mathrm{Cos}\left(\mathrm{Tan}^{-1}\frac{r}{aB_2} - \mathrm{Tan}^{-1}\frac{r(1 - f_m)}{aB_2}\right) \qquad \text{AIV.11}$$

Due to the finite Larmor radius of the electrons there is a spread in $v_\parallel$ at any one point in space given by

$$\Delta v_\parallel \simeq \frac{\partial v_\parallel}{\partial r}\, r_L$$

using the above equation for $v_\parallel(r)$ this yields

$$\Delta v_\parallel \simeq -v_0\, r_L\left[\mathrm{Sin}\left(\mathrm{Tan}^{-1}\frac{r}{aB_2} - \mathrm{Tan}^{-1}\frac{r(1 - f_m)}{aB_2}\right)\right]\cdot\left[\frac{aB_2}{a^2B_2^2 + r^2} - \frac{aB_2(1 - f_m)}{a^2B_2^2 + r^2(1 - f_m)^2}\right] \qquad \text{AIV.12}$$

for $r \le a$

If prior to the discontinuity $v_\perp \neq 0$ then the process becomes one of scattering as the phase of the azimuthal velocity component will be random at the discontinuity.

Equation AIV.12 is plotted in Fig. AIV.2 in the form $(\Delta v_\parallel / v_\parallel)$ versus r for various values of f_m. B_z is fixed at 1.6 T, I_B at 50 kA.

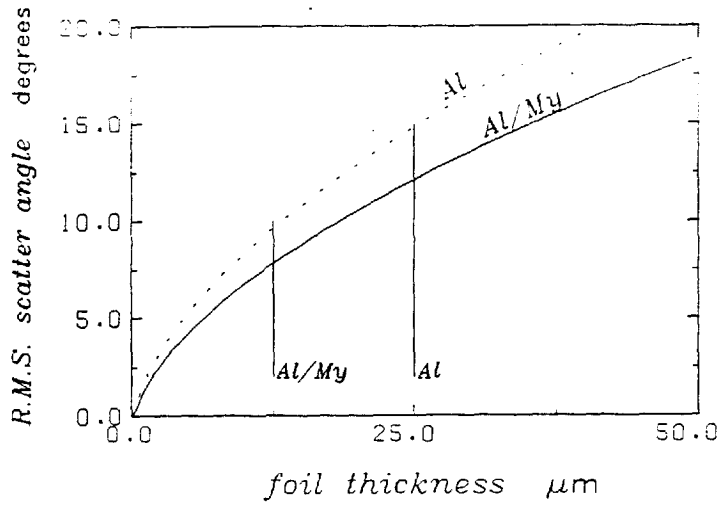

Fig. AIV.1 Plot of R.M.S. beam scatter angle, $\sqrt{\bar{\theta}^2}$, versus foil thickness, t, for Al/My and Al foils.

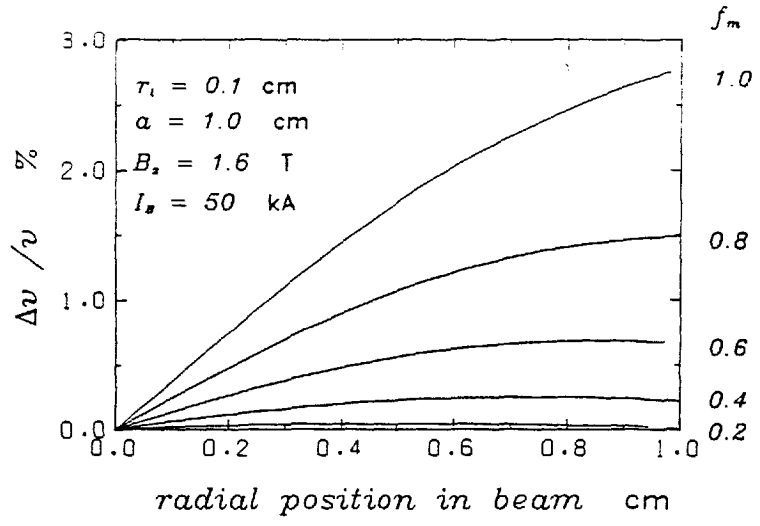

Fig. AIV.2 Plot of $^{\Delta v_{\perp}}/_{v_{\parallel}}$ versus r for a range of f_m. B_z = 1.6 tesla, I_{BEAM} = 50 kA.

APPENDIX V

SELF FOCUSSING IN THE DIODE

In the absence of an applied B_z field intense electron beams may self focus in the diode under the $\underline{j}_z \wedge \underline{B}_\theta$ force. The close proximity of the plane anode and cathode surfaces effectively short circuits the radial space-charge electric field. A simple criterion which gives useful results in determining if a diode will pinch in this manner is obtained by comparing the Larmor radius of a peripheral electron with the A - K gap, s.

i.e. $r_L < s$ for pinching

$$r_L = \frac{mv}{e\,B_\theta} = \frac{m\gamma\beta c}{e\,B_\theta} \qquad \text{AV.1}$$

$$B_\theta = \frac{\mu_0\, j\, a}{2} \qquad \text{AV.2}$$

where j is the beam current density and a the beam radius.

$$j = 9362\, V^{3/2}\, s^{-2} \qquad \text{AV.3}$$

where V is the applied voltage in megavolts. This is a relativistically corrected formula for the Child-Langmuir space-charge limited current flow in a planar diode. It is only valid for $V \sim 0.5$. Values of the relativistic correction factor are given by M.J. GOODMAN (1968). Hence for pinching we have

$$\frac{2\, m\gamma\beta c\, s^2}{9362\, e\, \mu_0 a\, V^{3/2}} < s \qquad \text{AV.4}$$

or $\frac{a}{s} > 9.56 \cdot 10^{-2}\, \gamma\beta V^{-3/2}$

$$\frac{a}{s} > 0.1912\, \frac{\sqrt{V+1}}{V} \quad \text{for } v \sim 0.5 \qquad \text{AV.5}$$

APPENDIX VI

OSCILLATOR STRENGTHS FOR HYDROGEN LINES

(Calculated from L.C. JOHNSON (1972))

LYMAN SERIES

n'	$f_{1n'}$	$\lambda(\mathring{A})$	
2	.416	1215.68	L_α
3	.079	1025	L_β
4	.029	972	L_γ
5	.014	949	
6	.0078	937	
7	.0048	911	

BALMER SERIES

n'	$f_{2n'}$	$\lambda(\mathring{A})$	
3	.641	6562.85	H_α
4	.119	4861.33	H_β
5	.045	4340	H_γ
6	.022	4101	
7	.013	3970	
	$\lim_{n'\to\infty}$	3646	

PASCHEN SERIES

n'	$f_{3n'}$	$\lambda(\mathring{A})$
4	.842	18746
5	.151	12815
6	.056	10935
7	.028	10047
8	.016	9543

9	.010	9227
	$\lim_{n' \to \infty}$	8201

$$\lim_{n' \to \infty} f_{nn'} \doteq 1.95 \frac{n}{n'^3}$$

APPENDIX VII

NUMERICAL INTEGRATION OF ENERGY BALANCE EQUATIONS

The following is the Fortran program used to integrate the energy balance equations, see Chapter 5. The program was run interactively on a CDC Cyber 174.

```
      PROGRAM RUN(INPUT,OUTPUT,TAPE5=INPUT,TAPE6=OUTPUT,TAPE7,TAPE8,
     +TAPE9)
C     THIS PROGRAM BASICALLY JUST CALLLS SUBROUTINE ENGBAL
C     THE ENERGY BALANCE ROUTINE WHICH INTEGRATES AN ENERGY
C     BALANCE EQATION.
C     MOST PARAMETERS ARE GIVEN DEFAULT VALUES IN THIS PROGRAM
C     THE VARIABLE NAMES REPRESENT THE FOLLOWING QUANTITIES
C
C
C     TE          =ELECTRON TEMPERATURE
C     NE          =ELECTRON NUMBER DENSITY
C     T           =TIME
C     E           =TOTAL ENERGY CONTENT
C     BZ          =Z MAGNETIC FIELD
C     TSTOP       =RUN TIME
C     DELTAT      =TIME STEP
C     NFILL       =FILLING DENSITY
C     NESTART     =INITIAL ELECTRON NUMBER DENSITY
C     TESTART     =INITIAL ELECTRON TEMPERATURE
C     TSTART      =INITIAL TIME
C     RM          =ION MASS
C     RME         =ELECTRON MASS
C     EICOL       =ELECTRON ION COLLISION FREQUENCY
C     TI          =ION TEMPERATURE
C     DELTAZ      =SCALE LENGTH FOR THERMAL CONDUCTION
C     LNEI        =ELECTRON ION PLASMA PARAMETER
C
C
C     THE FOLLOWING ARE FUNCTIONS WHICH CONTRIBUTE TO THE ENERGY BALANCE
C
C     ETAJSQ      =RETURN CURRENT ENERGY INPUT  J.E
C     PLINE       =ENERGY LOST BY LINE RADIATION
C     PBREM       =ENERGY LOST BY BREMSTAUHLUNG
C     PCOND       =ENERGY LOST BY THERMAL CONDUCTION
C     PEQ         =ENERGY GAINED BY ELECTRON ION EQUIPARTITION
C     SI          =IONIZATION RATE COEFFICIENT
C
C
C     THE VALUES OF THESE FUNCTIONS ARE HELD IN THE FOLLOWING
C     VARIABLES FOR USE IN THE INTEGRATION AND IN THE OUTPUT
C
C     ETAJSV
C     PLINEV
C     PBREMV
C     PCONDV
C     PEQV
C     SIV
C
C
C
C      DATA FOR THE FUNCTIONS SI AND ETAJSQ IS STORED ON TAPES 7 AND 8
C      TAPE7 FOR ETAJSQ
C      TAPE8 FOR SI
C
C      FOR TAPE8 THE FORMAT IS AS FOLLOWS
C
C      1ST. LINE      TITLE   THIS IS READ IN IN A FORMAT  MAX 80 CHARACTERS
C      2ND. LINE      NUMBER OF DATA PAIRS   THIS IS FORMAT FREE
C      REMAINING LINES CONTAIN THE DATA PAIRS
C      FREE FORMAT   TEMPERATURE FIRST  THEN  IONIZATION RATE COEFFICIENT
C
C      THE TITLE IS STORED IN ARRAY TITLEI(8)
C      THE NUMBER OF DATA PAIRS IS STORED AS NIONR
```

```
C       THE DATA IS READ INTO ARRAYS IONRTE , FOR THE TEMPERATURE, AND
C                                    IONRV, FOR THE IONIZATION RATE COEFFICIENT
C
C
C       FOR TAPE7 THE FIRST LINE AGAIN CONTAINS THE TITLE (TITLEW)
C       THE SECOND LINE CONTAINS THE FILLING DENSITY  FORMAT FREE
C       THE THIRD LINE CONTAINS THE NUMBER OF DATA PAIRS (NWOHM)
C       FORMAT FREE
C       THE NEXT NWOHM LINES CONTAIN THE DATA PAIRS IN FREE FORMAT
C       FIRST THE TIME  (WOHMT)
C       THEN THE VALUE OF J.E  (WOHMV)
C
C
C
C       TAPE7 MAY CONTAIN ANY NUMBER OF SUCH DATA SETS AS DESCRIBED ABOVE
C
C       TAPES 7 SAND 8 ARE READ BY SUBROUTINE INPUT3 ONLY
C       THE DIFFERENT DATA SETS MAY BE RUN WITH THE SAME OR DIFFERENT
C       INITIAL CONDITIONS
C       IF THE BOTTOM OF TAPE 7 IS REACHED AND ANOTHER RUN IS ATTEMPTED
C       A RUN COMPLETE PROMPT IS PRINTED
C
C       PRIOR TO RUNNING A DATA SET ITS TITLE IS DISPLAYED AND INITIAL
C       DATA IF REQUIRED IS REQUESTED
C
C
C
C
      COMMON/ONE/TESTART,NESTART,DELTAT,NFILL,TSTOP,BZ,TE,NE
     +,T,E,I,TSTART
      REAL NFILL,NESTART
      TSTOP=.2
      DELTAT=.05*1.0E-9
      TESTART=20
      NESTART=1.E13
      BZ=15000
      CALL ENGBAL
      PRINT 3000
 3000 FORMAT("RUN COMPLETE")
      REWIND 9
      STOP
      END
C*************************************************************************
C
C
C
C
      SUBROUTINE ENGBAL
C       THIS IS THE MAIN ROUTINE. IT INTEGRATES THE ENERGY BALANCE
C       EQUATION.
C       INPUT3 IS CALLED TO READ IN DATA FOR THE IONIZATION RATES
C       AND THE RETURN CURRENT DEPOSITION.
C       INPUT2 THEN READS IN THE INITIAL CONDITIONS, THE TIME STEP
C       AND THE RUN TIME.
C       FULL PROMPTS ARE GIVEN AND THE FORMAT FOR ALL TERMINAL DATA
C       INPUT IS FREE.
C       THE ROUTINE THEN INITIALIZES THE VARIABLES NE, TE, T.
C
C       THE VALUES OF TSTOP, DELTAT AND THE NUMBER OF INTEGRATION
C       STEPS ARE PRINTED
C
C       THE PROGRAM THE REQUESTS THE OUTPUT DATA FREQUENCY (NFEQ)
C       THIS IS THE NUMBER OF INTEGRATION STEPS BETWEEN EACH OUTPUT
C       OF T, TE, NE, ETC.  WHICH AREWRITTEN WRITTEN ONTO TAPE9.
```

```
C       TAPE9 IS INITIALLY LABELED BY SUBROUTINE LABEL
C       THIS WRITES OUT THE INITIAL CONDITIONS, THE TIME STEP, ETC
C
C
C       THE FUNCTIONS INTEGRATED ARE  "NEDOT" AND  "TEDOT"
C
C
C
C
      COMMON/ONE/TESTART,NESTART,DELTAT,NFILL,TSTOP,BZ,TE,NE
     +,T,E,I,TSTART
      REAL NE,NFILL,NESTART,NEDOTE,LNEI,NEDOT,NENEW
C
C
      COMMON/TWO/WOHMT(20),WOHMV(20),IONRTE(20),IONRV(20),TITLEW(8),
     +TITLEI(8),NWOHM,NIONR,W(21),D(21)
C
C
      COMMON/FOUR/ETAJSV,PLINEV,PEQV,PBREMV,
     +PCONDV,SIV
C
C
      REAL IONRTE,IONRV
C
C
      COMMON/THREE/OSCST(500)
C
C
C
   46 CALL INPUT3
      CALL INPUT2
C
C
C
C       CALCULATE ALL THE OSCILLATOR STRENGTHS
C
      CALL OSCSTC
C
C     INITIALIZATION
C
      NE=NESTART
      TE=TESTART
      T=TSTART
C
C
      WRITE(6,2001)TSTOP,DELTAT
 2001 FORMAT("ENGBAL   TSTOP=",F8.1,"  DELTAT=   ",F5.2)
C
C
      N=((TSTOP-TSTART)/DELTAT)+0.5
      WRITE(6,3000)N
 3000 FORMAT("ENGBAL  N= ",I10)
      DELTAT=DELTAT*1.0E-9
      PRINT 6000
 6000 FORMAT("ENTER OUTPUT DATA FREQUENCY TO TAPE9 AND TO TERMINAL "
     +/"2 NUMBERS")
      READ,NFEQ,NFEQ6
      CALL LABEL
C
C    ENTER  MAIN  INTEGRATING  DO  LOOP
C
      DO 1 I=1,N-1
      IF(  TE  .LE.  0.0  )  GO TO 44
C    ABORT  ON  NEGATIVE  TEMPERATURE
```

```
      E=NE*TE
      TEDOTE=TEDOT(NE,TE,T)
      NEDOTE=NEDOT(NE,TE)
      IF((TE+DELTAT*TEDOTE)    .LT.    0.0    ) GO TO 43
C     ABORT  ON  NEGATIVE  TEMPERATURE  ESTIMATE
      NENEW=NE+0.5*DELTAT*(NEDOTE+NEDOT(NE+DELTAT*NEDOTE,TE
     ++DELTAT*TEDOTE))
      TENEW=TE+0.5*DELTAT*(TEDOTE+TEDOT(NE+DELTAT*NEDOTE,
     +TE +DELTAT*TEDOTE,T+DELTAT))
      IF(  MOD(I-1,NFEQ)   .EQ.   0)    CALL OUTPUT
      IF(MOD(I-1,NFEQ6) .EQ. 0) WRITE(6,9998) T,TE,NE
 9998 FORMAT("TIME",11X,"=",E9.3,"SECS"/
     +       "TEMPERATURE     =",E9.3,"EV"/
     +       "NUMBER DENSITY =",E9.3,"CM-3")
      TE=TENEW
      NE=NENEW
    1 T=T+DELTAT
C
C
C
      GO TO 5
C
C
C
C     ABORT  OUTPUT  INDICATION
   44 PRINT 4000
 4000 FORMAT("NEGATIVE TEMPERATURE HALTED RUN")
      GO TO 5
   43 PRINT 3001
 3001 FORMAT("NEGATIVE TEDOTE HALTED RUN")
      CALL OUTPUT
C
C
C     OUTPUT  DATA
    5 CALL EXTRA
      PRINT 3002
 3002 FORMAT("DO YOU WISH TO RUN NEXT DATA FILE"/"CR = NO")
      READ(5,5665) AGAIN
      IF(EOF(5)) 45,46,45
   45 PRINT,"DO YOU WISH TO RERUN THIS DATA SET  CR=NO"
      READ(5,5665) AGAIN
      IF(EOF(5)) 5432,6543,5432
 5665 FORMAT(A10)
 6543 REWIND 7
      GO TO 46
 5432 CONTINUE
      RETURN
      END
C*****************************************************************************
C
C
C
C
C
C
C
      FUNCTION PBREM(ANE,ATE)
      PBREM=1.06*(1.E-13)*ANE*ANE*SQRT(ATE)
 1000 FORMAT("PBREM= ",E8.2)
      RETURN
      END
C*****************************************************************************
C
C
```

```
C
      FUNCTION PEQ(ANE,ATE,AT)
      REAL LNEI
      LNEI=9.
      RMI=1.6726*(1.E-24)
      RME=9.1095*(1.E-28)
      EICOL=1.8*(1.E-19)*SQRT(RMI*RME)*ANE*LNEI/((RMI*ATE)**(1.5))
      TI=120.0*EXP(-EICOL*AT)+ATE
      PEQ=9.0*ANE*ANE/ATE**1.5*3.23*(1.E-9)*(TI-ATE)
      RETURN
      END
C*******************************************************************************
C
C
      FUNCTION PLINE(ANE,ATE)
C
C       THIS FUNCTION USES OSCILLATOR STRENGTHS FOUND BY OSCSTC
C
      COMMON/ONE/TESTART,NESTART,DELTAT,NFILL,TSTOP,BZ,TE,NE
     +,T,E,I,TSTART
      REAL NE,NFILL,NESTART,NEDOTE,LNEI,NEDOT
      COMMON/TWO/WOHMT(20),WOHMV(20),IONRTE(20),IONRV(20),TITLEW(8),
     +TITLEI(8),NWOHM,NIONR,W(21),D(21)
      COMMON/FOUR/ETAJSV,PLINEV,PEQV,PBREMV,
     +PCONDV,SIV
      REAL M,IONRTE,IONRV
      COMMON/THREE/OSCST(500)
      TOT=0.0
      DO 2 K=3,20
      M=FLOAT(K)
      SUM=(OSCST(K)*(M**4.)/(4.*(M**4-1.0)))/EXP(13.53/ATE*(1.0-
     +1.0/(M**2)))
      TOT=TOT+SUM
      IF(SUM.LT.(TOT*1.E-4))GO TO 3
    2 CONTINUE
    3 PLINE=ANE*(NFILL-ANE)*1.6*1.E-5/SQRT(ATE)*TOT
      RETURN
      END
C*******************************************************************************
C
C
      SUBROUTINE OSCSTC
      COMMON/THREE/OSCST(500)
      OSCST(3)=0.079
      OSCST(4)=0.029
      OSCST(5)=0.014
      DO 1 KK=6,500
    1 OSCST(KK)=1.56/FLOAT(KK*KK*KK)
      RETURN
      END
C*******************************************************************************
C
C
C
      REAL FUNCTION NEDOT(ANE,ATE)
      COMMON/ONE/TESTART,NESTART,DELTAT,NFILL,TSTOP,BZ,TE,NE
     +,T,E,I,TSTART
      REAL NE,NFILL,NESTART,NEDOTE,LNEI
      NEDOT=ANE*(NFILL-ANE)*SI(ATE)
      RETURN
      END
C*******************************************************************************
C
C
```

```
      FUNCTION TEDOT(ANE,ATE,AT)
      COMMON/ONE/TESTART,NESTART,DELTAT,NFILL,TSTOP,BZ,TE,NE
     +,T,E,I,TSTART
      REAL NE,NFILL,NESTART,NEDOTE,LNEI,NEDOT
      COMMON/FOUR/ETAJSV,PLINEV,PEQV,PBREMV,
     +PCONDV,SIV
      HION=13.53
      ETAJSV=ETAJSQ(AT)
        PEQV=   PEQ(ANE,ATE,AT)
      PLINEV=  PLINE(ANE,ATE)
      PCONDV= PCOND(ANE,ATE)
      PBREMV=  PBREM(ANE,ATE)
         SIV=     SI(ATE)
       TEDOT=(2.0/(3.0*ANE))*(ETAJSV+
     +       PEQV-PLINEV-PCONDV-PBREMV)
     +       -(ATE    +2.0*HION/3.0)*SIV*(NFILL-ANE)
      RETURN
      END
C*******************************************************************************
C
C
C
      FUNCTION PCOND(ANE,ATE)
      COMMON/ONE/TESTART,NESTART,DELTAT,NFILL,TSTOP,BZ,TE,NE
     +,T,E,I,TSTART
      REAL NE,NFILL,NESTART,NEDOTE,LNEI,NEDOT
      RME=9.1095*1.E-28
      DELTAZ=7.0
      RMI=1.6726*1.E-24
      LNEI=9.
      PCOND=(2.16*1.E+20*ATE**3.5+9.97*1.E-4*ANE*ANE*LNEI*
     +SQRT(RMI/RME*ATE)/BZ/BZ)/DELTAZ/DELTAZ
      RETURN
      END
C*******************************************************************************
C
C
C
      SUBROUTINE LABEL
      COMMON/ONE/TESTART,NESTART,DELTAT,NFILL,TSTOP,BZ,TE,NE
     +,T,E,I,TSTART
      REAL NE,NFILL,NESTART,NEDOTE,LNEI,NEDOT
      COMMON/TWO/WOHMT(20),WOHMV(20),IONRTE(20),IONRV(20),TITLEW(8),
     +TITLEI(8),NWOHM,NIONR,W(21),D(21)
      COMMON/FOUR/ETAJSV,PLINEV,PEQV,PBREMV,
     +PCONDV,SIV
      REAL IONRTE,IONRV,NT
      WRITE(9,2000) TITLEI
      WRITE(9,1001) TESTART,NESTART,BZ,DELTAT,NFILL,TSTOP,TSTART
 1001 FORMAT("INITIAL TE=",E9.2/"INITIAL NE=",E9.2/"BZ=",8X,F9.2/
     +"TIMESTEP  =    ",E10.3/"NFILL      =    ",E10.3/
     +"RUN TIME  =    ",E10.3/"INITIAL T  =    ",E10.3,"SECS"//////)
C
C
 2000 FORMAT(8A10)
      WRITE(9,3000)
 3000 FORMAT("   TIME       TE            NE            J.E        PCOND
     +PLINE          PION          PEQ           ETA")
      WRITE(9,4000)
 4000 FORMAT("    NS        EV          CM-3                              EV/CC
     +/SEC                            OHM-CM"//)
      RETURN
      END
C*******************************************************************************
```

```
      SUBROUTINE OUTPUT
      COMMON/ONE/TESTART,NESTART,DELTAT,NFILL,TSTOP,BZ,TE,NE
     +,T,E,I,TSTART
      REAL NE,NFILL,NESTART,NEDOTE,LNEI,NEDOT
      COMMON/TWO/WOHMT(20),WOHMV(20),IONRTE(20),IONRV(20),TITLEW(8),
     +TITLEI(8),NWOHM,NIONR,W(21),D(21)
      COMMON/FOUR/ETAJSV,PLINEV,PEQV,PBREMV,
     +PCONDV,SIV
      REAL IONRTE,IONRV,NT
      NT=T/1.E-9
      SIVM=SIV*(NFILL-NE)*13.53*NE
      SQTE=SQRT(TE)
        ETA=5.27*1.E-4*(NFILL/NE -1.0)*SQTE
     +     +4.68*1.E-2/(TE*SQTE)
    1 WRITE(9,5000)NT,TE,NE,ETAJSV,PCONDV,
     +PLINEV,SIVM,PEQV,ETA
 5000 FORMAT(F6.2,X,E9.3,7(3X,E9.3))
      RETURN
      END
C*******************************************************************************
      SUBROUTINE EXTRA
      COMMON/ONE/TESTART,NESTART,DELTAT,NFILL,TSTOP,BZ,TE,NE
     +,T,E,I,TSTART
      REAL NE,NFILL,NESTART,NEDOTE,LNEI,NEDOT,NT
      NT=T/1.E-9
      WRITE(9,7000)NT,TE,NE
      WRITE(6,9999)T,TE,NE
 9999 FORMAT("SUBROUTINE EXTRA"/"TIME              =",E9.3,"NS"/
     +"TEMPERATURE     =",E9.3,"EV"/
     +"NUMBER DENSITY =",E9.3,"CM-3"/)
 7000 FORMAT(F5.2,X,E9.3,3X,E9.3//////////)
      RETURN
      END
C*******************************************************************************
C
C
      FUNCTION ETAJSQ(AT)
      COMMON/TWO/WOHMT(20),WOHMV(20),IONRTE(20),IONRV(20),TITLEW(8),
     +TITLEI(8),NWOHM,NIONR,W(21),D(21)
      REAL IONRTE,IONRV
      IG=NWOHM+1
      CALL E01ADF(NWOHM-1,AT,WOHMT,WOHMV,W,D,IG,VAL)
      IF(VAL .LT. 1.E23)VAL=1.E23
      ETAJSQ=VAL
C      NOTE THAT UNITS FOR ETAJSQ ARE EV/CC/SEC
      RETURN
      END
C*******************************************************************************
C
C
C
      FUNCTION SI(ATE)
      COMMON/TWO/WOHMT(20),WOHMV(20),IONRTE(20),IONRV(20),TITLEW(8),
     +TITLEI(8),NWOHM,NIONR,W(21),D(21)
      REAL IONRTE,IONRV
      IG=NIONR+1
      CALL E01ADF(NIONR-1,ATE,IONRTE,IONRV,W,D,IG,VAL)
      SI=VAL
      RETURN
      END
C*******************************************************************************
C
C
```

```
      SUBROUTINE INPUT2
      COMMON/ONE/TESTART,NESTART,DELTAT,NFILL,TSTOP,BZ,TE,NE
     +,T,E,I,TSTART
      REAL NFILL,NESTART
      PRINT 1004
 1004 FORMAT(A10)
      READ(5,1004) CHANGE
      IF(EOF(5))10,11,10
   11 CONTINUE
      PRINT 1000
 1000 FORMAT("ENTER RUN TIME AND TIMESTEP BOTH IN NS")
    6 READ,TSTOP,DELTAT
      PRINT 1009
 1009 FORMAT("ENTER INITIAL TIME IN NS"/"CR=0.0")
      READ,TSTART
      IF( EOF(5))13,14,13
   13 TSTART = 0.0
   14 IF(DELTAT .LT. TSTOP-TSTART)GO TO 5
      PRINT 1007
 1007 FORMAT("TIMESTEP LONGER THAN RUN TIME   TRY AGAIN")
      GO TO 6
    5 PRINT 1001
 1001 FORMAT("ENTER INITIAL TEMP IN EV")
      READ,TESTART
      PRINT 1002
 1002 FORMAT("ENTER INITIAL NE")
    3 READ,NESTART
    2 IF( NESTART .LT. NFILL ) GO TO 4
      PRINT 1005
 1005 FORMAT("NE IS GREATER THAN FILLING DENSITY,
     + TRY AGAIN")
      GO TO 3
    4 PRINT 1006
 1006 FORMAT("ENTER BZ IN GAUSS")
      READ,BZ
      TSTART=TSTART*1.E-9
      GO TO 12
   10 DELTAT=DELTAT*1.0E9
   12 RETURN
      END
C*****************************************************************
C
C
C
      SUBROUTINE INPUT3
      COMMON/ONE/TESTART,NESTART,DELTAT,NFILL,TSTOP,BZ,TE,NE
     +,T,E,I,TSTART
      REAL NE,NFILL,NESTART,NEDOTE,LNEI,NEDOT,NENEW
      COMMON/TWO/WOHMT(20),WOHMV(20),IONRTE(20),IONRV(20),TITLEW(8),
     +TITLEI(8),NWOHM,NIONR,W(21),D(21)
      REAL IONRTE,IONRV
C
C     DATA FOR WOHM ON TAPE7
C     DATA FOR IONR ON TAPE8
      REAL IONR
      REWIND 8
      READ(7,1001) (TITLEW(IP),IP=1,8)
      WRITE(6,1001) (TITLEW(IP),IP=1,8)
      WRITE(9,1001) (TITLEW(IP),IP=1,8)
      IF(EOF(7))  1,2,1
 1001 FORMAT(8A10)
    1 PRINT 103
  103 FORMAT("NO MORE WOHM DATA")
      STOP
    2 READ(8,1001) (TITLEI(IP),IP=1,8)
      READ(7,)NFILL
      READ(7,)NWOHM
      READ(8,)NIONR
C
C    NWOHM=NUMBER OF WOHM POINTS.
C     NIONR=NUMBER O IONR POINTS
C
      DO 10 IK=1,NWOHM
   10 READ(7,)WOHMT(IK),WOHMV(IK)
      DO 11 IK=1,NIONR
   11 READ(8,)IONRTE(IK),IONRV(IK)
  101 FORMAT(E8.2,3X,E8.2)
      RETURN
      END
```

APPENDIX VIII

INJECTION INTO A PREFORMED PLASMA

AVIII.1 The Target Plasma

The z-discharge plasma was diagnosed with laser scattering using the system described in Chapter 4. The fill pressure varied from 30 → 100 mtorr of hydrogen, corresponding to atomic densities of $2 \rightarrow 6.67 \cdot 10^{21}$ m^{-3}. Temperatures varied from 3 → 6 eV and electron densities were ~ $1 \rightarrow 4.7 \cdot 10^{21}$ m^{-3}. The density depended on both the fill pressure and the time since initiation of the discharge. It usually peaked at ~ 30 μs, with a maximum of ~ 60% ionization. The applied magnetic field of 2 → 2.5 tesla prevented the discharge current channel pinching and enhanced the breakdown rate. The magnetic fields used were generally higher than used for the neutral gas measurements due to the better penetration of the field through the glass wall (compared to the stainless-steel wall).

The beam was fired into the plasma afterglow, about 40 μs after the start of the z-discharge current which had fallen to ~ 200A at this time.

AVIII.2 Diagnostics and Results

The diagnostics were restricted to laser scattering, beam current and net current at two radii. Laser scattering indicated that at the end of the beam pulse the density had dropped from ~ 3.10^{21} to ~ $1.4 \cdot 10^{21}$ m^{-3} whilst the temperature had risen from ~ 5 to 15 eV.

Measurements of the net current just outside the chamber wall, made with a Rogonski coil, indicated near zero currents. However, by removing the foil from the Faraday cup net current measurements at a 2 cm radius were made. Typical currents were ~ 1.5 kA. The beam was

found to propagate well with no indication of unneutralized current flow as observed for neutral gas injection. Typical traces of beam and net currents taken from sequential shots are shown in Fig. AVIII.1.

As it was not possible to measure the beam and net currents simultaneously W_{OHM} has not been calculated. The small multiturn probe was not available at this time and may have given ambiguous results due to disturbance of the current flow paths.

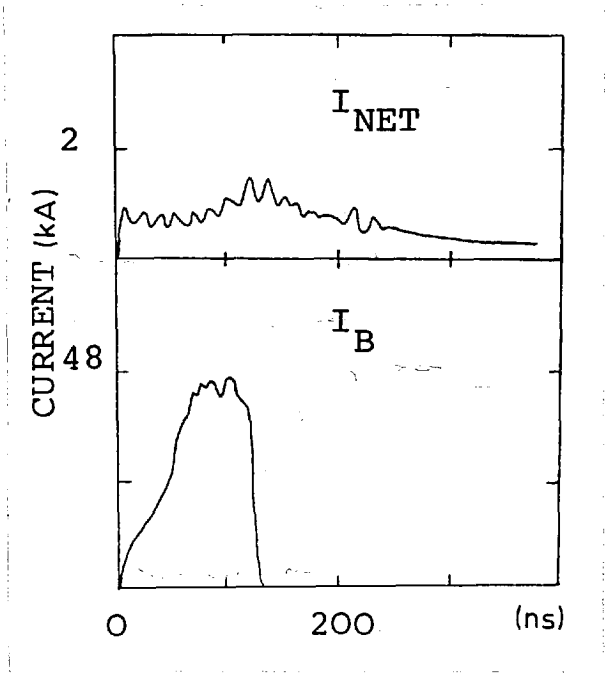

Fig. AVIII.1 Example waveforms of I_{NET} (r=2cm) and I_{BEAM} for injection into a preformed plasma. Traces are from sequential shots. Note the lack of an unneutralized current - compare with Fig. 4.8.

AVIII.3 Discussion

The observed net current of 1.5 kA gives a value ~ 0.03 for the ratio I_{NET}/I_{BEAM}. This is twice the value expected for a sharp boundary beam, LEE and SUDAN (1971) and some 150 times that for a smoothly varying current profile, KUPPERS et al. (1973). A similar discrepancy has been observed by DOVE et al. (1976) and may be due to enhanced plasma resistivity causing decay of the plasma return current.

The 40% drop in electron density may be due to a radial plasma expansion or the production of a high energy tail to the electron velocity distribution. For expansion to be the cause a value of 0.5 is required for the plasma β, corresponding to an energy density of ~ 2.10^{18} eV cm^{-3}, some two orders of magnitude greater than that obtained from laser scattering. A similar discrepancy has been experienced for neutral gas injection. The arguments regarding an electron tail closely follow those for injection into neutral gas, i.e. such tails would be unobservable here but have been observed by others. No conclusions can be drawn until this uncertainty has been resolved or some other interpretation is found.

Experiments with a preformed plasma were stopped when the glass chamber was damaged by a breakdown on a coil module. Future work is planned with a modified chamber having an outer screen. This will aid diamagnetic loop measurements. Spectroscopic measurements similar to those used in neutral gas are also planned. A variety of initial densities will also be tried.

ACKNOWLEDGEMENTS

This work was performed in the Plasma Physics Group at Imperial College of Science and Technology, University of London. I would like to thank all the past and present members of the group who have helped in various ways towards the realization of this thesis. Amongst these I would like to mention:

Mr. A.E. Dangor, my supervisor, for his constant encouragement, advice, assistance and considerable time working on the experiment

Dr. J.D. Kilkenny for his advice and assistance, particularly with the laser scattering work and the construction of the B_θ probes

Mr. J. Westlake and Mr. A. Cobley for technical assistance, notably the construction of the diode and laser amplifier

Professor M.G. Haines, Head of the Group, for his advice.

Considerable assistance also came from outside the group; in particular I would like to thank:

Dr. N. Ebrahim for his assistance with the absorption spectroscopy experiment

Mr. J.C. Martin and Mr. D. Forster for advice in the design and construction of high voltage pulse generators and vacuum diodes, and for the continued loan of the Marx generator

Dr. D.A. Hammer for his advice and assistance with the soft X-ray experiments

Miss Sarah F. Cowen for the typing of this manuscript

Mr. M. Pimm for technical assistance and instruction in the use of machine tools

Members of staff of the mechanical and glassblowing workshops, for technical assistance

Dr. S. Hamberger (now Professor) for his continued interest in the project

The Culham Laboratory for the loan of spark gaps and isolation

inductors, and for their financial support under E.M.R. contract CUL/899

The Science Research Council for their financial support under grant B/RG/64243.

Lastly, and by no means least, I thank my parents for their constant support, without which this work would not have been possible.

REFERENCES

ALFVEN, H., Phys. Rev., 55, p.425, 1939. On the Motion of Cosmic Rays in Interstellar Space.

ALTYNTSEV, A.T. et al. 4th I.A.E.A. conf. proc., 2, p.309, 1972. Collisionless Relaxation of an Ultrarelativistic Electron Beam in a Plasma.

ANDERSON, J.M. Rev. Sci. Inst., 42, No. 7, p.915, 1971. Wide Frequency Range Current Transformers.

BATES, D.R. et al. Proc. Royal Soc., 267 and 270, 1962. Recombination Between Electrons and Atomic Ions: I) Optically Thin Plasmas
II) Optically Thick Plasmas.

BOGDANKEVICH, L.S. and RUKHADZE, A.A. Sov. Phys. J.E.P.T., 14, No. 2, 1971. Stability of Relativistic Electron Beams in a Plasma and the Problem of Critical Currents.

BOOK, D.L. Revised N.R.L. Plasma Formulary, 1976 edit.

CHEN, F. Introduction to Plasma Physics, p.238, Plenum Press, 1974.

COOPER, J. Plasma Phys. (J. of Nucl. Energy), 5, p.285, 1963. On the High-Frequency Response of a Rogowski Coil.

DANGOR, A.E. et al. Proc. of the 9th European Conf. on Controlled Fusion and Plasma Physics, DP28, p.122, 1979. Axial Variation of the Energy Transfer From an Intense Relativistic Electron Beam to a Plasma.

DOVE, W.F. et al. A.P.L., 28, p.701, 1976. Localized Measurements During Intense Relativistic Electron Beam Interaction With a Cool Theta Pinch Plasma.

DREIKE, P. Proc. 6th I.A.E.A. conf. LAEA-CN-35/H4, 1977. Generation of Intense Ion Beams and their Application to Controlled Fusion Research.

EKDAL, C. et al. Phys. Rev. Lett., 33, No.6, p.346, 1974. Heating of a Fully Ionized Plasma Column by a Relativistic Electron Beam.

EVANS, D.E. and KATZENSTEIN, J. Rep. Prog. Phys., 32, p.207, 1969. Laser Light Scattering in Laboratory Plasmas.

FAINBERG, Ya.B. et al. Sov. Phys. J.E.P.T., 30, No.3, 1970. First pub. Zh. Eksp. Teor. 1969. Nonlinear theory of Interaction Between a "Monochromatic" Beam of Relativistic Electrons and a Plasma.

FREEMAN, J.R. et al. Proc. 6th I.A.E.A. conf. 1976. pub. 1977. IAEA-CN-35/F6. Particle Beam Fusion Research.

FRIED, B. and GOULD, R.W. Phys. Fluids, 4, No.1, p.139, 1961. Longitudinal Ion Oscillations in a Hot Plasma.

FRIEDMAN, M. Phys. Rev. Lett., 24, p.1098, 1970. Passage of an Intense Relativistic Electron Beam Through a Cusped Magnetic Field.

FORSTER, D. et al. Radiation Production Notes, Note 10. A.W.R.E. Report SSWA/JCM/714/162. Electron Beam Diagnostics Using X-rays.

GALEEV, A.A. et al. Sov. J. Plasma Phys., 1, No.1, p.5, 1975. Nonlinear Theory of the Modulation Instability of Plasma Waves.

GOLDENBAUM, G.C. Phys. Rev. Lett., 32, No.15, 1974. Plasma Heating by Intense Relativistic Electron Beams.

GOODMAN, M.J. Radiation Production Notes, Note 6, A.W.R.E. Report SSWA/MJG/6812/106. 30th Dec. 1968. Fig. 3. The Production, Transport and Focussing of Electron Beams with a $^{\nu}/_{\gamma} < 1$.

GRAYBILL, S.E. et al. J. App. Phys., 14, No.1, 1970. Observation of Energetic Ions from a Beam Generated Plasma.

GREENSPAN, M. Ph.D. Thesis, Lab. of Plasma Studies, Cornell University, 1976. Plasma Heating by a Relativistic Electron Beam: An Experimental Study.

GRIEM, H.R. Plasma Spectroscopy. McGraw-Hill Book Company. 1964.

GROVER, F.W. Inductance Calculations, Working Formulas and Tables. Dover Pub. Inc., 1962 edit.

HAMMER, D.A. Private Communication, 1977.

HAMMER, D.A. et al. J. App. Phys., 43, No.1, 1972. Interaction of Accelerating High Current Electron Beams with External Magnetic Fields.

HAMMER, D.A. and PAPADOPOLOUS, K. Nuc. Fus., 15, p.977, 1975. Tokamak Heating by Relativistic Electron Beams.

HUMPHRIES, S. et al. J. Appl. Phys., 48, p.2738, 1977. Extraction and Propagation of Rotating Intense Proton Beams from a Magnetically Insulated Diode.

JOHNSON, L.C. Astrophysical J., 174, p.227, 1972. Approximations for the Collisional and Radiative Transition Rates in Atomic Hydrogen.

JOHNSON, L.C. and HINNOV, E. J. Quant. Spec. Rad. Trans., 13, p.333, 1973. Ionization, Recombination and Population of Excited Levels in Hydrogen Plasmas.

JURGENS, B. et al. Proc. of 6th I.A.E.A. Conf., Vol. II, 1976. Energy Transfer of a Relativistic Electron Beam to a Plasma.

KAPETANAKOS, C.A. and HAMMER, D.A. Appl. Phys. Lett., 23, No.17, p.17, 1973. Plasma Heating by an Intense Relativistic Electron Beam.

KAYE, G.W.C. and LABY, T.H. Tables of Physical and Chemical Constants. 12th ed. Pub. Longmans, Green and Co. 1959.

KUPPERS, G. et al. Plasma Phys., 15, p.429, 1973. Current and Fields Induced in Plasmas by Relativistic Electron Beams with Arbitary Radial and Axial Density Profiles.

LAMPE, M. and SPRANGLE, P. Phys. of Fluids, 18, No.4, p.475, 1975. Saturation of the Relativistic Two-stream Instability by Electron-Trapping.

LEE, R.E. and SUDAN, R.N. Phys. of Fluids, 14, p.1213, 1971. Return Current Induced by a Relativistic Beam Propagating in a Magnetized Plasma.

MARTIN, J.C. High Voltage Notes, Note 2, A.W.R.E. Report SSWA/JCM/713/157. 16th March 1971. Fast Pulse Vacuum Flashover.

MILLER, P.A. and KUSWA, G.W. Phys. Rev. Lett., 30, No.20, p.958, 1973. Plasma Heating by an Intense Electron Beam.

NATION, J.A. and GARDNER, W.L. Nuc. Fusion, 11, p.5, 1971. An Experimental Investigation of the Microwave Radiation Emitted by a High Current Relativistic Electron Beam.

NISHIKAWA, K. J. of the Phys. Soc. of Japan, 24, No.5, 1968. Parametric Excitation of Coupled Waves. II Parametric Plasma-Photon Interaction.

OLSON, C. Phys. Rev. A, 11, No.1, p.288, 1975. Charge-neutralization Processes for Intense Relativistic Electron Beams in Low Pressure Neutral Gas.

and Phys. of Fluids, 18, No.5, p.585, 1975. Theory of Ion Acceleration by Drifting Intense Relativistic Electron Beams.

PAPADOPOLOUS, K. Phys. of Fluids, 18, No.12, p.1769, 1975. Non Linear Stabalization of Beam Plasma Interactions by Parametric Effects.

PAPADOPOLOUS, K. and PALMADESSO, P. Phys. of Fluids, 19, p.605, 1976. Excitation of Lower Hybrid

PIERCE, J.R. J. Appl. Phys., 19, p.231, 1948. Possible Fluctuations in Electron Streams Due to Ions.

PRONO, D. et al. Phys. Rev. Lett., 35, No.7, p.438, 1975. Plasma-Return-Current Heating by Relativistic Electron Beams with $\nu/\gamma \sim 10$.

and Physics International Report PIFR-557 Plasma Heating with Ultra-Intense Relativistic Electron Beams.

RANDER, J. et al. Phys. Rev. Lett., 24, No.6, p.283, 1970. Charge Particle Acceleration by Intense Electron Streams.

RUDAKOV, L.I. Sov. Phys. J.E.P.T., 32, No.6, 1971. Collective Slowing Down of an Intense Beam of Relativistic Electrons in a Dense Plasma Target.

SAGDEEV, R. Proc. of Symposium on Appl. Math., H. Grad, ed., 18, p.18, 1967.

SCHAMEL, H. et al. Phys. of Fluids, 19. No.6, 1976. Parametric Excitation of Ion Density Fluctuations in the Relativistic Beam Plasma Interaction.

SKINNER, C.H. Ph.D. Thesis, University of London, 1974. Absorption and Fluorescence Studies of Hot Plasmas Using Tuneable Dye Lasers.

SPITZER, l. Physics of Fully Ionized Gases, 1962. Pub. John Wiley and Sons, Inc.

SUNKA, P. Proc. of the 8th. European Conference on Controlled Fusion and Plasma Physics. Plasma Heating and Ion Acceleration by a Relativistic Electron Beam - R.E.B. Accumulation.

TAJIMA, T. J. Plasma Phys., 19, part I, p.63, 1978. Plasma Heating by a Relativistic Electron Beam with Secondary Instabilities.

THODE, L.E. Ph.D. Thesis, Cornell University, 1975. Plasma Heating by Intense Relativistic Electron Beams Due to Two-Stream and Return Current Interactions.

THODE, L.E. Phys. of Fluids, 19, No.2, p.305 and 831, 1976. Energy Lost by a Relativistic Electron Beam Due to Two-Stream Instability.

THODE, L.E. Phys. of Fluids, 20, No.12, p.2121, 1977. Effect of Electron-Ion Collisions on the Non-Linear State of the Relativistic Two-Stream Instability.

THODE, L.E. and SUDAN, R.N. Phys. Rev. Lett., 30, No.16, p.732, 1973. Two-Stream Instability Heating of Plasmas by Relativistic Electron Beams.

VANDEVENDER, J.P. Ph.D. Thesis, University of London, 1974. The Interaction of a High Current, Relativistic Electron Beam with a Plasma.

VANDEVENDER, J.P. et al. J. Appl. Phys., 47, No.5, 1976. Interaction of a High Current Relativistic Electron Beam with a Dense Plasma.

WEAST, R.C. Handbook of Chemistry and Physics. 52nd. edit. 1972. The Chemical Rubber Co.

WONG, A.Y. and QUON, B.H. Phys. Rev. Lett., 34, No.24, p.1499, 1975.

Spatial Collapse of Beam-Driven Plasma Waves.

Reprint from

"PLASMA PHYSICS
AND CONTROLLED
NUCLEAR FUSION RESEARCH"
1976
VOL.II

INTERNATIONAL ATOMIC ENERGY AGENCY
VIENNA, 1977

PLASMA HEATING BY AN INTENSE RELATIVISTIC ELECTRON BEAM

A.K.L. DYMOKE-BRADSHAW, A.E. DANGOR,
J.D. KILKENNY
Blackett Laboratory,
Physics Department,
Imperial College,
London,
United Kingdom

Abstract

PLASMA HEATING BY AN INTENSE RELATIVISTIC ELECTRON BEAM.

Experiments are reported on the heating of a hydrogen plasma by a relativistic electron beam with $v/\gamma \sim 2.4$, maximum voltage 350 kV, maximum current 50 kA, diameter 2 cm and duration 100 ns. The beam is injected along a magnetic field of 2 T into both neutral gas and preformed plasma. Experiments with neutral gas show that the heating depends on the beam pulse shape and angular scatter but that in all cases the primary heating mechanism is that due to return current dissipation. The maximum plasma energy observed is 3.3×10^{18} eV·cm^{-3} for injection of a fast-rising cold beam into 100 mtorr hydrogen. Preliminary heating experiments in a preformed plasma show that there is both expansion of the plasma and probably a high-energy tail.

1. INTRODUCTION

The heating of a plasma by a high-current relativistic electron beam has been observed in a number of previous experiments (1). In all these experiments the energy transfer to the plasma has been shown to be due to collective beam-plasma interactions. Two types of interactions have been identified: the e-e mode and the e-i mode. In the e-e mode, heating is due to the decay of the plasma waves generated directly by the electron beam; in the e-i mode, heating occurs due to the enhanced dissipation of the return current by the ion acoustic turbulence generated by the drifting plasma electrons. In a recent survey made by Thode (2), results of all the previous experiments have been interpreted as being due to the e-e mode by making allowance for the angular scatter of the beam electrons. However, this survey did not include the experiment of Prono et al. (3), in which a beam with a high v/γ and much larger current density was injected into a neutral gas. Significantly higher energy deposition (up to 10^{19}eVcm^{-3}) was observed and the energy transfer was unambiguously identified as being due to return current dissipation. Further it was found that the observed heating was such that the ion acoustic instability could exist only if the ionization was much smaller than seemed likely in the experiment. As a result the authors concluded that the enhanced return current dissipation was due to a replenishment of the low-frequency turbulence via a non-linear coupling of the e-e mode to ion density fluctuations as suggested by Papadopoulos (4).

In the experiments reported here we repeat the neutral gas injection experiments reported by Prono et al. with a beam having a similar current density but much lower v/γ. The observed heating is found to be nearly as large as that reported by Prono et al. but only for a beam having a low angular scatter. A dependence on the shape of the beam pulse is also observed. In all cases the heating is found to be due to dissipation of the return current, the anomalous resistivity being generated as described by Papadopoulos (4). However, observations of the broadening of H_α and H_β lines indicate that turbulence persists for long times after the beam.

A preliminary experiment on injection into a preformed plasma is also reported.

2. EXPERIMENTAL DETAILS

The nominal parameters of the beam used in the experiments are 350kV, 50kA, 100ns and 2cm diameter, giving a current density of $15kA \cdot cm^{-2}$ and a v/γ of 2.4. The beam is injected through an anode foil into the interaction chamber, filled with hydrogen at pressures from 0.1 to 3Torr, 30 cm long and 7.6 cm diameter. Three types of anode foils are used: 1) aluminized Mylar; 2) 12.5μm aluminium; and 3) 25μm aluminium. The chamber and diode are of stainless steel and are immersed in a slowly varying axial magnetic field. Typical magnetic fields used are 1.2 to 1.8T.

For injection into a preformed plasma the stainless steel chamber is replaced by a Pyrex tube of similar dimensions. The plasma source is the afterglow of a 20kV, 2μF z-discharge with coaxial return. Typical axial magnetic fields are about 50% higher due to the shorter penetration time of the pinch discharge assembly. The initial plasma conditions, measured by ruby laser Thomson scattering, can be varied from 5×10^{14} cm^{-3}, 1.5eV to 3×10^{15} cm^{-3}, 5eV, depending on the filling pressure and time at which the beam is injected. Approximately 50% ionization is obtained.

A combined calorimeter and Faraday cup with a self-integrating Rogowski coil is used to monitor the transmitted beam energy and the beam current. The device has an aperture of 4cm and is located at the far end of the interaction chamber.

In the neutral gas experiments the net current is monitored at three axial positions by Rogowski coils located at the wall of the chamber. The Faraday cup can be used to measure the net current within a 2cm radius by eliminating the foil and vacuum gap. However, when this is done, simultaneous measurement of the beam current is precluded. A small RC integrated multiturn probe coil is used to monitor B_θ at a radius of 2.4cm. The plasma diamagnetism is measured by a single-turn coaxial loop of radius 2.6cm located inside the chamber. Measurements of the broadening of H_α and H_β lines are made with a five-channel polychromator with 2.2A per channel and sighted transverse to the beam direction. The rise time of the monitoring equipment is restricted to 25ns for these measurements to improve the signal-to-noise ratio. An image-converter streak camera is used to monitor the radial extent of the light emission.

In the preformed plasma experiments the net current is measured by a Rogowski coil situated on the outside wall of

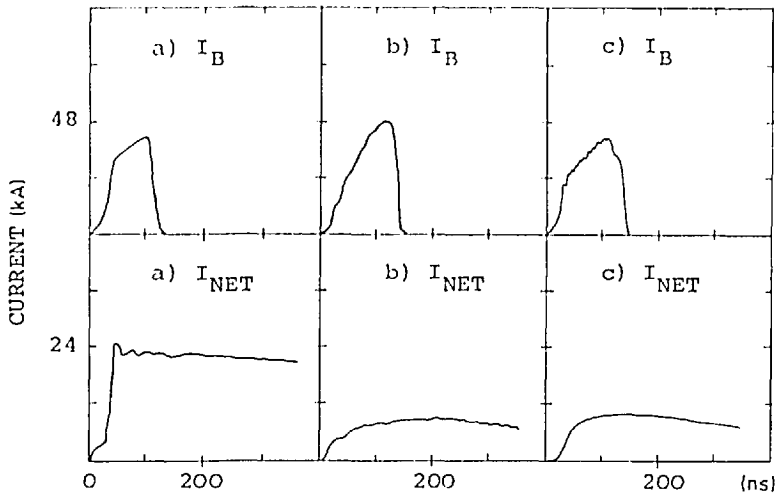

FIG.1. I_B and I_{net} waveforms for three cases:
(a) Fast beam with aluminized Mylar foil.
(b) Slow beam with aluminized Mylar foil.
(c) Fast beam with 25 μm aluminium foil.
All are for a 200 mtorr filling pressure.

the glass discharge tube and also by the Faraday cup with the vacuum region removed. Low-α ruby laser scattering is used to measure the electron density and the velocity distribution perpendicular to the beam. A seven-channel polychromator (13.4A per channel) is used in these measurements.

In the neutral gas experiments the energy deposited by return current heating and the resistivity are obtained by calculating $W_{ohm} = \int J_{pz} E_z \, dt$ and $\eta = E_z/J_{pz}$, where E_z is the inductive electric field and J_{pz} is the axial plasma current density. Both E_z and J_{pz} are obtained from the beam and net currents and by assuming that the current flow channels are equal and confined to the beam radius. The value of W_{ohm} and η so obtained neglects dissipation due to J_θ currents and is valid only if there is negligible plasma motion.

The diamagnetic loop signals are used to measure the perpendicular energy density by assuming pressure balance. The calculation neglects the paramagnetism due to helical current flow along the combined B_z and B_θ field lines and beam diamagnetism due to beam rotation and perpendicular beam temperature. Reversal of the signal is obtained when the B_z field is reversed and the polarity of the observed signal is consistent with diamagnetism.

3. RESULTS

3.1. Propagation characteristics

For injection into neutral gas, the diode behaviour is very dependent on the anode foil material and the gas pressure

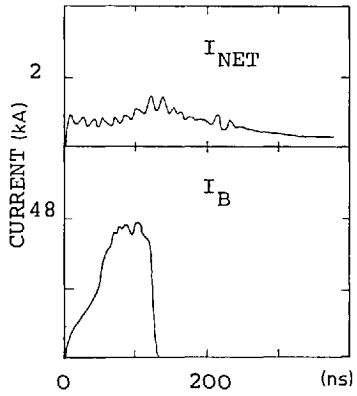

FIG.2. I_B and I_{net} waveforms for injection into a preformed plasma.

in the interaction chamber. With 25 μm aluminium anode foils, no significant change in performance is found over the pressure range 0.1 to 3 Torr H_2. However, for aluminized Mylar foils the performance degrades rapidly as the pressure is reduced to 100mTorr and by 20mTorr the transmitted current is only a few kA. This effect was also observed by Prono et.al. (3). Damage patterns at both ends of the interaction chamber show that the beam diameter is equal to that of the cathode. For all foils, the diode behaviour is such that two classes of beam pulses are generated: a slow pulse rising at about $3\times10^{11} A\cdot s^{-1}$ for the whole pulse duration and a fast pulse which has an initial rise of $1.2\times10^{12} A\cdot s^{-1}$ for 20ns and then a slower rise for the rest of the pulse. Both types of pulse have a fall time of less than 20ns. Some waveforms are shown in Fig.1.

When injecting into a low-pressure neutral gas, an initial I_{net} and an equal I_{beam} are observed corresponding approximately to the space charge unneutralized critical current (5). The duration is of some tens of nanoseconds and varies inversely with filling pressure. Again no such effect is observed for injection into a preformed plasma,

The streak photography shows that the light emission is confined at all times to a region of about 2cm diameter corresponding to the diameter and location of the beam channel. The photographs show that at low pressure there is an intense emission early in the beam and that at the end of the beam the light level falls. At higher pressures of around 1 Torr there is a more gradual increase of intensity during the beam followed by a rapid decrease on beam termination.

The net current is found to be a strong function of a) neutral gas filling pressure, b) beam rise time, c) anode foil material, and weak function of radius. No axial dependence is found. Some net current waveforms are shown in Fig.1. At filling pressures below 200mTorr, the net current has a fast rise followed by a slow decay. Typical waveforms are shown in Fig.1. At higher pressure the rise continues throughout the beam. The lowest degree of current

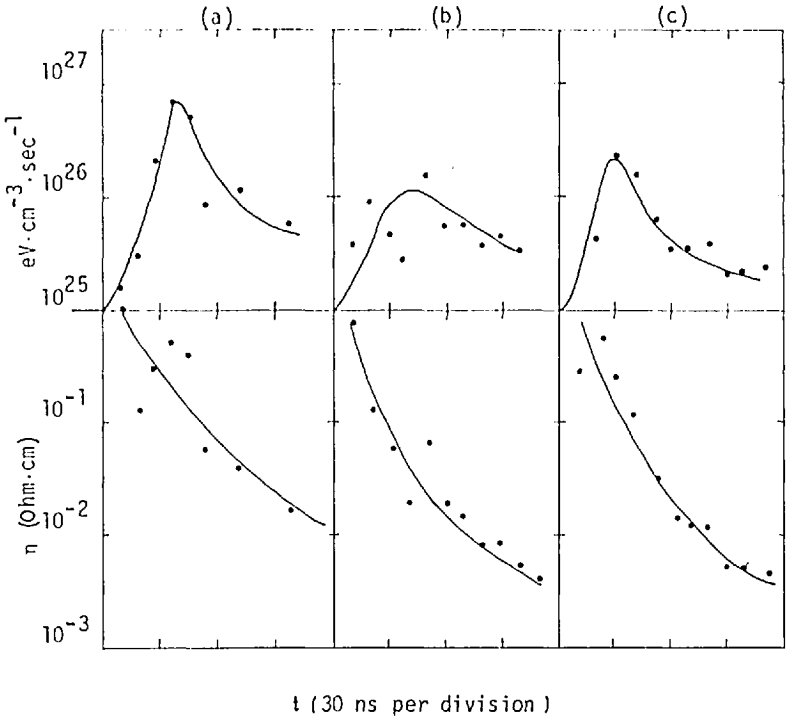

FIG.3. Energy deposition rates and plasma resistivities as a function of time for three cases shown in Fig.1.

neutralization, about 17%, is obtained at low pressures with an aluminized Mylar foil for a fast-rising beam. Current neutralization as high as 80% is observed for a slow-rising beam and aluminium anode foils also at low pressure. At pressures of 1Torr, the neutralization is fairly independent of beam shape or foil and is about 85%. Further increase in pressure results in a slightly lower neutralization.

Simultaneous measurements of I_{net} with the Faraday cup and wall monitors indicate that the return current channel is larger than the beam channel and that consequently there is a return current flow outside the Faraday cup aperture.

For injection into a preformed plasma the net current monitored at the wall is zero. The Faraday cup monitor, however, shows a small net current of about 1,5kA. A waveform is given in Fig.2. The value of the observed net current gives a value of I_{net}/I_{beam} of 0,03, which is twice the expected value for a beam with a sharp boundary (6) and a factor of 150 times that for a smoothly varying current profile (7). A similar discrepancy with theory has been reported by Dove et al. (1).

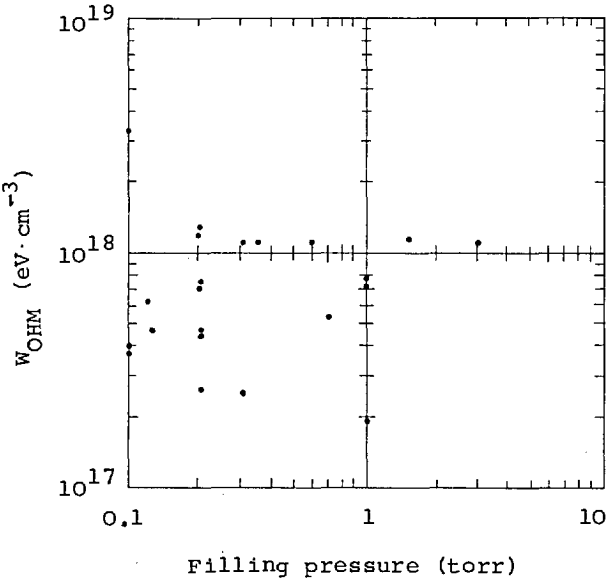

FIG.4. Plot of W_{ohm} versus filling pressure for various foils and beam rise times.

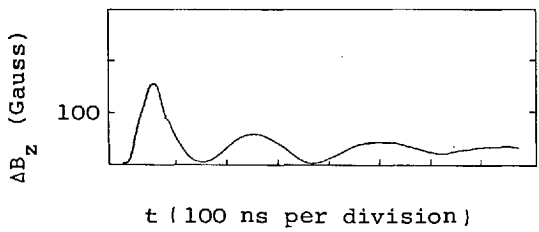

FIG.5. A typical diamagnetic loop waveform for injection into 0.5 torr with an aluminized Mylar foil.

3.2. Heating

The calculated values of J_{pz} E_z and the resistivity are shown in Fig.3 for three different cases. The net and beam current waveforms are given in Fig.1. Fig.4 is a plot of W_{ohm} vs pressure for all anode foils used and for both types of beam pulse.

The cases shown in Fig.3 indicate the variation of ohmic dissipation and resistivity with a) beam current rise time and b) anode foil. It is this dependence which leads to the large scatter of the points in Fig.4. An aluminized Mylar foil rather than solid aluminium foil or a fast-rising beam pulse invariably results in a higher total energy dissipation. Note that the resistivity drops significantly faster for shots with slow beam rise time or aluminium foils.

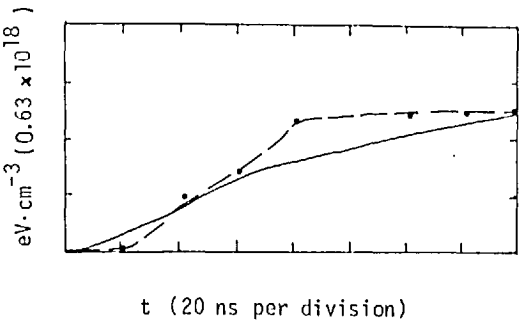

FIG.6. Comparison between the energy density measured from the diamagnetic loop (solid line) and from W_{ohm} (broken line), for injection into 0.2 torr with an aluminized Mylar foil.

A typical diamagnetic loop signal is shown in Fig.5. The first peak usually occurs at the end of the beam pulse or in some cases shortly afterwards. The characteristic oscillations shown are observed in all cases. The height of the first peak of the diamagnetic signal is closely correlated to the calculated ohmic heating as in the experiments reported by Prono et al. (3). Indeed, the energy density obtained from the diamagnetic signal closely follows $W_{ohm}=\int J_{pz}E_z dt$ up to the end of the beam pulse. This is illustrated in Fig.6 for a particular case. In all cases the agreement between the energy density derived from the diamagnetic signal and W_{ohm} is within a factor of two. These observations indicate that the heating is primarily due to ohmic dissipation of the return current.

For experiments with a preformed plasma, simultaneous measurements of I_{beam} and I_{net} have not been made. However, the decrease of I_{net} during the initial part of the beam (see Fig.2) indicates that there is an expansion of the heated plasma channel. Also, the inductance is not known since there is no detailed knowledge of the current paths. Hence the deposition of energy by return current heating in the preformed experiment has not been determined. However, laser scattering shows that for an initial plasma of number density 2.4×10^{15} cm^{-3} and electron temperature 3eV, the temperature increases to 15eV whilst the number density drops to 1.4×10^{15} cm^{-3} at the end of the beam pulse. The 40% drop in the number density can be due either to plasma expansion or a high-energy tail in the electron velocity distribution. However, if expansion is solely responsible for the observed change in number density, a value of 0.5 is required for the β of the plasma. This corresponds to an energy density in the plasma of 2×10^{18}eV·cm^{-3}, which is two orders of magnitude greater than the value obtained in the laser scattering experiment. Hence we conclude that there is high-energy tail which is beyond the spectral range monitored in the laser scattering experiment.

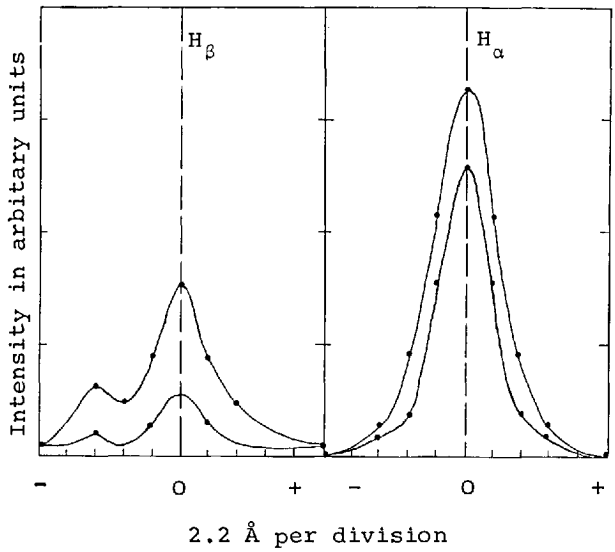

FIG.7. Line profiles for H_β at 80 and 300 ns and H_α at 60 and 300 ns for injection into 0.15 torr with 12.5 μm foils. In both cases the profile of lower intensity is that at 300 ns.

3.3. Line Broadening

Line broadening measurements of H_α and H_β lines are available only for injection into neutral gas with 12.5μm aluminium foils. Typical line profiles are shown in Fig.7. For the H_β line no significant polarization dependence is observed and the large subsidiary line on the blue side is presumed to be an impurity line. The half-half widths of both H_α and H_β typically vary from 2 to 4A, H_β remaining broad for a longer time than the H_α line after the beam.

The large widths observed for both H_α and H_β are not consistent with Doppler broadening even if the atom temperature is assumed to be that given by W_{ohm} and diamagnetic measurements. Neither can the thermal Stark broadening account for the observed width of the H_α line. The width of the H_β line can be due to thermal Stark broadening but only if the electron temperature is of the order of a few eV. Thus we conclude that there is a substantial contribution to the widths of the lines due to Stark broadening by the electric fields associated with plasma turbulence (8).

Information on the nature and level of the turbulence is not possible as the resolution of the polychromator is too coarse, the ion temperature is unknown, and thermal Stark broadening parameters for temperatures above 4eV are not available.

4. DISCUSSION AND CONCLUSION

The results presented above show that for injection into a neutral gas the energy transfer is due to return current

heating. The measured resistivity at the end of the beam pulse ranges from a few 10^{-2} ohm·cm to 10^{-3} ohm·cm, which is the limit of the measurement. The effective collision frequency cannot be obtained from these measurements since the number density is not known. However, for the 100 mTorr case which shows the highest observed plasma energy density (3.3×10^{18}eV·cm^{-3}), the ionization energy is small, and hence complete ionization may be assumed at the end of the beam. The measured resistivity at this time is 1.7×10^{-2} ohm·cm and this gives a value of ν_{eff} equal to 3.5×10^{11} s^{-1}, which is some four orders of magnitude greater than the classical electron-ion collision frequency for a temperature $T_e=W_{ohm}/n_c$ = 450eV. This value of ν_{eff} is about a tenth of the electron plasma frequency. Assuming complete ionization of course gives an upper bound to the ratio $\nu_{eff}/\nu_{classical}$.

That the heating depends on the angular spread and rise time of the beam indicates that the mechanism responsible for the enhanced return current heating is that proposed by Papadopoulos (4). According to this theory, the level of the ion acoustic turbulence is determined by the growth rate of the plasma waves generated by the beam electrons and this depends on both the angular spread of the beam and beam electron density. Thus for the fast pulse the initial beam electron density is high and hence a higher level of ion-acoustic turbulence is generated. Turbulence has been inferred from the broadening of H_α and H_β lines and it is found that the turbulence persists for times long after the beam.

The experiments on the heating of a preformed plasma are only preliminary. However, the observations do indicate that there is some heating which leads to an expansion of the plasma channel and that there is probably a high-energy tail in the electron velocity distribution. The mechanism responsible for the energy transfer has yet to be identified.

Acknowledgements

We wish to acknowledge the generous assistance of Mr.J.C.Martin and his group at AWRE Aldermaston with the generator, and members of the Plasma Physics Group at I.C., in particular Mr.L. Phillips, with the experiment. One of us (A,K,L,D-B) is supported by a UKAEA Culham Laboratory studentship. The work was partly funded by a grant from the Science Research Council.

REFERENCES

(1) DOVE, W.F., GERBER, K.A., HAMMER, D.A., Appl.Phys.Lett. 28 701 (1976) and references therein.

(2) THODE, L.E., Phys. Fluids 19 831 (1976)

(3) PRONO, D., ECKER, B., BERGSTROM, N., BENFORD, J., Phys.Rev.Lett. 35 438 (1975).

PRONO, D., ECKER, B., BERGSTROM, N., BENFORD, J., PUTNAM,S., Physics International Company report PIFR-557 (Feb.1975).

(4) PAPADOPOULOS, K., Phys. Fluids 18 1769 (1975)

(5) BOGDANKEVICH, L.S., RUKHADZE, A.A., Sov.Phys.-Uspekhi 14 163 (1971)

(6) LEE, R.E., SUDAN, R.N., Phys.Fluids 14 1213 (1971)

(7) KUPPERS, G., SALAT, A., WIMMEL, H.K., Plasma Phys. 15 429 (1973).

(8) GALLAGHER, C.C., LEVINE, M.A., Phys.Rev.Let. 30 897 (1973).

DISCUSSION

ON PAPERS IAEA-CN-35/G 2-1, G 2-2, G 2-3, G 2-4

K. PAPADOPOULOS: Not only the Naval Research Laboratory, Physics International and Imperial College experiments, which you mentioned, are consistent with the theory of non-linear stabilization of the kinetic instability by parametric effects (which we developed at NRL in 1973); the scalings of the Cornell and Netherlands experiments are likewise consistent with that theory. This is obvious, because in the kinetic stage the energy transfer efficiency depends on the growth rate (γ_L), which is inversely proportional to the square of the angular spread ($\gamma_L \propto 1/(\Delta\vartheta)^2$).

Also, I should point out that, even if the notions of the quasi-hydrodynamic instability are valid, they can cover at most a stage of only a few 5–10 ns. Accordingly, I would reject any attempt to interpret a steady-state injection experiment – in the presence of trapped-electron density fluctuations with $\delta n/n \approx 1$ and strong Langmuir turbulence – on the basis of such a theory.

J.N. BENFORD: Yes, the scaling of heating with $1/\overline{\Delta\vartheta^2}$ is a general feature of both hydrodynamic and kinetic modes. Note that in the hydrodynamic regime the saturation level is correlated with growth rate, which scales as $1/\overline{\Delta\vartheta^2}$.

The hydrodynamic regime has been taken as applying until an angular spread of $\overline{\Delta\vartheta} \sim 1/\gamma$ results. However, its range of applicability is in fact larger, namely until $\overline{\Delta\vartheta} \sim 1/\overline{\gamma}_{\|}$, which means that longer durations can be affected. This has been shown by Ferch and Sudan.

R.N. SUDAN: In the plasma heating scheme with electrons reflexing from a virtual cathode, how does the rate of plasma heating compare with the rate of disappearance of the virtual cathode due to build-up of ionization?

J.N. BENFORD: The virtual cathode apparently is destroyed by emission of ions from the plasmoid surface, driven by the electric field of the virtual cathode. When this occurs, the collector at the end of the system detects a burst of relativistic electrons leaving the system, corresponding to loss of the accumulated beam.

I. ALEXEFF: Supporting the suggestion that enough energy must be put into a plasma-gas mixture to support radiation losses before plasma heating can occur, I would note that this scaling of power versus pressure was demonstrated at Oak Ridge some ten years ago. These "burnout" experiments were reported in Phys. Rev. Letters. The required power for heating onset scales as the square of gas pressure.

PLASMA HEATING BY INJECTION OF RELATIVISTIC ELECTRON BEAMS IN NEUTRAL GAS

A.K.L.Dymoke-Bradshaw, A.E.Dangor, D.A.Hammer*, J.D.Kilkenny.
Blackett Laboratory, Imperial College, London, United Kingdom.

Abstract

We report laser scattering measurements of the electron density of a magnetized plasma produced by a relativistic electron beam (350kV, 50kA, 100ns, 2 cm diameter) injected into neutral hydrogen. Electron number densities of $\sim 5\ 10^{15}$ cm^{-3} corresponding to $\gtrsim$ 20% ionization and electron temperatures < 10eV are observed during the late stages of the e beam pulse. The corresponding electron thermal energy is much smaller than can be expected from the measured resistive heating due to the plasma return current. The measured resistivity appears to be classical. An ion temperature of $\sim$ 100eV is inferred from Doppler broadening of H_α and H_β radiation of charge exchange neutrals. This ion thermal energy is in reasonable agreement with the observed plasma diamagnetism. Soft X-ray measurements put a limit ($n_e < 3.7\ 10^{14}$cm^{-3}, $T_e > 2.6$keV) on the electron tail if the energy density in the tail is assumed equal to the plasma diamagnetism.

*Cornell University, Ithaca, New York 14853.

Two previous experiments[1,2], one at Physics International and the other at Imperial College, have demonstrated appreciable heating of a plasma by an intense relativistic electron beam. The beam was injected along a strong magnetic field into hydrogen gas. In the Physics International experiment energy densities up to 10^{19}eV cm^{-3} were observed with a beam of 200-500kA ($^{\nu}/_{\gamma} \sim 10$) and current density > 10kA cm^{-2}. Energy densities $\lesssim 3\ 10^{18}$ eV cm^{-3} were obtained in the Imperial College experiment with a beam of comparable current density but smaller current (50kA, $^{\nu}/_{\gamma} \sim 2.8$). The measured energy density could be accounted for in both experiments by the ohmic dissipation of the return current induced in the plasma by the beam. In our experiment the energy density is found to depend on the angular scatter of the beam. These observations are consistent with the non-linear interaction theories[3] according to which return current heating can occur at an enhanced rate due to ion acoustic turbulence generated by the parametric decay of the Langmuir wave instability driven by the beam electrons.

In both experiments the energy density was inferred from measurements of the plasma diamagnetism. In the present paper, we report direct measurements of the electron and ion temperatures. These show that the electron temperature is very much less than the ion temperature and that there may be an additional energy loss from the electrons. The measured ion temperature can account for the observed plasma diamagnetism.

The beam, 350kV, 50kA, 100ns and 2cm diameter, is injected through a 12.5μm aluminized mylar foil into an interaction chamber immersed in a uniform longitudinal magnetic field of about 15k Gauss. The chamber is of stainless steel, 7.6cm diameter, and 30cm long.

The electron temperature and number density were measured by laser scattering using a 400MW, 25ns ruby laser pulse. The laser beam was perpendicular to the e-beam and 90° scattering was observed from the plasma region 10cm downstream of the foil. The scattered profile was monitored with a seven channel polychromator over a range of 120Å to the blue side of the ruby line. In all instances, the scattering was low $\alpha(=1/|\underline{k}_i-\underline{k}_s|\lambda_D)$. Thus the scattered profile observed determines the electron velocity distribution perpendicular to the electron beam direction. Signal to noise limitations preclude any observation of a possible high energy tail.

The ion temperature was obtained by unfolding the H_α and H_β line profiles to give the Doppler and Stark broadening contributions. This is a relatively simple procedure since the Stark broadening for H_β is an order of magnitude larger than that for H_α. The Stark broadening measurement together with T_e from scattering yielded a value of n_e compatible with n_e from scattering. If a broadening other than thermal Stark, such as turbulence, were responsible for a significant part of the broadening, then agreement would not be expected. The Doppler width measured is due directly to neutral hydrogen

atoms. However, due to the large charge exchange cross section , the neutrals and ions are expected to be in equilibrium. The emission lines were observed perpendicular to the electron beam direction and thus the measurement represents the perpendicular temperature. The self absorption correction for the H_α emission line was determined in a separate experiment by measuring the optical depth with an H_α dye laser. Details of this experiment will be published elsewhere. Optical depth correction for the H_β line is small due to the much smaller oscillator strength of the transition.

On some shots laser scattering observations were made simultaneous with measurements of the ohmic dissipation of the return current. The ohmic dissipation per unit volume is given by $\int \eta J_p^2 \, dt$, where $J_p = J_{net} - J_B$ is the plasma current density, and $\eta = E_z/J_p$ is the resistivity. Here $E_z = L \frac{d I_{net}}{dt}$ is the inductive electric field and L is the inductance per unit length of the current channel. The quantities J_p and E_z depend on the beam and plasma current distributions. The beam current distribution, inferred from damage patterns, was found to be uniform and equal to the cathode diameter. The plasma current distribution was assumed to be the same. This assumption is in agreement with streak photography, laser scattering and H_α absorption measurements, which indicate that the plasma was uniform and existed only within the beam channel. Measurement of B_θ at 100mT with two magnetic probes at 2.8cm and 3.6cm from the axis

indicated that the current density outside the beam channel was about 60 A cm^{-2} compared with 8 kA cm^{-2} within the beam at 100mT.

Laser scattering measurements were not possible during the first portion of the beam pulse due to large background light emission. Figs. 1 and 2 show typical scattering data and H_α, H_β line profiles. Clearly, the distribution is non Maxwellian at the early time and has been interpreted as a two temperature component distribution. Fig.3 is a plot of n_e and T_e as a function of time at two pressures. (The larger temperature is plotted where non-Maxwellian distributions were observed). The scatter is large presumably due to beam non-reproducibility. The plots clearly show that the electron temperature is low, $T_e \lesssim$ 10eV and that the degree of ionization high, varying from 0.2 to 1.0. Both n_e and T_e show little variation after the beam. The ion temperature, shown as a function of time in Fig.4, is much larger than the electron temperature, at early times $T_i \sim$ 100eV.

The decay of the ion temperature can be explained by equipartition to the electrons. The dashed line in Fig.4 is the equipartition curve for a constant T_e equal to 5eV. Note that at late times T_i appears to be larger than can be expected from equipartition.

The measured resistivity is plotted as a function of time in Fig.5, and is compared in Table 1 with the classical value using the observed n_e and T_e from the scattering measurements. Good agreement is shown. This is to be

expected since $T_i >> T_e$ precludes, by ion Landau damping, the growth of ion acoustic turbulence. Note that the resistivity comparison is restricted to late times when n_e and T_e are known. Table 2 compares the energy density in the electrons with that due to return current heating. The ion energy density and that inferred from plasma diamagnetism is also given. Clearly the electron energy density is too low, even if ionization energy is included. The ion energy density can account for the diamagnetism observed.

The energy balance of the electrons is determined by

$$\frac{d}{dt}\{\frac{3}{2} n_e k T_e\} = \eta J_p^2 + P_{eq} - P_{ion} - P_{line} - P_{br} - P_{cond}$$

where ηJ_p^2 is the return current heating rate, P_{eq} is the equipartition term and P_{ion}, P_{line}, P_{br} and P_{cond} are due to ionization, line radiation, bremsstrahlung and electron thermal conduction. These terms are:

$$P_{eq} = n_e \nu_{eq} (T_e - T_i) \qquad eV\ s^{-1}\ cm^{-3}$$

$$P_{ion} = n_e n_o S_i I = \frac{n_e n_o 10^{-5} T_e^{\frac{1}{2}} e^{-I/T_e}}{I(6+T_e/I)}$$

$$P_{line} = \sum_{n=3} n_e n_o \chi_{1n} I_{n2} = \sum_{n=3} n_e n_o 1.6\ 10^{-5} f_{1n} \bar{g} \frac{I_{n2}}{I_{n1}} e^{-I_{n2}/T_e}$$

$$P_{br} = 1.06\ 10^{-13}\ n_e^2\ T_e^{\frac{1}{2}}$$

$$P_{cond} = \frac{\partial}{\partial z} (\kappa \frac{\partial T_e}{\partial z})$$

where ν_{eq} is the e-i equipartition rate, S_i and χ_{1n} are the rate coefficients for ionization and excitation from the ground state to level n, I is the ionization energy of hydrogen, I_{n2} the energy difference between level n and 2,

and κ is the electron thermal conductivity. Temperatures are in eV and densities in cm^{-3}. To calculate P_{line} we have assumed that the plasma is optically thick to the Lyman series and that all downward transitions are radiative. Collisional de-excitation and self absorption is neglected and thus P_{line} is an over estimate. Conduction perpendicular to the beam is small since $\omega_{ce}\tau$ is large.

Typically for $n_o \sim 10^{16} cm^{-3}$, $\eta J_p^2 > 10^{25}$ eVs^{-1} cm^{-3} is observed as shown in Fig.5. Taking $n_e \sim 5\ 10^{15} cm^{-3}$, $T_e \sim 5eV$, $T_i \sim 100eV$, and the scale length of the temperature variation as 10 cms, we find $P_{eq} \sim 10^{25}$ eV s^{-1} cm^{-3}, which is a transfer of energy to the electrons. The loss terms are

$P_{ion} \sim 9\ 10^{23}, P_{line} \sim 5\ 10^{23}, P_{br} \sim 6\ 10^{18}, P_{cond} \sim 5\ 10^{20}$ eV $s^{-1} cm^{-3}$

Clearly, there is a large unaccounted loss of the order of 10^{25} eV s^{-1} cm^{-3}. Impurity line radiation ($\sim Z^2$) cannot effect the energy balance since large Z is not expected at these low temperatures. This could be explained by an ionization rate five times larger than calculated.

A possible mechanism for ion heating is that due to ion Landau damping of the ion acoustic wave generated by the parametric decay of the beam excited Langmuir instability. However it is not clear whether the parametric decay will occur for situations where ion Landau damping is large. The process, if it occurs, should give rise to a high energy electron tail. An attempt has been made to detect such a tail by looking at the soft X-ray emission from the plasma. No such emission was detected above the sensiti-

vity of the detectors, which gives a tail with $n<4\ 10^{14}cm^{-3}$ and $\bar{\varepsilon}>3$ keV, if $n\bar{\varepsilon}$ is taken to be equal to the diamagnetic signal. Ion heating by radial space charge fields generated by beam trapping has been observed[4]. Beam trapping is unlikely in our experiment as the beam is cold and the field uniform. Increasing the beam scatter by using a thick anode foil significantly decreased the diamagnetic signal.

References

1. D.Prono et al, Appl.Phys.Lett. 28,701 (1976)
2. A.K.L.Dymoke-Bradshaw et al Plasma Physics and Controlled Nuclear Fusion Vol II,555 (IAEA, 1977)
3. L.E.Thode and R.N.Sudan Phys.Fluids 18,1552 (1975)
   K.Papadopolous Phys.Fluids 18, 1769 (1975)
   H.Schamel et al Phys.Fluids, 849 (1976).
4. Yu.E.Kolyada et al, Sov.Phys,Tech.Phys,47,47 (1977)

TABLE 1

SHOT	τ ns	η measured	η classical
(2) 17-2-77	150	$5\ 10^{-3}$	$4.6\ 10^{-3}$
(2) 1-3-77	170	$1\ 10^{-3}$	$4.9\ 10^{-3}$
(1) 4-3-77	90	$3\ 10^{-3}$	$4.3\ 10^{-3}$

η is in ohm cm

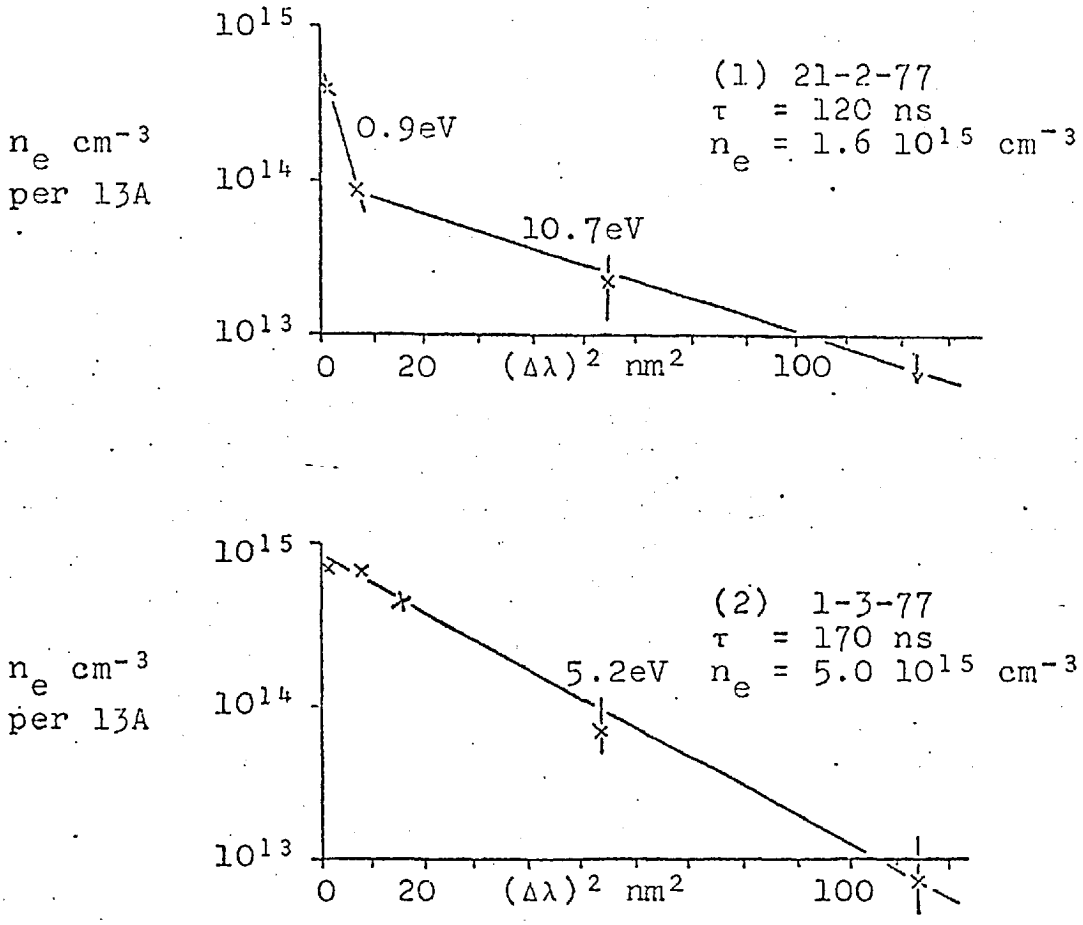

Fig. 1 Low α scattering spectra showing relaxation to a Maxwellian.

TABLE 2

SHOT	$\int nJ_p^2\,dt$	$n_e\{^3{}_2\,kT_e+I\}$	$^3{}_2 n_i kT_i$	W_{dl}
(2) 17-2-77	6.8 10^{17}	0.5 10^{17}		
(2) 1-3-77	7.3 10^{17}	0.9 10^{17}		
(1) 4-3-77	5.6 10^{17}	0.5 10^{17}		
Averaged over 2 shots			1.3 $10^{18}\pm.3$	
Averaged over 5 shots				1.2 $10^{18}\pm.6$

Filling pressure 200mT H_2. Energy densities in eV cm^{-3}

SHOT (1) 26-7-77

FWHM = 4.1

$\Delta\lambda_d$ = 4.1 → 65.6 eV

$\Delta\lambda_s$ = 0.16 → 5.0 $10^{15}cm^{-3}$

H_α @ 50ns

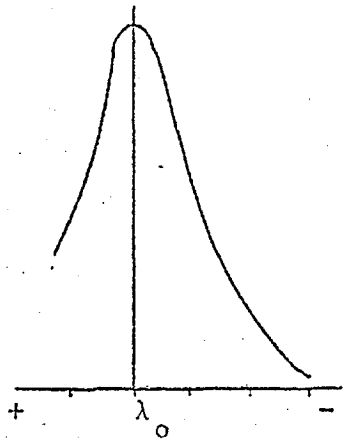

2.2A/div

FWHM = 2.2

$\Delta\lambda_d$ = 2.2 → 19 eV

$\Delta\lambda_s$ = 0.13 → 3.8 $10^{15}cm^{-3}$

H_α @ 150ns

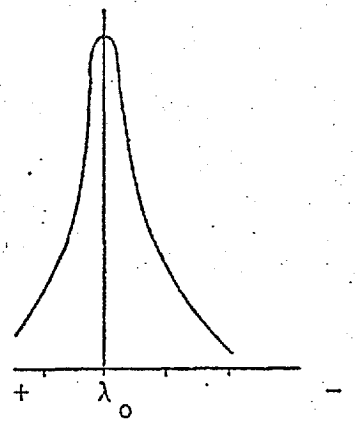

2.2A/div

SHOT (6) 26-7-77

FWHM = 6.82

$\Delta\lambda_d$ = 3.04 → 65.6 eV

$\Delta\lambda_s$ = 6.1 → 5.0 $10^{15}cm^{-3}$

H_β @ 50ns

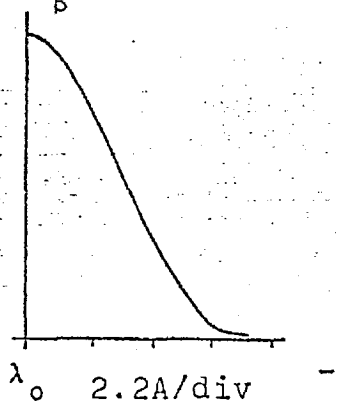

FWHM = 5.28

$\Delta\lambda_d$ = 1.6 → 19 eV

$\Delta\lambda_s$ = 5.03 → 3.8 $10^{15}cm^{-3}$

H_β @ 150ns

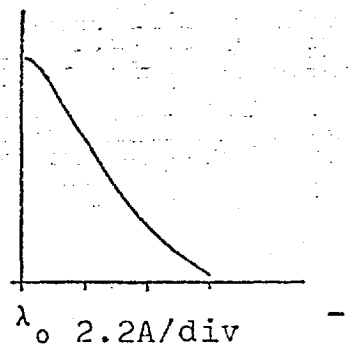

Fig. 2 Typical Hα and Hβ line profiles. Hα corrected for self adsorption

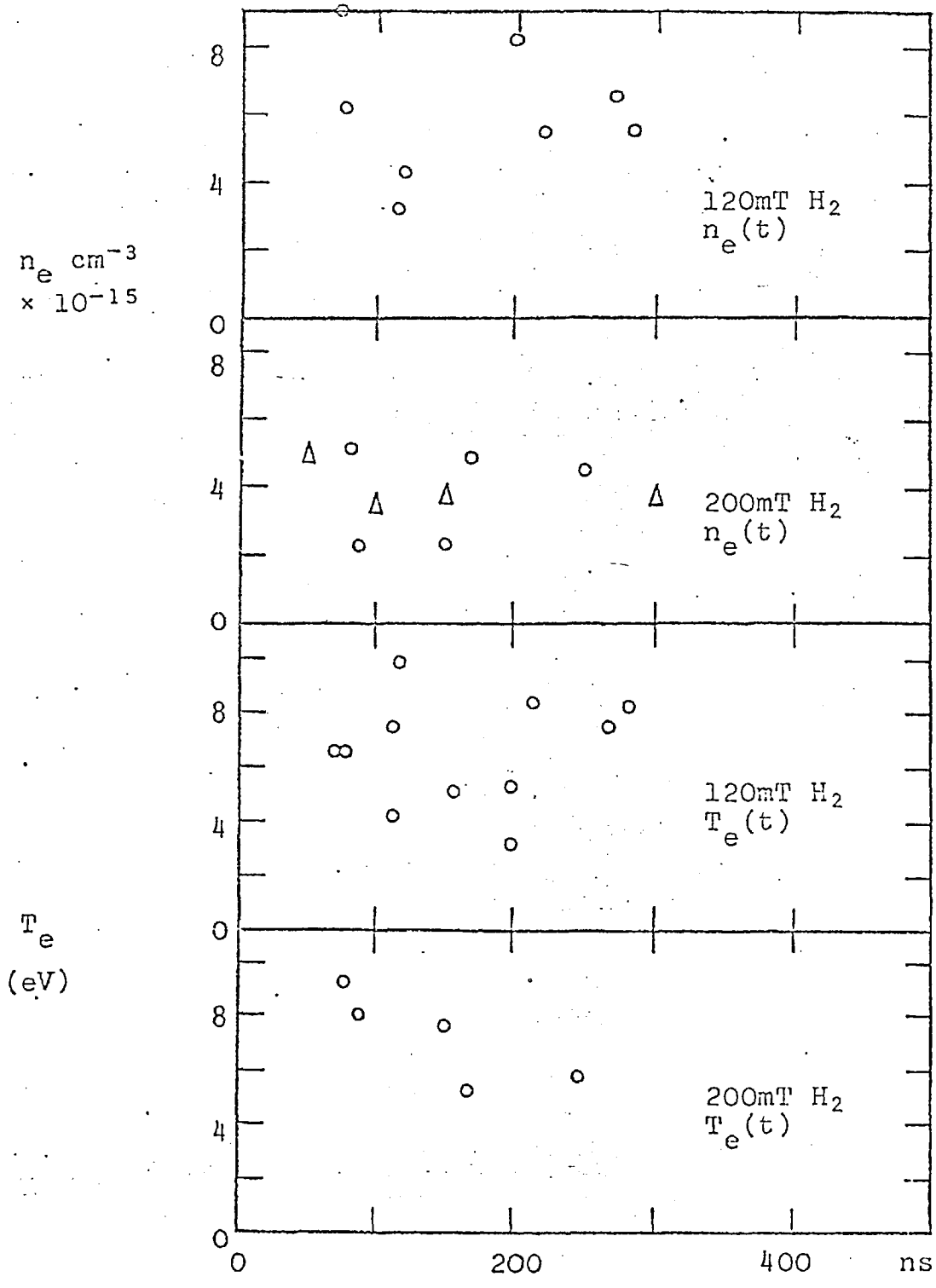

Fig. 3 Plots of n_e and T_e versus time for two filling pressures.

o points are from laser scattering

Δ points are from Stark broadening of H_α & H_β.

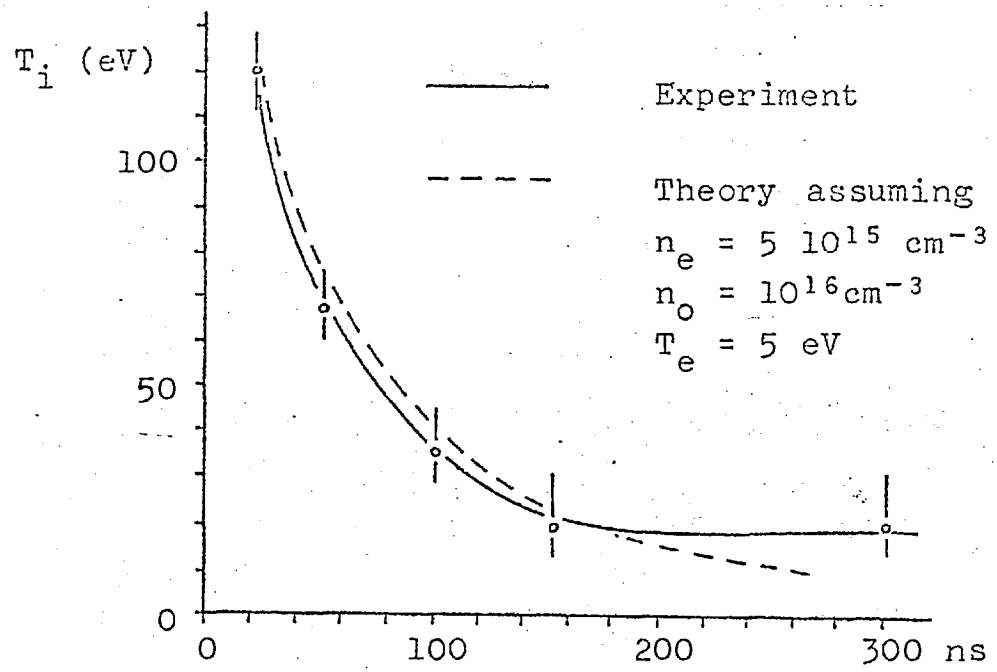

Fig. 4 Plot of T_i versus time from Hα profiles. Theoretical plot is from electron-ion equipartition.

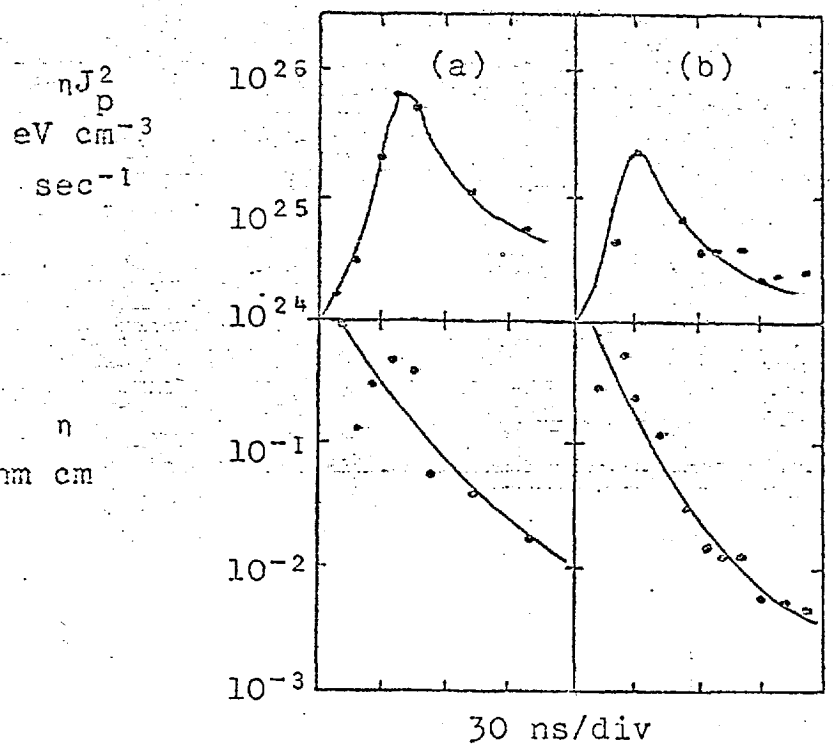

Fig. 5 Plots of ηJ_p^2 and η versus time.
(a) 12.5μm Al/My anode. (b) 25μm Al anode.

ENERGY DEPOSITION IN NEUTRAL HYDROGEN BY AN INTENSE RELATIVISTIC ELECTRON BEAM

A.K.L. Dymoke-Bradshaw, A.E. Dangor, J.D. Kilkenny, L.J. Phillips
Blackett Laboratory, Imperial College, London, United Kingdom

Abstract: Measurements of the energy dissipated by the return current induced when an intense relativistic electron beam is injected into neutral hydrogen are compared with the observed plasma diamagnetism and the electron energy obtained by laser scattering. These show that there is either a high energy electron tail or that the ions are heated preferentially.

In a previous paper (1) we reported that the energy deposited in a plasma by a relativistic electron beam injected into neutral hydrogen was primarily due to return current dissipation, the evidence being a close correlation between W_{OHM} ($= \int J_p . E_z . dt$) and W_{DL} the plasma diamagnetic energy. In this paper we report further evidence for this and measurements of low $\alpha (= 1/k_s \lambda_D)$ scattering to determine the electron number density and the low energy electron velocity distribution. Simultaneous W_{OHM} measurements were performed. The radial distribution of B_θ outside the beam channel has been investigated by a double probe arrangement.

The beam, whose parameters, as in (1) are 350kV, 50kA, 100ns, 2 cm diameter, is injected through a 12.5μm aluminised mylar foil into a 7.6 cm diameter chamber immersed in an axial magnetic field of ~ 1.5 Tesla. Filling pressures varied from 0.1 to 1 Torr hydrogen. Scattering was performed with a 400MW ruby laser incident perpendicular to the beam. The light scattered perpendicular to both the laser and the electron beam was spectrally resolved with a 7 channel polychromator over 12 nm on the blue side of 694.3 nm. Scattering was restricted to filling pressures in the range 0.1 to 0.2 Torr where high values of W_{OHM} have been obtained. B_θ probe measurements indicate that the axial current outside the beam channel is small, typically 60 amps/cm^2 at 0.1 Torr, compared with 8kA/cm^2 in the beam channel. This confirms the assumption made for calculating W_{OHM} in (1), that the return current is confined to the beam channel. Analysis shows that the resistivity is 10 Ω-cm, giving $n_e < 10^{-4}\, n_{neutral}$ outside the beam channel. This resistivity is a factor 5 times larger than can be derived from data in (2).

Results of some shots are summarised in Table 1 and some typical scattering data shown in Figure 1. This shows a non-Maxwellian velocity distribution at early times, which has been interpreted as a two temperature component plasma. Figure 1 also shows that at late time relaxation to a Maxwellian is observed. Ionization greater than 20% was observed in all shots, increasing to $\geq$50% at late times. The observed energy W_{the} (including ionization) in the electron velocity distribution sampled in the scattering experiment is ~ 20% of W_{OHM} as can be seen in the table. The largest value of W_{OHM} measured was found to be associated with a low degree of ionization.

Measurements of W_{OHM} and peak W_{DL} as shown in the Table are in reasonable agreement. So is their temporal variation as shown in (1). This indicates that there is no rapid loss of energy from the system due to radiation or thermal conduction. The discrepancy in the observed energies, W_{OHM} and W_{the}, must be due either to energetic ions or to a very high velocity tail in the electron distribution.

Electron tails have been predicted, (3) and there is some experimental evidence for this from X ray emission, (2). However, spectral profile measurements of the H_α and H_β emission lines which were previously reported, (1) suggest that the energy could be in the ions. The lines have typical f.w.h.m. of 0.56 nm. H_α broadening is a factor of 10 larger than that due to thermal Stark effects for the measured n_e. If the broadening is interpreted as a Doppler width this corresponds to energies $\geq$200 ev thus accounting for the observed discrepancy. A high α scattering experiment is in progress to measure the ion temperature to check this.

References:

(1) A.K.L. Dymoke-Bradshaw, A.E. Dangor, J.D. Kilkenny 6th IAEA Conference on Plasma Physics and Controlled Nuclear Fusion September 1976

(2) D.S. Prona et. al., Physics International report PIFR-557 February 1975

(3) L.E. Thode and R.N. Sudan Phys. Rev. Lett. 30, 732 (1973)
K. Papadopoulos Phys. Fluids, 18, 1769 (1975)

TABLE 1.

Shot No.	W_{OHM} eVcm^{-3}	W_{DL}(max) eVcm^{-3}	$n_e(t)$ cm^{-3}(ns)	T_{e1} eV	T_{e2} eV	W_{the} eVcm^{-3}
1	$7.0 \cdot 10^{17}$		$5.0 \cdot 10^{15}$(170)	5.2		$1.1 \cdot 10^{17}$
2	$2.3 \cdot 10^{18}$		$1.6 \cdot 10^{15}$(120)	0.9	10.7	$3.6 \cdot 10^{16}$
3			$5.0 \cdot 10^{15}$(144)	3.4	8.4	$1.2 \cdot 10^{17}$
4	$7.5 \cdot 10^{17}$	$5.5 \cdot 10^{17}$				
5	$1.4 \cdot 10^{18}$	$1.2 \cdot 10^{18}$				

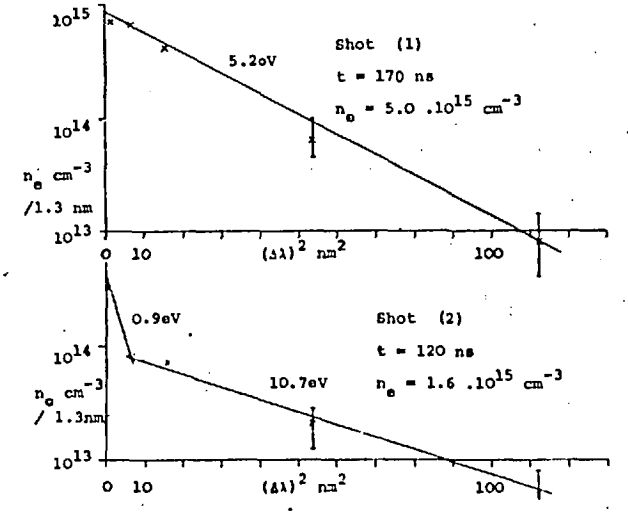

Fig. 1 Showing scattered light spectra of table 1.